INFORMATION TO USERS

NONINVASIVE IMAGING

OF EPICARDIAL POTENTIALS:

REGIONAL CONSTRAINTS AND CLINICAL

APPLICATIONS

By

Cindy Jane Penney

SUBMITTED IN PARTIAL FULFILLMENT OF THE
REQUIREMENTS FOR THE DEGREE OF
DOCTOR OF PHILOSOPHY
AT
DALHOUSIE UNIVERSITY
HALIFAX, NOVA SCOTIA
SEPTEMBER 1999

0-612-49284-2

Canada

DALHOUSIE UNIVERSITY

FACULTY OF GRADUATE STUDIES

The undersigned hereby certify that they have read and recommend to the Faculty of

Graduate Studies for acceptance a thesis entitled "Noninvasive Imaging of Epicardial

Potentials: Regional Constraints and Clinical Applications"

by   Cindy Jane Penney

in partial fulfillment of the requirements for the degree of Doctor of Philosophy.

Dated: August 23, 1999

External Examiner

Research Supervisor

Examining Committee

ii

DALHOUSIE UNIVERSITY

Date: **September 1999**
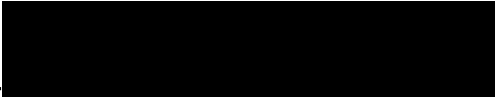
Author: **Cindy Jane Penney**

Title: **Noninvasive Imaging of Epicardial Potentials:**
Regional Constraints and Clinical Applications

Department: **Physiology and Biophysics**

Degree: **Ph.D.**   Convocation: **October**   Year: **1999**

Permission is herewith granted to Dalhousie University to circulate and to have copied for non-commercial purposes, at its discretion, the above title upon the request of individuals or institutions.

Signature of Author

iii

I dedicate this work

to my family.

Contents

List of Tables

List of Figures

Abstract

Electrocardiograms (ECGs) recorded from the body surface reflect electrical activity of the heart. When a coronary artery is occluded, as occurs in balloon-inflation coronary angioplasty, blood flow is suspended, cellular oxygen supplies are depleted, and ischemia develops, altering cardiac electrical activity. The aim of this study is to locate ischemic regions of the heart by computing an image of the potentials on the heart surface from the body-surface ECGs. Rigorous mathematical methods are developed, which introduce regional constraints to overcome the ill-posed nature of this problem.

Applying analytical techniques to increase the accuracy of the discretized torso-heart system improved a first estimate of the epicardial-potential distribution, as tested by simulated potential distributions. The composite regional constraint—with spatial smoothing of low-amplitude potentials, removal of spurious extrema, and temporal smoothing—was developed and applied, further refining the solution. Calculating the regularization parameter with the newly introduced Slope Estimation Method resulted in near-optimal solution for simulated potential data. This inverse solution was successful in localizing the ischemic zone to a region perfused by the occluded artery, and showed very good spatial agreement with localization by radionuclide myocardial-perfusion imaging. During balloon inflation, epicardial electrograms from the ischemic zone had ST-segment and QRS-complex changes indicative of ischemia. Overall, the results suggest that the technique of calculating epicardial potentials from multiple ECGs recorded on the body surface holds great promise as a noninvasive imaging modality.

Acknowledgements

I wish to thank my supervisors, Dr. B. Milan Horáček and Dr. John C. Clements for their support, guidance and encouragement. I would also like to thank Brian Hoyt, Paul MacInnis and Jim Warren for always being there when I needed technical support and Clyde Clements for sharing his vast knowledge of LaTeX.

Finally, I would like to thank my family: my parents, Andrew (1929-1985) and Winifred Ross, who always believed I could achieve any goal, my mother-in-law, M. Beulah Penney who passed away before the completion of this work, but was always one of my greatest supporters, and, most of all, my husband Joseph and son Stephen who loved and encouraged me throughout the course of this work.

Chapter 1

Introduction

Electrocardiograms (ECGs) recorded on the body surface reflect electrical activity within the heart. Standard clinical ECGs are routinely used to diagnose abnormalities in electrophysiological cardiac events, and they are sufficient in many circumstances. Occasions do arise, however, when relevant information is located outside the sampling area. Body-surface mapping of electrical potentials collects data from all regions of the torso and contains valuable diagnostic information. To extract this information requires an understanding of the relationship between this extensive set of data and the underlying cardiac electric activity. The ability to translate this noninvasively accessible data from the body surface to the surface of the heart would allow better diagnosis of underlying cardiac events. Although exact transformations of this kind are unknown, rigorous mathematical methods have been developed to calculate estimates of the electrical activity on the heart (epicardial) surface.

Estimation techniques for noninvasively imaging epicardial potentials are solutions to the inverse problem of electrocardiography. Difficulties arise in the computation of these images because the problem is ill-posed; that is, small perturbations of the potentials recorded on the body can cause large deviations in the computed epicardial potentials. Mathematical methods which impose physiological constraints on the solution are used to overcome this difficulty. The quality of the estimated epicardial image depends upon the choice of these constraints.

The aim of this study was to compute, from noninvasively sampled body-surface data, estimates of epicardial potentials that would be sufficiently accurate for use in clinical applications. A major part of this study is concerned with an in-depth analysis of mathematical techniques for refining the estimated epicardial-potential images. As a result of this analysis, specific constraints were selected for assessing the ability of these techniques to compute noninvasive images of epicardial potentials which would successfully reflect underlying cardiac activity in patients with acute regional ischemia induced by balloon-inflation coronary angioplasty.

The mathematical formulation of the forward problem, a prerequisite to solving the inverse problem, is presented in Chapter 2. Chapter 3 introduces the inverse problem with Tikhonov regularization methods. Regional constraints for the estimated epicardial images are extensively discussed in Chapter 4. Chapter 5 explores the capability of several mathematical methods to consistently determine an appropriate regularization parameter. Based on this analysis, a specific method was selected for use in a clinical application. Chapter 6 presents the results of applying this method in a controlled model of acute regional ischemia. The conclusions of the completed study are summarized in Chapter 7. In addition, Appendix A describes the tesselated torso and epicardial surfaces required for formulation of the problem, Appendix B describes the propagation model used to create activation-wavefront maps for testing the forward and inverse solutions, and Appendix C describes the test distributions for single- and multiple-dipole sources.

Chapter 2

Forward Problem

2.1 Introduction

Basic methods for solving the forward problem of electrocardiography have been known since the 1960s. Initially, the forward solution was used to calculate potentials on the torso surface from dipolar sources located within the heart region [6, 8, 48]. Later, when inverse methods were sought for calculating potentials on the epicardial surface [7, 9, 132], a transfer matrix between epicardial and torso surfaces was required. This chapter describes the latter form of the forward problem, defined as the calculation of torso-surface potentials from the given potentials on the epicardial surface. The boundary-element method (BEM) for realistically shaped triangulated surfaces (Appendix A) of the heart and torso was used.

The forward problem is first formulated for triangles, and refinements to transfer-coefficient matrix calculations are described. Next, the test data sets of epicardial and torso-surface potential distributions for various single-dipole or multiple-dipole sources are described, and forward solutions are calculated, forward errors are quantified, and results are presented and discussed.

2.2 Problem Formulation

The forward problem of electrocardiography can be formulated as a calculation of the potentials $\mathbf{\Phi}_B = (\phi_B^1, \ldots, \phi_B^m)$ at $m(m > n)$ area elements on the body surface S_B from the observed potentials $\mathbf{\Phi}_H = (\phi_H^1, \ldots, \phi_H^n)$ at n area elements on the epicardial surface S_H.

For applications in electrocardiography, the quasistatic approximation of Maxwell's equations adequately describes [126] the system depicted in Fig. 2.1.

This leads to the boundary-value problem for Laplace's equation

$$\mathbf{\nabla} \cdot \sigma \mathbf{\nabla} \phi(\mathbf{p}) = 0, \qquad \mathbf{p} \in B; \qquad \mathbf{\nabla} \phi(\mathbf{p}) \cdot \mathbf{n}_B = 0, \qquad \mathbf{p} \in S_B \qquad (2.1)$$

where B is a homogeneous and isotropic volume conductor (the human torso) containing the region of bioelectric sources H, σ is the scalar conductivity of B, $\phi(\mathbf{p})$ is the electric potential at a field point $\mathbf{p} = (x, y, z)$, and S_H and S_B are smooth surfaces with unit normals $\mathbf{n}_H$ and $\mathbf{n}_B$ that are oriented outward with respect to region H [7].

The problem stated as Eq. 2.1 can be solved for an arbitrarily shaped volume conductor by means of either a finite-element [140, 142, 162] or boundary-element [5, 6, 8, 43, 48, 94] methods. The boundary-element method, which was employed in this study, requires the application of Green's integral identity

$$\int_V \left[\phi \Delta \frac{1}{r} - \frac{1}{r} \Delta \phi \right] dV = \int_S \left[\phi \mathbf{\nabla} \frac{1}{r} - \frac{1}{r} \mathbf{\nabla} \phi \right] \cdot \mathbf{n} dS \qquad (2.2)$$

to transform Eq. 2.1 into an equivalent boundary-integral equation for the potential ϕ at field point $\mathbf{p}$ on $S_H \cup S_B$ [7, 126]

$$2\pi \phi(\mathbf{p}) = \int_{S_B^-} \phi_B \mathbf{\nabla} \frac{1}{r} \cdot \mathbf{n}_B dS - \int_{S_H^-} \phi_H \mathbf{\nabla} \frac{1}{r} \cdot \mathbf{n}_H dS - \int_{S_H^-} \frac{1}{r} \mathbf{\nabla} \phi_H \cdot \mathbf{n}_H dS, \qquad (2.3)$$

where S_B^- and S_H^- denote integration over the surfaces S_B and S_H, with the singularity removed (thus yielding the result -2π instead of -4π [5, 29, 149]); $dS = dS(\mathbf{q})$ is the differential of the integration surface; and the term $\mathbf{\nabla} r^{-1} \cdot \mathbf{n} dS = (1/r^3) \mathbf{r} \cdot \mathbf{n} dS$ is the incremental solid angle $d\Omega$, with $\mathbf{r} = \mathbf{q} - \mathbf{p}$ being the directed distance from the field point $\mathbf{p}$ to the source point $\mathbf{q}$ and $r = |\mathbf{r}|$.
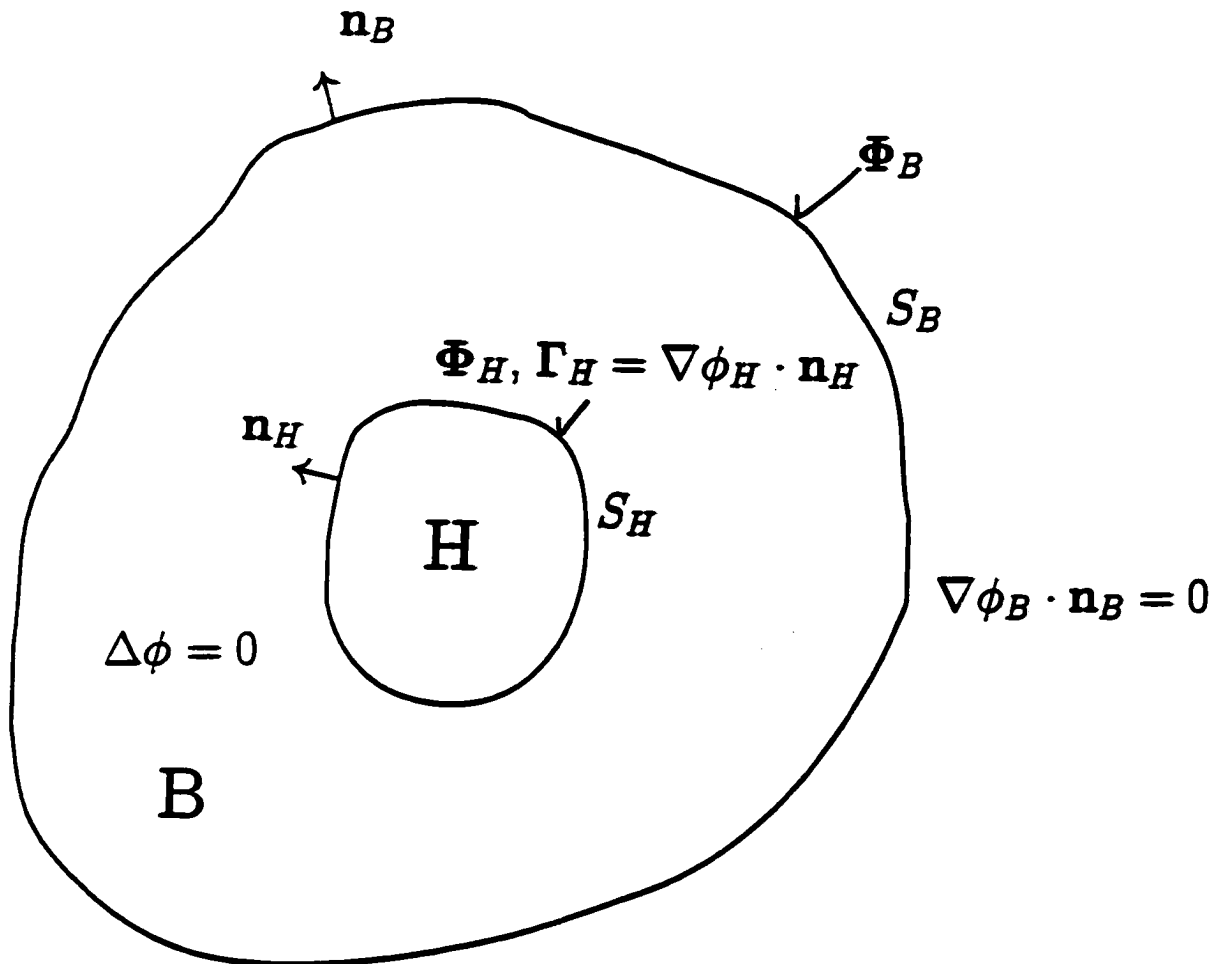
Figure 2.1: The volume conductor problem of interest in this study. The human thorax B is bounded by a closed surface, S_B, and surrounded by nonconductive air; all cardiac bioelectric sources are embedded in the region H enclosed by an epicardial surface S_H. The aim of the inverse problem of electrocardiography—as it is defined in this study—is to calculate epicardial potentials, Φ_H, from measured body-surface potentials, Φ_B. Γ_H, the normal component of gradient of Φ_H on S_H; n_H/n_B, outward-oriented unit normals to S_H/S_B; $\Delta\phi = 0$, Laplace equation applies to region B bounded by S_H and S_B; $\nabla\phi_B \cdot n_B = 0$, no current leaves region B.

If S_H and S_B are each subdivided into plane triangles Δ_H^i and Δ_B^i, with areas μ_H^i and μ_B^i, respectively, so that

$$S_H = \bigcup_{i=1}^{n} \Delta_H^i \quad \text{and} \quad S_B = \bigcup_{i=1}^{m} \Delta_B^i,$$

and

$$\phi_H^i = \frac{1}{\mu_H^i} \int_{\Delta_H^i} \phi_H dS, \quad i = 1,\ldots,n \quad \text{and} \quad \phi_B^i = \frac{1}{\mu_B^i} \int_{\Delta_B^i} \phi_B dS, \quad i = 1,\ldots,m$$

denote the mean potentials at these triangles, then Eq. 2.3 gives, for a centroid p_i of any triangle Δ_H^i or Δ_B^i,

$$-\phi_H^i - \frac{1}{2\pi} \int_{S_H^-} \phi_H d\Omega_{HH}^i + \frac{1}{2\pi} \int_{S_B} \phi_B d\Omega_{HB}^i - \frac{1}{2\pi} \int_{S_H^-} r_i^{-1} \nabla\phi_H \cdot n_H dS = 0 \quad (2.4)$$

$$-\phi_B^i - \frac{1}{2\pi} \int_{S_H} \phi_H d\Omega_{BH}^i + \frac{1}{2\pi} \int_{S_B^-} \phi_B d\Omega_{BB}^i - \frac{1}{2\pi} \int_{S_H} r_i^{-1} \nabla\phi_H \cdot n_H dS = 0, \quad (2.5)$$

where $r_i = |q - p_i|$ and $d\Omega_{rs}^i$ denotes the solid angle subtended by a differential of the integration surface S_s at the ith centroid p_i on the surface S_r. The integrals in Eqs. 2.4 and 2.5 can be discretized in terms of the coefficients that depend only on the geometry of S_B and S_H.

The discretization method must separate the potential or gradient values from the geometric coefficients. This is accomplished by adopting the following definitions:

$$-\phi_H^i - \frac{1}{2\pi} \int_{S_H^-} \phi_H d\Omega_{HH}^i = \sum_{j=1}^{n} p_{HH}^{ij} \phi_H^j, \quad (2.6)$$

$$\frac{1}{2\pi} \int_{S_B} \phi_B \, d\Omega_{HB}^i = \sum_{j=1}^{m} p_{HB}^{ij} \phi_B^j, \quad (2.7)$$

$$-\frac{1}{2\pi} \int_{S_H^-} r_i^{-1} \nabla\phi_H \cdot n_H dS = \sum_{j=1}^{n} g_{HH}^{ij} \Gamma_H^j, \quad (2.8)$$

$$-\frac{1}{2\pi} \int_{S_H} \phi_H d\Omega_{BH}^i = \sum_{j=1}^{n} p_{BH}^{ij} \phi_H^j, \quad (2.9)$$

$$-\phi_B^i + \frac{1}{2\pi} \int_{S_B^-} \phi_B \, d\Omega_{BB}^i = \sum_{j=1}^{m} p_{BB}^{ij} \phi_B^j, \quad (2.10)$$

$$-\frac{1}{2\pi}\int_{S_H} r_i^{-1}\boldsymbol{\nabla}\phi_H\cdot\boldsymbol{n}_H dS = \sum_{j=1}^{n} g_{BH}^{ij}\Gamma_H^j,\qquad(2.11)$$

where $\Gamma_H^j = \boldsymbol{\nabla}\phi_H^j\cdot\boldsymbol{n}_H$, $j = 1,\ldots,n$.

The argument of each of these summations can be separated into the product of a potential on either surface or the gradient of a potential at a specific point j on the epicardial surface and a second factor (the coefficients p_{rs}^{ij} and g_{rH}^{ij}) based entirely on the geometry of S_B and S_H. In general, the g_{rH}^{ij} coefficient links the value of the potential gradient (Γ^j) at point j on surface S_H to the observation point i on surface S_r, whereas p_{rs}^{ij} is the geometric coefficient which weights the contribution of the mean potential at triangle j of surface S_s to the potential at i on surface S_r. Thus, for example, p_{HB}^{ij} is the coefficient for the observation point i on the epicardial surface and for point j on the body surface.

Applying these definitions gives the summations for each $i = 1,\ldots,m$ on S_B and each $i = 1,\ldots,n$ on S_H

$$\sum_{j=1}^{m} p_{HB}^{ij}\phi_B^j + \sum_{j=1}^{n} p_{HH}^{ij}\phi_H^j + \sum_{j=1}^{n} g_{HH}^{ij}\Gamma_H^j = 0\qquad(2.12)$$

$$\sum_{j=1}^{m} p_{BB}^{ij}\phi_B^j + \sum_{j=1}^{n} p_{BH}^{ij}\phi_H^j + \sum_{j=1}^{n} g_{BH}^{ij}\Gamma_H^j = 0.\qquad(2.13)$$

The sums in Eqs. 2.6 to 2.11 have distinct properties that reflect the geometric characteristics of the volume conductor; some of these properties, stated below, can serve as a check of the accuracy with which quadrature formulas discretize surface integrals.

$$-\frac{1}{2\pi}\int_{S_H^-} d\Omega_{HH}^i = \sum_{\substack{j\neq i\\j=1}}^{n} p_{HH}^{ij} = -1,\quad p_{HH}^{ii} = -1,\qquad(2.14)$$

$$\frac{1}{2\pi}\int_{S_B} d\Omega_{HB}^i = \sum_{j=1}^{m} p_{HB}^{ij} = 2,\qquad(2.15)$$

$$-\frac{1}{2\pi}\int_{S_H^-} r_i^{-1}dS = \sum_{\substack{j\neq i\\j=1}}^{n} g_{HH}^{ij},\qquad(2.16)$$

$$-\frac{1}{2\pi}\int_{S_H} d\Omega_{BH}^i = \sum_{j=1}^{n} p_{BH}^{ij} = 0,\qquad(2.17)$$

$$\frac{1}{2\pi} \int_{S_B^-} d\Omega_{BB}^i = \sum_{\substack{j \neq i \\ j=1}}^{n} p_{BB}^{ij} = 1, \quad p_{BB}^{ii} = -1, \tag{2.18}$$

$$-\frac{1}{2\pi} \int_{S_H} r_i^{-1} dS = \sum_{j=1}^{n} g_{BH}^{ij}. \tag{2.19}$$

The coefficients p_{rs}^{ij} have been calculated in this study by means of analytical formulas from spherical trigonometry [6]

$$\alpha = \tan^{-1} \frac{|(r_3 \times r_1) \times (r_1 \times r_2)|}{-(r_3 \times r_1) \cdot (r_1 \times r_2)} \tag{2.20}$$

$$\Omega = (\alpha + \beta + \gamma - \pi)(c \cdot n) / |c \cdot n|, \tag{2.21}$$

where r_1, r_2, r_3, and c are vectors from the observation point to the three vertices and the centroid of the observed triangle; β and γ are determined by using formulas analogous to Eq. 2.20, with cyclic permutations of the indices.

The coefficients g_{rH}^{ij} have been approximated by means of Radon's seven-point formula [32, 131, 151], as a weighted sum of the distance from the observation point— centroid of the observation triangle—to the seven Radon points on the observed triangle. The observed triangle is subsequently divided into four congruent triangles by connecting the mid-points of the sides, and, after a weighted sum is calculated for each subtriangle, the result is compared to that of the previous step. The procedure is repeated until the estimate stabilizes. To check the accuracy of Radon's formula, Horáček and Clements [71] used it to calculate p_{rs}^{ij} and found that calculations in double precision yielded row sums that agreed with Eqs. 2.14, 2.15, 2.17, and 2.18 to five decimal places for the respective P matrices. When the observation triangle is the observed triangle, then a singularity arises when one tries to calculate $1/r$ for the centroid. MacLeod [97] has developed a semianalytical method for integrating the function $d\Psi = dS/r$ in this special case, derived from the formula used by Barr *et al.* [7], who approximated each triangle by a sector S and placed an observation point p on a line perpendicular to S, through the center of the circle, at a distance d.

$$\int_{S^-} r^{-1} dS = r_T^2 \theta_T^2, \tag{2.22}$$

where θ_T is an angle subtended by S, and S^- denotes integration over the sector's surface with the singularity removed. This expression can be used to derive an estimate for the Ψ^i_{HH} terms in Eq. 2.22 for $i = j$. One can approach the problem of determining an equivalent radius of the triangle by first noting that the area of a circular sector A_T is

$$A_T = \frac{\theta_T r_T^2}{2},$$ (2.23)

from which one can write

$$r_T \theta_T = \sqrt{2 A_T \theta_T},$$ (2.24)

and, by substitution into (2.22), one gets the surface integral over triangle Δ^j_H

$$\Psi^i_{HH} = \int_{\Delta^j_H} r_i^{-1} dS = \sqrt{2 A_T \theta_T}.$$ (2.25)

Thus, only the area of the triangle and the angle subtended by the two sides which join at the observation point i are required to estimate g^{ii}_{HH}.

One can improve the accuracy of this estimate by dividing the original triangle into subtriangles about the observation point i; the resulting subtriangles better approximate the circular sector, which is still the basis of this solution. In computing g^{ii}_{HH}, one can successively bisect the base angle θ and recalculate the integrals for the resulting subtriangles. The sum of these values is the estimate of the total integral and is compared with that of the previous iteration until the difference drops below a predefined value. This approach was implemented as follows: a vector $\vec{\rho}$ was anchored at the observation point (vertex 1) and was swept through the triangle from vertex 2 to vertex 3 in N equiangular increments. The sides of the triangle were defined as vectors $\vec{a}, \vec{b}$, and $\vec{c}$, opposite vertices 3, 1, and 2, respectively. As $\vec{\rho}$ sweeps through the triangle, it makes an angle δ_j with side a. Side b can be viewed as the base of the triangle and the height relative to this base as h. With α defined as the angle between h and side a, $\vec{\rho}$ makes an angle $\alpha - \gamma_j$ with h, and one can write for the magnitude of $\vec{\rho}$,

$$\rho_j = \frac{h}{\cos(\alpha - \delta_j)}.$$ (2.26)

Each increment made by $\vec{\rho}$ through the triangle defines another subtriangle made up of the vectors $\vec{\rho}_j$ and $\vec{\rho}_{j-1}$ The area of this subtriangle is

$$A_j = \frac{\rho_j \rho_{j-1} \sin \delta}{2},\qquad(2.27)$$

where δ is the angle subtended at each increment (that is, where $\delta_j = \delta_{j-1} + \delta$ and $\delta = \theta/N$).

One can apply Eqs. 2.26 and 2.27 to each subtriangle and calculate the sum for the whole triangle. This yields for any triangle Δ_H^i in which one of the vertices is the observation point

$$\Psi_{HH}^{ii} = \int_{T^{ii}} \frac{dS}{r} \approx \sum_{j=1}^{N} \sqrt{2\delta A_j} = \sqrt{2\delta} \sum_{j=1}^{N} \sqrt{\frac{\rho_j \rho_{j-1} \sin \delta}{2}} = \sqrt{\delta \sin \delta} \sum_{j=1}^{N} \sqrt{\rho_j \rho_{j-1}},\qquad(2.28)$$

where N is the number of subtriangles into which Δ_H^i has been divided.

Returning to the system defined by Eqs. 2.12 and 2.13, this system can be described in matrix notation as

$$P_{HB(n \times m)} \Phi_B + P_{HH(n \times n)} \Phi_H + G_{HH(n \times n)} \Gamma_H = 0\qquad(2.29)$$

$$P_{BB(m \times m)} \Phi_B + P_{BH(m \times n)} \Phi_H + G_{BH(m \times n)} \Gamma_H = 0,\qquad(2.30)$$

for matrices P_{rs} and G_{rH}, where $\Phi_B = (\phi_B^1, \ldots, \phi_B^m)$, $\Phi_H = (\phi_H^1, \ldots, \phi_H^n)$ and $\Gamma_H = (\Gamma_H^1, \ldots, \Gamma_H^n)$, or more simply, in the form

$$Z_{BH} x = b.\qquad(2.31)$$

The approach to solving the system defined by Eqs. 2.29 and 2.30 which has been employed by Barr *et al.* [7] has been, first, to reduce the size of the discretized system by solving Eq. 2.29 for $\Gamma_H = -G_{HH}^{-1}(P_{HB}\Phi_B + P_{HH}\Phi_H)$ and, then, to substitute the result into Eq. 2.30 to obtain the $(m \times n)$ system

$$Z_{BH}\Phi_H = (P_{BB} - G_{BH}G_{HH}^{-1}P_{HB})^{-1}(G_{BH}G_{HH}^{-1}P_{HH} - P_{BH})\Phi_H = \Phi_B.\qquad(2.32)$$

In an attempt to reduce the size of the system to be solved even further, Barr *et al.* [7] used node-to-node discretization, and their original technique has been further refined by other investigators [72, 103, 105, 125].

2.3 Towards Increased Quadrature Accuracy

Horáček and Clements [71] found that the triangle-to-triangle method produced lower forward and inverse errors than the node-to-node system for the single central dipole and three eccentric dipole sources they examined. Expanding the tesselation to triple the number of triangles decreased forward errors, but not inverse errors. Based on these results, they concluded that better accuracy in the quadrature achieved by the triangle-to-triangle formulas was responsible for the increased accuracy of the inverse solution. This result raised the question of whether additional refinements to the quadrature will further improve forward and, especially, inverse accuracy, and the accompanying question of if, or how, this can be achieved.

First consideration was given to the method for calculating G matrices. Although all P matrix calculations are using an analytical formula, semianalytical methods have been used to calculate G matrices. In an attempt to increase quadrature accuracy in calculating the G matrices, an analytical solution to the integral of dS/r introduced by Ferguson et al. [44] (whose work expanded on that of Kuwahara and Takeda [89] and de Munck [33]) was adopted.

The problem can be stated as follows: For a given observation point x and a plane triangle with vertices (x_1, x_2, x_3), determine the shortest vector c which intersects the point and the plane of the triangle. Define vectors from the intersection point A to the three vertices of the triangle as c_1, c_2, c_3 and vectors from the observation point to the vertices of the triangle as y_1, y_2, y_3. Then the following equations provide a solution:

$$\beta_p = c \cdot (c_p \times c_{p+1}) \tag{2.33}$$

$$\gamma_p^0 = \frac{1}{\left|y_{p+1} - y_p\right|} \ln \left(\frac{\left|y_{p+1}\right| \left|y_{p+1} - y_p\right| + y_{p+1} \cdot \left(y_{p+1} - y_p\right)}{\left|y_p\right| \left|y_{p+1} - y_p\right| + y_p \cdot \left(y_{p+1} - y_p\right)} \right) \tag{2.34}$$

$$\iint_{\Delta_{ijk}} \frac{1}{|x - x'|} dS' = \left| \sum_{p=1}^{3} \text{sign}\,(\beta_p) \iint_{\Delta_{A,p,p+1}} \frac{1}{|y|} dS' \right| \tag{2.35}$$

$$\Omega_{ijk} = \sum_{p=1}^{3} \Omega_{A,p,p+1} \tag{2.36}$$

$$\iint_{\Delta_{ijk}} \frac{1}{|\boldsymbol{x} - \boldsymbol{x}'|} dS' = \left| -|\boldsymbol{c}| \, \Omega_{ijk} + \sum_{p=1}^{3} \text{sign} \, (\beta_p) \, |\boldsymbol{c}_p \times \boldsymbol{c}_{p+1}| \, \gamma_p^0 \right| \qquad (2.37)$$

It should be noted that no singularity arises in this formulation for the triangle-to-triangle system. G_{HH} and G_{BH} matrices were constructed using this formula.

A second consideration was whether the use of the centroid of the observation triangle to represent the mean value of the given integral over the observation triangle was a sufficiently accurate procedure. Tesselated triangles were formed to give a sufficiently accurate representation of the torso and epicardial surfaces. However, the triangles are not small enough to make values for solid angles and dS/r nearly constant for any point of the observation triangle. To test whether it was possible to improve on the centroid method, a double integral calculation method was implemented, where values were calculated for the seven Radon-point locations within the observation triangle and a weighted mean was determined. (It should be noted that the centroid is one of the Radon points.) The matrices P_{BH}, P_{BB}, P_{HH}, P_{HB}, G_{HH} and G_{BH} were all calculated using this double integral method.

Next, using a further expansion of this method, each observation and observed triangle was divided into 16 equiarea triangles, with the seven-Radon-point method then being used to calculate all coefficients.

All Ps and Gs for original semi-analytically computed Gs (G0) and new analytically computed Gs (G1) with the centroid method (Centroid) and the double integral seven-Radon-point method (Radon), as well as G1 with the 16-triangle (Om16) method were constructed. Using these matrices, five forward transfer matrices were calculated — Z_{BH}^1 (G0, Centroid); Z_{BH}^2 (G1, Centroid); Z_{BH}^3 (G0, Radon); Z_{BH}^4 (G1, Radon); and Z_{BH}^5 (G1, Om16).

Epicardial and torso potentials were calculated for a central dipole source and for three simultaneouly energized eccentric dipole sources with one located in the left-ventricular midlateral wall, one in the right-ventricular midlateral wall, and one near the left-ventricular apex. These three locations were determined by picking a triangle in the appropriate area of the epicardial surface, moving the dipole source inwards 10 mm along the inward-oriented normal to the triangle, and making the

dipole direction the same as the outward normal of this triangle. Solid angles used in the calculation of the epicardial and torso potentials for the given dipole source were calculated using the Centroid method. To match the Radon method for the forward problem, solid angles were also determined with the Radon method, and alternate potentials were calculated. All subsequent test-data calculations used this method.

As a second step, two additional sources were created in the same manner, one directed inwards from the midanterior wall along the septum, and one from the midposterior wall along the septum. These five eccentric sources were simultaneously energized.

The third step was to examine the results for individual dipole sources distributed throughout the heart. To obtain an extensive distribution over the entire epicardial surface, dipoles were located as described above, but for all 400 triangles of the tesselated epicardial surface. To represent different depths, dipoles were placed at 10-mm, 7.5-mm, 5.0-mm, and 2.5-mm depths from the epicardial surface into the ventricular wall along the normal for the given triangle, for a total of 1,600 separate dipole sources. For this data set, the node-to-node method was also applied to check whether the triangle-to-triangle method's superiority was retained for this distribution of sources.

The fourth step was to use simulated time sequences of the sources. This fourth set of data was generated by the anisotropic model of human ventricular myocardium (Appendix B). Dipole sources were calculated from the model's output (in terms of intracellular potential for every cell of the model) at sequential time steps of 2 ms. Sequences for a septal activation site and for a basal site (left postero-paraseptal site in Hren et al. [73]) were created for 36 time instants, at 2-ms time steps, from 2 ms to 72 ms.

2.4 Results

Table 2.1 displays the relative error (RE) and correlation coefficient (CC) values[1] for the one- and three-dipole source distributions used by Horáček and Clements [71]. Results for the Z_{BH}^1(G0, Centroid) and Z_{BH}^2(G1, Centroid) systems matched those they reported. Because the G0 and G1 systems yielded virtually identical results—in combinantion with Centroid, Radon, and Om16 methods—results will henceforth be reported only for G1 systems. RE measures (Table 2.1) for the Z_{BH}^4(G1, Radon) system show a 37% decrease for the central dipole source and a 46% decrease for the source consisting of three eccentric dipoles, compared to errors for the Z_{BH}^2(G1, Centroid) system, with a corresponding small increase in CC. The finer Z_{BH}^5(G1, Om16) system has a slightly higher RE than that of the Radon system for the central dipole, and a slightly lower RE for the three eccentric dipoles. The CCs for the central dipole are equal and there is a slight increase in CC for the Z_{BH}^5(G1, Om16) system for the three-dipole source.

Table 2.2 shows similar results when the Radon method was used to calculate potentials on the epicardial and torso surfaces. A third source with five eccentric dipoles has been added. There is the same relationship among the different systems here as in Table 2.1, with a 43% reduction in RE for the central dipole, 45% for the three eccentric dipoles, and 32% for the five eccentric dipoles. A comparison between

---

[1]Two distributions of N potentials from the same surface—e.g. a priori known potentials Φ^{ap} and calculated inverse-recovered potentials Φ^c—can be quantitatively compared by two numerical indices: RE and CC. The RE is the root-mean-square (rms) difference of the two distributions normalized by the rms value of the known distribution [136]:

$$RE = \sqrt{\frac{\sum_{i=1}^{N}(\Phi_i^c - \Phi_i^{ap})^2}{\sum_{i=1}^{N}\Phi_i^{ap}}}.$$

The smaller the value of RE, the more similar are the two distributions. CC is calculated as the dot-product of two vectors, Φ^{ap} and Φ^c, normalized by the product of their magnitudes, that is

$$CC = \frac{\Phi^c \cdot \Phi^{ap}}{|\Phi^c||\Phi^{ap}|}.$$

Table 2.1:

Error measures (RE, CC) of the forward solution using three differently discretized torso-heart systems, for single- and multiple-dipole sources

System	Source	RE	CC
Z_{BH}^{2}(G1, Centroid)	1Dip	.009195	.999968
	3Dip	.034316	.999432
Z_{BH}^{4}(G1, Radon)	1Dip	**.005811**	**.999987**
	3Dip	.018395	.999869
Z_{BH}^{5}(G1, Om16)	1Dip	.005819	.999987
	3Dip	**.017983**	**.999874**

G1, triangle-to-triangle system using analytical method of calculating G matrices of transfer matrix Z_{BH}; Centroid, system using centroid of observation triangle as a sole point from which integrals over observed triangles are determined; Radon, system using Radon's seven-point formula to determine double integrals over both observed and observation triangle; Om16, system using subdivision of both observed and observation triangle into 16 subtriangles to determine double integrals; RE, relative error; CC, correlation coefficient; 1Dip, a single central dipole; 3Dip, three eccentric dipoles; **bold font**, the best results.

Table 2.2:

Error measures (RE, CC) of the forward solution using three differently discretized torso-heart systems and with potentials determined by Radon's seven-point formula, for single- and multiple-dipole sources

System	Source	RE	CC
Z^2_{BH}(G1, Centroid)	1Dip	.008527	.999968
	3Dip	.033580	.999470
	5Dip	.030697	.999535
Z^4_{BH}(G1, Radon)	1Dip	.004871	.999989
	3Dip	.018467	.999883
	5Dip	.020888	.999803
Z^5_{BH}(G1, Om16)	1Dip	**.004864**	**.999989**
	3Dip	**.018066**	**.999888**
	5Dip	**.020494**	**.999810**

G1/Centroid/Radon/Om16, methods of discretizing torso-heart system (see the legend of Table 2.1); RE, relative error; CC, correlation coefficient; 1Dip, a single central dipole; 3Dip, three eccentric dipoles; 5Dip, five eccentric dipoles; **bold font**, the best results.

Tables 2.1 and 2.2 shows the error measures in the latter the same or better for all cases, except the three-dipole source with the Radon discretization (where differences are minute).

Table 2.3 shows forward errors for the set of 1,600 eccentric dipolar sources. Results are presented for the complete set and for subsets of 400 dipoles at each depth with respect to the epicardial surface. These results include maximum and minimum RE values, as well as mean and median values with their standard deviations. We again see that Radon and Om16 methods yielded consistently better results than the Centroid method. The decline in mean and median RE from Centroid to Radon systems was 26% and 31%, respectively, for a 10-mm depth, 27% and 31% for 7.5-mm, 29% and 41% for 5.0-mm, and 24% and 30% for 2.5-mm depths. The decrease in RE over all sources was 24% for the mean and 30% for the median. There was always

a decrease in standard deviation as well. Om16 method errors were close to those for the Radon method. An inspection of the data also shows that mean and median errors increased as the dipole source approached the epicardial surface.

For comparison, node-to-node forward errors were calculated for the 1,600 eccentric dipole sources (Table 2.4). Differences between the node-to-node and triangle-to-triangle methods were evaluated for each source with 1,564 values of RE lower for the Z^2_{BH}(G1, Centroid) system and only 36 lower for the node-to-node system. When node-to-node system's REs were compared to those for the Z^4_{BH}(G1, Radon) system, there were just 16 sources where the node-to-node system had smaller RE. An examination of maximum, minimum, mean, and median RE also showed better accuracy for the triangle-to-triangle methods.

In order to determine if results found here were due to the use of only one or a few single-dipole sources, forward errors were calculated for two simulated time sequences of oblique double layer sources (Appendix B). The RE results are in Table 2.5. Although calculated for a group size of 36, results are similar to those for the 1,600 single dipoles. Differences are greater and REs lower for the septal activation sequence compared to the basal sequence.

Results for 1,600 dipole sources and time sequences of oblique double-layer sources so far have compared systems based on group statistics. For the 1,600 dipole sources, Table 2.6 presents results of pairwise comparison of systems and displays the number of sources with RE smaller for system A, smaller for system B, and equal. Similar CC results are also given. There are large differences in favour of the Radon method when compared to the Centroid method. Note that the difference in the number of sources with less error for the Radon method decreases as the source is moved nearer to the epicardial surface; however, the Radon method always has the larger number of sources with less error.

For the time-sequence data (Table 2.7), the septal activation sequence gives results similar to those for 1,600 eccentric dipoles, whereas results for the basal activation sequence show smaller difference between the systems.

Table 2.3:

Relative errors of the forward solution obtained using three differently discretized torso-heart systems, for 1,600 eccentric dipole sources

System	Source	MaxRE	MinRE	Mean±SD	Median±SD
Z_{BH}^2(G1, Centroid)	10.0-mm	.2238	.0049	.0319±.0250	.0242±.0148
	7.5-mm	.2241	.0049	.0410±.0348	.0289±.0212
	5.0-mm	.4192	.0062	.0499±.0484	.0370±.0247
	2.5-mm	.3498	.0057	.0565±.0445	.0444±.0312
	All above	.4192	.0049	.0448±.0403	.0326±.0243
Z_{BH}^4(G1, Radon)	10.0-mm	.2497	.0019	**.0236±.0237**	**.0166±.0122**
	7.5-mm	**.1823**	**.0022**	**.0300±.0287**	.0200±.0158
	5.0-mm	.3361	.0023	**.0352±.0411**	.0218±.0182
	2.5-mm	**.2891**	.0035	**.0429±.0403**	**.0308±.0276**
	All above	**.3361**	**.0019**	**.0329±.0350**	**.0210±.0179**
Z_{BH}^5(G1, Om16)	10.0-mm	**.2081**	**.0019**	.0237±.0228	.0168±.0124
	7.5-mm	.1842	.0023	.0302±.0290	**.0198±.0157**
	5.0-mm	**.3348**	**.0022**	.0358±.0428	**.0217±.0186**
	2.5-mm	.6282	**.0028**	.0474±.0506	.0317±.0290
	All above	.6282	.0019	.0338±.0387	.0212±.0182

G1/Centroid/Radon/Om16, methods of discretizing the torso-heart system (see the legend of Table 2.1); MaxRE/MinRE, maximal/minimal relative error within the set of dipoles (400 at each depth, 1,600 overall); Mean, mean relative error for the given set of dipoles; Median, median of relative errors for the given set of dipoles; SD, standard deviation; **bold font**, the best results.

Table 2.4:

Relative errors of the forward solution obtained using a torso-heart system discretized by node-to-node method, for 1,600 eccentric dipole sources

Source	MaxRE	MinRE	Mean±SD	Median±SD
10.0-mm	**1.743**	.0203	**.1214±.1240**	**.0915±.0641**
7.5-mm	3.193	**.0154**	.1889±.2179	.1516±.1087
5.0-mm	2.184	.0251	.3398±.2382	.2915±.2105
2.5-mm	2.408	.0724	.8506±.4351	.8183±.4119
All above	3.193	.0154	.3752±.3984	.2193±.2192

MaxRE/MinRE, maximal/minimal relative error within the set of dipoles (400 at each depth, 1,600 overall); Mean, mean relative error for the given set of dipoles; Median, median of relative errors for the given set of dipoles; SD, standard deviation; **bold font**, the best results.

Table 2.5:

Relative errors of the forward solution obtained using three differently discretized torso-heart systems, for two time sequences of double-layer sources

System	Source	MaxRE	MinRE	Mean±SD	Median±SD
Z^2_{BH}(G1, Centroid)	Septal	`.1188	.0092	.0313±.0235	.0220±.0182
	Basal	.3321	.0175	.0776±.0765	.0520±.0328
Z^4_{BH}(G1, Radon)	Septal	.0973	.0062	.0218±.0156	.0148±.0114
	Basal	**.2496**	.0161	**.0669±.0544**	.0497±.0267
Z^5_{BH}(G1, Om16)	Septal	**.0970**	**.0062**	**.0218±.0156**	**.0147±.0112**
	Basal	.2673	**.0146**	.0671±.0564	**.0493±.0278**

G1/Centroid/Radon/Om16, methods of discretizing torso-heart system (see the legend of Table 2.1); Septal/Basal, a sequence of oblique dipolar layers generated by propagated activation initiated at the septal/basal site (Appendix B); MaxRE/MinRE, maximal/minimal relative error within the set of dipoles comprising the wavefront; Mean, mean relative error for the given set of dipoles; Median, median of relative errors for the given set of dipoles; SD, standard deviation; **bold font**, the best results.

Table 2.6:

Comparison of forward-solution errors (RE, CC) yielded by differently discretized torso-heart systems, for 1,600 eccentric dipole sources

System			RE			CC		
A	B	Source	#A	#B	=	#A	#B	=
(G1, Centroid)	(G1, Radon)	10.0-mm	56	**344**	0	37	**361**	2
		7.5-mm	70	**330**	0	53	**347**	0
		5.0-mm	82	**318**	0	70	**330**	0
		2.5-mm	141	**259**	0	138	**262**	0
		All above	349	**1,251**	0	298	**1,300**	2
(G1, Radon)	(G1, Om16)	10.0-mm	116	**284**	0	97	**228**	75
		7.5-mm	124	**276**	0	106	**228**	56
		5.0-mm	151	**249**	0	135	**222**	43
		2.5-mm	**232**	168	0	**224**	166	10
		All above	623	**977**	0	562	**854**	184

G1/Centroid/Radon/Om16, discretization methods (see the legend of Table 2.1); A/B, torso-heart system discretized by the specified methods; #A/#B, count of cases (out of a possible 400 or 1,600) when the RE/CC of the forward-calculated torso potentials for system A/B is smaller/greater than that for the other system it is being compared to; =, count of cases when the RE/CC of two compared systems are equal. RE, relative error; CC, correlation coefficient; **bold font**, the best results.

Table 2.7:

**Comparison between two differently discretized torso-heart systems in terms
of forward errors (RE, CC), for two time sequences of 36 double-layer sources**

System			RE			CC		
A	B	Source	#A	#B	=	#A	#B	=
(G1, Centroid)	(G1, Radon)	Septal	0	**36**	0	0	**36**	0
		Basal	14	**22**	0	14	**22**	0
(G1, Radon)	(G1, Om16)	Septal	16	**20**	0	7	**17**	12
		Basal	16	**20**	0	16	**20**	0

G1/Centroid/Radon/Om16, discretization methods (see the legend of Table 2.1); Septal/Basal, a sequence of oblique dipolar layers generated by propagated activation initiated at the septal/basal site (Appendix B); A/B, torso-heart system discretized by the specified methods; #A/#B, count of time instants (out of a possible 36) when the RE/CC of the forward-calculated torso potentials for system A/B is smaller/greater than that for the other system it is being compared to; =, count of instants when the RE/CC of two compared systems are equal. RE, relative error; CC, correlation coefficient; **bold font**, the best results.

Results so far showed a difference in forward error based on the depth of the source within the heart. From an examination of the maximum and minimum RE for each depth (Table 2.3), it is evident that RE also varies with location around the heart. For example, for either of the Radon systems and dipolar sources at 10.0-mm depth, the maximum RE is 24.97%, whereas the minimum RE is 0.19%. In Fig. 2.2, epicardial triangles are drawn with the forward RE value identified by the nearest integer. From the distribution of errors, it is evident that certain regions have larger RE than others. Note that this plot does not include the 40 triangles on the A-V "lid" that closes the ventricles.

An examination of time-sequence results shows that the maximum and minimum RE are larger for the basal activation sequence than for the septal sequence. This can be rationalized by the fact that the former sequence of oblique dipolar layers has, over the 72-ms time interval, more dipole sources near the epicardial surface than the septal sequence.

2.5 Discussion

The main purpose of the work reported in this chapter was to solve the forward problem for torso potentials from epicardial potentials as accurately as possible, given a tesselated model with heart and torso of realistic shape. Remarkable accuracy was achieved by use of a triangle-to-triangle approach to the discretization problem, which was demonstrated to outperform the corresponding node-to-node formulation.

The refinement of the forward transfer coefficient matrix Z_{BH}, involving the replacement of the semianalytical method for the G matrix calculation with an analytical procedure did not result in any appreciable numerical improvement in the forward solution. On the other hand, the analytical formula was faster to calculate, because triangles do not have to be subdivided until the result stabilizes, and there was no need to handle situations where the observation and observed triangles are the same as a special case (because the centroid and seven Radon points do not coincide with

G1/7-Rp
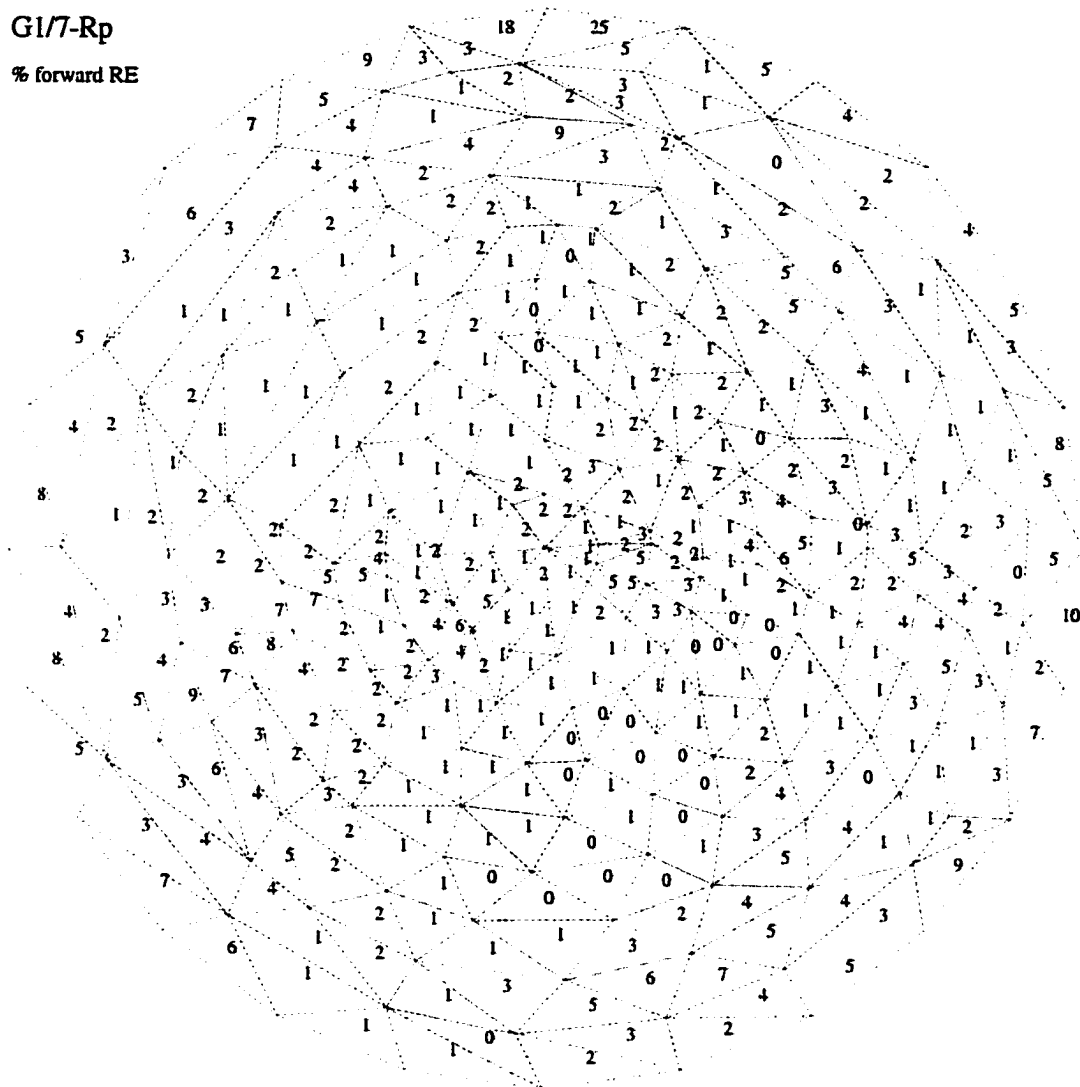
% forward RE

Figure 2.2: Mean relative errors of the forward solution for epicardial potentials, for test distributions generated by dipoles near the epicardial surface. Percent relative error (% RE, nearest integer) of the forward solution was evaluated, in turn, for 360 distributions generated by eccentric single dipoles placed near each triangle of the tesselated epicardial surface at a 10-mm depth into the ventricular wall. Results were obtained in the torso-heart system discretized by means of the G1/Radon method (see the legend of Table 2.1).

triangle vertices, which are the only points where a singularity would occur in the analytical formulation).

Based on results obtained, using a weighted mean for Radon's seven points as the mean integral value for an observation triangle does show improvement over the method using values for the triangle centroid to represent the mean. A longer time is required to calculate the transfer-coefficient matrices, as seven times as many values must be calculated; however, for the 700×400 system used here and the IBM RS/6000 computer, this does not represent an appreciable amount of time for a procedure that needs to be performed only once. Subdividing the observation and observed triangles into 16 equiarea triangles, and then, using the seven-Radon-point method for calculating mean integral values for each triangle improved forward calculations only slightly over the Radon method, and P and G matrices took a much longer time to calculate.

Next, the relationship between source location and the relative error in the forward solution was examined. A comparison of forward solution errors illustrates that the amount of forward error depends on epicardial and torso surface geometry in the area near the source, and the distance of the source from the epicardial surface. This was demonstrated by variations in maximum, minimum, mean and median RE values for the 1,600 dipole sources as well as the two simulated time sequences of potentials produced by the activation initiated at a septal and a basal site, respectively.

These results demonstrate that procedures introduced here to improve the quadrature for the forward problem give more accurate results. The next thing to be determined is whether or not these improvements will translate into an improved solution of the inverse problem.

Chapter 3

Inverse Problem

3.1 Introduction

The formulation of the forward problem $Ax = b$ enables calculation of torso potentials b for a given model $A = Z_{BH}^i, i = 1, \ldots, 5$ and set of epicardial potentials x. However, the desired goal for clinical applications is to determine the distribution of electrical potentials on the epicardial surface, given a known torso potential distribution. This problem is referred to as the inverse problem of electrocardiography for epicardial potentials. To solve this problem is mathematically difficult, because of the ill-conditioned nature of the transfer-coefficient matrix. Methods have been developed which handle this inherent difficulty by imposing conditions on the solution via some form of regularization [111]. The Tikhonov regularization method has been widely accepted for solving the inverse problem of electrocardiography [57, 155, 156], and it will be adopted in this study as well.

This chapter will deal with Tikhonov regularization using both zero- and second-order regularizing operators. All calculations reported in this chapter assumed *a priori* knowledge of the epicardial potentials in determining the regularization parameter. Methods for estimating this parameter without *a priori* information will be dealt with in Chapter 5. The generalized singular-value decomposition (GSVD) [1, 61] was used for the calculation of the singular values and vectors necessary for the inversion

process. Inverse solution errors for the test data sets introduced in Chapter 2 were calculated by comparison of the inverse-recovered potentials with those obtained by solving the forward problem; the latter potentials will be referred to throughout this study as "epicardial potentials known *a priori.*" Subsequent sections will describe our attempts to improve the inverse solution. Finally, the effects of distortion of the torso potentials (by Gaussian noise) on the inverse solution will be addressed.

3.2   Tikhonov Regularization and GSVD

When Tikhonov regularization [111] is used, the original inverse problem is replaced by the perturbed least-squares problem

$$\min_{x \in E^n}\{\|Ax - b\|^2 + t\|Bx\|^2\} = \min_{x \in E^n}\left\{\left\|\begin{pmatrix} A \\ \sqrt{t}B \end{pmatrix} x - \begin{pmatrix} b \\ O \end{pmatrix}\right\|^2\right\}, \tag{3.1}$$

where $\|.\|$ denotes the usual Euclidean norm, t is the regularization parameter, and B is a $p \times N$, $p \le N$, regularizing operator. This is essentially a constrained least-squares problem in which $\|Bx\|^2 = \gamma$ has been incorporated into the objective function [12, 24]. Therefore, for any $A \in E^{M \times N}$ and each $t > 0$, the solution $x(t)$ of the perturbed least-squares problem formulated as Eq. 3.1 satisfies the generalized normal equations

$$(A^T A + t B^T B)x(t) = A^T b. \tag{3.2}$$

Zero-, first-, and second-order Tikhonov regularizing operators, B, are the identity operator I_N, the discretized gradient operator $B = \nabla$, and the Laplacian differential operator $B = \Delta$, respectively.

Let $A \in E^{M \times N}$ be any $M \times N$ ($M \ge N$) real matrix, let $B \in E^{p \times N}$ be a $p \times N$ ($p \le N$) real matrix of rank $L \le N$, and let $K + L$ be the numerical effective rank of $\begin{pmatrix} A \\ B \end{pmatrix}$. In order to permit the generation of explicit representations for the solutions, the solution residuals and the bounding seminorms, we make the assumption that

$K + L = N$. The GSVD of A and B is then given by

$$A = UDRQ^T, \qquad B = VZRQ^T \tag{3.3}$$

with

$$D = \begin{pmatrix} I_K & O_{K \times L} \\ O_{L \times K} & C_{L \times L} \\ O_{(M-K-L) \times K} & C_{(M-K-L) \times L} \end{pmatrix}, \qquad Z = \begin{pmatrix} O_{L \times K} & S_{L \times L} \\ O_{(p-L) \times K} & O_{(p-L) \times L} \end{pmatrix},$$

$$R = \begin{pmatrix} R11_{K \times K} & R12_{K \times L} \\ O_{L \times K} & R21_{L \times L} \end{pmatrix},$$

where $C_{L \times L} = \mathrm{diag}(\alpha_{(K+1)}, \ldots, \alpha_{(K+L)})$, $S_{L \times L} = \mathrm{diag}(\beta_{(K+1)}, \ldots, \beta_{(K+L)})$ and $U \in E^{M \times M}$, $V \in E^{p \times p}$, and $Q \in E^{N \times N}$ have orthonormal columns. $O_{L \times K}$ is the $L \times K$ additive identity and $R \in E^{N \times N}$ is a nonsingular upper tridiagonal matrix [3]. In addition, the generalized singular values $\mu_i = \dfrac{\alpha_i}{\beta_i}, i = K + 1, \ldots, K + L$ satisfy

$$0 \leq \alpha_{K+1}, \cdots, \alpha_{K+L} \leq 1, \quad 1 \geq \beta_{K+1}, \ldots, \beta_{K+L} > 0$$

$$(\alpha_i)^2 + (\beta_i)^2 = 1, \quad i = K + 1, \ldots, K + L.$$

Since $K + L = N$, $A^T A + t B^T B$ is symmetric positive definite. Denoting the columns of $Y = (RQ^T)^{-1}$ by y_j and substituting Eq. 3.3 into Eq. 3.2 gives the unique solution

$$x(t) = Y(D^T D + t M^T M)^{-1} D^T U^T b, \tag{3.4}$$

or, equivalently,

$$x(t) = \sum_{i=1}^{K} (u_i \cdot b) y_i + \sum_{i=K+1}^{K+L} \frac{\alpha_i}{\alpha_i^2 + t \beta_i^2} (u_i \cdot b) y_i, \tag{3.5}$$

where u_i are the columns of U. Thus, the Tikhonov regularized solution $x(t)$ can be expressed simply as a vector-valued function of t, where α_i and β_i (for $i = K + 1, \ldots, K + L$) and y_i and $u_i \cdot b$ (for $i = 1, \ldots, M$) all have known fixed values. The GSVD was computed using the LAPACK routine DGGSVD [3].

Zero- (B0) and second-order (B2) regularizing operators were used with each of the $Z_{BH}^i, i = 1, \ldots, 5$ systems defined in Chapter 2. The Laplacian operator was calculated using the method described by Oostendorp *et al.* [116].

The best possible inverse solution is defined to be that for which the RE $\epsilon(t) = \|x(t) - x^*\|/\|x^*\|$ is a minimum, with x^* being the exact solution. If x^* is known *a priori*, the best-possible Tikhonov solution $x(t^*)$ to $Ax = b$ for any given b and regularizing operator B can be determined by using Eq. 3.5 to compute the $t = t^*$ which minimizes $\epsilon(t)$.

3.3 Results

Ten separate inverse procedures were tested using the five forward triangle-to-triangle systems, $A = Z_{BH}^i, i = 1, \ldots, 5$, with both zero- and second-order regularizing operators. Inverse procedures using a node-to-node method as in [71] were also tested for both regularizing operators. As an initial test of these procedures, forward solutions (Ax) for the 1,600 eccentric single-dipole sources were used as given torso potentials, b. The relative error (RE) of the inverse solution, with the regularization parameter t set to zero, ranged from a minimum of $.2584 \times 10^{-8}$ to a maximum of $.7627 \times 10^{-4}$ over all triangle-to-triangle systems tested. Errors for the node-to-node system were in the same range.

Then, the best-possible Tikhonov inverse solutions—with t^* as the regularization parameter—were calculated from directly computed torso potentials for the central dipole, and the three or five eccentric dipoles; RE and CC are shown in Table 3.1. There was no difference in error values between the G0 and G1 systems, and thus results for G0 systems are not shown. Both RE and CC measures clearly indicate that the Radon method generates inverse-recovered epicardial potentials with greater accuracy than the Centroid method. As a result of using a torso-heart system discretized with the Radon seven-point formula for both the observed and observation triangle, the RE of inverse-recovered epicardial potentials was reduced (compared to

Table 3.1:

Error measures (RE, CC) characterizing epicardial potentials recovered by means of the inverse solution with best-possible Tikhonov regularization of zero and second order, for three differently discretized torso-heart systems and potential distributions generated by single- and multiple-dipole sources

System	Source	B0		B2	
		RE	CC	RE	CC
Z_{BH}^2(G1, Centroid)	1Dip	.3623	.9321	.1133	.9936
	3Dip	.4661	.8848	.4200	.9083
	5Dip	.5687	.8225	.4956	.8695
Z_{BH}^4(G1, Radon)	1Dip	.3161	.9487	**.0582**	**.9983**
	3Dip	.3483	.9378	.2257	.9749
	5Dip	.4624	.8882	.3422	.9415
Z_{BH}^5(G1, Om16)	1Dip	**.3120**	**.9501**	**.0582**	**.9983**
	3Dip	**.3396**	**.9410**	**.2148**	**.9774**
	5Dip	**.4545**	**.8924**	**.3374**	**.9433**

B0/B2, zero-/second-order Tikhonov regularization; RE, relative error; CC, correlation coefficient; 1Dip, a single central dipole; 3Dip, three eccentric dipoles; 5Dip, five eccentric dipoles; G1, system using analytical method of calculating G matrices; Centroid, system using the centroid of each observation triangle as a sole point from which the integrals defining the elements of P and G matrices are determined by using analytical or Radon's seven-point formula, respectively; Radon, system using Radon's seven-point formula over both the observed and the observation triangle to approximate double integrals that define the elements of P and G matrices; Om16, system using subdivision of both the observed and the observation triangle into 16 congruent subtriangles to approximate double integrals that define the elements of P and G matrices (for all of the above, see Chapter 2); **bold font**, the best results.

that obtained with the torso-heart system generated by the Centroid method) by 13%, 25% and 19% for the single-,three- and five-dipole sources for zero-order Tikhonov regularization, and by 49%, 46% and 31% for second-order regularization. Relative errors obtained with Om16-discretized torso-heart system were still slightly smaller than those for Radon system. Comparing these results with those for forward-solution errors in Chapter 2, we see the same trends. Although RE values of the inverse solution were at a higher level, the percent reduction for forward-solution error from Centroid to Radon method was in the same range as that for inverse error. A comparison of regularizing operator effects shows that the second-order operator gives smaller errors than zero-order operator, with a decrease of 69%, 10% and 13% for the single-, three- and five-dipole sources with the Centroid method, and 82%, 35% and 26% with the Radon method.

Inverse-recovered epicardial potential maps were plotted in Fig. 3.1 for a qualitative assessment of the changes due to different torso-heart systems.

Next, errors for the set of 1,600 sources were examined. These results are shown in Table 3.2 for the zero-order regularizing operator and in Table 3.3 for the second-order operator. Again, there was no distinguishable difference between errors for G0 and G1 systems, and thus results for G0 systems are not shown. For both zero- and second-order regularizing operators, Radon systems have smaller maximum, minimum, mean and median RE than Centroid systems for all 1,600 sources and for each subset of 400 sources at each of the four depths into the ventricular wall. For the zero-order operator, there was an overall reduction of 24% in mean RE and 28% in median RE. The corresponding values for the second-order operator were 30% and 34%. Although RE values are higher for the inverse compared to the forward solution, the percentage decrease is in the same range for the two subsets of dipoles that are deeper in the ventricular wall. The two subsets at the shallowest depths showed larger decreases in RE for the forward solution.

Table 3.4 displays the results for comparisons of the two best torso-heart systems for zero- and second-order regularizing operators. Om16 had 1,400 of the 1,600 sources
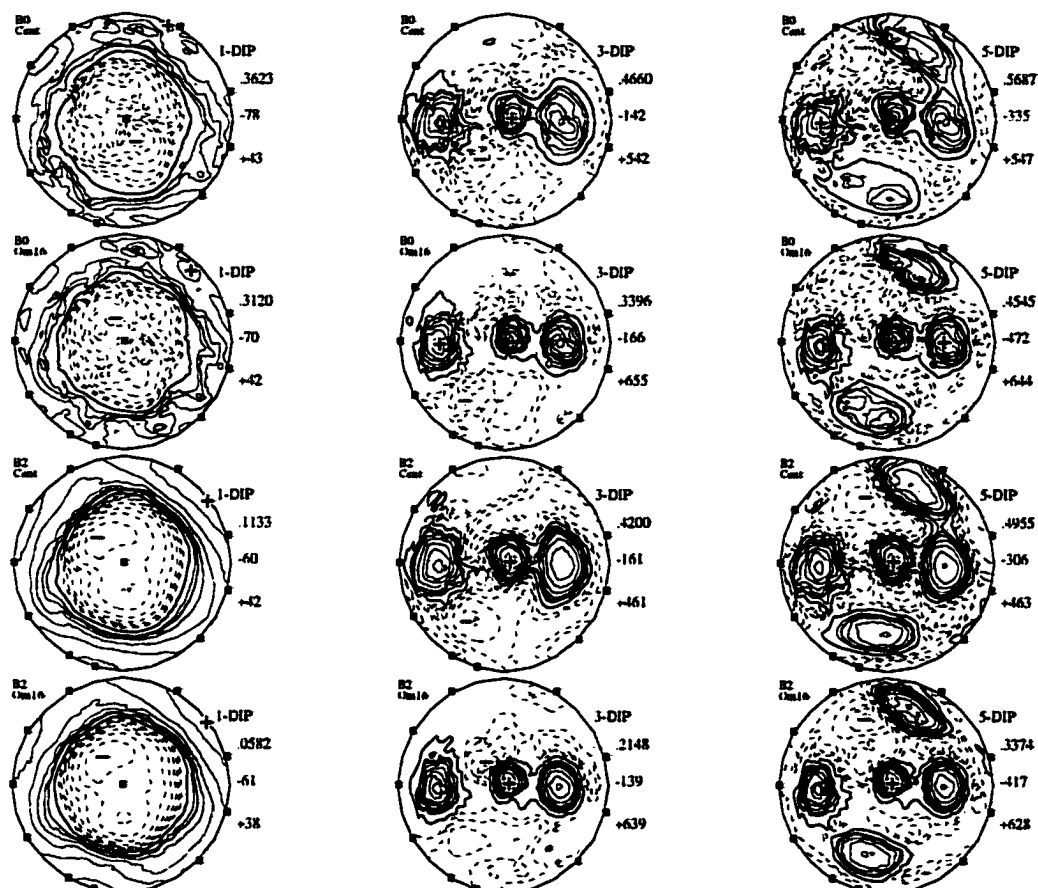
Figure 3.1: Epicardial potential maps for qualitative assessment of the effect of improved quadrature formulas (part 1). Columns show inverse-recovered epicardial potential maps for test potential distributions generated by a single central dipole (1-DIP) [left column], three eccentric dipoles (3-DIP) [center], and five eccentric dipoles (5-DIP) [right]. Rows, top to bottom, correspond to inverse solution with different torso-heart systems (G1/Cent, G1/Om16) and different regularizing operators (B0/B2) as follows: G1/Centroid for B0, G1/Om16 for B0, G1/Centroid for B2, and G1/Om16 for B2. B0/B2, zero-/second-order Tikhonov regularization; G1/Centroid/Om16, discretization methods (see the legend of Table 3.1).

Table 3.2:

Relative errors (RE) of inverse-recovered epicardial potentials for best-possible Tikhonov regularization of zero order with three torso-heart systems, for 1,600 eccentric dipole sources at various depths in the ventricular wall

System	Source	MaxRE	MinRE	Mean±SD	Median±SD
Z^2_{BH}(G1, Centroid)	10.0-mm	.8258	.2509	.4884±.1143	.4851±.1292
	7.5-mm	.8543	.2867	.5698±.1205	.5786±.1314
	5.0-mm	.9236	.3712	.6872±.1146	.7061±.1117
	2.5-mm	.9742	.5144	.8184±.0940	.8445±.0778
	All above	.9742	.2509	.6410±.1669	.6446±.1937
Z^4_{BH}(G1, Radon)	10.0-mm	.7624	**.1469**	.3544±.1121	.3401±.1140
	7.5-mm	.7781	.1627	.4124±.1319	.4104±.1400
	5.0-mm	.8665	.1763	.5140±.1573	.5244±.1655
	2.5-mm	.9421	**.2233**	.6603±.1684	.6914±.1652
	All above	.9421	**.1469**	.4853±.1849	.4617±.2119
Z^5_{BH}(G1, Om16)	10.0-mm	**.7542**	.1470	**.3409±.1082**	**.3301±.1113**
	7.5-mm	**.7713**	**.1592**	**.3946±.1281**	**.3937±.1305**
	5.0-mm	**.8584**	**.1634**	**.4890±.1575**	**.5017±.1676**
	2.5-mm	**.9380**	.2301	**.6326±.1761**	**.6723±.1721**
	All above	**.9380**	.1470	**.4643±.1822**	**.4348±.1971**

G1/Centroid/Radon/Om16, discretization methods (see the legend of Table 3.1); MaxRE/MinRE, maximal/minimal relative error within the set of dipoles (400 at each depth, 1,600 overall); Mean, mean relative error for the given set of dipoles; Median, median of relative errors for the given set of dipoles; SD, standard deviation; **bold font**, the best results.

Table 3.3:

Relative errors (RE) of inverse-recovered epicardial potentials for best-possible Tikhonov regularization of second order with three torso-heart systems, for 1,600 eccentric dipole sources at various depths in the ventricular wall

System	Source	MaxRE	MinRE	Mean±SD	Median±SD
Z_{BH}^2(G1, Centroid)	10.0-mm	.8047	.2537	.4432±.0714	.4441±.0635
	7.5-mm	.8393	.3265	.5589±.0726	.5667±.0653
	5.0-mm	.9355	.4695	.7004±.0692	.7127±.0526
	2.5-mm	.9865	.6421	.8420±.0554	.8538±.0375
	All above	.9865	.2537	.6361±.1643	.6270±.2004
Z_{BH}^4(G1, Radon)	10.0-mm	.7175	.1189	.2485±.0692	.2477±.0635
	7.5-mm	.6341	.1920	.3520±.0767	.3608±.0830
	5.0-mm	.7175	.2266	.5003±.0906	.5166±.0921
	2.5-mm	.9029	.3328	.6851±.1029	.7131±.0778
	All above	.9029	.1189	.4465±.1854	.4170±.2173
Z_{BH}^5(G1, Om16)	10.0-mm	**.7109**	**.1183**	**.2393±.0692**	**.2358±.0664**
	7.5-mm	**.6188**	**.1394**	**.3367±.0780**	**.3398±.0881**
	5.0-mm	**.7076**	**.2199**	**.4783±.0954**	**.4877±.1087**
	2.5-mm	**.9015**	**.2992**	**.6634±.1098**	**.6902±.0959**
	All above	**.9015**	**.1183**	**.4294±.1830**	**.3979±.2092**

G1/Centroid/Radon,Om16, discretization methods (see the legend of Table 3.1); MaxRE/MinRE, maximal/minimal relative error within the set of dipoles (400 at each depth, 1,600 overall); Mean, mean relative error for the given set of dipoles; Median, median of relative errors for the given set of dipoles; SD, standard deviation; **bold** font, the best results.

Table 3.4:

Comparison between two differently discretized torso-heart systems in terms
of relative errors (RE) of epicardial potentials recovered by means of
best-possible Tikhonov regularization of zero and second order, for 1,600
eccentric dipole sources at various depths in the ventricular wall

System			B0			B2		
A	B	Source	#A	#B	=	#A	#B	=
(G1, Radon)	(G1, Om16)	10.0-mm	80	**316**	4	78	**318**	4
		7.5-mm	60	**337**	3	67	**331**	2
		5.0-mm	33	**367**	0	41	**357**	2
		2.5-mm	18	**380**	2	36	**363**	1
		All above	191	**1,400**	9	222	**1,369**	9

B0/B2, zero-/second-order Tikhonov regularization; G1/Radon/Om16, discretization
methods (see the legend of Table 3.1); A/B, torso-heart system discretized by specified
methods; #A/#B, count of cases (out of a possible 400 or 1,600) when RE of inverse-
recovered epicardial potentials for system A/B is smaller than that for the other system
it is being compared to; =, count of cases when REs of two compared systems are equal;
bold font, the best results.

with lower error than Radon method for zero-order regularizing operator and 1,369 for second-order operator (Table 3.4). This is a higher percentage than for forward-solution error.

A comparison of regularizing operator effects (Tables 3.2 and 3.3) gives mean RE for the second-order operator 1% smaller than with the zero-order operator for the Centroid method and 8% smaller for the Radon method. For a depth of 10 mm, there is a decrease of 9% for Centroid and 30% for Radon method, and at 7.5-mm depth these decreses are 2% and 15%. Contrary to results so far, at 5-mm depth there is a 2% increase in RE for Centroid, while still a 3% decrease for Radon method. Finally, at 2.5-mm depth, there is an increase in RE of 3% for Centroid and 4% for Radon method.

Comparisons between best-possible Tikhonov regularization ($t = t^*$) of zero and second order are given—for the three G1 systems—in Table 3.5, for 400 eccentric dipoles at four depths into the ventricular wall. Overall, the inverse-recovered potentials for a greater number of sources have smaller RE with second-order than with zero-order regularizing operator. At a 10-mm depth, there is the largest difference in the number of more accurately recovered potentials with the second-order operator – with Radon and Om16 methods showing a greater distinction than the Centroid method. As the source is moved closer to the epicardial surface, the variation between the Laplacian and Identity operator lessens and at 2.5-mm depth there is only a small difference.

Inverse solutions using $t = t^*$ were also computed, for comparison, for the torso-heart system discretized by the node-to-node method; results are in Table 3.6. As was seen in the solution to the forward problem, mean RE for all 1,600 sources and for each subset of 400 sources is larger for the node-to-node system than for any of the triangle-to-triangle systems. Comparing with triangle-to-triangle systems on an individual source basis, there were 698 inverse-recovered epicardial potential distributions, out of 1,600, with the node-to-node system showing smaller RE in comparison with the Z^2_{BH}(G1, Centroid) system regularized by the Identity operator, 573 in comparison

Table 3.5:
Comparison between best-possible Tikhonov regularization of zero and second order, in terms of relative errors (RE) of inverse-recovered epicardial potentials, for three differently discretized and regularized torso-heart systems and 1,600 eccentric dipole sources at various depths in the ventricular wall

System					
A	B	Source	#A	#B	=
(G1, Centroid, B0)	(G1, Centroid, B2)	10.0-mm	130	**270**	0
		7.5-mm	179	**221**	0
		5.0-mm	199	**201**	0
		2.5-mm	**216**	184	0
		All above	724	**876**	0
(G1, Radon, B0)	(G1, Radon, B2)	10.0-mm	37	**362**	1
		7.5-mm	113	**287**	0
		5.0-mm	176	**223**	1
		2.5-mm	**216**	184	0
		All above	542	**1,056**	2
(G1, Om16, B0)	(G1, Om16, B2)	10.0-mm	38	**362**	0
		7.5-mm	114	**284**	2
		5.0-mm	188	**212**	0
		2.5-mm	**226**	174	0
		All above	566	**1,032**	2

B0/B2, zero-/secord-order Tikhonov regularization; G1/Centroid/Radon/Om16, discretization methods (see the legend of Table 3.1); A/B, torso-heart system discretized by specified methods; #A/#B, count of cases (out of a possible 400 or 1,600) when RE of inverse-recovered epicardial potentials for system A/B is smaller than that for the other system it is being compared to; =, count of cases when REs of two compared systems are equal; **bold font**, the best results.

Table 3.6:

Relative errors (RE) of inverse-recovered epicardial potentials for best-possible Tikhonov regularization of zero and second order with the torso-heart system discretized by the node-to-node method, for 1,600 eccentric single-dipole sources at various depths in the ventricular wall

Operator	Source	MaxRE	MinRE	Mean±SD	Median±SD
B0	10.0-mm	.8645	.2871	.5249±.1006	.5209±.1115
	7.5-mm	.9998	.3302	.5986±.1046	.5915±.1068
	5.0-mm	.9317	.4092	.6939±.0887	.6965±.0800
	2.5-mm	.9951	.5746	.8530±.0728	.8629±.0656
	All above	.9998	.2871	.6676±.1536	.6645±.1744
B2	10.0-mm	.8069	.2661	.4897±.0754	.4891±.0672
	7.5-mm	1.002	.3304	.5971±.0863	.5969±.0593
	5.0-mm	1.086	.4217	.7219±.0970	.7102±.0739
	2.5-mm	1.370	.5908	.9085±.1389	.8884±.1236
	All above	1.370	.2661	.6793±.1863	.6517±.1850

B0/B2, zero-/second-order regularizing operator; MaxRE/MinRE, maximal/minimal relative error within the set of dipoles (400 at each depth, 1,600 overall); Mean, mean relative error for the given set of dipoles; Median, median of relative errors for the given set of dipoles; SD, standard deviation; bold font, the best results.

with the Z_{BH}^2(G1, Centroid) system regularized by the Laplacian operator, 78 in comparison with the Z_{BH}^4(G1, Radon) system regularized by the Identity operator, and only 38 in comparison with the Z_{BH}^4(G1, Radon) system regularized by the Laplacian operator. For the Z_{BH}^2(G1, Centroid) systems, the sources for which the node-to-node system performed better were distributed over the four source depths. In the cases of the Z_{BH}^2(G1, Radon) systems, the potential distributions generated by sources nearer the epicardial surface had the greatest number of instances where the node-to-node system had smaller RE, with 51 distributions out of 78 for the Identity operator and 37 out of 38 for the Laplacian operator being generated by dipoles at 2.5-mm depth into the ventricular wall. These results are in the same range as those for forward-solution error of the torso-heart system discretized by the Radon method, but for the system discretized by the Centroid method, there are many more distributions for which the node-to-node system produces a smaller RE of inverse-recovered potentials than the corresponding triangle-to-triangle system. Comparing node-to-node systems for zero- and second-order operators, we see the same type of results as for triangle-to-triangle systems.

As in the case of forward-solution errors, an examination of the maximum and minimum RE for any depth of dipole sources shows a large variation (Tables 3.2 and 3.3). For example, sources at a 10-mm depth with Radon system and second-order regularizing operator, RE of inverse-recovered epicardial potentials ranges from 11.83% to 71.09%. To understand this dispersion, one should examine the spatial distribution of it, such as that shown in Fig. 3.2. It is evident that, as for the forward solution, RE varies with the location of the source around the heart as well as its depth within the heart.

The best-possible inverse solution was also computed for the septal and basal time sequences of data (Appendix B). Results are shown in Tables 3.7 and 3.8. There was no difference between G0 and G1 methods, and thus only results for G1 methods are shown. Once again, there was a decrease in maximum, minimum, mean and median RE for the Radon discretization method over the Centroid method. The
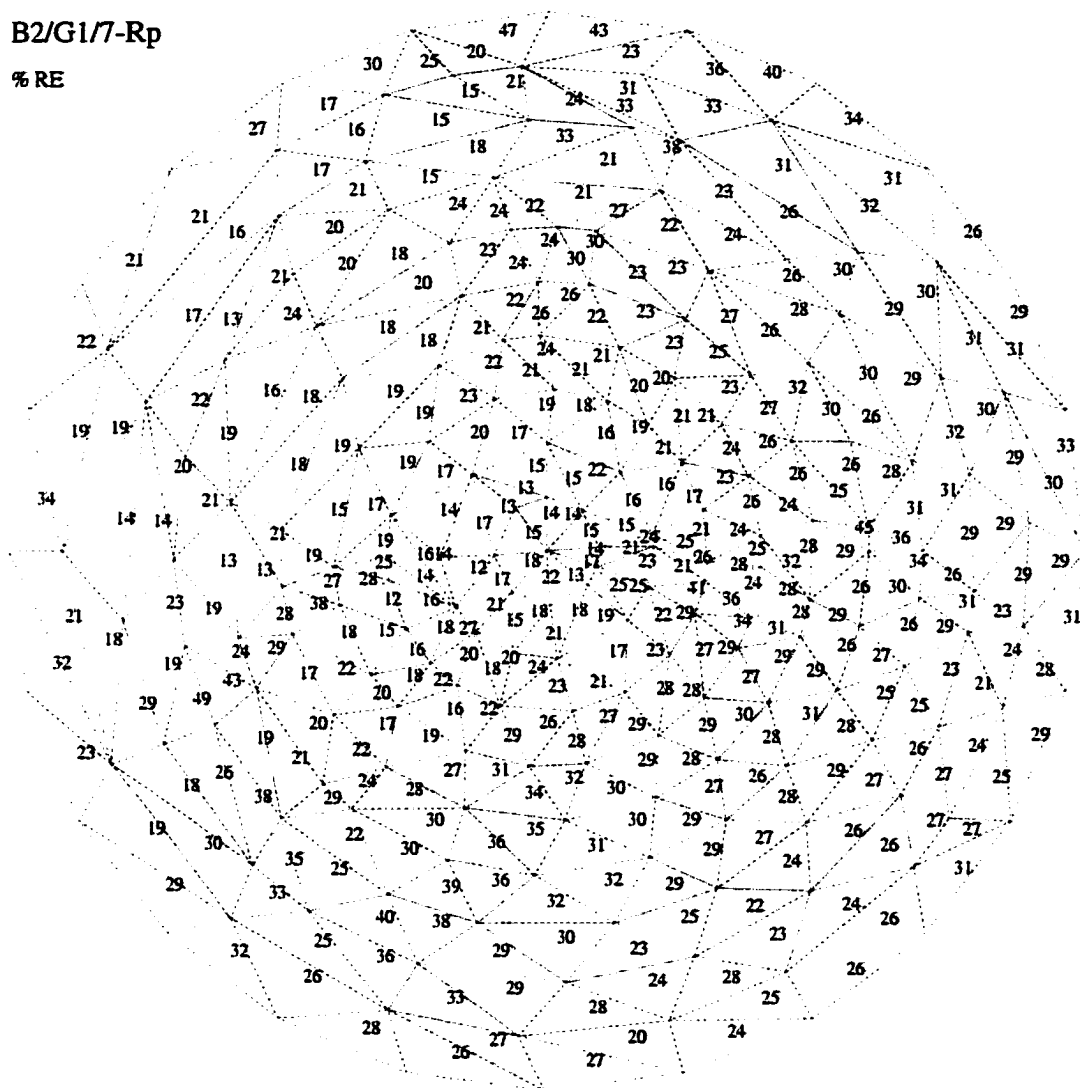
Figure 3.2: Mean relative errors of inverse-recovered epicardial potentials for test distributions generated by dipoles near the epicardial surface. Percent relative error (% RE, nearest integer) of the inverse solution with second-order Tikhonov regularization was evaluated, in turn, for 360 distributions generated by single eccentric dipoles placed near each triangle of the tesselated epicardial surface at 10-mm depth into the ventricular wall. Results were obtained in the torso-heart system discretized by means of the G1/Radon method (see the legend of Table 3.1).

Table 3.7:

Relative errors (RE) of inverse-recovered epicardial potentials for best-possible Tikhonov regularization of zero-order with three torso-heart systems, for two time sequences of double-layer sources

System	Source	MaxRE	MinRE	Mean±SD	Median±SD
Z_{BH}^2(G1, Centroid)	Septal	.7156	.3256	.4999±.1126	.5132±.1437
	Basal	.9103	.5128	.6461±.1132	.6277±.0793
Z_{BH}^4(G1, Radon)	Septal	**.6269**	**.2931**	**.4397±.0919**	**.4470±.1083**
	Basal	**.8736**	**.4800**	**.6007±.1000**	**.5950±.0864**
Z_{BH}^5(G1, Om16)	Septal	.6276	.2950	.4409±.0914	.4499±.1108
	Basal	.8748	.4818	.6023±.1001	.5972±.0878

G1/Centroid/Radon/Om16, discretization methods (see the legend of Table 3.1); Septal/Basal, a sequence of oblique dipolar layers generated by propagated activation initiated at the septal/basal site (Appendix B); MaxRE/MinRE, maximal/minimal relative error within the set of dipoles comprising the wavefront; Mean, mean relative error for the given set of dipoles; Median, median of relative errors for the given set of dipoles; SD, standard deviation; **bold font**, the best results.

Table 3.8:

Relative errors (RE) of inverse-recovered epicardial potentials for best-possible Tikhonov regularization of second-order with three torso-heart systems, for two time sequences of double-layer sources

System	Source	MaxRE	MinRE	Mean±SD	Median±SD
Z^2_{BH}(G1, Centroid)	Septal	.5449	.1580	.3479±.1134	.3675±.1351
	Basal	.9054	.4030	.5657±.1547	.5104±.0730
Z^4_{BH}(G1, Radon)	Septal	.4237	.1062	**.2735±.1059**	**.2676±.1460**
	Basal	.8502	**.3822**	**.5016±.1363**	**.4476±.0692**
Z^5_{BH}(G1, Om16)	Septal	**.4216**	**.1060**	.2736±.1054	.2688±.1469
	Basal	**.8496**	.3824	.5025±.1363	.4479±.0696

G1/Centroid/Radon/Om16, discretization methods (see the legend of Table 3.1); Septal/Basal, a sequence of oblique dipolar layers generated by propagated activation initiated at the septal/basal site (Appendix B); MaxRE/MinRE, maximal/minimal relative error within the set of dipoles comprising the wavefront; Mean, mean relative error for the given set of dipoles; Median, median of relative errors for the given set of dipoles; SD, standard deviation; **bold font**, the best results.

Table 3.9:

Comparison among three differently discretized torso-heart systems in terms of relative errors (RE) of inverse-recovered epicardial potentials calculated by means of best-possible Tikhonov regularization of zero and second order, for two time sequences of 36 double-layer sources

System			B0			B2		
A	B	Source	#A	#B	=	#A	#B	=
(G0, Centroid)	(G1, Centroid)	Septal	21	0	15	4	0	**32**
		Basal	3	3	**30**	6	0	**30**
(G1, Centroid)	(G1, Radon)	Septal	0	**36**	0	0	**36**	0
		Basal	0	**36**	0	0	**36**	0
(G1, Radon)	(G1, Om16)	Septal	**29**	7	0	**18**	17	1
		Basal	**36**	0	0	**29**	6	1

B0/B2, zero-/secord-order Tikhonov regularization; G0/G1/Centroid/Radon/Om16, discretization methods (see the legend of Table 3.1); A/B, torso-heart system discretized by specified methods; #A/#B, count of time instants (out of a possible 36) when RE of inverse-recovered epicardial potentials for system A/B is smaller than that for the other system it is being compared to; =, count of time instants when REs of two compared systems are equal; **bold font**, the best results.

decrease in RE due to discretization accuracy for the septal sequence was 12% for the mean and 13% for the median when the zero-order regularizing operator was used; the corresponding values were 21% and 27% for the second-order operator. For the basal sequence, these percentages were 7%, 5%, 11% and 12%, respectively. A paired system comparison (Table 3.9) also shows, as was seen for the 1,600 sources, that the Radon method of discretizing the torso-heart system produces better inverse-solution results for all sources. This differs from the forward error results for the basal sequence, where a large number of distributions had a lower RE for torso-heart system discretized by the Centroid method. The inverse errors in Table 3.9 for the septal sequence were, for all 36 instantaneous distributions and for both regularizing operators, better for the torso-heart system constructed by the Radon method. A

Table 3.10:

Comparison between best-possible Tikhonov regularization of zero and second order in terms of relative errors (RE) of inverse-recovered epicardial potentials, for three differently discretized torso-heart systems and two time sequences of 36 double-layer sources

| System | | | | |
A	B	Source	#A	#B
(G1, Centroid, B0)	(G1, Centroid, B2)	Septal	0	**36**
		Basal	3	**33**
(G1, Radon, B0)	(G1, Radon, B2)	Septal	0	**36**
		Basal	3	**33**
(G1, Om16, B0)	(G1, Om16, B2)	Septal	0	**36**
		Basal	3	**33**

B0/B2, zero-/secord-order Tikhonov regularization; G1/Centroid/Radon/Om16, discretization methods (see the legend of Table 3.1); Septal/Basal, a sequence of oblique dipolar layers generated by propagated activation initiated at the septal/basal site (Appendix B); A/B, torso-heart system discretized by specified methods; #A/#B, count of time instants (out of a possible 36) when RE of inverse-recovered epicardial potentials for system A/B is smaller than that for the other system it is being compared to; **bold font**, the best results.

comparison of the zero-order and second-order operators (Tables 3.7 and 3.8) showed the latter always better, with decreases of 30% for the Centroid and 37% for the Radon method for the septal sequence, and 12% and 16% for the basal sequence. An examination of minimum and maximum RE in Tables 3.7 and 3.8 shows that time-sequence results also agree with forward solution in that, with the basal sequence, (where sources are close to the epicardial surface) there are larger errors than in the septal sequence (where sources are at a greater distance from the epicardial surface). A comparison of zero- and second-order regularizing operators in Table 3.10 indicates that the latter gives lower REs of inverse-recovered epicardial potentials for 69 of the 72 time-sequence maps.

A qualitative assessment of the different quadrature methods was undertaken by an examination of inverse-recovered epicardial potential maps for selected sources with different torso-heart systems (Fig. 3.3). It is evident that these inverse-recovered distributions are affected by both discretization schemes and regularizing operators. To what extent the inverse solution benefits from these techniques is difficult to judge (nevertheless, it seems that distributions for the Z_{BH}^5(G1, Om16) systems regularized by the Laplacian operator have the best definition and confluence of positive and negative areas). Thus the choice of methodology—be it discretization or regularization—can best be made on the basis of quantitative measures, such as RE and CC.

In order to determine the effect of extraneous distortions in the torso-surface potentials on inverse solution, various levels of Gaussian noise were added to the torso potential distributions generated by the one-, three- and five-dipole sources. RE for the source consisting of three simultaneously energized eccentric dipoles with Gaussian rms noise of 1%, 5%, 10% and 20% of the torso distribution's mean is shown in Table 3.11. Results were similar for other sources. The addition of noise to the torso potentials caused an increase in RE of inverse-recovered epicardial potentials. The higher the level of noise, the greater the increase in error. No differences between G0 and G1 methods were observed, and thus results for G0 are not presented. Radon and Om16 methods give less error than the Centroid method with only very slight differences between Radon and Om16 results. Second-order Tikhonov regularization has smaller RE than zero-order regularization for this particular distribution. Therefore, the trends found for non-perturbed torso potentials still hold for those with noise.

3.4 Discussion

The main purpose of the work reported in this chapter was to solve the inverse problem of electrocardiography for epicardial potentials, by means of best-possible Tikhonov regularization. This was done for various data sets of known potentials, on both torso and epicardial surface, in order to test the inverse solution for torso-heart systems
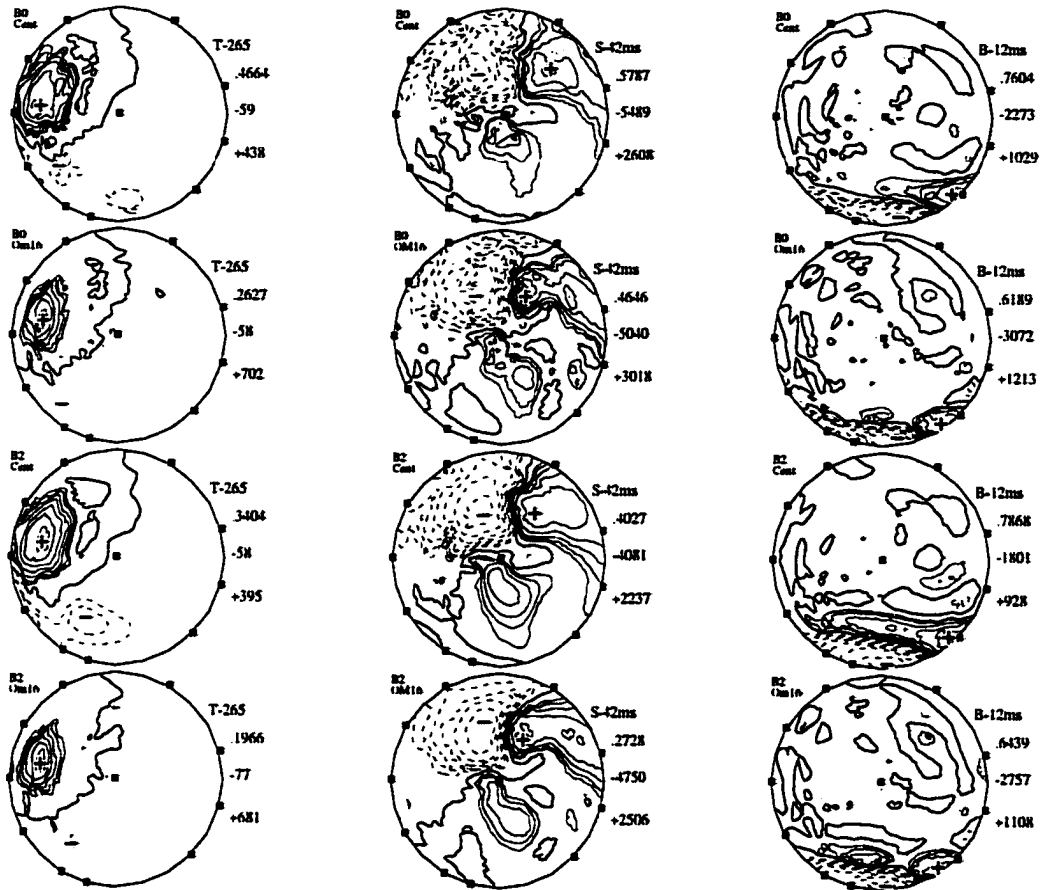
Figure 3.3: Epicardial potential maps for qualitative assessment of the effect of improved quadrature formulas (part 2). Columns show inverse-recovered epicardial potential maps for test potential distributions generated by a single eccentric dipole near Δ265 at a 10-mm depth (T-265) [left column], an oblique dipolar layer representing an activation wavefront at 42 ms after the onset of activation at the septal site (S-42ms) [middle], and an oblique dipolar layer representing an activation wavefront at 12 ms after the onset of activation at the basal site (B-12ms) [right]. Rows, from top to bottom, correspond to inverse solution with different systems (G1/Centroid, G1/Om16) and different regularizing operators (B0/B2) as follows: G1/Centroid for B0, G1/Om16 for B0, G1/Centroid for B2, and G1/Om16 for B2. G1/Centroid/Om16, system discretization methods (see the legend of Table 3.1).

Table 3.11:

Relative errors (RE) of inverse-recovered epicardial potentials for best-possible Tikhonov regularization of zero and second order with Gaussian noise added, for three different torso-heart systems and three eccentric dipole sources

System	Gaussian Noise (%)	B0	B2
Z^2_{BH}(G1, Centroid)	1	.4661	.4202
	5	.4667	.4211
	10	.4681	.4229
	20	.4727	.4285
Z^4_{BH}(G1, Radon)	1	.3609	.2515
	5	**.3856**	.3041
	10	**.4036**	.3369
	20	**.4287**	**.3680**
Z^5_{BH}(G1, Om16)	1	**.3605**	**.2506**
	5	.3864	**.3039**
	10	.4046	**.3367**
	20	.4296	**.3680**

B0/B2, zero-/second-order Tikhonov regularization; G1/Centroid/Radon/Om16, discretization methods (see the legend of Table 3.1); RE, relative error; **bold font**, the best results.

discretized by different methods. Tikhonov regularization methods have been widely used in solving the inverse problem of electrocardiography, and they were applied here as well. GSVD techniques were employed to enable the use of either the Identity (zero-order) operator or the Laplacian (second-order) differential operator in the regularization process. Inverse solution error results for five torso-heart systems and both regularizing operators were compared in terms of RE with respect to the known epicardial distributions. Trends established for the forward problem—regarding the best discretization methods—were also apparent in the solution of the inverse problem.

Regardless of the method and operator which was used to determine the inverse solution, the RE was much larger than that for the forward problem. However, the range of percentage changes in RE between different methods for the inverse was comparable to those for the forward solution. The magnitude of the relative error varied with location around the epicardial surface and the depth of the source within the heart. This comparison illustrates that the amount of error depends on both the epicardial surface geometry in the area near the source and the geometric relationship with the torso surface, as well as the distance of the source from the epicardial surface. Error was not directly related to the number of source dipoles generating the epicardial potential distribution.

It is of interest to note that when torso potentials calculated by applying the forward solution (multiplication by the transfer-coefficient matrix Z_{BH}) to the epicardial potentials were used as input to the inverse procedure, there was no error whatsoever in the inverse solution. This result held true regardless of which node-to-node or triangle-to-triangle system was employed, as long as forward and inverse torso-heart systems matched. Therefore, differences in inverse error with different systems must depend on how each system handles the discrepancy between given torso potentials and those generated by solving the forward problem.

Based on data presented here, triangle-to-triangle methods outperform node-to-node methods—in terms of lower RE of the inverse-recovered epicardial potentials—in a large majority of cases. There are two possible reasons for this result to occur.

First, it could be that when there is no exact match of forward values and known torso potentials, the more locations at which the potential is known, the less error there is in the inverse solution. A second reason is the use of better quadrature methods for evaluating double integrals of p and g coefficients for the triangle-to-triangle than for node-to-node systems, leading to more accurate solutions. In light of these reasons, the question arises as to why, in some cases, the node-to-node method produces smaller error. Most likely the explanation is in the epicardial distribution which the inverse solution is attempting to retrieve. Although the underlying potential distribution is the same, in the node-to-node system the potentials we are trying to match are fewer and more widespread. For the larger triangle-to-triangle system there are not only more potentials to match, but, with locations closer together, it may require achieving potential distributions with a higher spatial gradient. This is supported by the results with node-to-node systems compared with triangle-to-triangle systems constructed with Radon double-integral method, where the majority of smaller errors for the node-to-node system occurred for sources at the shallowest depth, and therefore were associated with the highest spatial gradients.

Our first attempt to increase the accuracy of the quadrature involved the replacement of the semi-analytical method for G matrix calculation with an analytical one. This substitution did not change results, as corresponding inverse solutions with G0 and G1 were virtually identical. Therefore, the only reasons for selecting G1 as opposed to G0 would be the desire to use the mathematically elegant solution.

The second method that was incorporated to increase quadrature accuracy used a weighted mean of p- and g-coefficient values for 7 Radon points in the observation triangle instead of just the centroid. An extension of this method, involving the subdivision of all triangles into 16 subtriangles during calculations (Om16 method) was also evaluated. There is a preponderance of evidence provided by the results to establish that Radon and Om16 methods outperform the Centroid method in the ability to yield the more accurate solution to the inverse problem. This result was upheld when Gaussian noise was added to the torso potentials. When Radon and

Om16 methods were compared, much more ambiguous results emerged. In many cases Om16 performed better, but in others, Radon methods resulted in smaller error for the inverse solution, although the amount of difference in error was never large. Therefore, it appears that these two methods have equal merit. The additional time required to calculate Om16 matrices is not an issue, because these matrices need to be determined only once for each torso-heart system.

Results presented in this chapter provide evidence that for most potential distributions, the Laplacian differential operator outperforms the Identity operator as a regularizor in the Tikhonov inverse solution. This is more evident for torso-heart systems discretized by the Radon and Om16 methods than for those discretized by the Centroid method. However, for distributions with high spatial gradients on the epicardial surface, zero-order Tikhonov regularization has smaller errors more often. In studies which compared these operators plus the Gradient operator using eccentric and concentric spheres as a model of the torso-heart geometry [28, 105], there was no significant difference in inverse solution errors, although the Gradient operator faired slightly better [27, 28]. When noise was added to the input data, there was no consistent advantage to any particular method of regularization. Therefore, the Identity operator has been most commonly used [120], because of its simplicity, although the Laplacian has been used nearly as often [71, 75, 78].

The Identity operator regulates the amplitude of the solution. The largest amplitudes often control the results, and one ends up with low-level potentials that are very noisy in spatial terms (i.e., distributions contain many "spurious" extrema). The Laplacian operator regulates the curvature of the solution. In areas of high spatial gradients, the degree to which the Laplacian holds is less than for smoother areas. Therefore, the Laplacian does a better job at smoothing low-level potentials than the Identity operator, but at the expense of too much smoothing of potentials where a high spatial gradient exists. This leads to two suggestions on how to further improve the inverse solution's accuracy. One is to decrease triangle size; using this type of approach for the finite element method, Johnson and MacLeod [78] used, with

some success, a technique they called regional adaptation to decrease the size of the volume elements in areas with known higher gradients. But even with such an approach, there will always be potentials which are smoothed too much and the size of the system will grow very rapidly. The second suggestion follows from the idea that, intuitively, it seems appropriate that some form of regional adaptation or variation in constraints should be applied. For a given source distribution, there can be very diverse amplitudes, spatial gradients, and spatial curvatures at different locations on the epicardial surface. With global procedures, the regularization may be dominated by a particular region with extreme values, so that other areas are not regularized appropriately. In an attempt to improve the solution to the inverse problem, *regional constraints* will be investigated in Chapter 4.

With the results of Chapters 2 and 3, it is not necessary to retain all torso-heart systems for further investigations. The Z_{BH}^5(G1, Om16) system has been selected for further testing. Both the Identity and Laplacian operators will be retained, as no conclusive result regarding the merit of one over the other has been reached.

Chapter 4

Regional Constraints

4.1 Introduction

This chapter deals with the application of regional constraints to the solution of the inverse problem of electrocardiography for epicardial potentials. Constraints may be considered "regional" on the basis of spatial, temporal or frequency criteria. Tikhonov regularization involves minimization of the norm of either the epicardial potentials or the spatial gradient or curvature. If there is a large spatial variation in these values, the norm is dominated by areas with the largest magnitudes. This generally causes underregularization in areas with low magnitudes and oversmoothing in areas where magnitudes are the highest. This observation has led to the development of methods which attempt to incorporate the regional nature of the epicardial potential distributions into the inverse solution procedure.

One of the first attempts to do so was a method now referred to as Twomey regularization [105, 158], which minimizes the difference between the inversely calculated epicardial potentials and some *a priori* estimate of these potentials:

$$\min_{x \in \mathbb{E}^n} \{ \|Ax - b\|^2 + t\|x - \hat{x}\|^2 \}, \tag{4.1}$$

where $\hat{x}$ is an estimate of the epicardial potentials and other parameters are as defined

in Chapter 3. This requires a solution to the equation

$$x = (A^T A + tI)^{-1}(A^T Ax + t\hat{x}).$$ (4.2)

The regional nature of the solution is addressed by the estimate of the epicardial potentials, $\hat{x}$. If the "true" solution is used as the estimate and the regularization parameter is very large, then the regularizing term dominates and the inverse solution is equivalent to the "true" solution with no error. If the optimal Tikhonov solution—either for zero-, first-, or second-order regularization—is used as the estimate, there is no improvement in the solution. An undersmoothed estimate gives the same result. However, Messinger-Rapport and Rudy [105] found that if they used an oversmoothed solution as the estimate, there was a small decrease in RE. They suggested the use of a "feature map" as an estimate of the epicardial potentials. The feature map had regions of peak magnitudes only. Although the location of the peaks was exact, the magnitude of the potentials was intentionally set smaller than that of the *a priori* solution. The idea was to show that identifying the region in which epicardial potentials were at a peak would be sufficient to reduce the error in the Twomey inverse solution. And indeed, for the exact peak location, there was some improvement in the solution.

The use of temporal regions for constraining the solution was introduced when measured epicardial potentials from a time instant 2 ms prior to the required time were used as the Twomey estimate [105]. The underlying assumption was that there is temporal continuity in epicardial potentials, so that within this time interval there should not be any large changes in potential distributions. This assumption is also exploited when the inverse solution is computed for isochrones instead of epicardial potentials [30, 31, 55, 74, 135]; the latter approach has not been pursued in the present study. The temporal constraint approach was extended by Oster and Rudy [117], who explored the use of various temporal regions in determining the Twomey estimate. They found that the best estimate was an average of either the values at the preceding and following time steps, or these two values plus the value at the time instant for which the inverse calculation was being computed. The largest decreases in error were achieved with the shortest time step tested, 0.5 ms. This method requires potentials,

or estimates of potentials, at the time instants used to calculate the Twomey estimate. For *a priori* known potentials, this method showed both quantitative and qualitative improvement over Tikhonov regularization. When the inverse-recovered epicardial potentials 2 ms following the required distribution were used as the estimate, there was no improvement in quantitative results. However, qualitative changes could be seen; in particular, the site of right-ventricular breakthrough, present on the measured map but not on the Tikhonov inverse map, was evident as a minimum when Twomey regularization was applied. The selection of the temporal region was important in this case, as the selection of an estimate using distributions only at an earlier time instant would not have been able to make this change. For all Twomey methods, as the estimate of the desired epicardial potentials diverges from the actual values, so does the inverse solution. A weakness of this method is that it biases the inverse solution towards the Twomey estimate, including the magnitudes and locations of peak values.

Combined temporal and spatial constraints were explored by Brooks *et al.* [18, 19] and Maratos [100], who incorporated several consecutive time steps into the input data for the inverse problem to regularize simultaneously in time and space. They used a global regularization over space while considering only a small temporal region. Another approach to time-constraining the inverse solution assumes that the change in potential at a given location from one time instant to another may be represented by a linear prediction equation with subsequent use of Kalman filtering techniques to determine the epicardial potentials [39, 80]. This method requires the calculation of several parameters which are originally estimated from epicardial potentials known *a priori*. Ultimately, only body-surface potentials are used to determine parameters in the final step [39]. Published results pertaining to this approach are still scanty, but they show a promising improvement on Tikhonov regularization, even when only body-surface data are used. Temporal regularization methods generally attempt to constrain the inverse solution at a given time step, based on estimates or predictions

from a neighbouring temporal region that includes instants preceding and/or following the time of the distribution under investigation. Therefore, the solution is very dependent upon these estimates.

Addressing spatial regularization on a more regional basis, Iakovidis and Gulrajani [76] introduced the idea of a hybrid inverse solution. They first made the observation that in a solution where smoothing is greater than that for the optimal solution, the low-level potentials were smoothed more appropriately and there was a more realistic zero-line. On the other hand, when the solution was slightly underregularized, the locations and magnitudes of extrema were recovered with more accuracy. Their innovation was to calculate both over- and undersmoothed Tikhonov solutions, and then create a hybrid solution. For a chosen ε-band around zero, the oversmoothed potentials were used. Outside of this band, the underregularized solution was used, unless there was a discrepancy between the sign of the potential in the two initial estimates. For these locations, a value of ε was assigned, with the sign of the over-smoothed solution. This method requires the selection of a regularization parameter for both the under- and overregularized solutions, plus the selection of a bandwidth ε. There is a true regionalization to this method with varying amounts of regularization for low-level and large potentials. However, if the smoothed solution has a significant area of sign difference from the true solution, then it will not be possible to get good results. This can happen when there is a steep gradient of potential around the zero-line.

Inequality constraints are an extension of the potential estimate methods. Instead of estimating the exact potential at a given site, upper and lower bounds are imposed on the possible potential:

$$l_i \leq x_i \leq u_i. \tag{4.3}$$

Each location has its own bounds, so there is a definite regional structure to this constraint. Various methods have been proposed for determining the best bounds. Messinger-Rapport and Rudy [105] explored three different criteria. Their first method set a constant variation in potential and disregarded the magnitude of the potential

at the site. The range was determined from the *a priori* known potentials. They found that the largest errors occurred for the smallest potentials, where the variation was significantly larger than the actual potential. The second method still kept the variation constant for any given instant map, but let it vary with time. Here the maximum increase and decrease from the previous instant map to the one required were used as the range limits. The third method assumed that the position of the extrema and accompanying features were approximately known. Epicardial potentials were constrained only in these extremal regions, and were required to be at least 75% of the magnitude known *a priori*. The effect of this constraint was that the extrema were allowed to increase without associated increase in low-level potentials. Although all of these methods showed some improvement in quantitative measures of the inverse solution's accuracy and in the qualitative appearance of the inverse-recovered epicardial potential maps, they still required a good *a priori* estimate of the epicardial potentials.

Horáček and Clements [71] introduced a method of calculating the inequality bounds which is spatially regional in nature. They allowed the potential and the normal component of the potential gradient at the epicardial surface to vary as a factor of these estimated values at a given site. Therefore, potentials of small magnitude were allowed to vary over a smaller interval than the peak values. By setting the original estimate as a slightly oversmoothed Tikhonov solution, they have incorporated the idea of retaining the oversmoothed zero-line, while allowing the extrema to increase in magnitude as for the under-regularized solution. This method requires the selection of the bound factor and the appropriate regularization parameter t; it will be investigated further in this chapter (section 4.2).

Expanding on the idea of hybrid solutions or inequality constraints based on different regularization parameters, several investigators have suggested the possibility of determining more than one regularization parameter value for a given inverse procedure. The terms adaptive, local, and regional regularization have been used to describe this methodology. Khoury and Rudy [83] addressed the mathematically

equivalent inverse problem of determining endocardial potentials from those measured on an intracavitary probe. They calculated the appropriate t-parameter for each singular value. This can be done by substituting the epicardial potentials known *a priori* for x in Eq. 3.5 and replacing t with $\hat{t}_i$, so that each singular value and vector pair is associated with a separate regularization parameter. This can be formulated as follows:

$$x = \sum_{i=1}^{K} (u_i \cdot b) y_i + \sum_{i=K+1}^{K+L} \frac{\alpha_i}{\alpha_i^2 + \hat{t}_i \beta_i^2} (u_i \cdot b) y_i. \tag{4.4}$$

Using the endocardial potentials known *a priori*, the authors demonstrated the advantages of applying multiple regularization parameters, rather than a single global one.

When this method was tested on the data sets of epicardial and body-surface potentials generated as described in Chapters 2 and 3, it was noted that some of the $\hat{t}_i$ values were negative. In general, all $\hat{t}_i$ values associated with singular values which had a magnitude less than t^*, plus a few which were larger, were negative. In some cases this had the effect of scaling the resulting value, but for many other cases the problem was that $u_i \cdot b$ had the wrong sign and a negative t was necessary to correct it. Therefore, this problem would never be corrected by a positive t value and it is definitely adviseable to minimize the contribution of this singular vector to the inverse-recovered potentials.

Johnson and MacLeod [78] also suggested using more than one regularization parameter. In their case, they varied the parameter for different submatrices of the finite element system with which they were working. Their initial work was done on a two-dimensional model, but the results were promising. Oster and Rudy [118] used idealized heart-torso models—consisting of both concentric and eccentric spheres—to test the idea of regional regularization. They defined regional regularization as the subdivision of a potential map into functional regions based on spatial characteristics or frequencies. Their initial work used Legendre decomposition and graphically showed differences in different "regions" when there was error in the potentials on the outer sphere. To make the method applicable to arbitrary surfaces, they used the

singular value decomposition (SVD) to represent potential maps by their component parts. Several terms of the decomposition were grouped together for parameter selection. Their results demonstrated that, in the presence of noise, there are advantages to regional regularization over standard Tikhonov global regularization. By means of SVD, it was possible to correct for noise, but not for geometrical error, whereas the Legendre decomposition could correct for both. The authors felt that the arbitrary nature of the grouping of component maps for parameter selection with SVD may be responsible for the discrepancy, and suggested this as an area for further investigation. Another problem to be explored is the selection of a method for determining the multiple regularization parameters.

Calculating a separate regularization parameter for each region of the potential map is desirable. However, intuitively, it would be more advantageous to be able to separately regularize spatial regions instead of functional regions. Oster and Rudy [118] made the point that in the eccentric spheres model, necessary spatial features for reproducing the potentials for a source in the anterior heart are found in vectors corresponding to large singular values. Posterior sources required many more singular vectors to properly construct the potential map. In this way, they tried to relate spatial regionalization to regularization-parameter selection. Ideally, it is desirable to weight the regularizing operator based on *a priori* knowledge of the corresponding potential, gradient of potential or the second derivative at a given location. Then, even when a global regularization parameter is selected, it will actually represent different amounts of smoothing in different regions of the potential map. This method, along with its application with the Laplacian operator are presented later in section 4.3. The changes in singular vectors due to this regional weighting were noted along with increases in the time required for processing.

A second method of regional smoothing is introduced in section 4.4. Instead of weighting the Laplacian operator during the inversion procedure, a weighted Laplacian smoothing is applied to the first estimate. The weights are dependent on the

magnitude and curvature of the potential with respect to the maximum of these values on the map. The standard Tikhonov inverse is used as the initial estimate of the epicardial potential distribution to which weighted spatial smoothing is applied. The optimal t-parameter is selected based on this weighted solution. In a variation of the method, the optimal t value is selected prior to the weighting procedure. No *a priori* estimate is required for this computation.

The temporal continuity of the epicardial electrogram will be exploited in establishing a method of regularizing the inverse potentials over time in section 4.5. An attempt was made to avoid biasing the inverse-recovered potentials by using a temporal estimate in the inverse procedure. For this regional constraint, instead of using estimates of epicardial potential distributions which are close to the desired distributions in a temporal sense, once a time sequence of inverse-recovered epicardial potential distributions has been calculated, the potentials comprising the electrogram at each location are smoothed temporally. In this way, low-frequency oscillations due to noise in the body-surface electrocardiograms, as well as noise introduced by the calculation of epicardial potentials at each time instant in isolation from other instants will be addressed.

When the distribution of potentials on the epicardial surface for inverse-recovered values was compared to the distribution known *a priori*, it was frequently observed that it included "spurious" or "extraneous" extrema [10, 76, 118, 140, 144, 145]. These were often of the wrong sign as well as magnitude. In order to view the entire distribution of positive and negative potentials, the zero-line must be plotted. On these plots, regions where potentials with the incorrect sign have been recovered disrupt the overall spatial distribution of epicardial potentials, even if they are of low value compared to the global extrema. In certain cases, it is possible to eliminate at least some of these spurious extrema by selecting a relatively large regularization parameter, but only at the expense of oversmoothing potentials and displacing correct extrema. These conditions made it desirable to develop a procedure with the express purpose of identifying, and eliminating, areas where the sign of the potential was

incorrect.

The composite regional constraint method, presented in section 4.6, attempts to provide this function, using some terminology borrowed from image understanding systems. This seems appropriate, since the solution of the inverse problem of electrocardiography for epicardial potentials can be regarded as "electrocardiographic imaging" [93, 119, 120, 123]. Image understanding systems are designed to recognize events and draw conclusions based on information gleaned from the image itself, and any appropriate additional information which is available to it [11, 36]. Inverse-recovered epicardial potentials, the corresponding measured torso potentials, and the relationship between these as defined by the torso-heart model are analyzed in order to generate an hypothesis as to whether an artifact has been found. Additional knowledge about spatial and temporal (if dealing with time-sequence data) potential relationships is then utilized to determine if this hypothesis can be confirmed or not. Potentials designated as artifacts are replaced by values interpolated from "non-artifact" values in neighbouring regions. Spatial and (in appropriate circumstances) temporal constraints were applied in further processing of the data.

All regional-constraint methods will be investigated with the data sets of *a priori* potential distributions on the epicardial and torso surface that were established in Chapters 2 and 3. The relative merits of different methods and conditions under which they might be applicable will be discussed.

4.2 Inequality Constraint Optimization

Bounds on the value for each element of the potential distribution on the epicardial surface recovered by the inversion procedure comprise an inequality constraint. Horáček and Clements [71] introduced a method of calculating inequality bounds which is spatially regional in nature. Both the potential and the normal component of the potential gradient at the heart surface were allowed to vary as a factor of

estimates of the required values at each location. This constraint permits small magnitude potentials to vary over a smaller interval than the peak values. By setting the original estimate as a slightly oversmoothed Tikhonov solution, they have incorporated the idea presented by Iakovidis and Gulrajani [76] of retaining the zero-line of oversmoothed solution while allowing the extrema to increase in magnitude as for an under-regularized solution. The inequality problem is given by Eqs. 4.5 and 4.6.

$$\min_{x \in E^n} \{\|Ax - b\|^2 + t\|Bx\|^2\} \text{s.t.} l_i \leq x_i \leq u_i, i = 1, \ldots, N, \tag{4.5}$$

where u_i and l_i are upper and lower bounds given by

$$l_i = x_i(t_o) - \alpha|x_i(t_o)|, u_i = x_i(t_o) + \alpha|x_i(t_o)|, i = 1, \ldots, N \tag{4.6}$$

and α is the empirically chosen bound constraint factor; A, x, and b are defined as in Eq. 4.2.

$$A = \begin{pmatrix} P_{HH(n \times n)} & G_{HH(n \times n)} \\ P_{BH(m \times n)} & G_{BH(m \times n)} \end{pmatrix}, \quad x = \begin{pmatrix} \Phi_H \\ \Gamma_H \end{pmatrix}, \quad b = \begin{pmatrix} -P_{HB(n \times m)}\Phi_B \\ -P_{BB(m \times m)}\Phi_B \end{pmatrix},$$

where P and G matrices and ϕ and Γ are defined in Chapter 2.

This method requires the selection of the bound constraint factor and the appropriate t-parameter and the calculation of the Γ_H values.

Based on the results presented for the source consisting of three dipoles and a system using Tikhonov regularization with a second-order regularizing operator, the authors suggest that using 2.5 times the optimal t value with a constraint factor of 0.4 will improve on the optimal Tikhonov solution. In fact, an oversmoothed solution with the t-parameter up to 15 times the optimal value still gave some improvement in RE measures of inverse-solution accuracy.

The larger system, which includes the gradient of the epicardial potential normal to the heart surface, is not included in the work presented here. To enable the use of inequality constraint optimization, estimates of the Γ_H values were calculated from the inverse-recovered epicardial potentials. Bound constraints were applied to all values and the NAG library routine E04NCF [1] was used to solve the system. The

potential distributions generated by a single central dipole as well as three and five eccentric dipoles were used to test various t-parameters and bound constraint factors.

4.2.1 Results

Results for single- and multiple-dipole sources using three different t-parameter factors (0.5, 1.0, 2.5) and three constraint factors (0.2, 0.4, 0.6) with zero- and second-order regularizing operators are presented in Table 4.1.

The factors giving the smallest RE vary with source and regularizing operator. For the single central dipole, there was a maximum decrease in RE of .0059 with t-factor 2.5 and constraint factor 0.4 for the zero-order regularizing operator. For the second-order regularizing operator, there was an increase in RE for all factors, the minimum being .0041 for t-factor 0.5 and constraint factor 0.2. The maximum decrease in RE for the three-dipole source with the zero-order regularizing operator was .0201 with factors 2.5 and 0.6, and for the second-order regularizing operator a difference of .0408 resulted when the t-factor was 1.0 and the constraint factor 0.6. The magnitude of the decrease with the second-order regularizing operator compared well with the decrease of .0456 reported by Horáček and Clements [71] for the same source with their second-order Tikhonov regularizing system. Their finding that the RE improved for factors 2.5 and 0.4 was not duplicated in the present study, as there was an increase in RE for these parameters. For the five-dipole source and the zero-order regularizing operator, the maximum decrease in RE was .0084 with t and constraint factors 1.0 and 0.6, respectively. When the second-order regularizing operator was used, the decrease was .0232 with corresponding factors 2.5 and 0.6. No clues emerged as to which combination of factors would give the best results. Not only were the improvements in accuracy of the inverse solution achieved with this method relatively minor, but the cost for achieving them was high in terms of CPU time required. In an attempt to decrease the computational requirements, the inequality constraint was incorporated without including Γ_H in the process. As a result, the computation time was decreased considerably, but there were no decreases

Table 4.1:

Error measures (RE, CC) of inverse-recovered epicardial potentials for zero-
and second-order Tikhonov regularization with linear constraints, for single-
and multiple-dipole sources

Source	t-factor	constraint factor	B0		B2	
			RE	CC	RE	CC
single central dipole	0.5	.2	.3468	.9433	**.0623**	**.9981**
	0.5	.4	.3688	.9359	.0784	.9969
	0.5	.6	.3545	.9400	.0972	.9953
	1.0	.2	.3147	.9536	.0627	.9980
	1.0	.4	.3129	.9537	.0787	.9969
	1.0	.6	.3221	.9503	.0975	.9952
	2.5	.2	.3343	.9477	.0650	.9979
	2.5	.4	**.3061**	**.9558**	.0783	.9969
	2.5	.6	.3189	.9515	.0974	.9952
three eccentric dipoles	0.5	.2	.3751	.9343	.2177	.9760
	0.5	.4	.3589	.9365	.2334	.9727
	0.5	.6	.4181	.9121	.1757	.9844
	1.0	.2	.3330	.9462	.1880	.9822
	1.0	.4	.3260	.9479	.1751	.9845
	1.0	.6	.3226	.9486	**.1740**	**.9848**
	2.5	.2	.3579	.9369	.2337	.9723
	2.5	.4	.3344	.9457	.2354	.9719
	2.5	.6	**.3195**	**.9496**	.1813	.9834
five eccentric dipoles	0.5	.2	.5119	.8872	.3584	.9394
	0.5	.4	.5182	.8836	.3228	.9475
	0.5	.6	.5096	.8732	.3259	.9460
	1.0	.2	.4627	.8987	.3240	.9472
	1.0	.4	.4509	.9026	.3167	.9494
	1.0	.6	**.4461**	**.9034**	.3217	.9476
	2.5	.2	.4882	.8831	.3412	.9406
	2.5	.4	.5008	.8814	.3594	.9354
	2.5	.6	.4518	.9019	**.3142**	**.9502**

B0/B2, zero-/second-order Tikhonov regularization; RE, relative error; CC, correlation
coefficient; **bold font**, the best results.

in RE. For these reasons, further trials with this method were not undertaken.

4.2.2 Discussion

This section explored the use of inequality constraint optimization as a regional constraint on the inverse problem of electrocardiography. Inequality constraint optimization decreased RE and increased CC for a set of t and constraint factors for all cases, except in the case of the single central dipole with the Laplacian operator. However, since for this single-dipole source there is already a very minimal inverse-solution error, the slight increase in RE is not significant. This is an extremely smooth distribution so that the problems of oversmoothing peak amplitudes and undersmoothing low-level potentials is not an issue. Therefore, any process—such as inequality constraint optimization—with the goal of correcting the balance between over- and under-regularization is unlikely to achieve results better than Tikhonov regularization with the optimal t-parameter.

On the other hand, for the multiple eccentric-dipole sources it was possible to improve the solution over that achieved with the optimal t parameter. However, based on results, it appears that the choice of both the appropriate t factor and constraint factor varies with source and regularizing operator. The maximum decrease in RE for the three-dipole source with the second-order regularizing operator compared well with the decrease found by Horáček and Clements [71], but with different t and constraint factors. The actual RE values could not be compared, because the results computed in the present study used the improved quadrature systems and did not use the large system which includes the gradient of epicardial potentials. Either of these differences, or their combination, could be responsible for the discrepancy.

Further research into inequality constraint optimization could seek some other regional method of identifying factors that would be superior to the *ad hoc* factor selection used here. At present this approach was not further pursued, because of the minimal improvements in inverse-solution accuracy for some sources.

4.3 Weighted Regularizing Operator

The selection of separate t-parameters for different functional regions, as proposed by Oster and Rudy [118], gives variable dampening for different singular values. However, what is really desirable is to vary the degree of regularization in a spatially regional manner. With one global parameter, a compromise has to be made between oversmoothing potentials, gradients and curvatures of high magnitude and undersmoothing these values in regions where they are low. This section will examine a way to improve the Laplacian regularizing operator by weighting it, so that high-curvature areas are not required to meet the same level of smoothness as lower-curvature areas. Although spatial smoothness is a proper constraint for any distribution if the tesselation is fine enough, in practice it is not necessarily true for areas on the epicardial surface where there are large potential values. This was seen in results from Chapter 3. The single central dipole is located in the heart's center of gravity and it produces a very smooth epicardial potential distribution. The RE for the inverse-recovered potentials using Tikhonov regularization with the second-order regularizing operator was the lowest of all test data at .0582. For the eccentric single-dipole sources, however, there was a region of high-magnitude potential, gradient and curvature with the remaining areas of epicardial surface having low values. As the source moved nearer to the epicardial surface, the potentials increased and the area of high values decreased. This was generally accompanied by an increase in RE of inverse-recovered epicardial potentials. Therefore, the second-order (Laplacian) regularizing matrix will be weighted so that the same degree of smoothness does not apply to all locations.

As a validation of the method, weighting factors were first determined using *a priori* knowledge of the epicardial potential distribution. The coefficients of the Laplacian regularizing operator were calculated using the method of Oostendorp *et al.* [116]. With this method, the distances d_{i,n_j} between the centroid of a triangle and the centroids of its neighbouring triangles are used to weight the contribution of each neighbour's potential to the Laplacian. Regional weighting of the matrix involved multiplying the distance separating the triangles by the square root of the magnitude

of the difference in potential.

$$d_{i,n_j}\sqrt{|\phi_i - \phi_{n_j}|},$$

where n_j is the jth neighbouring triangle which shares a side with triangle i. The larger the difference in potential there was for a neighbour, the smaller the degree of smoothing was required.

The Generalized Singular Value Decomposition (GSVD) was then calculated for this new system for the single central dipole and three or five eccentric dipoles which have been used previously. It was also calculated for the five individual dipoles which comprise the composite five-dipole source; these dipoles were located 10 mm internal to triangles 222, 4, 158, 255 and 187 of the epicardial surface. For the time sequences of data, the potential distribution at 36 ms was selected for testing, for activation sequences initiated at septal and basal site, respectively. Epicardial potentials were determined and RE and CC of the inverse-recovered potentials were compared to the results obtained without regional weighting. To assess the utility of this method, the epicardial potentials recovered using the Laplacian regularizing operator were used as an *a posteriori* estimate to calculate the weighted Laplacian. The GSVD was calculated using these estimates and inverse potentials and errors were determined.

4.3.1 Results

Error measures (RE and CC) for inverse-recovered epicardial potentials calculated via second-order Tikhonov regularization ($t = t^*$) either with no regional constraint or with one of the two weighted-regularization options are shown in Table 4.2. In all cases, the RE for the first weighted-regularization option (WR1)—which is using *a priori* known epicardial potentials to determine weighting factors—was lower than that for the second-order regularizing operator with no regional constraint. The minimum difference in RE was for the single central dipole, which produces the smoothest distribution of the test set. This was a differences of .0081 (14%). The maximum difference, .2670, occurred for the source distribution consisting of the dipolar layer of activation wavefront at 36 ms after stimulus at the basal site, whereas the maximum

percentage difference of 75% occurred for an eccentrically located single dipole near $\Delta 158$ (at 10-mm depth into the left-ventricular free wall). The RE of inverse solutions for remaining test sources decreased due to application of WR1 method within the range of 42% and 59%. For WR1 method, the minimum CC for the variety of dipolar and multipolar sources was .9800, and the largest increase of CC over results obtained with second-order regularizing operator with no regional constraint was .0977; interestingly, this largest improvement occurred for the most complex source represented by the dipolar layer of basal wavefront.

Table 4.2:

Error measures (RE, CC) of inverse-recovered epicardial potentials for second-order Tikhonov regularization with no regional constraint (NRC) and that with weighted regularization (WR1, WR2), for single- or multiple-dipole sources

Source	NRC		WR1		WR2	
	RE	CC	RE	CC	RE	CC
single central dipole	.0582	.9983	**.0501**	**.9987**	.0617	.9981
three eccentric dipoles	.2148	.9774	**.1067**	**.9946**	.1529	.9886
five eccentric dipoles	.3374	.9433	**.1421**	**.9905**	.3191	.9481
single eccentric dipole near $\Delta 222$	.1340	.9923	**.0766**	**.9976**	.1119	.9943
single eccentric dipole near $\Delta 4$	.1384	.9912	**.0805**	**.9970**	.0920	.9961
single eccentric dipole near $\Delta 158$	.2883	.9580	**.0710**	**.9978**	.1824	.9834
single eccentric dipole near $\Delta 255$	.3758	.9337	**.1533**	**.9894**	.2813	.9648
single eccentric dipole near $\Delta 187$	.3876	.9262	**.2149**	**.9810**	.3652	.9335
Septal wavefront	.2733	.9619	**.1304**	**.9915**	.2417	.9704
Basal wavefront	.4716	.8823	**.2046**	**.9800**	.3963	.9195

WR1, first weighted-regularization option; WR2, second weighted-regularization option; RE, relative error; CC, correlation coefficient; Septal/Basal wavefront, an oblique dipolar layer generated by propagated activation initiated at the septal/basal site (Appendix B); **bold font**, the best results.

When the second weighted-regularization option (WR2) was used to calculate epicardial potentials—using the second-order regularizing operator—there was a dampening of the effects of weighting. For the single central dipole there was an increase in RE of .0035 (6%) over results obtained with second-order regularizing operator with no regional constraint, and the maximum percent decrease in RE, occurring for the eccentric dipole near $\Delta 158$, was now only 37% (compared to 75% with WR1). For WR2 the maximum difference in RE from the case of no regional constraint occurs also for $\Delta 158$ at .1059. The rest of the differences ranged from 5% to 33%. The maximum CC increase was still for the basal wavefront source, but it was only .0372.

Epicardial potential maps are shown in Fig. 4.1 for single- and multiple-dipole sources, and for three regularizing operators: second-order (Laplacian) operator, and weighted-regularization options WR1 and WR2.

Every time the regularizing operator is altered, the GSVD must be recalculated for the inversion procedure. Since the method of weighting the regularization based on epicardial potentials that are either known a $priori$ or estimated a $posteriori$ requires the regularizing operator to be altered for each set of torso potentials, the GSVD must be determined for every set. The amount of time required for this calculation depends on the dimensions of the arrays involved. For the 700×400 model employed in this study, this requires approximately 12 minutes of CPU time on our RS/6000 computer.

4.3.2   Discussion

This section considered the use of weighted regularizing operators in determining inverse-recovered epicardial potentials. When results—in terms of RE and CC of the inverse solution—achieved by WR1 (in which a $priori$ known potentials are used to set weighting) were compared to regularization with no regional constraint, the advantages of WR1 were obvious. The results for the time-sequence data, generated for basal and septal wavefronts at 36 ms, showed improved RE and CC. Therefore, the
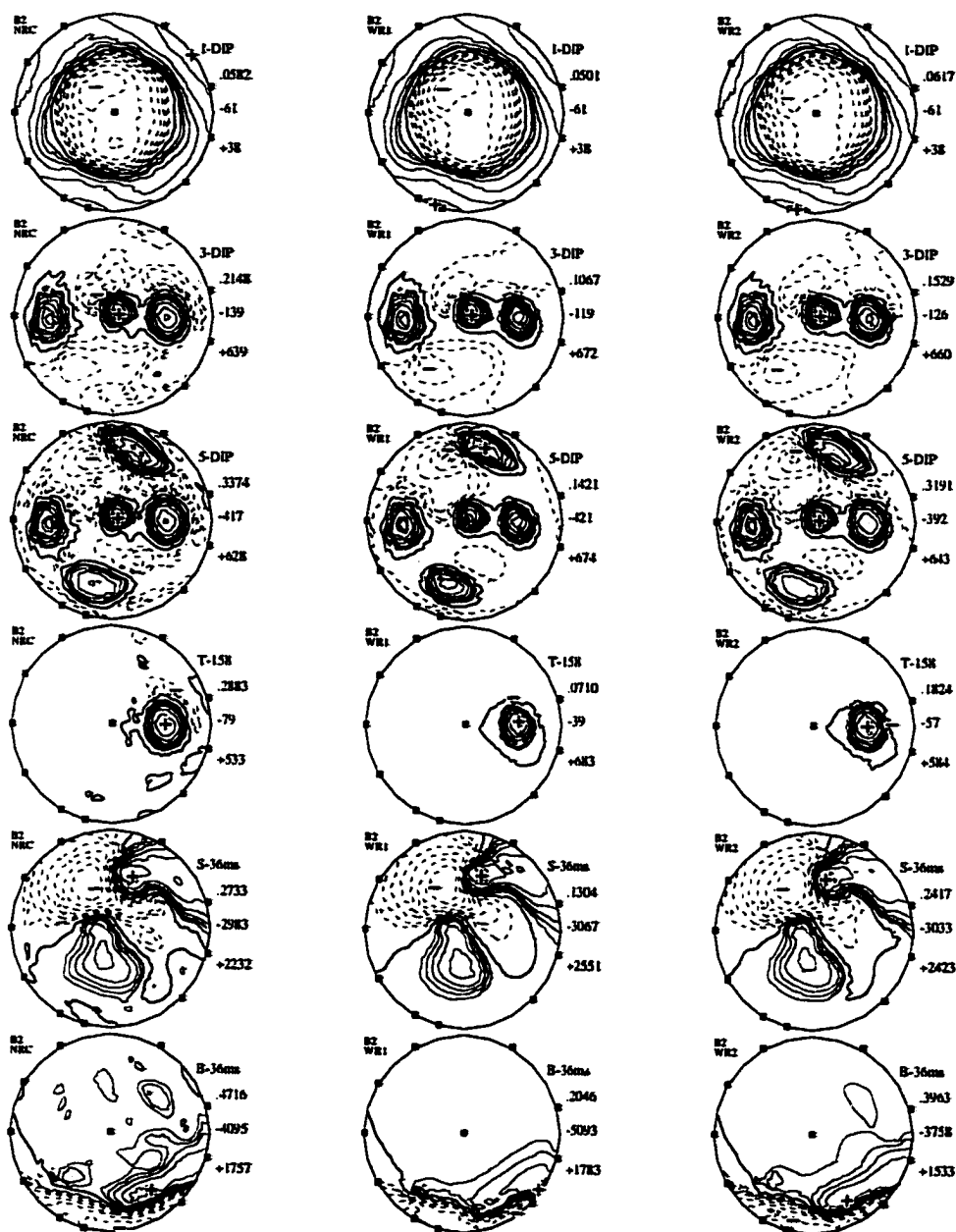
Figure 4.1: Effect of weighted spatial regularization on epicardial potentials generated by single- and multiple-dipole sources. The sources were (top to bottom) a single central dipole (1-DIP), three eccentric dipoles (3-DIP), five eccentric dipoles (5-DIP), a single eccentric dipole near $\triangle 158$ (T-158), and septal (S-36ms) and basal (B-36ms) oblique dipole layers at 36 ms into the activation sequence initiated at the single septal/basal site. Second-order Tikhonov regularization (B2) was performed with no regional constraint (NRC) [left column], weighted regularization with epicardial potentials known *a priori* (WR1) [center], or weighted regularization using epicardial potentials obtained by the NRC method as the *a posteriori* estimate (WR2) [right].

method should be as applicable to a realistic distribution with thousands of dipole sources as to the test cases with one or a few dipolar sources. This validates the premise of the method; however, to be of value, it must yield good results with *a posteriori* estimates. There was still change for the better with improvement in RE when the NRC inverse-recovered epicardial potentials were used to determine weighting, although the effect was dampened. This was to be expected, since these potentials were smoothed compared to the required ones, and they would not weight the system to the same extent. The degree of improvement when using a first estimate for weighting the regularizing operator varied with the source. In some cases, such as for an eccentric dipole near $\triangle 158$ at 10-mm depth, there was still a significant change. For other sources, for example an eccentric dipole near $\triangle 187$, there was now only a minor improvement seen in RE of the inverse solution.

From an examination of the singular vectors (column vectors of Q^T) it was noticed that weighting the regularizer imposed the major features of the epicardial potential distribution on the underlying singular vectors (results not shown). Therefore, it is apparent that the better the estimate used in the weighting process, the better the results. This is comparable to Messinger-Rapport and Rudy's finding that the better the estimate, the better the results of Twomey regularization [105]. For Twomey regularization, the estimate greatly influenced the resulting potentials; so that if the estimate was wrong, so was the distribution of inverse-recovered epicardial potentials. Since the singular vectors of Q^T incorporate information about the estimate used for weighting, it is clear that this method will also influence the solution incorrectly if the estimate is incorrect. However, unlike the Twomey method for which Messinger-Rapport and Rudy [105] found that using the regular Tikhonov zero-order inverse potentials as the comparison estimate resulted in no improvement in RE, unless the estimate was oversmoothed, in the present study there was still decreased RE and increased CC. This difference is inherent in the two methods. Twomey regularization minimizes the discrepancy between the inverse potentials and an estimate of their values, while the weighted regularization method alters the amount of regularization

at a given location based on the estimated potentials in relation to potentials in the neighbouring region.

Only second-order Tikhonov regularization was tested in this method; it is very likely that similar results would be obtained by analogously weighting the Identity (zero-order) or Gradient (first-order) regularizing operators.

The combination of the diminished improvement with *a posteriori* estimates and time involved in recalculating the GSVD for each set of input data (12 minutes on our RS/6000 computer) is a significant factor detracting from the usefulness of this method of regionally constraining the inverse problem.

Although there are some drawbacks to this implementation of regional constraints on the inverse problem, the results are a good indication that regional constraints and weighting the regularizing operator in particular, can be used to improve significantly the inverse-recovered epicardial potentials.

4.4   Weighted Spatial Smoothing

The issue of oversmoothing in some regions of the inverse-recovered epicardial potentials and undersmoothing in others will again be addressed in this section. Iakovidis and Gulrajani [76] dealt with the problem by using a hybrid solution where for small values they would use the results of an oversmoothed inverse, while using a slightly undersmoothed inverse for determining the larger potentials. The quality of their results depended upon the ability to properly define the correct sign to areas where there was a steep spatial gradient of potential on the epicardial distribution. The Weighted Regularizing Operator method (section 4.3) utilized the difference in potential between a given location and its neighbouring region to regionally constrain the inverse problem. However, although the resulting solutions improved on the Tikhonov inverse-recovered potentials, there was a significant increase in the time required for processing. A method to be introduced in this section is based on the same idea of regional weighting, but the significant requirements on computation time are avoided.

Weighted Spatial Smoothing (WSS) is a method of regionally constraining the inverse-recovered epicardial potentials which attempts to alleviate the problem of regional differences in the amount of smoothing required, taking into account the results for the inequality constraint optimization and weighted regularizing operator methods presented in previous sections of this chapter. Consideration was given to whether or not it was possible, using a Tikhonov inverse potential distribution as a first estimate, to apply regional constraints on the amount of regularization without recourse to re-inversion or multiple-inversion procedures. The goal was to reduce inverse-solution errors, compared to Tikhonov regularization with no regional constraint, without significantly increasing the time of processing.

To accomplish this, a method of weighted Laplacian smoothing was developed. Similar to the weighted regularization methods described in the previous section, the amount of smoothing is dependent on the difference in potential between one location and that of its neighbourhood. The magnitude of potential at any location was compared to the maximum amplitude for the potential distribution. The closer these were, the less smoothing was done. The maximum curvature (Laplacian) of the surface potential was computed as the maximum difference between the potential at any location and a weighted mean of the potentials of all other points in its neighbourhood. For the triangle-to-triangle systems, a neighbouring triangle was defined to be any triangle which shared two nodes with the given triangle. Because of the continuity of the tesselated epicardial surface, there were always three neighbours. For the node-to-node systems, neighbouring nodes were defined as any node which was the vertex of a triangle for which the given node was also a vertex. The number of neighbouring nodes varied. The difference between this maximum and the corresponding value at any given location also determined the amount of smoothing. Smoothness and amplitude were given equal value when calculating the weighting factors for each location. The weighted spatial smoothing solution, $\hat{x}$, was calculated via the formulation given in Eq. 4.7.

$$\hat{x}_i = (\omega_m + \omega_c)x_i + (1 - \omega_m - \omega_c)\bar{x}_i, \qquad (4.7)$$

where

$$\omega_m = .5 \frac{|x_i|}{\max\{|x_j| : j = 1, \ldots, n\}}$$

$$\omega_c = .5 \frac{|x_i - \tilde{x}_i|}{\max\{|x_j - \tilde{x}_j| : j = 1, \ldots, n\}},$$

with n the number of elements in x and ω_m and ω_c the weighting coefficients for magnitude and curvature, respectively, and $\tilde{x}$ the weighted mean neighbourhood potential value for x

$$\tilde{x}_i = -\frac{1}{B_{ii}} \sum_{j=n1,n2,n3} x_j B_{ij}$$

where $\triangle_{n1}, \triangle_{n2}, \triangle_{n3}$ are the three neighbouring triangles which share a side with $\triangle_i$ and B is the Laplacian operator. For a given t-parameter, the inverse solution was computed and then altered using the regional constraint stated in Eq. 4.7. The revised set of epicardial potentials which had the lowest RE in comparison with the a priori known potentials was determined. RE and CC for resulting solutions were computed and compared with results when regional constraints were not applied. The relative difference between the t-parameter selected by this weighted spatial smoothing procedure and that for the optimal Tikhonov solution was calculated to determine if there was a constant difference.

Although this procedure functions well for the optimal t method, when it is necessary to calculate the appropriate t value without the benefit of a priori knowledge of the epicardial potentials, determination of the optimal t-parameter would not be possible. Therefore, a variation of this method was developed, whereby the optimal solution is selected prior to applying the weighted spatial smoothing constraint. This method will function with any appropriate means of t-parameter selection. Results of this variation were compared to the original smoothing method. Both zero-order and second-order Tikhonov regularization were examined.

4.4.1 Results

The first variation of weighted spatial smoothing (WSS1) was tested initially on the data for sources consisting of a single central dipole and three and five eccentric

dipoles. Results in terms of RE and CC of the inverse-recovered epicardial potentials are displayed in Table 4.3. Error measures with no regional constraint (NRC) are given for comparison. With zero-order regularizing operator, there was a decrease in RE of .0891, .0866 and .0840 for the three distributions, respectively. CC increased in all cases. When the second-order regularizing operator was used, there were smaller changes. This was not unexpected with the Laplacian operator. Table 4.3 also contains a count of the number of triangles where the sign of the inverse-recovered epicardial potential did not match that of the *a priori* known potential value. Although numbers are small in all columns (considering that there are 400 epicardial triangles), WSS1 improved the count for all but two cases. In one of these, there was no change and for the other there was an increment of one.

The t-parameter selected by the WSS1 method was compared to the optimal t^* value for the corresponding Tikhonov solution with no regional constraint. The t selected for a system regularized by WSS1 operator was related to t^* by a factor of 0.52 for both zero-order and second-order regularizing operators and for the single central dipole, 0.31 and 0.41 for the source consisting of three eccentric dipoles and .30 and .35 for the source consisting of five eccentric dipoles. There was no discernible pattern to this factor, except that it showed a tendency to be higher for smoother distributions. The Tikhonov optimal t^*-parameter was chosen for use with the *a posteriori* WSS2 method, because no other selection method appeared to work for the entire range of distributions tested.

Inverse-solution errors in terms of RE, CC and sign mismatch counts for the second variation of weighted spatial smoothing (WSS2) are shown in the last three columns of Table 4.3. For these cases, there were only minor differences between results for WSS1 and WSS2, corresponding to only a 1% to 2% difference in the ability to improve the inverse solution. Based on this result, it seemed appropriate to use t^* to obtain the initial estimate of the epicardial distribution for the WSS2 method.

To further assess the effects of weighted spatial smoothing method WSS1, it was

Table 4.3:

Error measures (RE, CC, MM) of inverse-recovered epicardial potentials for zero- and second-order Tikhonov regularization with no regional constraint (NRC) and that with weighted spatial smoothing (WSS1, WSS2), for single- and multiple-dipole sources

Operator		NRC			WSS1			WSS2		
Order	Source	RE	CC	MM	RE	CC	MM	RE	CC	MM
B0	1Dip	.3120	.9501	12	**.2229**	**.9753**	9	.2246	.9750	**8**
	3Dip	.3396	.9410	16	**.2530**	**.9678**	**13**	.2577	.9667	13
	5Dip	.4545	.8924	30	**.3705**	**.9292**	**29**	.3765	.9271	29
B2	1Dip	**.0582**	**.9983**	**1**	.0586	.9983	2	.0592	.9983	4
	3Dip	.2148	.9774	14	**.1936**	**.9812**	**10**	.1976	.9804	11
	5Dip	.3374	.9433	24	**.3119**	**.9501**	**24**	.3169	.9486	25

B0/B2, zero-/second-order Tikhonov regularization; WSS1, first option of weighted spatial smoothing; WSS2, second option of weighted spatial smoothing; RE, relative error; CC, correlation coefficient; MM, total # of sign mismatches; 1Dip, single central dipole; 3Dip, three eccentric dipoles; 5Dip, five eccentric dipoles; **bold font**, the best results.

applied to the test data for a set of 1,600 dipoles in the proximity of the epicardial surface. For only 31 of the 1,600 dipoles was there any increase in RE when using the zero-order regularizing operator and in no case was there an increase using the second-order regularizing operator. Two thirds of dipoles showing increased RE were situated at a 2.5-mm distance from the epicardial surface – the closest proximity to the surface tested. Results were compared with the solution with no regional constraints and the differences are presented in Table 4.4. The maximum RE reflects the largest improvement in the inverse solution, and for different depths of the sources within the ventricular wall ranged around 0.2 for both the zero- and second-order operator. When the minimum RE is negative, it indicates the maximum increase in RE due to applying weighted spatial smoothing (WSS1). For the zero-order regularizing operator, these values range from $-.0163$ to $-.1020$; for the second-order operator the minimum RE ranges from a decrease of $.0021$ to $.0061$. The mean difference in RE was $.0777$ for the zero-order regularizing operator and $.0668$ for the second-order operator. These values are within the same range as previous results with the single central dipole and three/five eccentric dipoles.

Total sign mismatch counts (MM) and the mean value of sign mismatches per map (Mn) complementing results in Table 4.4 are shown in Table 4.5. Counts when the WSS1 method was used are lower than those for the best Tikhonov regularization with no regional constraint (NRC) in all cases. Overall, there was a 25% decline in the number of locations with an incorrect sign with weighted spatial smoothing WSS1, compared to NRC solution.

The same data set was then used with the second variation of the regional constraint, WSS2. A comparison was made of the ratio of the optimal t-parameters selected for each of the 1,600 dipoles for zero- and second-order regularizing operators using WSS1 to the optimal t value for the corresponding Tikhonov solution. Ratios ranged from $.2616 \times 10^{-5}$ to $.6288 \times 10^{+3}$. The mean value was 1.645 with a standard deviation of 18.098, while the median was $.3522$ with a standard deviation of $.1406$. The ratio was greater than 1.0 for 237 of the 3,200 cases included. Due to the

Table 4.4:

Differences in relative errors (RE) of inverse-recovered epicardial potentials between solution using zero- and second-order Tikhonov regularization with no regional constraint (NRC) and that with weighted spatial smoothing (WSS1), for 1,600 eccentric single-dipole sources at various depths in the ventricular wall

Order	Source	Max	Min	Mean±SD	Median±SD
B0	10.0-mm	.1913	−.0163	.0813±.0265	.0782±.0246
	7.5-mm	.2148	−.0189	.0854±.0351	.0792±.0299
	5.0-mm	.2243	−.0277	.0833±.0404	.0795±.0334
	2.5-mm	**.2024**	**−.1020**	**.0606±.0418**	**.0592±.0356**
	All above	**.2243**	−.1020	.0777±.0377	.0753±.0311
B2	10.0-mm	**.1107**	**.0021**	**.0425±.0178**	**.0399±.0136**
	7.5-mm	**.2128**	**.0026**	**.0640±.0282**	**.0601±.0252**
	5.0-mm	**.2161**	**.0041**	**.0809±.0394**	**.0749±.0379**
	2.5-mm	**.3586**	**.0061**	.0797±.0507	.0674±.0434
	All above	.3586	**.0021**	**.0668±.0393**	**.0585±.0320**

B0/B2, zero-/second-order Tikhonov regularization; WSS1, first option of weighted spatial smoothing; Max/Min, maximal/minimal difference in relative error within the set of dipoles (400 at each depth, 1,600 overall); Mean, mean difference in relative error for the given set of dipoles; Median, median of differences in relative errors for the given set of dipoles; SD, standard deviation; **bold font**, the best results.

Table 4.5:

Sign mismatch errors (MM, Mn) of inverse-recovered epicardial potentials for zero- and second-order Tikhonov regularization with no regional constraint (NRC) and that with weighted spatial smoothing (WSS1, WSS2), for 1,600 eccentric single-dipole sources at various depths in the ventricular wall

Order	Source	NRC		WSS1		WSS2	
		MM	Mn	MM	Mn	MM	Mn
B0	10.0-mm	16,051	40	11,033	28	8,669	22
	7.5-mm	23,406	58	16,787	42	12,815	32
	5.0-mm	**35,133**	**88**	26,534	66	**20,943**	**52**
	2.5-mm	50,366	126	41,630	104	34,017	85
	All above	124,956	78	95,984	60	76,494	48
B2	10.0-mm	**13,094**	**33**	**8,810**	**22**	**7,571**	**19**
	7.5-mm	**21,920**	**55**	**15,083**	**38**	**12,495**	**31**
	5.0-mm	35,137	88	**25,611**	**64**	21,309	53
	2.5-mm	**49,589**	**124**	**39,642**	**99**	**33,402**	**83**
	All above	**119,740**	**75**	**89,146**	**58**	**74,777**	**47**

B0/B2, zero-/second-order Tikhonov regularization; WSS1, first option of weighted spatial smoothing; WSS2, second option of weighted spatial smoothing; MM, total number of sign mismatches within the set of dipoles (400 at each depth, 1,600 overall); Mn, mean value of sign mismatches for the given set of dipoles; **bold font**, the best results.

Table 4.6:

Differences in relative errors (RE) of inverse-recovered epicardial potentials
between solution using zero- and second-order Tikhonov regularization with
no regional constraint (NRC) and that with weighted spatial smoothing
(WSS2), for 1,600 eccentric single-dipole sources at various depths in the
ventricular wall

Order	Source	Max	Min	Mean±SD	Median±SD
B0	10.0-mm	.1770	−.0186	.0744±.0256	.0711±.0166
	7.5-mm	.2144	−.0191	.0758±.0339	.0698±.0189
	5.0-mm	.2165	−.0365	.0725±.0391	.0670±.0210
	2.5-mm	**.1817**	−.1089	**.0498±.0386**	**.0474±.0306**
	All above	**.2165**	−.1089	.0681±.0363	.0648±.0301
B2	10.0-mm	**.0958**	−.0019	**.0378±.0170**	**.0352±.0136**
	7.5-mm	**.1351**	**.0010**	**.0562±.0252**	**.0531±.0160**
	5.0-mm	**.2158**	−.0033	**.0710±.0380**	**.0632±.0369**
	2.5-mm	.2372	.0030	.0679±.0455	.0547±.0372
	All above	**.2372**	−.0033	**.0582±.0357**	**.0496±.0278**

B0/B2, zero-/second-order Tikhonov regularization; WSS2, second option of weighted
spatial smoothing; Max/Min, maximal/minimal difference in relative error within the
set of dipoles (400 at each depth, 1,600 overall); Mean, mean difference in relative error
for the given set of dipoles; Median, median of differences in relative error for the given
set of dipoles; SD, standard deviation; **bold font**, the best results.

large variation in these results, and judging from the comparison of WSS1 and WSS2
results with the different sources (central dipole vs. eccentric multiple dipoles), it was
deemed appropriate to use the Tikhonov solution optimal t-parameter with the WSS2
method for the test data generated by 1,600 dipoles. Corresponding differences in
relative errors between the Tikhonov solution with no regional constraints and with
weighted spatial smoothing WSS2 are shown in Table 4.6.

The number of dipoles for which RE increased when using WSS2 with the zero-
order regularizing operator rose in comparison with results for WSS1 by 6, to 37, and
there were now three occasions where there was increased RE with the second-order
regularizing operator, but the latter increases were very small. Overall, WSS2 was

Table 4.7:

Differences in node-to-node relative errors (RE) of inverse-recovered
epicardial potentials between solution using zero- and second-order Tikhonov
regularization with no regional constraint (NRC) and that with weighted
spatial smoothing (WSS1), for 1,600 eccentric single-dipole sources at various
depths in the ventricular wall

Order	Source	Max	Min	Mean±SD	Median±SD
B0	10.0-mm	.1959	−.0286	.0822±.0340	.0819±.0319
	7.5-mm	.2196	−.0439	**.0785±.0388**	.0774±.0391
	5.0-mm	.2582	−.0587	**.0720±.0450**	**.0695±.0432**
	2.5-mm	.2197	−.0533	.0492±.0437	.0456±.0412
	All above	.2582	−.0587	.0705±.0425	.0709±.0411
B2	10.0-mm	**.1620**	−.0128	**.0674±.0311**	**.0638±.0322**
	7.5-mm	**.2029**	−.0036	.0790±.0400	**.0743±.0428**
	5.0-mm	**.2485**	.0010	.0797±.0447	.0726±.0451
	2.5-mm	**.2080**	.0006	**.0481±.0363**	**.0409±.0340**
	All above	**.2485**	−.0128	**.0685±.0404**	**.0630±.0396**

B0/B2, zero-/second-order Tikhonov regularization; WSS1, first option of weighted
spatial smoothing; Max/Min, maximal/minimal difference in relative error within the
set of dipoles (400 at each depth, 1,600 overall); Mean, mean difference in relative error
for the given set of dipoles; Median, median of differences in relative error for the given
set of dipoles; SD, standard deviation; **bold font**, the best results.

2–3% less effective in decreasing RE than WSS1.

Sign mismatch numbers are given in Table 4.5. Although by RE measures WSS2
was slightly less effective in improving the inverse-recovered potentials, sign mismatch
counts for WSS2 showed that there was better agreement in signs of potentials. WSS2
sign mismatch counts represented a decrease of 14–24% over WSS1 values.

As a next step, the node-to-node system was tested to see if the WSS1 and WSS2
methods would give equivalent results to those for the triangle-to-triangle system.
Table 4.7 presents the differences between errors when using WSS1 and when no
regional constraint was applied. RE increased for 90 of the 1,600 dipoles with the zero-
order regularizing operator and 4 of the 1,600 dipoles for the second-order operator;

Table 4.8:

Differences in node-to-node relative errors (RE) of inverse-recovered epicardial potentials using zero- and second-order Tikhonov regularization with no regional constraint (NRC) and that with weighted spatial smoothing (WSS2), for 1,600 eccentric single-dipole sources at various depths in the ventricular wall

Order	Source	Max	Min	Mean±SD	Median±SD
B0	10.0-mm	.1612	−.0300	.0650±.0297	.0628±.0256
	7.5-mm	.1551	−.0470	**.0564±.0307**	**.0550±.0257**
	5.0-mm	**.1587**	−.0590	**.0497±.0335**	**.0492±.0307**
	2.5-mm	.1555	−.0556	**.0326±.0315**	.0322±.0300
	All above	**.1612**	−.0590	.0509±.0336	.0508±.0303
B2	10.0-mm	**.1426**	−.0133	**.0530±.0271**	**.0530±.0271**
	7.5-mm	.1667	−.0037	.0596±.0318	.0564±.0328
	5.0-mm	.2010	.0009	.0573±.0328	.0507±.0322
	2.5-mm	**.1547**	**.0006**	.0327±.0241	**.0286±.0223**
	All above	.2010	**−.0133**	.0564±.0310	**.0457±.0291**

B0/B2, zero-/second-order Tikhonov regularization; WSS2, second option of weighted spatial smoothing; Max/Min, maximal/minimal difference in relative error within the set of dipoles (400 at each depth, 1,600 overall); Mean, mean difference in relative error for the given set of dipoles; Median, median of differences in relative error for the given set of dipoles; SD, standard deviation; **bold font**, the best results.

mean differences were .0705 for zero-order and .0685 for second-order operator. These were equivalent to approximately an 11% decrease in RE for each. Maximum decrease in RE was in the range of 30–40%. Improvement over optimal Tikhonov regularization solutions was found, but the effects were dampened somewhat in comparison to the triangle-to-triangle system.

Data for weighted spatial smoothing method WSS2 are in Table 4.8. With WSS2, 113 of the individual dipoles had an increased RE for the zero-order regularizing operator and 6 for the second-order operator; the mean difference was .0508 for the former and .0457 for the latter. These represent a decrease in RE of approximately 7%. Maximum decreases ranged from 25% to 35%. The decreases in RE values

Table 4.9:

Differences in relative errors (RE) of inverse-recovered epicardial potentials between solution using zero- and second-order Tikhonov regularization with no regional constraint (NRC) and that with weighted spatial smoothing (WSS1), for two time sequences of double-layer sources

Order	Source	Max	Min	Mean±SD	Median±SD
B0	Septal	.0948	.0456	.0697±.0116	.0707±.0059
	Basal	.0781	.0284	.0482±.0119	.0468±.0109
B2	**Septal**	**.0111**	**−.0012**	**.0035±.0038**	**.0021±.0033**
	Basal	**.0753**	**−.0035**	**.0147±.0236**	**.0035±.0049**

B0/B2, zero-/second-order Tikhonov regularization; WSS1, first option of weighted spatial smoothing; Septal/Basal, a sequence of oblique dipolar layers generated by propagated activation initiated at the septal/basal site (Appendix B); Max/Min, maximal/minimal difference in relative error within the set of dipoles comprising the wavefront; Mean, mean difference in relative error for the given set of dipoles; Median, median of differences in relative error for the given set of dipoles; SD, standard deviation; **bold font**, the best results.

are slightly lower than for weighted spatial smoothing method WSS1, as they were for the triangle-to-triangle system. They are also lower than those found for the triangle-to-triangle system.

To see what happened when a more realistic distribution was used as the source, the two time-sequence data sets were also tested. Results for WSS1 method, with differences from those where no regional constraint was applied are shown in Table 4.9. For both the septal and basal sequences, there was never an increase in RE with the zero-order regularizing operator. For the second-order regularizing operator there was an increase for 6 distributions for the activation sequence initiated at the septal site and 5 distributions for the activation sequence initiated at the basal site. The average change in RE for septal activation sequence was .0697 for the zero-order regularizing operator and .0035 for the second-order operator, with a maximum change of .0948. For the activation sequence initiated at the basal site these changes were .0482 and

Table 4.10:

Relative errors (RE) of inverse-recovered epicardial potentials for zero- and second-order Tikhonov regularization with weighted spatial smoothing (WSS2), for two time sequences of double-layer sources

Order	Source	MaxRE	MinRE	Mean±SD	Median±SD
B0	Septal	.5678	.2255	.3749±.0948	.3785±.1128
	Basal	.8182	.4259	.5589±.1039	.5570±.0951
B2	Septal	.4139	.1073	.2722±.1044	.2649±.1508
	Basal	.8207	.3792	.4908±.1197	.4485±.0747

B0/B2, zero-/second-order Tikhonov regularization; Septal/Basal, a sequence of oblique dipolar layers generated by propagated activation initiated at the septal/basal site (Appendix B); WSS2, second option of weighted spatial smoothing; MaxRE/MinRE, maximal/minimal relative error within the set of dipoles comprising the wavefront; Mean, mean relative error for the given set of dipoles; Median, median of relative errors for the given set of dipoles; SD, standard deviation; **bold** font, the best results.

.0147, with a maximum of .0781. The corresponding percent changes for the activation sequence initiated at the septal site were 17% and 1%, with a maximum of 24%, and for the activation sequence initiated at the basal site percent changes were 8% and 2%, with a maximum 13% difference.

The results for weighted spatial smoothing method WSS2 are shown in Table 4.10, with differences in Table 4.11. For both the septal and basal sequences, there was again no increase in RE with the zero-order regularizing operator. For the second-order regularizing operator there was an increase for 17 distributions for the septal site and 11 distributions for the basal site, but the maximum increase was small at .0043. The average change in RE for septal activation was .0660 for the zero-order regularizing operator and .0014 for the second-order operator with a maximum change of .0868. For the basal site these changes were .0435 and .0116, with a maximal change of .0703. The corresponding percent changes for the septal site were 16% and less than 1%, with a maximum of 24%, and for basal site were 8% and 2%, with a maximum

13% difference. There is no significant change in these values from those for WSS1. Changes are smaller than for the other data sets tested.

Table 4.11:
Differences in relative errors (RE) of inverse-recovered epicardial potentials between solution using zero- and second-order Tikhonov regularization with no regional constraint (NRC) and that with weighted spatial smoothing (WSS2), for two time sequences of double-layer sources

Order	Source	Max	Min	Mean±SD	Median±SD
B0	Septal	.0868	.0437	.0660±.0104	.0688±.0445
	Basal	.0703	.0171	.0435±.0127	.0427±.0110
B2	Septal	**.0077**	**−.0018**	**.0014±.0030**	**.0002±.0022**
	Basal	**.0635**	**−.0043**	**.0116±.0206**	**.0016±.0050**

B0/B2, zero-/second-order Tikhonov regularization; Septal/Basal, a sequence of oblique dipolar layers generated by propagated activation initiated at the septal/basal site (Appendix B); WSS2, second option of weighted spatial smoothing; Max/Min, maximal/minimal difference in relative error within the set of dipoles comprising the wavefront; Mean, mean difference in relative error for the given set of dipoles; Median, median of differences in relative error for the given set of dipoles; SD, standard deviation; **bold font**, the best results.

Sign mismatch counts for NRC and both WSS1 and WSS2 are in Table 4.12. The use of WSS1 results in a decrease in counts for both septal and basal activation-sequence data sets. These changes range from 14% to 28%. Further decreases of 7% to 15% are seen when WSS2 is used instead.

Epicardial potential maps were plotted in Fig. 4.2 for a qualitative assessment of the changes due to weighted spatial smoothing options WSS1 and WSS2 as compared to inverse-recovered maps obtained with no regional constraint.

Finally, WSS1 and WSS2 were tested in the presence of Gaussian noise. The source consisting of three eccentric dipoles was used for these tests. Noise levels of 1%, 5%, 10% and 20% were added to the torso potentials. These perturbed potential

Table 4.12:

Sign mismatch errors (MM, Mn) of inverse-recovered epicardial potentials for zero- and second-order Tikhonov regularization with no regional constraint (NRC) and that with weighted spatial smoothing (WSS1, WSS2), for two time sequences of double-layer sources

Order	Source	NRC		WSS1		WSS2	
		MM	Mn	MM	Mn	MM	Mn
B0	Septal	1549	43	1120	31	1003	28
	Basal	1727	48	1479	41	**1260**	**35**
B2	Septal	**1074**	**30**	**905**	**25**	**846**	**23**
	Basal	**1697**	**47**	**1416**	**39**	1309	36

B0/B2, zero-/second-order Tikhonov regularization; NRC, optimal Tikhonov solution with no regional constraint; WSS1, first option of weighted spatial smoothing; WSS2, second option of weighted spatial smoothing; Septal/Basal, a sequence of oblique dipolar layers generated by propagated activation initiated at the septal/basal site (Appendix B); MM, total number of sign mismatches within the set of dipoles comprising the wavefront; Mn, mean value of sign mismatches for the given set of dipoles; **bold font**, the best results.
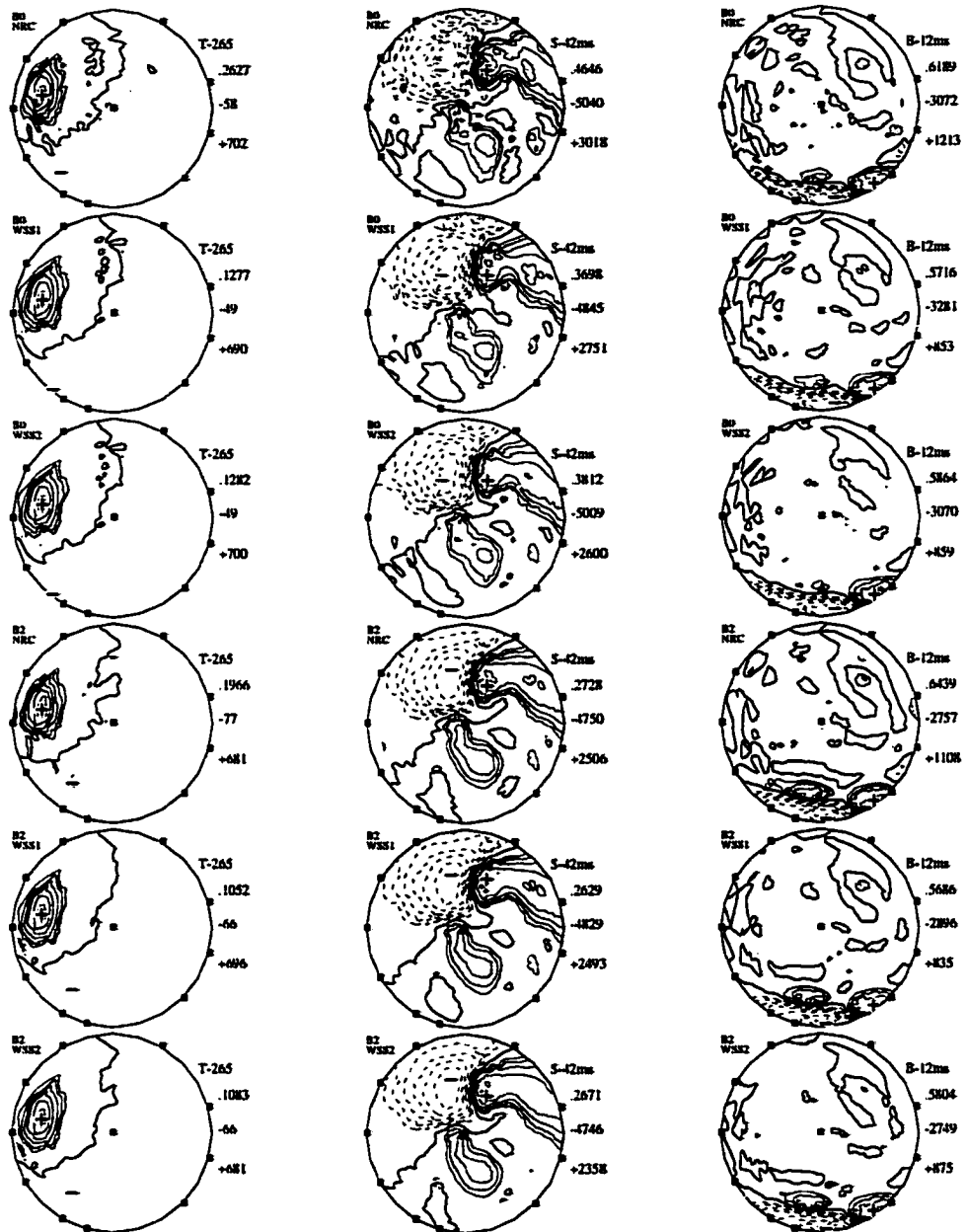
Figure 4.2: Epicardial potential maps obtained with and without weighted spatial smoothing. Columns, from left to right, show inverse-recovered epicardial potential maps for test distributions generated by a single dipole near $\triangle265$ (T-265); an oblique dipole layer at 42 ms after stimulation at the septal site (S-42ms), and an oblique dipole layer at 12 ms after stimulation at the basal site (B-12ms). Rows, from top to bottom, show maps regularized by means of zero- or second-order Tikhonov regularization (B0/B2) as follows: B0/NRC, B0/WSS1, B0/WSS2, B2/NRC, B2/WSS1, and B2/WSS2. NRC, no regional constraint; WSS1/WSS2, first/second variant of weighted spatial smoothing.

values were used as input data for zero- and second-order Tikhonov regularizing systems, first without applying any regional constraint methods and then with weighted spatial smoothing options WSS1 and WSS2. Results—including those for noiseless torso potentials, which have been included for comparison—are summarized in Table 4.13. For all noise levels, the difference between WSS1 and WSS2 results was small, with differences in RE less than .01 (2%). When RE for WSS1 method was compared to those obtained when no regional constraint was applied, differences were consistent over the different noise levels. For the zero-order regularizing operator the average difference was .0813 and for the second-order operator it was .0267. Percentage improvements in RE as a result of applying weighted spatial smoothing decreased somewhat, but this is to be expected as the amount of error increased with increasing noise levels. Therefore, although Gaussian noise affects actual error values, it does not appear to diminish the beneficial effects of the regional constraints imposed by weighted spatial smoothing methods WSS1 and WSS2.

4.4.2 Discussion

This section explored the use of regionally weighted spatial smoothing as a constraint on the epicardial potentials. The epicardial potentials were first calculated using Tikhonov regularization with no regional constraints. These potentials were then subjected to a weighted Laplacian smoothing procedure. Weights were determined by the difference in amplitude between the potential at a given location and the potential in a neighbouring region, as well as regional differences in curvature of the potential distribution, compared to the maximum of these values over the epicardial potential distribution. Regions of high amplitude and curvature received a moderate amount of smoothing compared to areas where these values were relatively low. Weighting due to amplitude and curvature were given equal value.

Two variants of weighted spatial smoothing were investigated. The first, WSS1, determined the optimal t-parameter to use by computing the regionally constrained

Table 4.13:

Effect of Gaussian noise, added to torso-surface potentials generated by a source consisting of three eccentric dipoles, on relative errors (RE) of inverse-recovered epicardial potentials for zero- and second-order Tikhonov regularization with no regional constraint (NRC) and that with weighted spatial smoothing (WSS1, WSS2)

Regional Constraint	Rms Noise (%)	B0 RE	B2 RE
NRC	0	.3396	.2148
WSS1	0	**.2530**	**.1936**
WSS2	0	.2577	.1976
NRC	1	.3605	.2506
WSS1	1	**.2746**	**.2239**
WSS2	1	.2810	.2290
NRC	5	.3864	.3039
WSS1	5	**.3040**	**.2739**
WSS2	5	.3114	.2796
NRC	10	.4046	.3367
WSS1	10	**.3246**	**.3097**
WSS2	10	.3327	.3153
NRC	20	.4296	.3680
WSS1	20	**.3527**	**.3449**
WSS2	20	.3602	.3475

B0/B2, zero-/second-order Tikhonov regularization; WSS1, first option of weighted spatial smoothing; WSS2, second option of weighted spatial smoothing; **bold font**, the best results.

potentials and then finding the best match, as measured by RE, with the epicardial potentials known *a priori*. For the different potential distributions tested, there was a large variation in the relative difference of the size of the selected *t*-parameter compared to the one chosen when there was no regional constraint. RE measures decreased as a result of applying the regional constraint imposed by WSS1 method for all but a few cases. The instances where an increase in RE occurred could be due to an area with high amplitude and curvature of potential, which deteriorated somewhat when smoothing was applied. For the large majority of cases where RE decreased, there was still variation in the degree of improvement. This could be due to the underlying epicardial potential distribution which the inverse procedure is attempting to reconstruct. The amount of decrease for some test distributions also varied depending on the Tikhonov regularizing operator which was employed. Tikhonov second-order regularization already makes use of Laplacian smoothing as a physiological constraint. For an epicardial map where there are no pronounced extremes of amplitude or curvature of potential, such as that for the single central dipole, inverse-recovered epicardial potentials obtained with second-order regularizing operator already incorporate the smoothing which is applied again as WSS1. Therefore, differences due to WSS1 method may be expected to be small. However, for the potential distributions generated by the same central dipole source, inverted with the zero-order regularizing operator, and then smoothed by applying WSS1, there was still a significant improvement in terms of a decreased RE. In the case of zero-order regularization, only the norm of the amplitudes had been constrained and thus low-level potentials still required additional smoothing. When dealing with epicardial distributions which do not exhibit the degree of smoothness characteristic for the central dipole source, the RE measure improves when using both second- and zero-order regularizing operators. For the set of 1,600 eccentric dipoles, the mean and median of improved RE were just slightly lower for second-order than for zero-order regularizing operator. The results produced with realistic time-sequence sources showed little change for the second-order regularizing operator, but still some decrease in RE for

applications where the zero-order regularizing operator was used. For many of these realistic torso-surface potential distributions, the optimal t-parameter is larger than for the dipole sources, so that results obtained with the second-order regularizing operator will have already incorporated a larger degree of smoothing.

When the distribution of potentials on the epicardial surface for values known *a priori* and the distribution obtained by the inverse solution were compared, WSS1 decreased the number of locations where there was a sign mismatch, for both regularizing operators and at all distances, regardless of corresponding changes in RE measures. These results support the notion [76] that potentials in the area of the zero-line require more smoothing than those in the areas surrounding extrema.

Results presented in Chapter 3 indicate that for most potential distributions in the test distributions used in this study, the node-to-node system is less successful in recovering the epicardial distribution than the system constructed by means of the triangle-to-triangle method. WSS1 method was tested on the node-to-node system to find out if it is robust enough to decrease RE under these conditions. Average decreases in RE as a result of applying WSS1 were somewhat smaller than for the triangle-to-triangle system, but they were more or less in the same range. Larger optimal t values necessary for node-to-node systems, and the associated inherent increase in the smoothness of the solution, could be responsible for this difference.

Results from this section support the use of the regional constraint based on weighted spatial smoothing. However, in clinical applications where the epicardial potentials are not available for comparison, the optimal t parameter must be selected differently. Methods for selecting these values for Tikhonov regularization will be discussed in Chapter 5. None of the methods to be presented allow for altering the inverse epicardial potentials after Tikhonov inversion and prior to t selection. Therefore, a variation of weighted spatial smoothing which determines an optimal parameter before applying the regional constraint was introduced. The ratio of the parameter used for WSS1 to that for the corresponding Tikhonov regularization method was examined. Large variations in this ratio were found; moreover, although t parameters

used for WSS1 were usually smaller than the Tikhonov optimal value, sometimes they were larger. The former was an expected result, since extra smoothing where required would allow a smaller t to give better peak values. The latter was not expected, but it could be explained by the fact that as the amount of regularization increases, the difference between potentials will decrease. This not only involves the dampening of some values, but also the relative increase in potential at others. In some cases, RE measures were smaller when a lower t parameter was used without WSS1. Although peaks had too large a magnitude, the underregularized inverse solution kept a better balance between values. When WSS1 was applied, the peaks could be decreased—because of the method's regionally weighted nature—without unwanted relative increases elsewhere in the distribution. No pattern which could be used to facilitate the selection of a t value for WSS2 was found; therefore, the Tikhonov optimal t value was used. Mean RE measures for WSS2 were only slightly higher (from 1% to 3%) than those for WSS1, although in individual cases there were larger differences.

The distributions of inverse-recovered epicardial potentials obtained with WSS2 were examined and compared (in terms of two error measures, MM and RE) with results obtained with WSS1. Mismatch counts for WSS2 decreased even further, in comparison with NRC, than those obtained with WSS1, but RE measures were worse. This may be explained by the fact that in all but a few cases the t parameter used for WSS2 was larger than for WSS1, allowing for more smoothing around the zero-line and resulting in less sign discrepancy. Based on these results, on average, the Tikhonov optimal t-parameter is appropriate for WSS2.

The effect of noise on the resulting decreases in RE with the application of this regional constraints WSS1 and WSS2 was also investigated. RE increased with increasing Gaussian noise level, but the difference between RE for Tikhonov regularization with and without weighted spatial smoothing constraints remained the same. Percent changes were smaller because of the increase in error values.

For WSS1 method, there was an increase in time required for processing—in

comparison with WSS2 method—as the regional constraint calculations had to be done for each t value in the selection procedure. This calculation has to be performed only once for WSS2.

4.5 Temporal Continuity

The regional constraint methods dealt with in this chapter thus far have all treated each spatial distribution of torso-surface potentials in temporal isolation. However, clinical torso-surface distributions are recorded as multiple electrocardiographic signals continuously sampled—typically at the rate of 1,000 samples per second—for at least 10 seconds. In this section, methods of constraining the inverse-recovered epicardial potentials by making use of data available in the chosen temporal region will be explored.

Brooks *et al.* [18, 19] and Maratos [100] included the time component in their analysis by incorporating several time steps into the inverse problem formulation, and thus regularizing in time and space domains simultaneously. The size of the system to be evaluated and the time required to analyze it increased greatly with the number of timesteps considered, and thus only a small number of samples was included in the analysis. In investigations by Joly *et al.* [80], later extended by El-Jakl *et al.* [39], it was assumed that the change in potential at a given location on the epicardial surface from one time instant to the next may be represented by a linear prediction equation. Kalman filtering techniques were applied to determine the resulting epicardial potentials. As a first step, *a priori* known potentials were used to compute the appropriate matrices for the finite element system. In a later version, measured torso-surface potentials alone were used to calculate the matrices. Without the *a priori* knowledge of epicardial potentials, improvements on Tikhonov regularization results without time constraint were not as great, but they were noticeable – at least on a qualitative basis.

A temporal estimate of the required epicardial potentials was used in the Twomey

method for regularizing the inverse problem of electrocardiography by Messinger-Rapport and Rudy [105]. This work was later expanded by Oster and Rudy [117] in a study designed to investigate what combination of neighbouring time instants gave the best estimate. When using epicardial potential values known *a priori* in estimate calculation, they determined that the average of the preceding and following time steps and a combination of these samples plus the values at the desired time step resulted in the most improvement in error measures. The shortest time step that was investigated, 0.5 ms, gave the best results. One example was documented where no *a priori* knowledge of the potentials was assumed. Using the inverse-recovered epicardial potential distribution at the first time instant where right-ventricular breakthrough was manifested in torso-surface potentials as the estimate for the previous time step, they were able to recover a minimum at the appropriate location – which Tikhonov regularization without time constraints was unable to do. Although there was a qualitative improvement in inverse-recovered epicardial potentials, quantitative results did not change. The qualitative improvement achieved with Twomey regularization was very dependent on the estimate. If just the preceding time step had been used as the estimate, one would not expect the minimum to be corrected.

When inverse-recovered epicardial potentials are calculated for a time sequence of torso-surface potential distributions, one can plot an electrogram of potential values versus time at each epicardial location. The temporal continuity (TC) method presented in this section makes an assumption of some degree of smoothness within these electrograms at each site on the epicardial surface. "Noise" found in the electrograms may be the result of the selection of separate t-parameters for each time instant, noise in the input data (torso-surface potentials) and the application of constraints on the inverse-recovered epicardial potentials. TC attempts to counteract these problems by imposing a degree of smoothness over each temporal complex of the time sequence of inverse-recovered epicardial potentials.

Numerical Recipes routine SMOOFT [128] was used in the calculation of the TC results. This routine smooths an array Y of length N, with a window whose full width

is of the order PTS neighbouring points. The value of PTS must be supplied and sets the amount of smoothing to be incorporated. A value of zero gives no smoothing at all. As PTS increases, so does the amount of smoothing. Values larger than about half the number of data points will make the data virtually featureless. The routine assumes that the abscissa are equally spaced. As a first step, any linear trend is removed. This is followed by the application of a Fast-Fourier Transform to filter the data by means of the low-pass filter. The linear trend is reinserted at the end.

The TC constraint is applied only after any other desired spatial regional constraints have been imposed on the inverse-recovered epicardial potentials. Keeping in mind that for clinical applications there would be no *a priori* knowledge of the epicardial potentials, the second variation of the weighted spatial smoothing (WSS2) was selected for use with temporal constraints in the test cases presented here. Results were calculated with temporal smoothing over temporal regions of several different lengths. Comparisons were made with inverse-recovered epicardial potentials obtained using only WSS2 without temporal constraints. Since the temporal constraints approach requires potentials at multiple time steps, the potential distributions used for testing these constraints were limited to the two time sequences of oblique double layers—septal and basal—each with 36 timesteps at 2-ms intervals.

4.5.1 Results

Inverse-recovered epicardial potentials were calculated for both zero- and second-order Tikhonov regularization for the 36 time instants of the septal and/or basal activation-sequence data sets. These values were then subjected to the weighted spatial smoothing (WSS2), described in section 4.4. The temporal continuity constraint was then used to compute revised values for each sequence, for $PTS = 5$ (TC5), 4 (TC4), 3 (TC3), and 2 (TC2). This required saving potential values for each time step so that the values at each location over all time instants could be input to the smoothing routine. For the 36 times steps considered here, this did not result in any significant increase in the time necessary for processing. Relative errors were

Table 4.14:

Relative errors (RE) of inverse-recovered epicardial potentials for zero- and second-order Tikhonov regularization with weighted spatial smoothing (WSS2) and temporal-continuity (TC) constraints, for two time sequences of double-layer sources

Order	Source	Stats	WSS2	TC5	TC4	TC3	TC2
B0	Septal	Mean	.3749	.7057	.6163	.5378	.4597
		Median	.3785	.3890	.3874	.3825	.3815
B2		Mean	**.2722**	**.6318**	**.5355**	**.4494**	**.3670**
		Median	**.2649**	**.2897**	**.2832**	**.2708**	**.2693**
B0	Basal	Mean	.5589	.5621	.5605	.5595	.5590
		Median	.5570	.5581	.5579	.5576	.5572
B2		Mean	**.4908**	**.4932**	**.4917**	**.4907**	**.4904**
		Median	**.4485**	**.4394**	**.4435**	**.4472**	**.4447**

B0/B2, zero-/second-order Tikhonov regularization; WSS2, second option of weighted spatial smoothing; TC2,...,TC5, temporal continuity constraints; Septal/Basal, a sequence of oblique dipolar layers generated by propagated activation initiated at the septal/basal site (Appendix B); Mean, mean relative error for the given set of dipoles; Median, median of relative errors for the given set of dipoles; **bold font**, the best results.

calculated for these temporally constrained potentials at each time instant. Mean and median values for WSS2 and the four TC variations are given in Table 4.14.

With the exception of the basal activation-sequence test set with the second-order regularizing operator, the WSS2 method had the lowest mean and median RE, with RE increasing as PTS increased. For basal activation-sequence source with the second-order operator, the mean RE for TC3 and TC2 are lower than WSS2 (with TC2 the smallest) and all TC variations had a median RE smaller than for WSS2 (with TC5 the smallest). The magnitude of the differences for all median values and for mean values with basal activation sequence were very small. There were larger increases in RE for mean values for the septal activation sequence. An examination of errors for individual samples showed that this discrepancy was due to very large

changes in the first few samples of the sequence where all potentials were of low magnitude. The number of samples affected depended upon the *PTS* number. This effect was not visible for the basal activation sequence, where the initial samples have potential values of much larger magnitude.

To further quantify any changes due to TC methods, a count was made of the number of time instants where RE decreased and CC increased compared to WSS2 results with no temporal constraint. These statistics are shown in Table 4.15. For the septal activation-sequence data and with the zero-order regularizing operator, the largest number of time instants where RE improved was 42% of the total and for CC 47%, both for TC2. For the second-order regularizing operator, TC2 also had the best results with 36% for RE and 42% for CC. The basal activation-sequence data with the zero-order regularizing operator also had 42% of time instants with improved RE, but in this case for TC3 and TC4 methods. The maximal improvement in CC, 53%, occurred for TC2 method. For the second-order regularizing operator, the best improvement for RE was 50% with TC3 and TC2 methods. The maximum improvement in CC was 56%, for TC2 and TC3 methods. Overall, TC2 method exhibited the largest number of instances where RE and CC improved over WSS2 method used alone.

Although averaged over the time sequence, the errors that have been considered so far are for a spatial distribution. In addition, for a temporal sequence of data, it is also possible to consider errors in the electrogram for a given location. These values were compared to the corresponding *a priori* known values, and mean and median errors were computed for all of the locations of the eccentric dipole sources. RE results are given in Table 4.16. Both data sets show little change in RE mean and median measures with any TC variant. In contrast to spatial error comparisons, the median of RE for septal activation-sequence data and the second-order regularizing operator with either TC5 or TC4 are the only occasions when errors surpass those for WSS2 alone. The results for the basal activation-sequence data consistently indicate that TC5 method has the lowest mean and median RE. The septal activation-sequence

Table 4.15:

Improvements in inverse-recovered epicardial potentials, in terms of relative error decrease (RE↓) and correlation coefficient increase (CC↑), achieved by adding temporal continuity constraints (TC) to zero- and second-order Tikhonov regularization with weighted spatial smoothing (WSS2), for two time sequences of 36 double-layer sources

Order	Source	TC5		TC4		TC3		TC2	
		RE↓	CC↑	RE↓	CC↑	RE↓	CC↑	RE↓	CC↑
B0	Septal	10	9	12	13	10	13	**15**	**17**
B2		8	9	10	9	12	13	**13**	**15**
B0	Basal	13	15	**15**	16	**15**	18	14	19
B2		17	19	17	17	**18**	**20**	18	20

B0/B2, zero-/second-order Tikhonov regularization; TC2,...,TC5, temporal continuity constraints; Septal/Basal, a sequence of oblique dipolar layers generated by propagated activation initiated at the septal/basal site (Appendix B); **bold font**, the best results.

data showed more variation with TC4 for the mean for both zero- and second-order regularizing operators, and with TC2 for the median for the zero-order regularizing operator, and TC3 for the second-order regularizing operator.

Temporal error changes were further quantified by counting the number of locations where RE and CC error measures improved with TC constraints. These numbers are displayed in Table 4.17. In this case all counts are greater than 50% of the 400 locations. This is in contrast to the spatial measure, where only a few results topped 50%. There appears to be a trend with lowest numbers for TC5 and highest numbers for TC2. With TC2 constraint and the septal activation-sequence data for the zero-order regularizing operator, 58% of the locations have lower RE and 57% have higher CC. Corresponding numbers for the second-order regularizing operator are 63% and 61%. Even better results were found for the basal activation-sequence data. With zero-order regularizing operator, 64% of the electrograms had improved RE and 76% had improved CC. Measured by both RE and CC, improvement occurred at 91% of

Table 4.16:

Relative errors of inverse-recovered epicardial electrograms for zero- and second-order Tikhonov regularization with weighted spatial smoothing (WSS2) or temporal continuity constraints, for two time sequences of double-layer sources

Order	Source	Stats	WSS2	TC5	TC4	TC3	TC2
B0	Septal	Mean	.4719	.4696	.4692	.4697	.4706
		Median	.3970	.3989	.3986	.3943	.3928
B2		**Mean**	**.3903**	**.3889**	**.3874**	**.3875**	**.3886**
		Median	**.2897**	**.2874**	**.2839**	**.2834**	**.2858**
B0	Basal	Mean	.3359	.3324	.3332	.3340	.3348
		Median	.2628	.2589	.2595	.2596	.2592
B2		**Mean**	**.2878**	**.2709**	**.2740**	**.2774**	**.2815**
		Median	**.1880**	**.1733**	**.1764**	**.1794**	**.1841**

B0/B2, zero-/second-order Tikhonov regularization; WSS2, second option of weighted spatial smoothing; TC2,...,TC5, temporal continuity constraints. Septal/Basal, a sequence of oblique dipolar layers generated by propagated activation initiated at the septal/basal site (Appendix B); Mean, mean relative error for the given set of dipoles; Median, median of relative errors for the given set of dipoles; **bold font**, the best results.

Table 4.17:

Count* of improvements in inverse-recovered epicardial electrograms, in terms of relative error decrease (RE↓) and correlation coefficient increase (CC↑), achieved by adding temporal continuity (TC) constraints to zero- and second-order Tikhonov regularization with weighted spatial smoothing (WSS2), for two time sequences of 36 double-layer sources

| | | TC5 | | TC4 | | TC3 | | TC2 | |
Order	Source	RE↓	CC↑	RE↓	CC↑	RE↓	CC↑	RE↓	CC↑
B0	Septal	209	**208**	218	213	221	223	231	227
B2		209	205	**227**	**220**	**244**	**238**	**251**	**243**
B0	Basal	240	284	239	286	245	300	257	305
B2		**341**	**342**	**353**	**344**	**359**	**353**	**363**	**364**

*Count, number of improved electrograms on the epicardial surface (out of 400). B0/B2, zero-/second-order Tikhonov regularization; TC2,...,TC5, temporal continuity constraints; Septal/Basal, a sequence of oblique dipolar layers generated by propagated activation initiated at the septal/basal site (Appendix B); **bold font**, the best results.

epicardial "recording" sites, for the second-order regularizing operator.

In another approach to quantifying changes due to TC constraints, the sign of the potential at each epicardial location was compared, over all 36 time instants of either septal or basal activation sequence, to the sign of the potential values known *a priori*. The total count of all space-time points (out of a possible 14,400) where signs did not agree is given in Table 4.18. From these results it is clear that there is good sign agreement, with only 6% to 10% of potential values disagreeing for each sequence of potential distributions and each operator. TC constraints do not improve on the number of sign agreements. In fact, there is a small increase in mismatches from TC2 to TC5 with WSS2 alone always having the smallest mismatch count.

The smoothness of the inverse-recovered electrograms was evaluated by counting the number of times the slope changed from positive to negative or *vice versa*; the corresponding count for *a priori* known epicardial electrograms was subtracted. Results

Table 4.18:

Sign-error count* of inverse-recovered epicardial potentials for zero- and second-order Tikhonov regularization with weighted spatial smoothing (WSS2) or temporal continuity (TC) constraints, for two time sequences of 36 double-layer sources

Order	Source	WSS2	TC5	TC4	TC3	TC2
B0	Septal	1003	1273	1187	1141	1118
B2		**846**	**1129**	**1060**	**996**	**972**
B0	Basal	**1260**	1412	1385	1362	1334
B2		1309	1491	1452	1431	1336

*Sign-error count, number of sign disagreements between inverse-recovered and known potentials (out of a possible 14,400).

B0/B2, zero-/second-order Tikhonov regularization; WSS2, second option of weighted spatial smoothing; TC2,...,TC5, temporal continuity constraints; Septal/Basal, a sequence of oblique dipolar layers generated by propagated activation at the septal/basal site (Appendix B); **bold font**, the best results.

are shown in Table 4.19, where positive values indicate that the *a priori* known electrograms are smoother than their inverse-recovered counterparts, and negative values indicate the opposite. From these results it is evident that utilizing TC constraints TC5 and TC4 will tend to smooth inverse-recovered electrograms, but for TC3 and TC2, whether smoothing occurs or not depends on the magnitude of the signal. The amount of smoothing increases as PTS increases. For the septal activation-sequence data, the inverse-recovered electrograms obtained with WSS2 agree in amount of smoothness most closely with electrograms known *a priori*. The amount of change caused by TC2 is small. For TC3, TC4, and TC5, there is more substantial smoothing. For basal activation-sequence data, all results obtained with TC constraints are closer in degree of smoothness to the *a priori* known distributions than those obtained with WSS2 constraints alone. With the zero-order regularizing operator, the best result is with TC3 and for the second-order operator, with TC4.

Table 4.19:

Direction-change count of inverse-recovered epicardial potentials for zero- and second-order Tikhonov regularization with weighted spatial smoothing (WSS2) or temporal continuity (TC) constraints, for two time sequences of 36 double-layer sources

Order	Source	WSS2	TC5	TC4	TC3	TC2
B0	Septal	**23**	−511	−449	−305	−44
B2		**−27**	−509	−443	−306	−72
B0	Basal	447	−301	−208	**−57**	131
B2		589	−160	**−30**	119	328

Direction-change count, number of slope changes in inverse-recovered electrograms minus number of slope changes for known electrograms (+/−, more/fewer changes); B0/B2, zero-/second order Tikhonov regularization; WSS2, second option of weighted spatial smoothing; TC2,....,TC5, temporal continuity constraints; Septal/Basal, a sequence of oblique dipolar layers generated by propagated activation initiated at the septal/basal site (Appendix B); **bold font**, the best results.

Next, qualitative changes due to TC constraints were investigated. Several locations where TC constraints improved error measures over WSS2 alone were selected, and inverse-recovered electrograms obtained with WSS2 and with all of the TC constraints were plotted for comparison in Fig. 4.3.

4.5.2 Discussion

The use of electrogram continuity over regions of time as a constraint on the solution of the inverse problem of electrocardiography for epicardial potentials was investigated in this section. The spatial regional constraint, WSS2, was applied prior to application of any temporal constraint, in order to establish the best possible results at each isolated time step. WSS2 was selected because of its previously documented improvement of error measures (section 4.3), low computation time, and its independence of a priori knowledge of the epicardial potentials. As a first step, the inverse solution with both
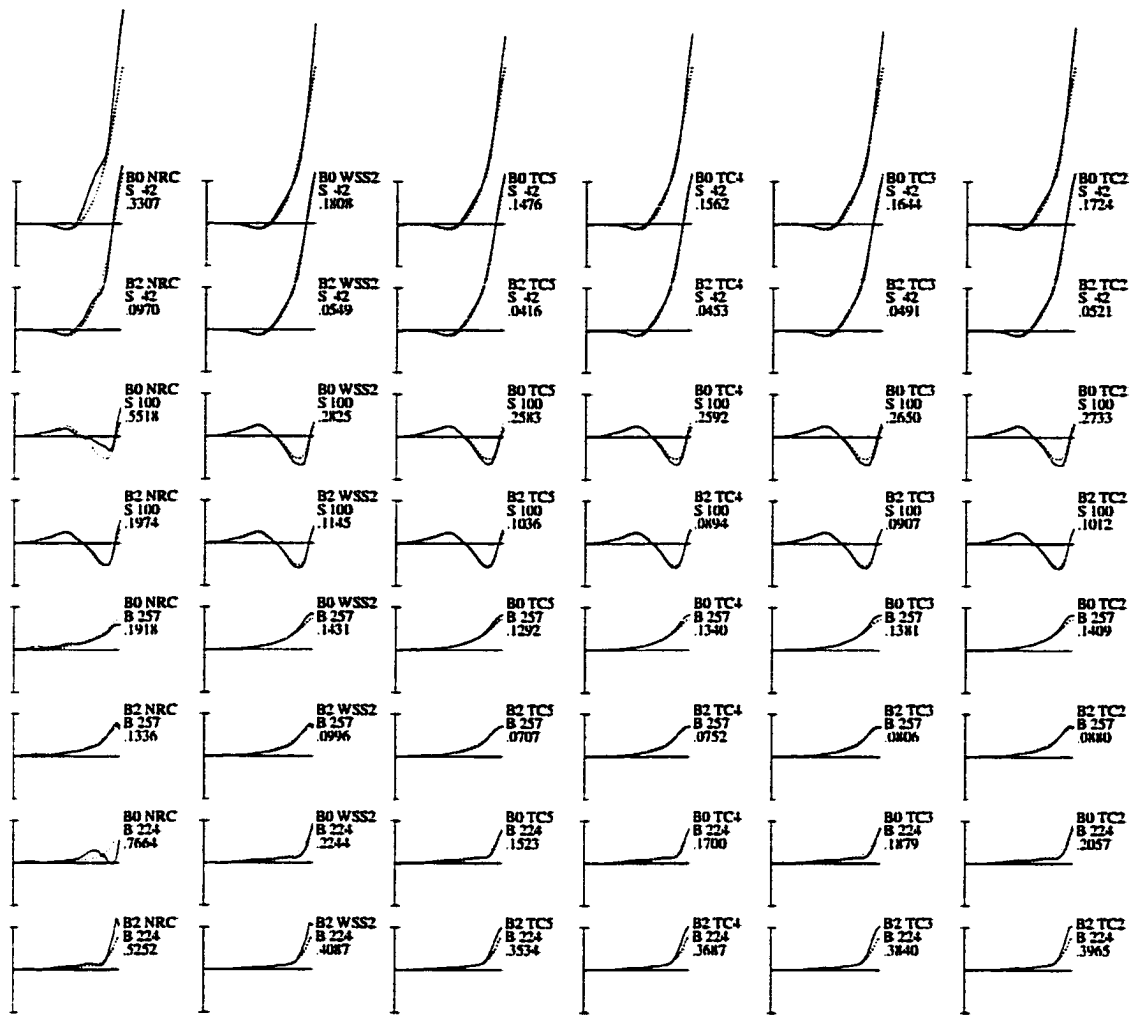
Figure 4.3: Changes in morphology of inverse-recovered epicardial electrograms due to the application of spatial or temporal constraints. Columns, left to right, show electrograms calculated with different constraints: no regional constraint (NRC), weighted spatial smoothing (WSS2), and temporal constraints (TC5, TC4, TC3, TC2). Rows correspond with different regularization methods used in inverse calculations (B0/B2), different sources (S/B), and different "recording" sites (triangles 42, 100, 257, 224), as indicated near each tracing; in addition, relative error (RE) for each inverse-recovered electrogram is given. Solid line, inverse-recovered epicardial electrogram; dotted line, a priori known electrogram; abscissa, time axis (0-72 ms, corresponds to "paper speed" of 87.5 mm/s); ordinate, amplitude (0-2.5 mV); B0/B2, zero-/second-order Tikhonov regularization; S/B, test distributions generated by oblique dipole layers representing wavefronts of activation sequence initiated at the single septal/basal site; triangle numbers correspond to epicardial topography as indicated in Fig.A.3.

zero- and second-order Tikhonov regularization was computed, followed by applying the WSS2 constraint. Then variations of the TC constraint method were used to constrain the epicardial potentials over temporal regions of length 5, 4, 3, and 2 time steps. The maximum interval length was chosen to be significantly less than half the number of time steps considered, and to correspond to the maximum number of points considered by Oster and Rudy [117]. The largest interval they considered was from two steps preceding to two steps following the timestep for which the Twomey estimate was to be determined, a total of five.

An examination of mean and median of RE for each data set and each regularizing operator, with WSS2, TC5, TC4, TC3 and TC2 constraints, indicated that in the majority of cases there was a change in RE measures of less than 0.01. For the septal activation-sequence data, there was an increase in mean RE which was not reflected in the median RE values. Relatively large changes of potential in the first three time steps, where magnitudes were very low, caused this discrepancy. Therefore, it appears that TC constraints do not significantly alter error measures. This result was not unexpected, as Oster and Rudy [117] found that using inverse-recovered epicardial potentials when calculating their temporal constraint, resulted in qualitative improvements in terms of recovering spatial features (extrema), but not in quantitative improvements in terms of decreased RE. Although the changes were small, it was of interest to note that for TC2, from 36% to 56% of electrograms had the RE values improved over those obtained with no temporal constraint. Thus, this latter measure reflects the fact that although the spatial distribution of inverse-recovered epicardial potentials was more in line with *a priori* known values, the improvement occurred predominantly in areas of low-level potentials—compared to the overall signal energy of the distribution—and thus it was not reflected in RE measures.

The temporal nature of TC constraints required adjustment of error measures to capture the inverse solution's ability to recover epicardial electrograms rather than instantaneous epicardial maps. Mean and median values of RE for the 400 electrograms

over 36 time steps were computed. RE measures changed little with different constraints; however, a definite pattern appeared showing—with only two exceptions—that TC error measures are smaller than those with no temporal smoothing. For the electrogram errors, over 50% had improved RE measures over WSS2 for all test sets, regularizing operators and TC constraints variations. TC2 showed the best results for all data and operators, featuring a high of 91% improvement—measured in terms of both RE and CC—for basal test data with the second-order regularizing operator. This result suggests that it may be important to consider temporal errors, as well as spatial errors, when determining the efficacy of regional constraints. The possibility exists that these small error changes could reflect qualitative improvements in the electrograms and spatial maps.

Oster *et al.* [118, 120] determined the CC for electrograms of inverse-recovered potentials of data measured on a torso tank, compared with those measured close to a canine heart suspended within the tank. They found that a number of the electrograms had a "jagged" appearance, which was not seen with the measured potentials, and they attributed these discontinuities to the fact that each time step was computed in isolation, with no temporal smoothing. Fig. 4.3 displays some electrograms for the septal and basal activation-sequence data sets. Note the smoothness of the electrograms with weighted spatial smoothing.

The degree of smoothness of the electrograms was quantified by counting the number of times the slope changed sign. The effectiveness of TC methods in smoothing the electrograms was evident, with counts decreasing with an increase in the number of points over which smoothing occurred. For the septal activation-sequence data, TC constraints oversmoothed the distribution, while for basal activation-sequence data, all TC constraints brought down the number of changes with respect to the *a priori* known distribution (Table 4.19). This result is probably due to the difference in the type of distribution. It is important to note that no attempt was made to determine whether changes occurred at the same time as those of the *a priori* known values.

When Oster and Rudy [117] used a temporal constraint to retrieve a minimum

seen in measured data, but not in inverse-recovered data, the spatial feature was restored with wrong sign. In the present study, when the sign of inverse-recovered potentials was compared to that of the *a priori* known potentials, agreement was found in all but 6% to 10% of cases. Applying temporal constraints increased the number of mismatches. Therefore, TC constraints do not appear to be helpful in correcting discrepancies between positive and negative values.

Results with methods based on TC constraints do not convincingly indicate that temporal regions can constrain the inverse epicardial potentials (when there is no *a priori* knowledge of the solution) in such a way that solutions are improved. However, there is evidence to suggest that TC constraints may do so in some circumstances. Torso-surface potential distributions with a time step shorter than the 2-ms sampling interval chosen in this study, could potentially increase the usefulness of this constraint as well. Although not explicitly tested in this study, it may be assumed that results would be similar for node-to-node systems, because the TC constraints are applied at each epicardial location independently.

4.6 Composite Regional Constraint

A comparison of maps of an epicardial potential distribution, either from measured or simulated data, with maps recovered via the inverse solution [10, 76, 97, 117, 140, 144, 145], frequently reveals the presence of "spurious" extrema where magnitudes, and sometimes sign, do not match the potential values known *a priori*. Extrema with the incorrect sign exist as both isolated regions and as pseudopod-like structures which protrude out of areas where that sign is the correct one. Discrepancies in boundaries between positive and negative regions also occur.

Several methods have been suggested for improving the recovery of the zero-line. The hybrid inverse solution proposed by Iakovidis and Gulrajani [76], described in section 4.1, uses the assumption that an oversmoothed solution better recovers the location of the zero-line. Problems arise with this method when there is a high spatial

gradient of potentials around the zero-line. The inequality constraint of Horáček and Clements [71], presented in section 4.2, also makes effective use of this assumption, provided bounds are appropriately chosen. Weighted spatial smoothing constraints, as described in section 4.4, were shown to decrease error measures and the number of locations where there was a mismatch of sign between *a priori* known and inverse-recovered potentials. The position of the zero-line as opposed to the removal of isolated or pseudopod-like regions of incorrect sign was the main emphasis of the investigations presented in this section.

The presence of regions with the wrong sign is an artifact of the inverse solution. An examination of the singular vectors shows a tendency for extrema to be surrounded by extrema of the opposite sign. The number of extrema increases as the singular value associated with the vectors decreases. Non-regularized inverse-recovered potential maps, calculated from measured torso potentials , feature a mass of positive and negative extrema. As the amount of regularization is increased, the number of these extremes decreases, larger areas are smoothed out, and spatial gradients and curvatures decrease. The optimal solution must achieve a balance such that it recovers maximal amplitudes and gradients, and their locations, as closely as possible, while at the same time removing extraneous extrema. Although the remaining spurious extrema are often of low amplitude compared to the correctly recovered extrema, and may be disguised by producing maps where only contours above a given potential value are plotted, to view the complete distribution of positive and negative values over the epicardial surface, the zero-line must be plotted. Extra zero-lines necessary because of extraneous extrema greatly disrupt the final pattern.

The composite regional constraint (CRC) method, presented in this section, was designed to identify and eliminate regions on the epicardial surface where the sign of inverse-recovered potentials does not match that of *a priori* known values, using some terminology borrowed from image understanding systems. This seemed appropriate since the solution of the inverse problem of electrocardiography for epicardial potentials can be regarded as "noninvasive electrocardiographic imaging" [119, 123, 93].

Image understanding systems are designed to recognize events and to draw conclusions based not only on information gleaned from the image itself, but also on any appropriate additional information which is available to it [11, 36]. In our case, the event to be recognized is the presence of an artifact in the "electrocardiographic image". Additional information is drawn from the corresponding torso potentials, the torso-heart model and, when available, electrograms for the region under investigation.

The following algorithm defines the sign constraint portion of the CRC method.

algorithm

(i) define

> m: # of torso surface area elements,
>
> n: # of heart surface area elements,
>
> l: # of timesteps,
>
> $[b_1, \ldots, b_m]$: input torso potentials,
>
> $[x_1, \ldots, x_n]$: estimate of epicardial potentials,
>
> $[h_1, \ldots, h_n]$: hypothesis for each epicardial potential,
>
> $[\hat{x}_1, \ldots, \hat{x}_n]$: updated potentials,
>
> $[\hat{h}_1, \ldots, \hat{h}_n]$: updated hypotheses,
>
> P_{BH}: as defined in chapter 2,
>
> $nb(b_k)$: set of torso potentials at area elements which share at least one vertex with area element k,
>
> $nnb(x_k)$: set of epicardial potentials at area elements which share at least one vertex with area element k with h OK.

(ii) set initial hypotheses

> For $t = 1$ to l do
>
> For $i = 1$ to n do

If $\text{sign}(x_i) \neq \text{sign}(nb(b_k))$: where k index with $\max_{1 \leq j \leq m}\{P_{BH}^{ji}\}$)

Then set h_i artifact, Else set h_i OK

** End of Loops **

(iii) update hypotheses with temporal information if $l \geq 4$

For $i = 1$ to n do

Search over timesteps for sequence of artifact values $\{x_i^{t_{k1}}, \ldots, x_i^{t_{k2}}\}$

Search for following sequence of OK values $\{x_i^{t_{k2}+1}, \ldots, x_i^{t_{k2}+j}\}$

If $j \geq 3$ and $\text{sign}\{x_i^{t_{k1}}, \ldots, x_i^{t_{k2}}\} = \text{sign}\{x_i^{t_{k2}+1}, \ldots, x_i^{t_{k2}+j}\}$

Then reset $\{h_i^{t_{k1}}, \ldots, h_i^{t_{k2}}\}$ OK

** End of Loops **

(iv) update hypotheses with spatial information

For $t = 1$ to l do

Set $[\hat{h}_1, \ldots, \hat{h}_n] = [h_1, \ldots, h_n]$

For $j = 1, 2, \ldots$ satisfied do ** Loop Until No More Updates **

Initialize artifact count to 0

For $i = 1$ to n

If h_i = artifact Then if $\text{sign}(x_i)$ = $\text{sign}(nnb(x_i))$

    Then set $\hat{h}_i$ OK Else increment artifact count

** End i Loop **

Reset $[h_i, \ldots, h_n] = [\hat{h}_1, \ldots, \hat{h}_n]$

If artifact count same as last pass, Then satisfied

** End j and t Loops **

(v) replace artifact potentials

For $t = 1$ to l do

```
Set [x̂₁,...,x̂ₙ] = [x₁,...,xₙ], [ĥ₁,...,ĥₙ] = [h₁,...,hₙ]

For j = 1,2,..., satisfied do ** Loop Until All Artifacts Replaced

Set artifact count to 0

For i = 1 to n do

If hᵢ = artifact

Then If hₖ = OK for ≥ 3 neighbours k of xᵢ

    Then interpolate x̂ᵢ from OK neighbours, set ĥᵢ OK

    Else increment artifact count

** End i Loop **

Reset [x₁,...,xₙ] = [x̂₁,...,x̂ₙ], [h₁,...,hₙ] = [ĥ₁,...,ĥₙ]

If artifact count = 0, Then satisfied

** End j and t Loops **
```

The first step requires the generation of an hypothesis for each epicardial element as to whether the inverse-recovered potential is appropriate or an artifact. The potential at any point on the torso surface is a summation of the contributions from all cardiac sources. However, the assumption is made that for each epicardial location there exists a region on the torso surface, whose potential will have the largest effect. The degree of this effect will depend on the magnitude of the potential gradients in the epicardial region, the extent of cardiac sources around this region, and the distance to the torso surface [144, 145]. Although the potentials in the torso region will be of a different magnitude, some should have the same sign as that of the epicardial potential in question. This assumption was supported by the work performed by Monro's group [20, 108], who found that the QRS complex of ventricular electrograms recorded in human subjects correlated well with torso-surface electrocardiograms recorded simultaneously at certain electrode-positions. Unipolar electrograms were recorded from 2-3 epicardial sites in 21 patients approximately one week after aortocoronary bypass surgery, while torso-surface electrocardiograms were recorded at 37 sites. The authors

found a number of torso leads where the CC with the electrogram was greater than 0.8.

For the CRC method proposed here, the heart-torso model was used to determine the maximum positive solid angle over the torso surface elements subtended at the epicardial triangle for which an hypothesis was to be generated. By considering the solid angle as a measure of the geometrically similar position, distance and orientation of the epicardial surface element with respect to the torso surface element—both affecting the desired epicardial potentials—are taken into account; the P_{BH} matrix, defined in Chapter 2, was used. If the sign of the potential for the torso triangle with the largest solid angle subtended at the given epicardial triangle, or the sign of the potential of any of its one-node neighbours (triangles which share at least one vertex with the given triangle), matched the sign of the epicardial potential in question, there was no artifact. If there was no match, it was hypothesized that this was an artifact.

The next step of the CRC method considers information about neighbouring regions, both spatial and temporal (if available), of any potential deemed an artifact. Based on the interpretation of this information, the hypothesis may be changed. Some extrema, such as breakthrough sites, arise as a small area of low magnitude. Their effect on torso potentials may not be sufficient to recover the appropriate sign. Therefore, these epicardial potentials may be incorrectly designated as artifacts. Their magnitude and extent increase over time, so that temporal information can be used to update the hypothesis that an artifact is present. If the sign which is considered an artifact for a given time and spatial location is found at a minimum of three time steps immediately following a run of artifact potentials, then the hypothesis for each potential in this run is updated to non-artifact. Low-amplitude gradients of epicardial potential around the zero-line may also result in incorrect artifact assignment. In this case, information about spatial neighbours is considered. The sign of each epicardial potential which has been designated an artifact is compared to that of all one-node

neighbours which are non-artifacts. If two or more agree, then the hypothesis is updated to non-artifact after all sites have been investigated. This update procedure is repeated as long as more updates are made.

With artifacts now identified, they must be reassigned a potential value. If at least three one-node neighbours are non-artifacts, then the original potential is replaced by one interpolated from the values at all non-artifact neighbours, and the hypothesis is updated. Potentials are updated at the time they are computed. This procedure is repeated until all artifacts have been replaced.

Following these procedures, the second variation of the weighted spatial smoothing constraint was applied. The rationale for this included the fact that WSS2 was shown to decrease RE and the number of sign mismatches, and therefore seemed appropriate, and secondly, that the potentials which replaced the artifactual values may require spatial smoothing.

For time-sequence data, temporal continuity constraints were also tested. The data set used to test the CRC method was the same as for the WSS methods in section 4.4.

4.6.1 Results

The first variation of the composite regional constraint method (CRCM), which did not use temporal data for updating artifact assignment, was tested on the sources consisting of a single central dipole, and three and five eccentric dipoles. RE, CC and sign MM measures did not change compared to those for WSS2. Results with CRCM for the 1,600 eccentric single-dipole sources are presented in Table 4.20. Only minor differences in RE measures are seen compared to errors with WSS2, although CRCM results tend to be slightly worse. The last column of Table 4.20 contains sign mismatch counts with CRCM compared to WSS2. For all subsets of dipole sources and with both zero- and second-order regularizing operators, the number of locations where the signs do not match decreases.

Table 4.20:

Relative errors (RE) of inverse-recovered epicardial potentials for zero- and second-order Tikhonov regularization with composite regional constraint (CRCM), and comparison (in terms of MM) with weighted spatial smoothing (WSS2), for eccentric single-dipole sources at various depths in the ventricular wall

Operator Order	Source	RE				WSS2–CRCM
		Max	Min	Mean±SD	Median±SD	MM
B0	10.0-mm	.7243	.1079	.2674±.1069	.2497±.1037	575
	7.5-mm	.7219	.0979	.3216±.1321	.3098±.1531	**1,287**
	5.0-mm	.8236	.1286	.4209±.1667	.4306±.2099	**3,360**
	2.5-mm	.9187	.2731	**.5850±.1799**	**.6151±.2241**	6,994
	All above	.9187	.0979	.3987±.1919	.3601±.2026	12,216
B2	10.0-mm	.7119	.0745	**.2014±.0739**	**.1931±.0753**	**335**
	7.5-mm	.6088	.0859	**.2833±.0877**	**.2851±.1061**	1,292
	5.0-mm	.6744	.1663	**.4121±.1153**	**.4271±.1322**	3,384
	2.5-mm	.8827	.2815	.5984±.1377	.6347±.1304	**6,064**
	All above	.8827	.0745	**.3738±.1839**	**.3366±.1954**	**11,075**

B0/B2, zero-/second-order Tikhonov regularization; WSS2, second option of weighted spatial smoothing; CRCM, variant of composite regional constraint method; RE, relative error; MM (WSS2 – CRCM), reduction in sign mismatch count for CRCM compared to WSS2 (number of mismatches with *a priori* potentials, out of a possible 160,000, for 400 dipoles and 400 epicardial triangles); Max/Min, maximal/minimal relative error within the set of dipoles (400 at each depth, 1,600 overall); Mean, mean relative error for the given set of dipoles; Median, median of relative errors for the given set of dipoles; SD, standard deviation; **bold font**, the best results.

Table 4.21:

Relative errors of inverse-recovered epicardial potentials for zero- and second-order Tikhonov regularization with weighted spatial smoothing (WSS2) or composite regional constraint (CRC) methods, for two time sequences of double-layer sources

Order	Source	Stats	WSS2	CRCM	CRCF	CRC5	CRC4	CRC3	CRC2
B0	Septal	Mean	**.3749**	.4006	.3759	.7078	.6184	.5387	.4609
		Median	.3785	.4015	**.3782**	.3877	.3867	.3815	.3808
B2		Mean	**.2722**	.3031	.2736	.6328	.5365	.4506	.3682
		Median	.2649	.3086	**.2643**	.2894	.2831	.2700	.2686
B0	Basal	Mean	**.5589**	.5590	.5591	.5618	.5604	.5594	.5590
		Median	.5570	.5569	**.5567**	.5580	.5577	.5574	.5571
B2		Mean	**.4908**	.4916	.4911	.4931	.4917	.4909	**.4908**
		Median	.4485	.4500	.4510	**.4391**	.4432	.4472	.4450

B0, zero-order Tikhonov regularization; B2, second-order Tikhonov regularization; WSS2, second option of weighted spatial smoothing; CRCM, CRCF, CRC2,...,CRC5, variants of composite regional constraint method (PTS = 2, 3, 4, 5); Septal/Basal, a sequence of oblique dipolar layers generated by propagated activation initiated at the septal/basal site (Appendix B); Mean, mean relative error for the given set of dipoles; Median, median of relative errors for the given set of dipoles; **bold font**, the best results.

The 36 time steps for both septal and basal activation-sequence data were processed with CRCM, as well as the variation where temporal data were included in hypothesis testing (CRCF), and CRC5, CRC4, CRC3, CRC2 where the TC constraint was applied as a final step with PTS set at 5, 4, 3, and 2, respectively, as described in section 4.5. CRC methods did not add any appreciable processing time. Mean and median RE values for WSS2 and all six CRC variations are given in Table 4.21. CRCF relative errors differ little from those with WSS2. For the basal activation-sequence data set, CRCM and CRCF results are virtually identical, whereas CRCM has higher RE of inverse-recovered potentials for the septal activation-sequence data. Results for CRC5, CRC4, CRC3, and CRC2 tend to follow the same trend as seen in section 4.5 for TC constraint methods. The number of times (out of a possible 36) when RE and CC results for CRC methods improved on those for WSS2 were counted and are shown in Table 4.22. The use of the CRCM method produced a greater number of improved error measures than did the CRCF variation. The maximal number of instants with less error occurs with the CRC3 option for septal activation-sequence data, and with both CRC3 and CRC4 for basal activation-sequence data. When equal error results are added, then the CRC2 variation performs best. Even though trends were visible, it should be noted that the improvement in RE was very small in most cases.

Mean and median RE for the 400 electrograms are displayed in Table 4.23. WSS2 results are given for comparison. The CRCM method increases RE for the septal activation-sequence data, but not for the basal activation-sequence data, where CRCM and CRCF results are nearly identical. An examination of the effects of imposing TC constraints on the CRCF method shows that all levels of smoothing decrease mean and median RE. The smallest error for basal activation-sequence data is found with CRC5, but is variable for the septal activation-sequence data. The number of locations where RE and CC measures improved with CRC method compared to WSS2 alone, are in Table 4.24. For these electrogram error counts, the CRCF method is always better than CRCM. The largest number of counts, 60% or better (out of

Table 4.22:

Count* of improvements in inverse-recovered epicardial potentials, in terms of relative error decrease (RE↓) and correlation coefficient increase (CC↑), achieved by using zero- and second-order Tikhonov regularization with composite regional constraints (CRC) instead of just weighted spatial smoothing (WSS2), for two time sequences of 36 double-layer sources

Order	Source	CRCM		CRCF		CRC4		CRC3		CRC2	
		RE↓	CC↑	RE↓	CC↑	RE↓	CC↑	RE↓	CC↑	RE↓	CC↑
B0	Septal	12	13	9	9	12	14	13	16	18^1	18^1
B2		9	10	10	11	14	16	19	18	22^2	22^2
B0	Basal	24	25	15	17	18	21	16	22	30^3	30^3
B2		22	23	19	21	20	23	21	21	34^4	34^4

*Count, number of time steps (out of a possible 36) for which improvements occured. B0/B2, zero-/second-order Tikhonov regularization; WSS2, second option of weighted spatial smoothing; CRCM, CRCF, CRC2,...,CRC4, variants of composite regional constraint method ($PTS = 2, 3, 4$); Septal/Basal, a sequence of oblique dipolar layers generated by propagated activation initiated at the septal/basal site (Appendix B); **bold font**, the best results.
[1] 17 with equal RE, [2] 21 with equal RE, [3] 30 with equal RE, [4] 31 with equal RE.

Table 4.23:

Relative errors of inverse-recovered epicardial electrograms for zero- and second-order Tikhonov regularization with weighted spatial smoothing (WSS2) or various composite regional constraint (CRC) methods, for two time sequences of 36 double-layer sources

Order	Source	Stats	WSS2	CRCM	CRCF	CRC5	CRC4	CRC3	CRC2
B0	Septal	Mean	.4719	.5053	.4743	.4676	.4680	.4694	.4714
		Median	.3970	.4110	.3970	.3922	.3924	.3911	.3918
B2		**Mean**	**.3903**	**.4173**	**.3957**	**.3906**	**.3898**	**.3906**	**.3925**
		Median	**.2897**	**.3020**	**.2925**	**.2889**	**.2874**	**.2859**	**.2893**
B0	Basal	Mean	.3359	.3361	.3359	.3322	.3330	.3339	.3348
		Median	.2628	.2624	.2620	.2589	.2595	.2596	.2592
B2		**Mean**	**.2878**	**.2879**	**.2871**	**.2706**	**.2737**	**.2772**	**.2814**
		Median	**.1880**	**.1879**	**.1869**	**.1693**	**.1712**	**.1771**	**.1819**

B0/B2, zero-/second-order Tikhonov regularization; WSS2, second option of weighted spatial smoothing; CRCM, CRCF, CRC2,...,CRC5, variants of composite regional constraint method ($PTS = 2, 3, 4, 5$); Septal/Basal, a sequence of oblique dipolar layers generated by propagated activation initiated at the septal/basal site (Appendix B); Mean, mean relative error for the given set of dipoles; Median, median of relative errors for the given set of dipoles; **bold font**, the best results.

a possible 400), are achieved for the septal activation-sequence data when CRC3 is used. CRC3 also gives the largest improvement for basal activation-sequence data with 68% and 78% for RE and CC, respectively, with zero-order regularizing operator and 91% each with second-order operator. When equal errors are included, CRC2 has the largest numbers—at 91% for basal activation sequence data—with zero-order regularizing operator.

Next, the sign of the potential at each epicardial location was compared, over all 36 time instants, to the sign of the *a priori* known values. The total count of all space-time points (out of a possible 14,400) where signs of inverse-recovered and known potentials did not agree is given in Table 4.25 for WSS2 and each of the CRC variants. For the septal activation-sequence data set, the sign mismatch count

Table 4.24:

Count* of improvements in inverse-recovered epicardial electrograms, in terms of relative error decrease (RE↓) and correlation coefficient increase (CC↑), achieved by using zero- and second-order Tikhonov regularization with composite regional constraints (CRCs) instead of just weighted spatial smoothing (WSS2), for two time sequences of 36 double-layer sources

Order	Source	CRCM RE↓	CC↑	CRCF RE↓	CC↑	CRC4 RE↓	CC↑	CRC3 RE↓	CC↑	CRC2 RE↓	CC↑
B0	Septal	203	198	230	217	244	235	**252**	**239**	177	181
B2		196	202	215	208	253	245	**261**	**252**	179	185
B0	Basal	212	202	250	291	257	310	273	312	362[1]	362[1]
B2		216	219	344	342	359	354	**363**	**364**	347[2]	347[2]

*Count, number of electrograms (out of a possible 400) for which improvements occured; bold font, the highest values.

B0/B2, zero-/second-order Tikhonov regularization; CRCM, CRCF, CRC2,...,CRC4, variants of the composite regional constraint method ($PTS = 2, 3, 4$); RE, relative error; CC, correlation coefficient; Septal/Basal, a sequence of oblique dipolar layers generated by propagated activation initiated at the septal/basal site (Appendix B); bold font, the best results.

[1]347 with equal RE, [2]339 with equal RE.

Table 4.25:

Sign-error count of inverse-recovered epicardial potentials for zero- and second-order Tikhonov regularization with weighted spatial smoothing (WSS2) or composite regional constraint (CRC) methods, for two time sequences of 36 double-layer sources

Order	Source	WSS2	CRCM	CRCF	CRC5	CRC4	CRC3	CRC2
B0	Septal	1003	1098	**957**	1223	1140	1096	1075
B2		846	990	**823**	1104	1036	970	946
B0	Basal	1260	**1105**	1111	1213	1192	1189	1158
B2		1309	**1146**	1164	1264	1247	1252	1186

Sign-error count, number of sign disagreements between inverse-recovered and known epicardial potentials (out of a possible 14,400, for 400 "recording" sites and 36 instants; bold font, the lowest values); B0/B2, zero-/second-order Tikhonov regularization; WSS2, second option of weighted spatial smoothing; CRCM, CRCF, CRC2,...,CRC5, variants of the composite regional constraint method ($PTS = 2, 3, 4, 5$); Septal/Basal, a sequence of oblique dipolar layers generated by propagated activation initiated at the septal/basal site (Appendix B); bold font, the best results.

increased for CRCM and was at its lowest for CRCF (bold font in Table 4.25), where there was a 38% decrease over NRC values and 13% over WSS2 results when the zero-order regularizing operator was used. These statistics were 23% and 3% for the second-order regularizing operator. The application of TC constraints resulted in larger mismatch counts, increasing with the value of PTS. Sign-error counts were different for basal activation-sequence data. In this case, all CRC methods had lower sign mismatch counts than WSS2. CRCM had the lowest numbers (bold font in Table 4.25), with CRCF a close second. There was a 36% decrease from NRC to CRCF values and 12% decline over WSS2 results for the zero-order regularizing operator. The corresponding values with the second-order operator were 31% and 11%. Although remaining below WSS2 values, counts with TC constraints increased in the same manner as for the septal activation-sequence data.

The smoothness of the electrograms was evaluated by counting the number of

Table 4.26:
Direction-change count of inverse-recovered epicardial potentials for zero- and second-order Tikhonov regularization with weighted spatial smoothing (WSS2) or composite regional constraint (CRC) methods, for two time sequences of 36 double-layer sources

Order	Source	WSS2	CRCM	CRCF	CRC5	CRC4	CRC3	CRC2
B0	Septal	**23**	371	211	−499	−416	−241	91
B2		−27	217	71	−490	−422	−275	**−15**
B0	Basal	447	807	804	−348	−242	**−7**	293
B2		589	954	926	−212	**−46**	199	526

Direction-change count, number of slope changes in inverse-recovered electrogram minus number slope changes for known electrograms (+/−, more/fewer changes; bold font, values nearest to zero); B0/B2, zero-/second-order Tikhonov regularization; WSS2, second option of weighted spatial smoothing; CRCM, CRCF, CRC2,...,CRC5, variants of the composite regional constraint method (PTS = 2, 3, 4, 5); Septal/Basal, a sequence of oblique dipolar layers generated by propagated activation initiated at the septal/basal site (Appendix B); bold font, the best results.

times the slope changed from positive to negative and *vice versa*. The corresponding count for epicardial electrograms known *a priori* was subtracted. Results are presented in Table 4.26, where positive numbers indicate that the inverse-recovered potentials are less smooth than their *a priori* known counterparts. Smoothness decreased, compared to WSS2, when using CRCM and CRCF. When TC constraints were added, an additional level of smoothness was imposed. For the septal activation-sequence data with the zero-order regularizing operator, WSS2 remained the closest to known potentials, but CRC2 was nearest to zero for the second-order regularizing operator. CRC3 gave the best results for basal activation-sequence data with the zero-order regularizing operator and CRC4 with the second-order operator.

Qualitative changes due to composite regional constraints can be assessed in Fig. 4.4, which shows epicardial maps for the septal activation data set, constrained with either weighted spatial smoothing (WSS2) or composite regional constraints

(CRC).

Electrograms are compared in Fig. 4.5.

4.6.2 Discussion

The effects of composite regional constraint methods on the solution of the inverse problem of electrocardiography for epicardial potentials were investigated in this section. As noted previously (section 4.3), when weighted spatial smoothing constraints were applied to the Tikhonov inverse solution, an improvement occurred in RE measures, as well as in the distribution of positive and negative potentials over the epicardial surface. However, a closer examination of epicardial potential maps showed that there still existed areas, with either isolated or pseudopod-like structures, where the sign of the potential was not correct. The goal of the CRC methods introduced in this section was to detect these areas and replace potentials with values interpolated from a neighbouring region of valid potentials.

The detection step of the CRC method required matching the sign of the potential at an epicardial location with that of a potential in the *closest* torso neighbourhood. Closeness was defined in terms of the solid angle relationship as established by the tesselated torso-heart model. The aim of the CRC method is to use information about the torso-heart geometry and torso potentials to constrain the inverse solution; the method succeeded in making use of the *sign* of the torso potentials to locate artifacts, and significant improvement in the fidelity of inverse-recovered epicardial potentials were achieved. However, there were situations—mostly for low-level potentials and for certain kind of focal cardiac sources [144, 145]—where values were incorrectly designated as artifacts. Therefore, subsequent procedures were developed to correct the problem. The CRCM method used knowledge of the sign of the potentials at non-artifact epicardial locations, which were neighbours of the site in question, to adjust the artifact/non-artifact designation. When a time sequence of torso-surface potentials was available, the CRCF method included the potentials at subsequent time steps in its evaluation.
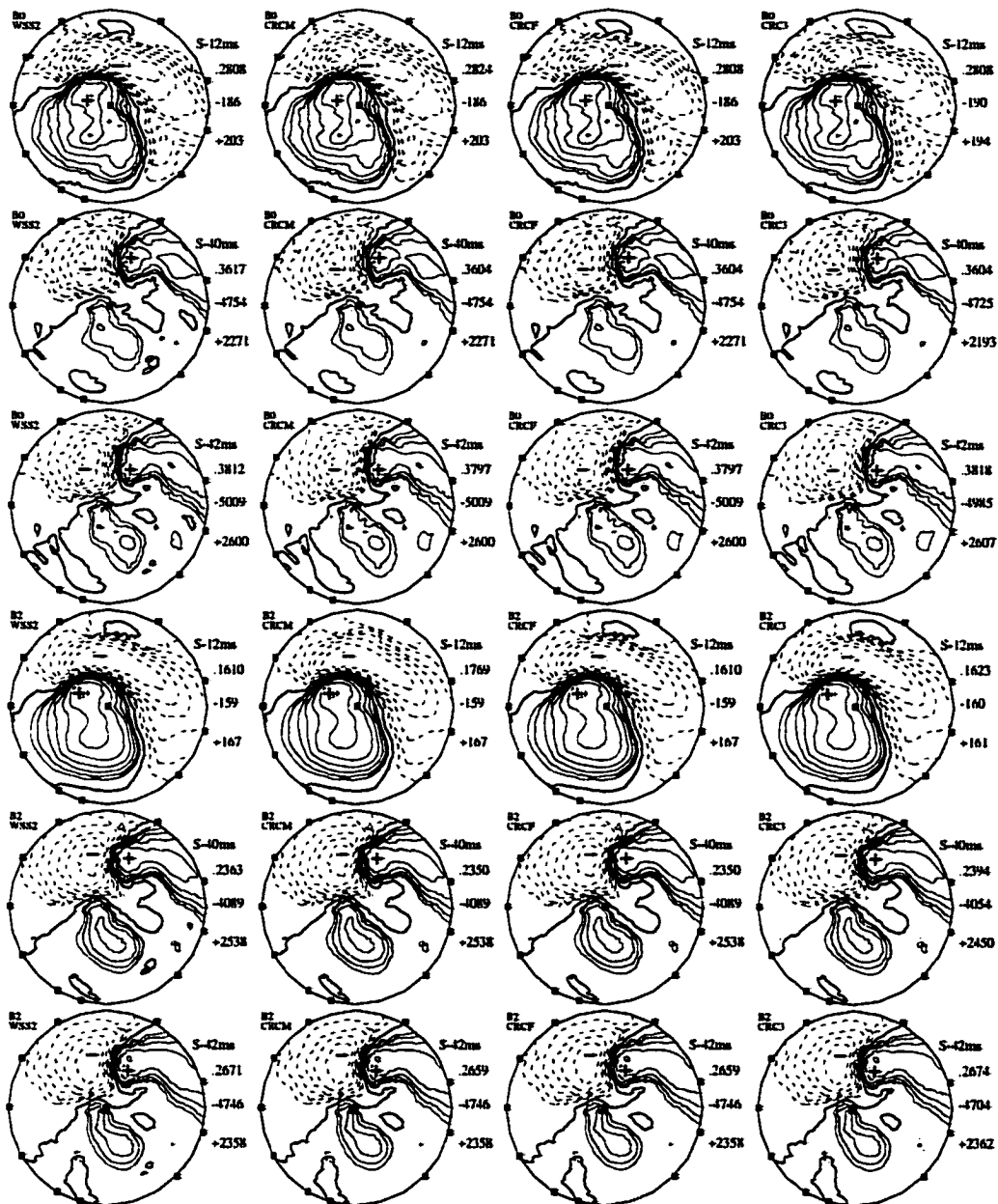
Figure 4.4: Epicardial potential maps for septal activation sequence with and without the application of composite regional constraints. Columns, left to right, show inverse-recovered epicardial potentials regularized as follows: B0/B2 with WSS2, B0/B2 with CRCM, B0/B2 with CRCF, and B0/B2 with CRC3. Rows, from top to bottom, show inverse-recovered epicardial potential maps for test distributions generated by oblique dipole layers at 12 ms (S-12ms), 40 ms (S-40ms), and 42 ms (S-42ms) into activation sequence initiated at single septal site. B0/B2, zero-/second-order Tikhonov regularization; WSS2, second variant of weighted spatial smoothing; CRCM, CRCF, CRC3, variants of composite regional constraint method.
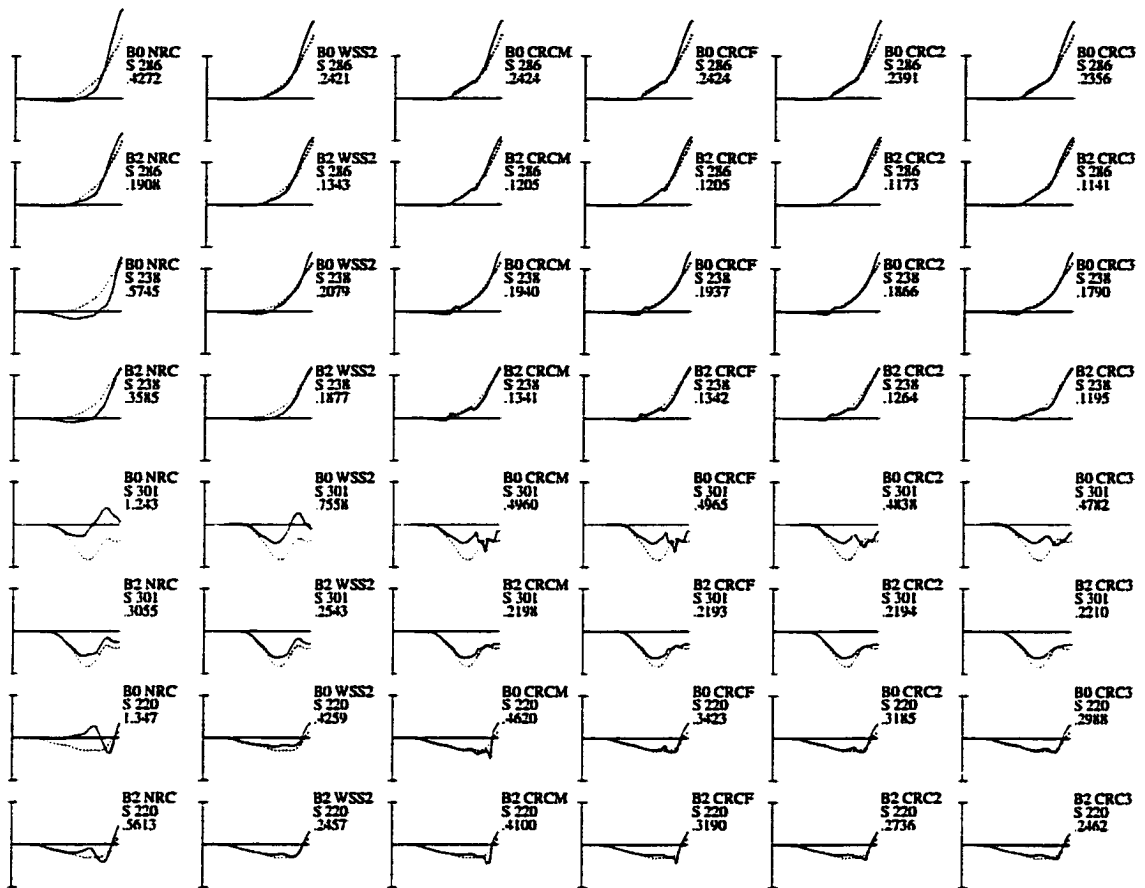
Figure 4.5: Changes in morphological features of inverse-recovered epicardial electrograms due to the application of weighted spatial smoothing and composite regional constraints. Columns, left to right, depict electrograms calculated with different constraints: no regional constraint (NRC), weighted spatial smoothing (WSS2), and four types of composite regional constraints (CRCM, CRCF, CRC2, CRC3). Rows correspond with different regularization methods used in inverse calculations (B0/B2) and different "recording" sites (triangles 286, 238, 301, 220) as indicated near each tracing; in addition, the relative error (RE) for each inverse-recovered electrogram is given. Test distributions were generated by oblique dipole layers representing 36 consecutive wavefronts of activation sequence initiated at single septal (S) site. Solid line, inverse-recovered epicardial electrogram; dotted line, a priori known epicardial electrogram; abscissa, time axis (0–72 ms, corresponding to "paper speed" of 87.5 mm/s); ordinate, amplitude of electrogram (0–2.5 mV); B0/B2, zero-/second-order Tikhonov regularization; triangle numbers correspond to epicardial topography depicted in Fig.A.3.

The number of locations where the sign of the inverse-recovered epicardial potential did not match that of the potential known *a priori* was reduced when the CRCM method was tested using potential distributions generated by the set of 1,600 eccentric dipoles. An examination of the results for these distributions showed that the number of sign mismatches, and the number by which they decreased with CRCM, increased as the dipole source was moved closer to the epicardial surface. The extent of low-level potentials and the presence of high spatial gradients varied in the same way. These results appear to indicate that the likelihood of the existence of extraneous extrema increases under these same conditions.

An example of the errors that can arise when temporal data are not included in the process of determining artifacts was seen in Fig. 4.4. Early in the time sequence, an anterior basal positive area appears. CRCM considers this an artifact and removes it. With CRCF, it is properly identified and the area remains in the distribution. Appearing at a later time step are left posterior extraneous extrema, which were correctly removed from the map by both CRCM and CRCF. The incorrect removal of the presumed artifact was reflected in higher RE statistics for CRCM than CRCF.

When applied to the time sequence data sets, CRCF did not significantly alter mean and median values of RE for spatial electrogram, while more than 50%, and as many as 91%, of the 400 electrograms showed improvement in RE and CC measures with CRC methods compared to WSS2, with the exception of CRCM and CRC2 for septal activation-sequence data. Based upon these results, along with the assessment of qualitative changes shown in Fig. 4.4, CRCF method appears to achieve its purpose. Results for cases when TC constraints have been applied with CRCF are variable. An examination of results suggests that—when all measures are taken into account—the CRC3 variant of the composite regional constraint method would seem to be the most acceptable choice.

4.7   Conclusions

The aim of the work described within this chapter was the introduction and examination of methods for the regional constraint of the inverse problem of electrocardiography for epicardial potentials. A brief overall assessment of these methods is as follows: *Inequality constraint optimization* had results which were too variable, and difficulty arose in the rationalization of the selection of parameters that would consistently yield inprovement in the epicardial image. The *weighted regularizing operator method (WR)* produced excellent results with *a priori* known values, and still more than credible improvements when estimated values were used for weighting. However, the computing time required by this method diminishes its usefulness in clinical applications. *Weighted spatial smoothing* introduced the concept of applying a second-pass, or post-inverse, constraint, and was shown to both improve on relative error measures and incorrect sign counts, as well as having minimal computing time requirements. This method is easily applied and has potential for clinical applications. *Temporal continuity (TC)* was incorporated as a second-pass constraint in conjunction with weighted spatial smoothing. Although imposing temporal continuity on electrograms should intuitively be successful, it produced only minimal changes. The smoothness of the test data was a confounding factor and, while it is possible that the small changes found could extrapolate to large changes with noisier electrograms, that has not been proven. The *composite regional constraint (CRC)* has great potential for use as a tool in clinical applications. This is a post-inverse procedure with variants for single distributions (e.g., QRS or ST-integral potential maps) and time sequences of data (e.g., continuous data throughout the depolarization/repolarization cycle). Epicardial potential images recovered from measured data often contain islands where the sign of the potentials is incorrect. The CRC utilizes body surface potential input, along with spatial and temporal relationships to evaluate whether first-pass regularization was successful in determining positive and negative regions in the epicardial image. After adjustments are made, the weighted spatial smoothing constraint and, when applicable, the temporal continuity constraint, are incorporated.

Overall, results presented in this chapter suggest that regional constraints can refine the inverse-recovered epicardial potentials, with weighted spatial smoothing a good choice for any application, and the composite regional constraint the best choice for use with measured data in clinical applications.

Chapter 5

Regularization Parameters

5.1 Introduction

In all results computed thus far, the regularization parameter t—required to solve the inverse problem of electrocardiography for epicardial potentials with Tikhonov regularization—has been selected on the basis of *a priori* knowledge of these potentials. When the t-parameter must be determined without direct knowledge of the epicardial distribution, as is the case in clinical applications, an alternate method must be applied. Considerable attention has been given to this problem [136]. The purpose of this chapter is to describe and compare several different methods of determining the criteria by which a value may be assigned to the t-parameter.

The **Minimum RMS Method** assigns a t-parameter based on an estimate of noise levels in torso potentials [106], and is equivalent to the original method described by Foster [45] and Strand and Westwater [150], and applied by Barr and Spach [10], with

$$t = \frac{\|e\|^2}{\|\phi_H\|^2},\tag{5.1}$$

where e is the noise vector at each torso surface location and ϕ_H are the exact epicardial potentials. This method is limited by the ability to calculate this ratio, which requires *a priori* knowledge of the solution.

The **Discrepancy Principle** was introduced by Morozov [111]. This method makes the assumption that the residual norm is non-zero for the optimal t-parameter. The value of t is chosen such that

$$\|A\boldsymbol{x}(t) - \boldsymbol{b}\|^2 = \|\epsilon\|^2, \tag{5.2}$$

where $\|\epsilon\|$ is an estimate of the error due to noise present in the torso-surface potential measurements. A variant of the discrepancy method was proposed by Gfrerer [50], and further refined by Engl and Grever [41]. As for the minimum rms method, the performance of all variants of this method also depend upon the ability to accurately estimate the error measure. Oversmoothing of the solution has been reported with the discrepancy principle [22].

Generalized Cross-validation [22, 79] is a parameter-selection method which does not require an error estimate. This technique has been used with the application of Tikhonov regularization in the field of statistics. The procedure determines the t-parameter which minimizes

$$\frac{\|A\boldsymbol{x}(t) - \boldsymbol{b}\|}{\left(\text{trace}(AA^T + tI)^{-1}\right)}. \tag{5.3}$$

Correlated errors, which are likely to occur in the clinical electrocardiographic measurements, affect the performance of this method since it assumes that any error is due to the presence of white noise only.

The **Derivative or Quasi-optimality Criterion** [27, 156] has been suggested as another means of estimating the t-parameter without *a priori* information about the error levels of input data. This method selects the $t > 0$ which minimizes the term

$$\left\| t\frac{d}{dt}\boldsymbol{x}(t) \right\|. \tag{5.4}$$

It appears that this approximation is valid only when the t-parameter required is relatively small in comparison with $\|A\|$ or $\|\boldsymbol{x}\|$ [106].

The **Composite Residual and Smoothing Operator (CRESO) Method** was developed by Colli Franzone and co-workers [27]. It was presented as an empirical approach which does not require any *a priori* information about the measured

or computed potential distributions (including the amount or type of noise in input data). The smallest t-parameter for which there exists a local maximum of the equation

$$\frac{d}{dt}(t\|Rx(t)\|^2) - \frac{d}{dt}\|Ax(t) - b\|^2, \quad t \geq 0 \tag{5.5}$$

is chosen as most suitable. This value represents the point where the derivatives of the constraint and residual terms are changing at exactly the same rate [24]. Alternately, it can be defined as the first point where the curve

$$t\|Rx(t)\|^2 - \|Ax(t) - b\|^2 \tag{5.6}$$

changes concavity [106]. Equation 5.5 may also be written as

$$\|Rx(t)\|^2 + 2t\frac{d}{dt}\|Rx(t)\|^2. \tag{5.7}$$

To solve for t, $\|Rx(t)\|^2$ is expressed in terms of the GSVD of the Tikhonov regularization system (Chapter 3) as

$$\|Rx(t)\|^2 = \sum_{j=K+1}^{K+L} \left(\frac{\mu_j}{\mu_j^2 + t}u_j b\right)^2 \tag{5.8}$$

and $\frac{d}{dt}\|Rx(t)\|^2$ as

$$\frac{d}{dt}\|Rx(t)\|^2 = -2\sum_{j=K+1}^{K+L} \frac{\mu_j^2}{(\mu_j^2 + t)^3}(u_j b)^2. \tag{5.9}$$

Which leaves the problem of determining t from

$$\sum_{j=K+1}^{K+L} \frac{\mu_j^2(\mu_j^2 - 3t)}{(\mu_j^2 + t)^3}(u_j \cdot b)^2. \tag{5.10}$$

Many of the methods described so far have been compared [27, 106], using data from forward simulations (as in the present study) or data measured in an electrolytic tank representing the human torso. Although no method clearly outperformed the others—in terms of consistently giving the results closest to the optimal t-parameter—when the whole QRS complex was considered, the CRESO method was the most

consistent. However, it has been shown [22, 24] that this method may fail for some non-trivial b vectors, such that Eq. 5.5 has no maximum within a realistic range of t values.

Another method, called the **Zero–Crossing (ZC) Method**, was recently introduced by Johnston and Gulrajani [79]. The value of t which satisfies the following equation is selected:

$$\|A\boldsymbol{x}(t) - \boldsymbol{b}\|^2 = t\|R\boldsymbol{x}(t)\|^2. \tag{5.11}$$

The authors point out that this method is based on a much simpler concept than CRESO, and that this simplicity carries over to the computation of the regularization parameter. For simulated dipole sources in a concentric spheres model, they found two t values which satisfied their condition. The lowest value was selected, because it was closest to the optimal t. When dipole sources were simulated in a realistic heart-torso model, conditions were found where the zero-crossing point disappeared. The absence of Gaussian noise in the torso potentials was suggested as the cause. Based on further experiments using realistic geometry and realistic potential distributions, the authors found that ZC produced inverse-recovered potentials as effectively as, if not better than, the CRESO method. A common drawback of both CRESO and ZC methods is the necessity of determining the smallest of potentially multiple values which satisfy the given criteria, and the possibility that no solution exists over a realistic range of t values.

The L-**curve** defined by

$$C : (x(t), y(t)) = (f(\|A\boldsymbol{x}(t) - \boldsymbol{b}\|), g(\|R\boldsymbol{x}(t)\|)), \qquad t > 0 \tag{5.12}$$

is so named because of its shape. Functions f and g have been assigned [22, 24, 62, 67] such that either the norm of the residual and the seminorm of the solution or their corresponding squares or logarithms were used. The shape of the curve is fundamental to the criterion proposed by Hansen and O'Leary [63] for determining the appropriate t-parameter. The "corner" of the L curve, defined by the value at which there is

maximum curvature, given by

$$\kappa(t) = \frac{[x'(t)y''(t) - y'(t)x''(t)]}{[(x'(t))^2 + (y'(t))^2]^{3/2}}, \tag{5.13}$$

determines the selection of the regularization parameter.

The residual norm can be computed by Eq. 5.14 and the seminorm of the solution by Eq. 5.15.

$$\|Ax(t) - b\| = \left(\sum_{i=K+1}^{K+L} \left[\frac{t}{\mu_i^2 + t}(u_i \cdot b) \right]^2 + \sum_{i=K+L+1}^{M} (u_i \cdot b)^2 \right)^{1/2} \tag{5.14}$$

$$\|Rx(t)\| = \left(\sum_{i=K+1}^{K+L} \left[\frac{\mu_i}{\mu_i^2 + t}(u_i \cdot b) \right]^2 \right)^{1/2}. \tag{5.15}$$

The term δ_0, defined by

$$\delta_0 \equiv \|(UU^T - I_M)b\| = \left(\sum_{i=K+L+1}^{M} (u_i \cdot b)^2 \right)^{1/2} \tag{5.16}$$

is the norm of that component of b which is outside the range of the matrix A. When no regularization is used, $t = 0$ and $\|Ax(t) - b\|^2 = \delta_0^2$. The magnitude of δ_0 is sometimes referred to as the incompatibility measure [62].

Given these formulae, it is possible to compute all of the derivatives required for determining the t-parameter using the L-curve method. The intuitive thought behind this method is that a smaller t would produce a larger solution seminorm while only marginally reducing the residual, and, on the other hand, a larger t would increase the residual but only marginally reduce the solution seminorm. From a computational standpoint, the calculations required to determine a point of maximum curvature on the L-curve can be highly unstable. This instability is, to a large extent, due to the scaling factors introduced by the singular values $\mu_i, i = K + 1, ..., K + L$, particularly in the second-derivative terms.

This method has been shown to be more robust than generalized cross-validation in the presence of correlated errors [62]. Johnston and Gulrajani [79] visually compared CRESO and ZC to the corner point of the L-curve where the logarithm function was

used. Clements et al. [24] computed the t-parameter using the L-curve method and found good results when compared to those for the CRESO criterion. Horáček and Clements [71] and Hoekema [67] also obtained reasonable results.

Engl and Grever [41] examined the L-curve method as the residual error noise level tends to zero. They found that when using the point of maximal curvature for the t-parameter, there was no convergence. The authors suggested that the L-curve graph could be used in conjunction with the discrepancy principle to yield better results. Using the squared norm L-curve as an example, they presented an algorithm for computing the regularization parameter. Their method requires an estimate, $\|\epsilon\|$, of the error due to noise in the torso-surface data as in Eq. 5.2. The L-curve is first plotted, then a vertical line is drawn at $\|Ax - b\|^2 = \|\epsilon\|^2$. Then the point of intersection of the L-curve and the vertical line is determined. The slope of the L-curve at the point of intersection is then determined by plotting the tangent at the intersection point and computing the descent s_2 of the tangent. Since

$$\frac{d}{dt}\|Ax(t) - b\|^2 = 2t \sum_{i=K+1}^{K+L} \frac{\mu_i^2}{(\mu_i^2 + t)^3}(u_i \cdot b)^2, \tag{5.17}$$

and

$$\frac{d}{dt}\|Rx(t)\|^2 = -2 \sum_{i=K+1}^{K+L} \frac{\mu_i^2}{(\mu_i^2 + t)^3}(u_i \cdot b)^2, \tag{5.18}$$

$$\frac{d}{dt}\|Ax(t) - b\|^2 = -t\frac{d}{dt}\|Rx(t)\|^2 \tag{5.19}$$

and

$$s_2 = -\frac{1}{t}, \tag{5.20}$$

where s_2 is the slope of the squared norm L-curve for a given value of t. Therefore, the regularization parameter can be determined by setting

$$t = -\frac{1}{s_2}. \tag{5.21}$$

If the error value is valid, then the strategy of this algorithm is convergent.

Unlike the original L-curve criterion, the error level ϵ is explicitly used to calculate the slope of the L-curve for the appropriate regularization parameter, and thus the t

value itself. However, the method still depends on the accuracy of the error estimate. This raises the question of whether or not there is another way to estimate the slope of the L-curve corresponding to the optimal t-parameter without this restriction. The following section will explore this possibility.

5.2 Slope Estimation Method

The aim of this section is to determine a method for estimating the slope of the L-curve which corresponds to an optimal regularization parameter. Then the slope estimation method (SEM) could be used to determine the appropriate t-parameter. Both the norm and the squared norm L-curve representations will be considered—as in the previous section.

The slope of the norm L-curve at t is computed by:

$$\frac{\frac{d}{dt}\|Rx(t)\|}{\frac{d}{dt}\|Ax(t) - b\|}. \tag{5.22}$$

Utilizing the fact that

$$\frac{d}{dt}\|Ax(t) - b\|^2 = 2\|Ax(t) - b\| \cdot \frac{d}{dt}\|Ax(t) - b\| \tag{5.23}$$

and equivalently,

$$\frac{d}{dt}\|Rx(t)\|^2 = 2\|Rx(t)\| \cdot \frac{d}{dt}\|Rx(t)\|, \tag{5.24}$$

the first derivative of the residual norm and the semi-norm of the solution may be computed by

$$\frac{d}{dt}\|Ax(t) - b\| = \frac{\frac{d}{dt}\|Ax(t) - b\|^2}{2\|Ax(t) - b\|} \tag{5.25}$$

and

$$\frac{d}{dt}\|Rx(t)\| = \frac{\frac{d}{dt}\|Rx(t)\|^2}{2\|Rx(t)\|}. \tag{5.26}$$

Utilizing 5.25 and 5.26 with substitution using 5.19, gives

$$s_1 = -\frac{1}{t} \cdot \frac{\|Ax(t) - b\|}{\|Rx(t)\|}, \tag{5.27}$$

where s_1 is the slope of the norm L-curve for a given value of t. It follows that

$$t = -\frac{1}{s_1} \cdot \frac{\|Ax(t) - b\|}{\|Rx(t)\|}.$$

(5.28)

For the squared-norm L-curve, t is given by Eq. 5.21. With these equations for t, the problem becomes one of estimating the appropriate values for s_1 and/or s_2.

An examination of the GSVD solutions for the residual norm given by Eq. 5.14 and the solution semi-norm given by Eq. 5.15, reveals two differences. The residual norm includes the δ_0 term, or incompatibility measure, which is constant regardless of the value chosen for t. Secondly, there is a t in the numerator of the summation for the residual, where the solution semi-norm has μ_i, the singular value corresponding to the singular vector u_i. If the value selected for the t-parameter is equal to that of the singular value, μ_i, then the contribution to the residual norm is equal to that for the solution semi-norm for this singular vector. For all $\mu_i < t$, there is a greater contribution to the residual norm and for all $\mu_i > t$, the amount added to the solution semi-norm is greater. Therefore, as t is increased, the number of singular vectors making a larger contribution to the residual norm than the solution semi-norm also increases. If t is specifically chosen to be equal to the value of the non-zero singular value of smallest magnitude, μ_{min}, then for the corresponding singular vector there will be equal contributions to the two norms and all other singular vectors will make a larger contribution to the semi-norm of the solution. On the other hand, if t is set at the value of the largest singular value, μ_{max}, the corresponding singular vector contributes equally to each norm and the remainder contribute a larger amount to the residual norm.

When t is small ($t \leq \mu_{min}$), the amount of residual error is dependent upon input data error and is more or less independent of regularization [62]. For large t ($t \geq \mu_{max}$), the opposite is true, with the residual error dependent on regularization and fairly independent of data error [62]. The relative change, r_c, in the residual norm from error due to regularization only, may be approximated by

$$r_c = \frac{\|Ax(\mu_{max}) - b\|^2 - \delta_0^2}{\|Ax(\mu_{min}) - b\|^2 - \delta_0^2}.$$

(5.29)

The numerator of this ratio is, more or less, constant regardless of the level of data error. For very low error values, the denominator will be small compared to the numerator, making r_c large. As the error increases, the denominator increases and r_c decreases. From an inspection of L-curve plots, it was noted that this ratio exhibits the same relationship to error size as does the magnitude of the slope of the L-curve at the optimal t-value. That is, as error increases, the optimal t increases and the corresponding magnitude of the slope of the L-curve decreases. It follows from Eqs. 5.21 and 5.28 that the slope of both the norm and squared norm L-curves must be negative. It was hypothesized that the value $-r_c$ could be used to estimate the slope, s_2, of the squared norm L-curve at the optimal t value and that, using Eq. 5.21, the appropriate value for t could be determined. The norm L-curve could also be used, with the value $-\sqrt{r_c}$ as the estimate of the slope, s_1, and using Eq. 5.28 to compute the optimal t-parameter. Figure 5.1 shows an example of a norm L-curve for a single dipole source using second-order Tikhonov regularization. Slope is plotted against residual norm in the bottom trace. The residual norm corresponding to the t-parameter selected by the Slope Estimation Method and the best possible parameter are indicated.

The t-parameter selected by the norm (t_{s_1}) and squared-norm (t_{s_2}) slope estimation methods were compared to the optimal t-parameter giving the minimum RE when compared to the epicardial potential distribution known *a priori*. All major methods for t-parameter selection without *a priori* knowledge of the potentials distributions were compared in the present study. A comparison was made for the values selected by the CRESO (t_{cr}), ZC (t_{zc}), L-curve with lognorm values (t_{ln}), and L-curve with norm values (t_{lc}). As in the previous chapters, the test data included the single central dipole, the three/five eccentric dipoles, the 1,600 eccentric dipoles, and the two time-sequences of 36 consecutive oblique dipolar layers. In addition, t-parameters for Hilbert systems—known to be very ill-conditioned—were determined. Results with the node-to-node system were also calculated. As a step towards determining how these methods will work with the measured data (to be presented in Chapter 6), values
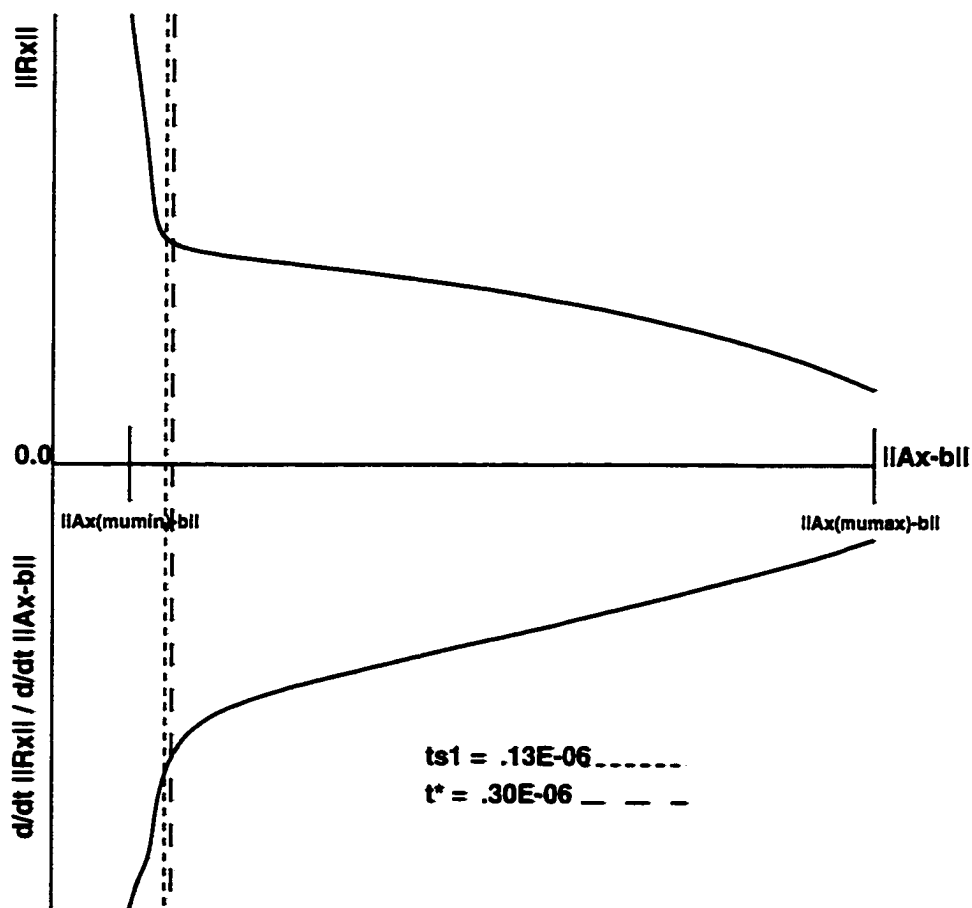
Figure 5.1: Top trace is L-curve for a single dipole source with second-order regularization plotted for t-values in the interval $[\mu_{min}, \mu_{max}]$. The slope of the L-curve is plotted against the residual norm in the lower trace. The shorter dashed line indicates the residual norm for the t-parameter selected by the Slope Estimation Method, the longer dashed line is for the best possible t-parameter. Traces are plotted with a logarithmic scale.

corresponding to the locations of the 117 torso-surface leads were determined for the set of 1,600 eccentric dipoles. From these, the 700 potential values for torso triangles were interpolated and t values were computed for all methods. Finally, t-parameters for the above methods were determined for a sequence of epicardial distributions for measured data from a normal subject, starting prior to QRS onset and continuing past QRS offset.

5.3 Results

Utilizing the methods described in previous sections, the seven t-parameters, t^*, t_{s_1}, t_{s_2}, t_{cr}, t_{zc}, t_{ln}, and t_{lc} were calculated. NAG Library routine c05adf [1], which finds the first zero of a function, was used to determine the closest value for t_{zc}. The NAG Library minimizing routine, e04abf, was utilized for all other methods, with the exception of t_{s_2}, which did not require a search. To find the maximum curvature for t_{ln} and t_{lc}, the function was multiplied by -1 and the minimum was determined. Search intervals were set with the lower bound set by machine precision and the upper bound by the magnitude of the largest generalized singular value. Although these bounds were sufficient for SEMs and the optimal value, there were circumstances for all other methods where it was necessary to start with a smaller upper bound and then increase it until a value less than the latest upper bound was selected.

Parameters were first determined for the Hilbert matrices. The forward solution was performed and then Gaussian error of varying amounts was added prior to the inverse procedure. Table 5.1 displays all t-values with RE and CC for three error levels and two sizes of Hilbert matrices. The optimimum t-value and RE increased as the Gaussian noise level increased, while CC decreased for both matrices. The SEMs achieved results as close to t^*, or closer, as all other methods. For t_{zc}, there were very good results for the two higher error levels, but a suitable parameter value was not detected for the lowest error. The values for t_{cr} were in an acceptable range for the lowest error, but did not increase at the higher levels, resulting in very large

Table 5.1:

Comparison of regularization parameters selected by different methods for Hilbert matrices

Error Factor	t Selection	Hilbert (18 × 15)			Hilbert (50 × 30)		
		t	RE	CC	t	RE	CC
10^{-5}	t^*	$.8075e^{-12}$	.2233	.9748	$.1911e^{-12}$	.1986	.9801
10^{-5}	t_{s_1}	$.4805e^{-11}$	.2404	.9707	$.4456e^{-11}$	**.2236**	**.9747**
10^{-5}	t_{s_2}	$.3980e^{-11}$	**.2380**	**.9713**	$.4843e^{-11}$	.2241	.9746
10^{-5}	t_{cr}	$.2991e^{-10}$	.2575	.9663	$.1891e^{-9}$	.2637	.9646
10^{-5}	t_{zc}	$.1110e^{-15}$	10.60	.1933	$.1110e^{-15}$	3.631	.1928
10^{-5}	t_{ln}	$.1488e^{-1}$	.4899	.8727	$.3693e^{-1}$	.5006	.8672
10^{-5}	t_{lc}	$.2737e^{-8}$	.2635	.9647	$.1420e^{-8}$	.2691	.9631
10^{-3}	t^*	$.5858e^{-7}$	.2649	.9643	$.2936e^{-7}$	.2707	.9627
10^{-3}	t_{s_1}	$.4806e^{-7}$	**.2653**	**.9642**	$.4457e^{-7}$	**.2717**	**.9624**
10^{-3}	t_{s_2}	$.4396e^{-7}$	.2658	.9640	$.4971e^{-7}$	.2723	.9622
10^{-3}	t_{cr}	$.7584e^{-10}$	2.117	.4011	$.8886e^{-10}$	.7723	.7858
10^{-3}	t_{zc}	$.4871e^{-7}$	**.2653**	**.9642**	$.6578e^{-7}$	.2745	.9616
10^{-3}	t_{ln}	$.1490e^{-1}$	.4898	.8727	$.3692e^{-1}$	.5006	.8672
10^{-3}	t_{lc}	$.1088e^{-4}$	.3495	.9369	$.3356e^{-4}$	.3585	.9336
10^{-1}	t^*	$.6662e^{-3}$	.3584	.9336	$.1935e^{-5}$	.3054	.9532
10^{-1}	t_{s_1}	$.4869e^{-3}$	**.3588**	**.9334**	$.4482e^{-3}$	**.3731**	**.9280**
10^{-1}	t_{s_2}	$.4612e^{-3}$	.3589	.9334	$.5329e^{-3}$	.3754	.9271
10^{-1}	t_{cr}	$.7682e^{-10}$	206.5	.0021	$.8311e^{-10}$	77.06	.0804
10^{-1}	t_{zc}	$.4343e^{-3}$	.3591	.9333	$.6421e^{-3}$	.3784	.9259
10^{-1}	t_{ln}	$.8348e^{-4}$	.3620	.9325	$.5149e^{-3}$	.3749	.9273
10^{-1}	t_{lc}	$.4428e^{-9}$	160.2	.0337	$.3619e^{-1}$	.5008	.8672

t^*, optimal t parameter selected on the basis of *a priori* knowledge of both torso-surface and epicardial potentials; t_{s_1}/t_{s_2}, t selected by variants of Slope Estimation method; t_{cr}, t selected by CRESO method; t_{zc}, t selected by Zero-Crossing method; t_{ln}, t selected by L-curve method with lognorm values; t_{lc}, t selected by L-curve method with norm values; RE, relative error; CC, correlation coefficient; **bold font**, the best results.

RE values. The L-curve methods tended to greatly overestimate the t-value with the exception of the highest error level.

The t-parameters for all methods were then computed for the single central dipole, and three or five eccentric dipoles. Results, using both zero- and second-order regularization, are shown in Table 5.2. For zero-order regularization, the SEMs achieved the best results with the exception of the central dipole source, where t_{cr} was marginally better than t_{s_1}. Otherwise, CRESO, ZC, and lognorm LC methods underestimated the appropriate values and the norm LC method overestimated them. When second-order regularization was used, the CRESO method failed to find an acceptable t-value for the central dipole source. For the other two distributions, there was little difference among the SEMs, CRESO, ZC, and the lognorm LC. The norm LC method consistently selected a value several orders of magnitude larger than optimum.

Next, all t-parameters and REs were computed for each of the 1,600 eccentric single dipoles, using both zero- and second-order regularization. Results were compared to the optimal values. Comparisons are displayed in Table 5.3 for zero-order regularization and in Table 5.4 for second-order regularization. The discrepancy in t values was computed as the maximum of t^* and the t for the comparison method, divided by the minimum of the two. Differences in RE were determined by subtracting the RE for the best-possible t, t^*, from the RE when using the comparison method. The median t discrepancy and RE difference, where results for 50% of the sources are less than or equal these values, as well as results for 80% and the maximum differences are given.

For both zero- and second-order regularization, the norm L-curve method had the largest differences in t and RE in comparison with optimal values. With zero-order regularization, results for t_{cr} and t_{s_1} were the best. Median RE differences were less than 2%, with a maximum of 5% at the 80% mark. It was noted that for CRESO the difference in RE decreased as the source was moved nearer the epicardial surface. The opposite occurred for the norm SEM, with error increasing. Results for t_{s_2}, t_{zc}, and t_{ln} were also good, but the 80% values for ZC and lognorm LC were higher. CRESO,

Table 5.2:

Comparison of regularization parameters selected by different methods for zero- and second-order Tikhonov regularization and potential distributions generated by single- and multiple-dipole sources

Source	t Selection	B0			B2		
		t	RE	CC	t	RE	CC
1Dip	t^*	$.1048e^{-8}$	.3120	.9501	$.1084e^{-4}$	.0582	.9983
	t_{s_1}	$.9651e^{-10}$	.3392	.9411	$.1203e^{-5}$	.0702	.9975
	t_{s_2}	$.2773e^{-9}$	**.3195**	**.9477**	$.3521e^{-6}$	.1022	.9948
	t_{cr}	$.1995e^{-9}$	.3241	.9462	$.7372e^{-13}$	63.19	.0060
	t_{zc}	$.2995e^{-10}$	.3870	.9244	$.6104e^{-5}$	**.0586**	**.9983**
	t_{ln}	$.3688e^{-10}$	.3756	.9285	$.5374e^{-5}$	.0588	**.9983**
	t_{lc}	$.3248e^{-5}$	.3774	.9261	$.1280e^{-1}$	.0951	.9956
3Dip	t^*	$.3634e^{-9}$	.3396	.9410	$.3072e^{-6}$	.2148	.9774
	t_{s_1}	$.1497e^{-9}$	.3439	**.9398**	$.2361e^{-7}$	.2788	.9635
	t_{s_2}	$.9463e^{-9}$	**.3428**	.9397	$.1167e^{-7}$	.3223	.9522
	t_{cr}	$.2956e^{-10}$	.3875	.9252	$.1651e^{-7}$	.2993	.9583
	t_{zc}	$.1817e^{-10}$	.4141	.9157	$.5768e^{-7}$	**.2405**	**.9723**
	t_{ln}	$.2053e^{-10}$	.4066	.9185	$.4602e^{-7}$	.2485	.9706
	t_{lc}	$.4113e^{-7}$	.3784	.9258	$.2195e^{0}$	.5442	.8394
5Dip	t^*	$.3800e^{-9}$	.4545	.8924	$.3967e^{-6}$	.3374	.9433
	t_{s_1}	$.2330e^{-9}$	**.4558**	**.8923**	$.2990e^{-7}$	.3936	.9275
	t_{s_2}	$.1620e^{-10}$	.4625	.8874	$.1791e^{-7}$	.4194	.9190
	t_{cr}	$.2882e^{-10}$	.5139	.8690	$.1057e^{-7}$	.4507	.9082
	t_{zc}	$.2151e^{-10}$	.5169	.8678	$.6221e^{-7}$	**.3645**	**.9364**
	t_{ln}	$.2188e^{-10}$	.5160	.8681	$.3316e^{-7}$	.3889	.9289
	t_{lc}	$.1130e^{-2}$	.7881	.6209	$.2345e^{0}$	.6463	.7633

B0/B2, zero-/second-order Tikhonov regularization; t, regularization parameter (see the legend of Table 5.1); RE, relative error; CC, correlation coefficient; 1Dip, a single central dipole; 3Dip, three eccentric dipoles; 5Dip, five eccentric dipoles; **bold font**, the best results.

Table 5.3:

Difference between the optimal regularization parameter t^* and that chosen by different parameter-selection methods, with associated differences in relative error (RE) of inverse-recovered potentials, for zero-order regularization and 1,600 eccentric single-dipole sources

t Selection	Source	t discrepancy			RE difference		
		50%	80%	MAX	50%	80%	MAX
t_{s_1}	10.0-mm	$.22e^1$	$.80e^1$	$.25e^8$	**.0036**	**.0233**	.4635
	7.5-mm	$.32e^1$	$.70e^1$	$.65e^7$	**.0075**	**.0200**	.3910
	5.0-mm	$.70e^1$	$.15e^2$	$.68e^4$	.0178	.0321	.3866
	2.5-mm	$.21e^2$	$.43e^2$	$.78e^4$	.0335	.0507	.4819
	All above	$.52e^1$	$.24e^2$	$.25e^8$	.0140	**.0365**	.4819
t_{s_2}	10.0-mm	$.59e^1$	$.14e^2$	$.43e^7$	.0133	.0285	**.3144**
	7.5-mm	$.16e^2$	$.34e^2$	$.99e^6$	.0308	.0485	**.2767**
	5.0-mm	$.49e^2$	$.97e^2$	$.11e^4$	.0496	.0734	**.2259**
	2.5-mm	$.17e^3$	$.35e^3$	$.38e^4$	.0673	.0940	**.2813**
	All above	$.26e^2$	$.15e^3$	$.43e^7$	.0364	.0697	**.3144**
t_{cr}	10.0-mm	$.57e^1$	$.15e^2$	$.33e^8$	.0169	.0522	.4967
	7.5-mm	$.41e^1$	$.13e^2$	$.11e^8$	.0121	.0442	.7371
	5.0-mm	$.21e^1$	$.68e^1$	$.11e^6$	**.0060**	**.0286**	.8006
	2.5-mm	$.18e^1$	$.41e^1$	$.23e^7$	**.0029**	**.0215**	1.747
	All above	$.28e^1$	$.11e^2$	$.33e^8$	**.0077**	.0408	1.747
t_{zc}	10.0-mm	$.15e^2$	$.56e^2$	$.10e^{14}$	.0760	.1423	.8268
	7.5-mm	$.80e^1$	$.53e^2$	$.42e^{14}$	.0535	.1442	.9487
	5.0-mm	$.41e^1$	$.31e^2$	$.14e^{15}$	.0273	.1313	.9156
	2.5-mm	$.20e^1$	$.12e^2$	$.33e^{15}$	.0051	.0707	.7058
	All above	$.63e^1$	$.41e^2$	$.33e^{15}$	.0421	.1336	.9487
t_{ln}	10.0-mm	$.13e^2$	$.43e^2$	$.13e^{16}$	.0555	.1066	.9387
	7.5-mm	$.69e^1$	$.54e^2$	$.13e^{16}$	.0402	.1072	.8326
	5.0-mm	$.37e^1$	$.54e^2$	$.13e^{16}$	.0197	.1069	.8796
	2.5-mm	$.23e^1$	$.22e^3$	$.13e^{16}$	.0067	.1074	.7330
	All above	$.58e^1$	$.54e^2$	$.13e^{16}$	.0337	.1075	.9387
t_{lc}	10.0-mm	$.16e^9$	$.12e^{10}$	$.33e^{13}$	.5083	.5988	.7477
	7.5-mm	$.73e^9$	$.44e^{10}$	$.38e^{13}$	.5060	.6122	.7686
	5.0-mm	$.37e^{10}$	$.17e^{11}$	$.43e^{13}$	.4576	.5834	.7969
	2.5-mm	$.14e^{11}$	$.90e^{11}$	$.54e^{13}$	.3191	.5120	.7227
	All above	$.19e^{10}$	$.14e^{11}$	$.54e^{13}$	.4637	.5909	.7969

t, regularization parameter (see the legend of Table 5.1); **bold font**, the best results.

Table 5.4:

Difference between the optimal regularization parameter t^* and that chosen by different parameter-selection methods, with associated differences in relative error (RE) of inverse-recovered potentials, for second-order regularization and 1,600 eccentric single-dipole sources

t Selection	Source	t discrepancy			RE difference		
		50%	80%	MAX	50%	80%	MAX
t_{s_1}	10.0-mm	$.34e^1$	$.43e^2$	$.34e^{10}$	.0119	.0810	.7648
	7.5-mm	$.28e^1$	$.21e^2$	$.15e^9$	**.0059**	.0552	.5115
	5.0-mm	$.40e^1$	$.10e^2$	$.11e^6$	.0106	**.0270**	.5721
	2.5-mm	$.73e^1$	$.15e^2$	$.21e^7$	.0155	.0296	1.106
	All above	$.43e^1$	$.17e^2$	$.34e^{10}$	.0115	.0435	1.106
t_{s_2}	10.0-mm	$.50e^1$	$.72e^2$	$.18e^{10}$	.0218	.1184	.7018
	7.5-mm	$.27e^1$	$.25e^2$	$.43e^8$	.0061	.0667	.5337
	5.0-mm	$.45e^1$	$.11e^2$	$.86e^5$	.0111	**.0270**	.5258
	2.5-mm	$.10e^2$	$.22e^2$	$.81e^6$	.0201	.0332	.9392
	All above	$.54e^1$	$.23e^2$	$.18e^{10}$	.0152	.0495	.9392
t_{cr}	10.0-mm	$.71e^1$	$.38e^2$	$.47e^9$	.0243	.0794	.4888
	7.5-mm	$.51e^1$	$.38e^2$	$.12e^9$	.0178	.0801	**.4577**
	5.0-mm	$.29e^1$	$.15e^2$	$.12e^6$	**.0087**	.0544	.5689
	2.5-mm	$.28e^1$	$.10e^2$	$.23e^9$	**.0065**	.0476	2.490
	All above	$.40e^1$	$.22e^2$	$.47e^9$	.0129	.0704	2.490
t_{zc}	10.0-mm	$.28e^1$	$.21e^2$	$.11e^{10}$	**.0060**	.0505	1.452
	7.5-mm	$.30e^1$	$.16e^2$	$.18e^8$	.0068	.0495	.4851
	5.0-mm	$.36e^1$	$.13e^2$	$.16e^6$	.0099	.0365	.7371
	2.5-mm	$.46e^1$	$.10e^2$	$.18e^{17}$	.0104	**.0283**	2.423
	All above	$.35e^1$	$.13e^2$	$.18e^{17}$	**.0087**	**.0410**	2.423
t_{ln}	10.0-mm	$.36e^1$	$.90e^2$	$.29e^8$	.0090	.0568	**.2932**
	7.5-mm	$.40e^1$	$.37e^3$	$.12e^8$	.0129	.0942	.4775
	5.0-mm	$.54e^1$	$.29e^4$	$.24e^8$	.0196	.1333	**.4315**
	2.5-mm	$.19e^2$	$.48e^5$	$.13e^{10}$	.0560	.1406	**.3554**
	All above	$.56e^1$	$.20e^4$	$.13e^{10}$	.0171	.1095	**.4775**
t_{lc}	10.0-mm	$.12e^7$	$.11e^8$	$.22e^{12}$	.3154	.3628	.5038
	7.5-mm	$.68e^7$	$.70e^8$	$.38e^{12}$	.3447	.3447	.5538
	5.0-mm	$.62e^8$	$.33e^9$	$.85e^{12}$	.3245	.3868	.5500
	2.5-mm	$.27e^9$	$.13e^{10}$	$.47e^{13}$	.2391	.3189	.5357
	All above	$.25e^8$	$.29e^9$	$.47e^{13}$	.3133	.3765	.5538

t, regularization parameter (see the legend of Table 5.1); **bold font**, the best results.

Table 5.5:

Difference between the optimal regularization parameter t^* and that chosen by different parameter-selection methods, with associated differences in relative error (RE) of inverse-recovered potentials, for zero-order regularization and a time sequence of double-layer sources

t Selection	Source	t discrepancy			RE difference		
		50%	80%	MAX	50%	80%	MAX
t_{s_1}	Septal	$.19e^1$	$.44e^1$	$.91e^1$	**.0025**	.0126	.0319
	Basal	$.31e^1$	$.20e^2$	$.57e^2$	.0073	.0258	**.0759**
t_{s_2}	Septal	$.34e^1$	$.84e^1$	$.11e^2$	.0072	.0169	**.0284**
	Basal	$.64e^1$	$.12e^3$	$.40e^3$	.0070	.0310	.1190
t_{cr}	Septal	$.25e^1$	$.34e^1$	$.51e^1$	.0061	**.0115**	.0336
	Basal	$.31e^1$	$.75e^1$	$.38e^2$	**.0069**	**.0251**	.0998
t_{zc}	Septal	$.66e^1$	$.15e^2$	$.27e^2$	.0306	.0689	.0882
	Basal	$.68e^1$	$.18e^2$	$.64e^2$	.0186	.0555	.1092
t_{ln}	Septal	$.69e^1$	$.16e^2$	$.90e^3$	.0383	.0645	.1149
	Basal	$.57e^1$	$.18e^2$	$.33e^3$	.0148	.0477	.1058
t_{lc}	Septal	$.26e^5$	$.45e^6$	$.18e^8$	.2072	.2670	.4410
	Basal	$.37e^7$	$.15e^9$	$.70e^9$	.1130	.3156	.4036

t, regularization parameter (see the legend of Table 5.1); **bold font**, the best results.

ZC, and LC methods had higher maximum RE differences than the SEMs. With second-order regularization, t_{zc} gave the best 50% and 80% values over all sources, but also had the largest maximum t discrepancy, for a source at the closest distance to the epicardial surface. Differences for the CRESO and the SEMs did not greatly differ from those for ZC.

In Table 5.5, the discrepancies from the optimal value, when using zero-order regularization with the two time-sequence data sets, are displayed. Results with second-order regularization are given in Table 5.6. Discrepancies for the SEMs and

Table 5.6:

Difference between the optimal regularization parameter t^* and that chosen by different parameter-selection methods, with associated differences in relative error (RE) of inverse-recovered potentials, for second-order regularization and a time sequence of double-layer sources

t Selection	Source	t discrepancy			RE difference		
		50%	80%	MAX	50%	80%	MAX
t_{s_1}	Septal	$.57e^1$	$.99e^1$	$.15e^2$	.0147	.0394	.0608
	Basal	$.44e^1$	$.19e^2$	$.68e^4$	.0132	.0461	.1704
t_{s_2}	Septal	$.18e^2$	$.36e^2$	$.68e^2$	.0577	.1146	.1410
	Basal	$.96e^1$	$.36e^2$	$.88e^4$	.0374	.0582	.1858
t_{cr}	Septal	$.26e^1$	$.42e^1$	$.10e^2$	.0040	.0078	.0536
	Basal	$.39e^1$	$.13e^3$	$.23e^5$	.0090	**.0285**	.3225
t_{zc}	Septal	$.12e^1$	$.17e^1$	$.46e^1$	**.0002**	**.0009**	**.0095**
	Basal	$.44e^1$	$.13e^2$	$.25e^4$	.0098	.0372	**.1321**
t_{ln}	Septal	$.15e^1$	$.21e^1$	$.11e^4$	.0007	.0017	.1272
	Basal	$.38e^1$	$.24e^3$	$.30e^4$	**.0062**	.0668	.1451
t_{lc}	Septal	$.51e^4$	$.27e^5$	$.38e^6$	.1380	.1825	.2919
	Basal	$.14e^5$	$.61e^7$	$.40e^8$	.1244	.1875	.3086

t, regularization parameter (see the legend of Table 5.1); **bold font**, the best results.

Table 5.7:

Difference between the optimal regularization parameter t^* and that chosen by different parameter-selection methods, with associated differences in relative error (RE) of inverse-recovered potentials, for node-to-node system with zero- and second-order regularization and 1,600 eccentric single-dipole sources

Operator Order	t Selection	t discrepancy			RE difference		
		50%	80%	MAX	50%	80%	MAX
B0	t_{s_1}	$.70e^1$	$.63e^2$	$.54e^6$	.0280	.0999	4.941
	t_{s_2}	$.17e^2$	$.61e^2$	$.15e^6$	.0475	**.0992**	**4.132**
	t_{cr}	$.28e^2$	$.19e^4$	$.70e^9$	.1810	.5390	14.23
	t_{zc}	$.49e^1$	$.65e^3$	$.55e^8$	.0298	.2966	9.881
	t_{ln}	$.43e^1$	$.14e^3$	$.35e^7$	**.0179**	**.1514**	6.344
B2	t_{s_1}	$.90e^1$	$.44e^4$	$.17e^9$	.0431	.3735	8.936
	t_{s_2}	$.27e^2$	$.10e^5$	$.17e^9$	.1295	.5261	8.620
	t_{cr}	$.15e^2$	$.54e^4$	$.24e^{10}$	.0641	.4392	14.87
	t_{zc}	$.95e^1$	$.81e^3$	$.17e^9$	**.0270**	.1849	9.746
	t_{ln}	$.15e^2$	$.24e^3$	$.10e^8$	.0377	**.1155**	**6.536**

t, regularization parameter (see the legend of Table 5.1); **bold font**, the best results.

CRESO are small with zero-order regularization. Median RE values are less than 1%. Those for ZC and lognorm LC are slightly larger, while REs for t_{lc} are still high. When second-order regularization was used, the results for t_{zc}, t_{s_1} and t_{cr} were very good. Those for t_{s_2} and t_{ln} were not far off. The median discrepancy for t_{lc} was still higher.

Table 5.7 displays the t discrepancy and RE difference values for the set of all 1,600 sources with zero- and second-order regularization when the node-to-node system was employed. The results for t_{lc} are not included. With zero-order regularization, the lognorm LC method had the lowest median RE difference, although differences for ZC and SEMs were also small. However, the SEMs had the smallest differences at the 80% level. CRESO had the largest differences. Second-order regularization results had the ZC and the lognorm LC the best. The median values were small for t_{s_1} and

t_{cr}, but the 80% values were higher. In all cases, with both zero- and second-order regularization, the maximum value was very large, with those for CRESO the largest.

When results were computed for the 1,600 dipoles with the triangle-to-triangle system, with values for the 117 torso lead locations as input, errors due to interpolation were evident. The optimal t-parameter and RE both increased. The ability of the different methods to find an acceptable t value was tested with results for zero-order regularization in Table 5.8. Values for t_{lc} were not included. The smallest median difference levels with zero-order regularization were seen with t_{ln}. All methods had acceptable results, but median values were highest for the SEMs and maximum values largest for CRESO. An examination of the t_{s_1} values indicated that there was a definite tendency to overestimate the optimal value. An arbitrary scaling factor of .25 was chosen to decrease the value selected. Results for this altered method, t_{s_m}, are also found in Table 5.8. Maximum differences increased, although still less than for CRESO, while median and 80% values decreased and were closer to those for other methods.

Equivalent results for second-order regularization are in Table 5.9. The CRESO method had the smallest median and 80% errors. However, at each distance from the epicardial surface, the maximum error indicates that an acceptable value for t_{cr} was not found. For t_{ln} and t_{s_1}, there were also small median errors. The SEM had large 80% values. Results for t_{zc} and t_{s_2} had larger median errors. When second-order regularization was used, it was noted that t_{s_1} showed a tendency to underestimate the optimal value. An arbitrary scaling value of 2. was selected, based on observations. Results for this altered method, t_{s_m}, are also found in Table 5.9. In this case, RE differences decreased for maximum, median and 80% levels.

In Table 5.10, the t-parameter estimates for t_{s_m}, t_{s_2}, t_{cr}, t_{zc}, t_{ln} and t_{lc} are given for a sequence of measured torso-surface potentials for a normal subject, with zero-order regularization. Since the solution for epicardial potentials is unknown, comparisons have to be made among the methods and with ranges of values from the 117-lead

Table 5.8:

Difference between the optimal regularization parameter t^* and that chosen by different parameter-selection methods, with associated differences in relative error (RE) of inverse-recovered potentials, for zero-order regularization, 1,600 eccentric single-dipole sources, and 117 torso-surface leads

t Selection	Source	t discrepancy			RE difference		
		50%	80%	MAX	50%	80%	MAX
t_{s_m}	10.0-mm	$.23e^1$	$.66e^1$	$.31e^3$	.0113	.0548	.9748
	7.5-mm	$.29e^1$	$.74e^1$	$.30e^3$	.0122	.0448	.9503
	5.0-mm	$.42e^1$	$.11e^2$	$.29e^3$	.0118	.0393	.7539
	2.5-mm	$.70e^1$	$.18e^2$	$.29e^3$	.0091	.0225	.3850
	All above	$.37e^1$	$.11e^2$	$.31e^3$	.0109	.0391	.9748
t_{s_1}	10.0-mm	$.59e^1$	$.14e^2$	$.82e^2$	.0342	.0796	**.5058**
	7.5-mm	$.83e^1$	$.20e^2$	$.11e^3$	.0352	.0757	**.4613**
	5.0-mm	$.12e^2$	$.30e^2$	$.13e^3$	.0300	.0555	**.3295**
	2.5-mm	$.20e^2$	$.52e^2$	$.29e^3$	.0188	.0337	.2101
	All above	$.99e^1$	$.28e^2$	$.29e^3$	.0275	.0593	**.5058**
t_{s_2}	10.0-mm	$.10e^2$	$.25e^2$	$.14e^3$	.0521	.1043	.5498
	7.5-mm	$.13e^2$	$.35e^2$	$.18e^3$	.0484	.0891	.5183
	5.0-mm	$.20e^2$	$.53e^2$	$.34e^3$	.0386	.0657	.3699
	2.5-mm	$.32e^2$	$.87e^2$	$.63e^3$	.0226	.0391	**.2011**
	All above	$.68e^2$	$.47e^2$	$.63e^3$	.0368	.0746	.5498
t_{cr}	10.0-mm	$.26e^1$	$.66e^1$	$.40e^3$	.0175	.0716	1.120
	7.5-mm	$.25e^1$	$.54e^1$	$.39e^3$	.0125	.0532	1.038
	5.0-mm	$.23e^1$	$.46e^1$	$.37e^3$	.0063	.0325	.8290
	2.5-mm	$.22e^1$	$.47e^1$	$.38e^3$	**.0024**	.0143	.4575
	All above	$.24e^1$	$.53e^1$	$.40e^3$	.0082	.0364	1.120
t_{zc}	10.0-mm	$.24e^1$	$.46e^1$	$.11e^3$	.0105	.0421	.5076
	7.5-mm	$.29e^1$	$.57e^1$	$.11e^3$	.0117	.0386	.4724
	5.0-mm	$.37e^1$	$.78e^1$	$.11e^3$	.0109	.0301	.3855
	2.5-mm	$.52e^1$	$.12e^2$	$.47e^5$	.0077	.0185	.2491
	All above	$.33e^1$	$.76e^1$	$.47e^5$	.0101	.0301	.5076
t_{ln}	10.0-mm	$.19e^1$	$.35e^1$	$.44e^2$	**.0068**	**.0315**	.5268
	7.5-mm	$.21e^1$	$.38e^1$	$.32e^2$	**.0065**	**.0259**	.5006
	5.0-mm	$.22e^1$	$.42e^1$	$.27e^2$	**.0048**	**.0194**	.3812
	2.5-mm	$.26e^1$	$.54e^1$	$.75e^2$	.0036	.0104	.3806
	All above	$.22e^1$	$.42e^1$	$.75e^2$	**.0051**	**.0219**	.5268

t, regularization parameter (see the legend of Table 5.1); **bold font**, the best results.

Table 5.9:

Difference between the optimal regularization parameter t^* and that chosen by different parameter-selection methods, with associated differences in relative error (RE) of inverse-recovered potentials, for second-order regularization, 1,600 eccentric single-dipole sources, and 117 torso-surface leads

t Selection	Source	t discrepancy			RE difference		
		50%	80%	MAX	50%	80%	MAX
t_{s_m}	10.0-mm	$.38e^1$	$.29e^2$	$.56e^4$	.0193	.1822	2.547
	7.5-mm	$.42e^1$	$.32e^2$	$.66e^4$	.0157	.1523	2.502
	5.0-mm	$.45e^1$	$.35e^2$	$.65e^4$	.0124	.0926	2.320
	2.5-mm	$.58e^1$	$.44e^2$	$.88e^4$	.0067	.0390	1.586
	All above	$.45e^1$	$.36e^2$	$.88e^4$	.0123	.1107	2.547
t_{s_1}	10.0-mm	$.57e^1$	$.59e^2$	$.11e^5$	.0412	.3033	3.121
	7.5-mm	$.47e^1$	$.64e^2$	$.13e^5$	.0239	.2636	3.155
	5.0-mm	$.46e^1$	$.67e^2$	$.13e^5$	.0146	.1531	2.953
	2.5-mm	$.54e^1$	$.76e^2$	$.18e^5$	.0075	.0660	2.060
	All above	$.51e^1$	$.65e^2$	$.18e^5$	.0174	.1919	3.155
t_{s_2}	10.0-mm	$.44e^2$	$.39e^3$	$.50e^5$	.3272	.9379	4.829
	7.5-mm	$.30e^2$	$.34e^3$	$.59e^5$	.2261	.7416	4.943
	5.0-mm	$.21e^2$	$.36e^3$	$.59e^5$	.1179	.5104	4.735
	2.5-mm	$.14e^2$	$.36e^3$	$.60e^5$	.0393	.2400	3.408
	All above	$.26e^2$	$.36e^3$	$.60e^5$	.1486	.6565	4.943
t_{cr}	10.0-mm	$.28e^1$	$.10e^2$	$.12e^{16}$	**.0091**	**.0446**	214800
	7.5-mm	$.34e^1$	$.15e^2$	$.26e^{16}$	**.0092**	**.0427**	181600
	5.0-mm	$.45e^1$	$.38e^2$	$.99e^{16}$	**.0094**	**.0427**	143600
	2.5-mm	$.64e^1$	$.19e^3$	$.79e^{16}$	**.0058**	.0354	108000
	All above	$.39e^1$	$.26e^2$	$.99e^{16}$	**.0081**	**.0416**	214800
t_{zc}	10.0-mm	$.14e^3$	$.78e^3$	$.14e^5$	.1039	.1670	**.2734**
	7.5-mm	$.32e^3$	$.20e^4$	$.34e^6$	.0923	.1430	**.2362**
	5.0-mm	$.60e^3$	$.50e^4$	$.11e^6$	.0662	.0986	**.1725**
	2.5-mm	$.18e^4$	$.16e^5$	$.36e^6$	.0324	.0515	**.0945**
	All above	$.44e^3$	$.42e^4$	$.36e^6$	.0673	.1223	**.2734**
t_{ln}	10.0-mm	$.78e^1$	$.38e^2$	$.73e^4$	.0321	.0918	3.754
	7.5-mm	$.82e^1$	$.37e^2$	$.60e^4$	.0258	.0757	2.060
	5.0-mm	$.94e^1$	$.42e^2$	$.81e^4$	.0192	.0479	1.556
	2.5-mm	$.11e^2$	$.58e^2$	$.73e^4$	.0089	**.0243**	.7828
	All above	$.91e^1$	$.44e^2$	$.14e^5$	.0191	.0590	3.754

t, regularization parameter (see the legend of Table 5.1); **bold font**, the best results.

Table 5.10:

Regularization parameter selected by different methods, for zero-order Tikhonov regularization, CRC3 method, and 117 measured ECG leads

sample	t_{s_m}	t_{s_2}	t_{cr}	t_{zc}	t_{ln}	t_{lc}
279	$.228e^{-1}$	$.444e^{-1}$	$.614e^{-2}$	$.000e^{+0}$	$.109e^{-1}$	$.758e^{-1}$
281	$.225e^{-1}$	$.446e^{-1}$	$.552e^{-2}$	$.000e^{+0}$	$.106e^{-1}$	$.809e^{-1}$
283	$.275e^{-1}$	$.506e^{-1}$	$.710e^{-2}$	$.000e^{+0}$	$.130e^{-1}$	$.808e^{-1}$
285	$.329e^{-1}$	$.526e^{-1}$	$.876e^{-2}$	$.000e^{+0}$	$.132e^{-1}$	$.879e^{-1}$
287	$.297e^{-1}$	$.472e^{-1}$	$.845e^{-2}$	$.000e^{+0}$	$.111e^{-1}$	$.966e^{-1}$
289	$.307e^{-1}$	$.479e^{-1}$	$.813e^{-2}$	$.000e^{+0}$	$.108e^{-1}$	$.112e^{+0}$
291	$.486e^{-1}$	$.612e^{-1}$	$.000e^{+0}$	$.000e^{+0}$	$.155e^{-1}$	$.104e^{+0}$
293	$.516e^{-2}$	$.196e^{-1}$	$.211e^{-2}$	$.268e^{-1}$	$.491e^{-2}$	$.274e^{-1}$
295	$.998e^{-3}$	$.395e^{-2}$	$.234e^{-2}$	$.407e^{-2}$	$.282e^{-2}$	$.147e^{-1}$
297	$.891e^{-3}$	$.325e^{-2}$	$.238e^{-2}$	$.422e^{-2}$	$.285e^{-2}$	$.174e^{-1}$
299	$.903e^{-3}$	$.331e^{-2}$	$.180e^{-2}$	$.439e^{-2}$	$.230e^{-2}$	$.266e^{-1}$
301	$.847e^{-3}$	$.311e^{-2}$	$.115e^{-2}$	$.440e^{-2}$	$.148e^{-2}$	$.486e^{-1}$
303	$.837e^{-3}$	$.287e^{-2}$	$.127e^{-2}$	$.600e^{-2}$	$.156e^{-2}$	$.615e^{-1}$
305	$.921e^{-3}$	$.292e^{-2}$	$.200e^{-2}$	$.000e^{+0}$	$.228e^{-2}$	$.501e^{-1}$
307	$.948e^{-3}$	$.296e^{-2}$	$.300e^{-2}$	$.807e^{-2}$	$.336e^{-2}$	$.324e^{-1}$
309	$.936e^{-3}$	$.287e^{-2}$	$.431e^{-2}$	$.742e^{-2}$	$.468e^{-2}$	$.247e^{-1}$
311	$.953e^{-3}$	$.288e^{-2}$	$.577e^{-2}$	$.733e^{-2}$	$.601e^{-2}$	$.220e^{-1}$
313	$.961e^{-3}$	$.296e^{-2}$	$.644e^{-2}$	$.642e^{-2}$	$.644e^{-2}$	$.185e^{-1}$
315	$.902e^{-3}$	$.283e^{-2}$	$.640e^{-2}$	$.551e^{-2}$	$.613e^{-2}$	$.162e^{-1}$
317	$.835e^{-3}$	$.266e^{-2}$	$.605e^{-2}$	$.493e^{-2}$	$.566e^{-2}$	$.156e^{-1}$
319	$.859e^{-3}$	$.272e^{-2}$	$.437e^{-2}$	$.515e^{-2}$	$.462e^{-2}$	$.157e^{-1}$
321	$.832e^{-3}$	$.256e^{-2}$	$.424e^{-2}$	$.641e^{-2}$	$.453e^{-2}$	$.223e^{-1}$
323	$.944e^{-3}$	$.274e^{-2}$	$.498e^{-2}$	$.109e^{-1}$	$.514e^{-2}$	$.302e^{-1}$
325	$.118e^{-2}$	$.317e^{-2}$	$.712e^{-2}$	$.000e^{+0}$	$.592e^{-2}$	$.449e^{-1}$
327	$.155e^{-2}$	$.385e^{-2}$	$.000e^{+0}$	$.000e^{+0}$	$.897e^{-2}$	$.599e^{-1}$
329	$.231e^{-2}$	$.528e^{-2}$	$.000e^{+0}$	$.000e^{+0}$	$.123e^{-1}$	$.673e^{-1}$
331	$.462e^{-2}$	$.898e^{-2}$	$.000e^{+0}$	$.000e^{+0}$	$.152e^{-1}$	$.836e^{-1}$
333	$.896e^{-2}$	$.162e^{-1}$	$.000e^{+0}$	$.000e^{+0}$	$.168e^{-2}$	$.111e^{+0}$
335	$.970e^{-2}$	$.187e^{-1}$	$.000e^{+0}$	$.000e^{+0}$	$.367e^{-2}$	$.135e^{+0}$
337	$.124e^{-1}$	$.221e^{-1}$	$.000e^{+0}$	$.000e^{+0}$	$.000e^{+0}$	$.000e^{+0}$
339	$.147e^{-1}$	$.250e^{-1}$	$.188e^{-2}$	$.000e^{+0}$	$.000e^{+0}$	$.000e^{+0}$
341	$.145e^{-1}$	$.251e^{-1}$	$.189e^{-2}$	$.000e^{+0}$	$.000e^{+0}$	$.000e^{+0}$
343	$.884e^{-2}$	$.188e^{-1}$	$.241e^{-2}$	$.000e^{+0}$	$.000e^{+0}$	$.000e^{+0}$
345	$.510e^{-2}$	$.121e^{-1}$	$.390e^{-2}$	$.000e^{+0}$	$.375e^{-2}$	$.112e^{+0}$
347	$.468e^{-2}$	$.109e^{-1}$	$.000e^{+0}$	$.000e^{+0}$	$.450e^{-2}$	$.915e^{-1}$
349	$.476e^{-2}$	$.111e^{-1}$	$.000e^{+0}$	$.000e^{+0}$	$.475e^{-2}$	$.927e^{-1}$

$t_:$ regularization parameter (see the legend of Table 5.1).

values for the 1,600 sources. Samples were recorded every 2 ms. The onset of the QRS complex was at sample 289 and the offset at sample 346. A value of zero indicates that a t parameter could not be found by the given method. It was noted that there were samples for which t could not be estimated by all methods but the SEMs. When t-values which met criteria existed, the values for all methods were within one to two orders of magnitude of each other. The values selected for t_{lc} were higher in all cases. Estimates for t_{s_m} were lower than those for t_{cr} during most of the QRS complex. However, at time instants with low amplitudes, including early and late QRS, the results were opposite. An examination of t_{s_m} values over time showed that they were at their largest around the onset of QRS complex. They decreased towards the peak of QRS and then began to increase, so that they were again in a higher range for the end of the QRS. There were no large fluctuations in the parameter values. The values selected were approximately one order of magnitude larger than those found for the 117-lead input for the 1,600 dipole sources.

Results for the measured data, when second-order regularization was used, are given in Table 5.11. It is evident from this table that t_{zc} was never found. For t_{cr}, a few values could be determined; however, these tend to be large. The LC methods found a t value every time, but there were some large jumps in value between samples. These values were also quite large. The SEMs selected a t-parameter for each sample. Patterns were the same as for zero-order regularization.

5.4 Discussion

The purpose of the work presented in this chapter was to investigate methods for determining the regularization parameter value without *a priori* information about the desired epicardial distribution. Determining criteria for this selection process is crucial for the ultimate goal of applying the inverse problem of electrocardiography to clinical data acquired by means of body-surface potential mapping.

CRESO, ZC, norm and lognorm versions of LC, and the norm and squared norm

Table 5.11:

Regularization parameter selected by different methods, for second-order Tikhonov regularization, CRC3 method, and 117 measured ECG leads

sample	t_{s_m}	t_{s_2}	t_{cr}	t_{zc}	t_{ln}	t_{lc}
279	$.513e^{+1}$	$.153e^{+0}$	$.000e^{+0}$	$.000e^{+0}$	$.324e^{+2}$	$.324e^{+2}$
281	$.563e^{+1}$	$.153e^{+0}$	$.000e^{+0}$	$.000e^{+0}$	$.314e^{+2}$	$.314e^{+2}$
283	$.552e^{+1}$	$.155e^{+0}$	$.000e^{+0}$	$.000e^{+0}$	$.325e^{+2}$	$.325e^{+2}$
285	$.494e^{+1}$	$.149e^{+0}$	$.000e^{+0}$	$.000e^{+0}$	$.314e^{+2}$	$.314e^{+2}$
287	$.406e^{+1}$	$.139e^{+0}$	$.000e^{+0}$	$.000e^{+0}$	$.315e^{+2}$	$.315e^{+2}$
289	$.439e^{+1}$	$.138e^{+0}$	$.000e^{+0}$	$.000e^{+0}$	$.303e^{+2}$	$.303e^{+2}$
291	$.539e^{+1}$	$.150e^{+0}$	$.000e^{+0}$	$.000e^{+0}$	$.297e^{+2}$	$.297e^{+2}$
293	$.669e^{+1}$	$.173e^{+0}$	$.000e^{+0}$	$.000e^{+0}$	$.454e^{+2}$	$.454e^{+2}$
295	$.113e^{+1}$	$.767e^{-1}$	$.378e^{+3}$	$.000e^{+0}$	$.506e^{+2}$	$.506e^{+2}$
297	$.802e^{+0}$	$.584e^{-1}$	$.230e^{+3}$	$.000e^{+0}$	$.466e^{+2}$	$.466e^{+2}$
299	$.673e^{+0}$	$.574e^{-1}$	$.127e^{+3}$	$.000e^{+0}$	$.376e^{+2}$	$.376e^{+2}$
301	$.433e^{+0}$	$.401e^{-1}$	$.724e^{+2}$	$.000e^{+0}$	$.309e^{+2}$	$.309e^{+2}$
303	$.288e^{+0}$	$.315e^{-1}$	$.753e^{+2}$	$.000e^{+0}$	$.306e^{+2}$	$.306e^{+2}$
305	$.279e^{+0}$	$.304e^{-1}$	$.000e^{+0}$	$.000e^{+0}$	$.301e^{+2}$	$.301e^{+2}$
307	$.330e^{+0}$	$.336e^{-1}$	$.000e^{+0}$	$.000e^{+0}$	$.293e^{+2}$	$.293e^{+2}$
309	$.385e^{+0}$	$.362e^{-1}$	$.000e^{+0}$	$.000e^{+0}$	$.677e^{-1}$	$.282e^{+2}$
311	$.462e^{+0}$	$.388e^{-1}$	$.000e^{+0}$	$.000e^{+0}$	$.102e^{+0}$	$.455e^{+1}$
313	$.637e^{+0}$	$.455e^{-1}$	$.000e^{+0}$	$.000e^{+0}$	$.354e^{+0}$	$.236e^{+2}$
315	$.761e^{+0}$	$.501e^{-1}$	$.000e^{+0}$	$.000e^{+0}$	$.436e^{+0}$	$.257e^{+2}$
317	$.776e^{+0}$	$.505e^{-1}$	$.000e^{+0}$	$.000e^{+0}$	$.260e^{+2}$	$.260e^{+2}$
319	$.654e^{+0}$	$.481e^{-1}$	$.000e^{+0}$	$.000e^{+0}$	$.292e^{+2}$	$.292e^{+2}$
321	$.396e^{+0}$	$.345e^{-1}$	$.000e^{+0}$	$.000e^{+0}$	$.457e^{+0}$	$.157e^{+2}$
323	$.294e^{+0}$	$.296e^{-1}$	$.000e^{+0}$	$.000e^{+0}$	$.154e^{+2}$	$.154e^{+2}$
325	$.228e^{+0}$	$.257e^{-1}$	$.000e^{+0}$	$.000e^{+0}$	$.160e^{+2}$	$.160e^{+2}$
327	$.219e^{+0}$	$.252e^{-1}$	$.000e^{+0}$	$.000e^{+0}$	$.144e^{+2}$	$.144e^{+2}$
329	$.267e^{+0}$	$.289e^{-1}$	$.000e^{+0}$	$.000e^{+0}$	$.314e^{+0}$	$.128e^{+2}$
331	$.384e^{+0}$	$.360e^{-1}$	$.000e^{+0}$	$.000e^{+0}$	$.384e^{+0}$	$.105e^{+2}$
333	$.837e^{+0}$	$.557e^{-1}$	$.000e^{+0}$	$.000e^{+0}$	$.124e^{+2}$	$.124e^{+2}$
335	$.112e^{+1}$	$.661e^{-1}$	$.000e^{+0}$	$.000e^{+0}$	$.192e^{+2}$	$.192e^{+2}$
337	$.159e^{+1}$	$.820e^{-1}$	$.000e^{+0}$	$.000e^{+0}$	$.187e^{+2}$	$.187e^{+2}$
339	$.233e^{+1}$	$.993e^{-1}$	$.000e^{+0}$	$.000e^{+0}$	$.195e^{+2}$	$.195e^{+2}$
341	$.240e^{+1}$	$.102e^{+0}$	$.000e^{+0}$	$.000e^{+0}$	$.195e^{+2}$	$.195e^{+2}$
343	$.169e^{+1}$	$.827e^{-1}$	$.000e^{+0}$	$.000e^{+0}$	$.203e^{+2}$	$.203e^{+2}$
345	$.933e^{+0}$	$.554e^{-1}$	$.000e^{+0}$	$.000e^{+0}$	$.214e^{+2}$	$.214e^{+2}$
347	$.726e^{+0}$	$.470e^{-1}$	$.000e^{+0}$	$.000e^{+0}$	$.319e^{+1}$	$.274e^{+2}$
349	$.680e^{+0}$	$.490e^{-1}$	$.000e^{+0}$	$.000e^{+0}$	$.300e^{+2}$	$.300e^{+2}$

t, regularization parameter (see the legend of Table 5.1).

variations of the proposed SEM method were chosen for examination. The CRESO method was chosen, because it has been shown to work better than other methods presented in this chapter (which were not, therefore, examined further) and has been used in several studies [27, 106, 120]. The ZC technique was included, because when it was previously compared to LC and CRESO [79] it appeared to give reasonable estimates of the regularization parameter. The LC method has also been previously used for the inverse problem of electrocardiography [18, 24, 67, 71, 122, 123] and has the advantage of being based on less empirical criteria. Therefore, results were also generated for this technique.

CRESO, ZC, and LC methods are capable of generating reasonable results; however, problems have been identified with each. With clinical applications, it is necessary to determine an estimate of the optimal regularization parameter for every case. The new SEM method introduced in this chapter seems to provide a more robust and stable method of t-parameter estimation that could meet this requirement.

Although the CRESO technique for determining the regularization parameter has been utilized for the solution of the inverse problem of electrocardiography by several investigators [27, 106, 120], it has also been demonstrated that a t parameter fitting the CRESO criteria may not exist [22, 24]. In the present study, the CRESO method was not successful in finding an appropriate t-parameter value for the Hilbert matrix problems. For the heart/torso model, the parameter was often near optimal. However, there were occasions with this model where a large discrepancy occurred, and sometimes no acceptable value was detected. Results tended to be better when the Identity operator, rather than the Laplacian, was used as the regularizing operator. The last two points were effectively demonstrated by the results for the time sequence of measured torso-surface potentials. In practice, the determination of the appropriate value was dependent upon the careful selection of the search interval.

The ZC method has not been in general use. However, it was recently suggested as a simpler substitute for the CRESO method [79]. Comparisons with CRESO and a visual determination of L-curve values gave the proponents of this method reason

to believe it would be effective at generating an acceptable value. Careful selection must be made as they also found two points satisfying their criteria. The lowest value was closest to the optimal value, but disappeared in cases with low torso data error. This was reflected in the results for the Hilbert matrices, where ZC could not find an appropriate value for the lowest errors, but was successful for higher levels. For other test sets ZC was often successful, and less likely than CRESO to fail to find a parameter value. However, when the measured sequence of torso-surface potentials was evaluated, this method failed to find an appropriate value more often than any other technique.

The L-curve method of determining the regularization parameter for the generation of inverse-recovered epicardial potentials has been employed by several investigators [22, 24, 67, 71, 122, 123]. Achieving a balance between the norm of the residual and the seminorm of the solution is fundamental to this technique. This is desirable, since it makes the selection process less empirical. The point where maximum curvature of the L-curve exists is intuitively a good definition of this balance [62]. However, it has been shown [41] that this method is not convergent. In this chapter, two L-curve variations were examined, the lognorm (as has been used by others [24, 62, 67, 120]), which is supposed to best define the corner location, and the norm (which has been used less frequently [122, 123]).

Neither variant was capable of selecting an appropriate parameter value for the error levels presented for the Hilbert matrices. When results were calculated for the dipole sources, these methods usually overestimated the parameter. However, the lognorm variant selected parameters within an acceptable range of the optimal value for the time-sequence data. This method also worked well for the dipole sources with the node-to-node system. When input potentials were calculated from 117 torso lead locations, the lognorm L-curve was one of the best methods. With measured torso-surface potentials as input, parameters selected were close to those determined by CRESO. There were also times when no value was detected by either variant of the method. The norm variation of the method generally selected larger values. Search

interval boundaries were also important for this method.

In this chapter, the Slope Estimation Method of determining an optimal regularization parameter has been introduced. Engl and Grever [41] suggested that there may be other ways to utilize the L-curve plot to determine a near-optimal regularization parameter. This idea led to the notion that it may be possible to estimate the slope of the curve at the point corresponding to the desired parameter. It was hypothesized that the negative of the relative change in residual norm from when t was equal to the minimum non-zero singular value, to that with the maximum singular value, was a good estimate of this slope. The hope was that this would provide an acceptable estimate of the regularization parameter under any conditions, as there were circumstances under which all the other methods failed.

Results for variations using the slope of the squared-norm and norm L-curve were computed. The SEM consistently achieved good results for the Hilbert matrices at all error levels, the dipole sources, and the time sequence data. The norm version tended to have better results than the squared-norm, although this was much simpler to calculate, requiring no search. For all cases examined, there was only one point found which satisfied the criteria. This was in contrast to the CRESO, ZC and LC methods which were sensitive to search boundaries, since it was necessary to find the "correct" match. The technique was also effective for the node-to-node system.

On the other hand, for the input data consisting of 117 torso leads, this method, although still acceptable, did not give the best results, showing a tendency to overestimate the optimal value with the Identity operator, and underestimate it with the Laplacian operator. When the parameter chosen by the norm variant was scaled by a constant factor, the overall results were in the same range as other methods. The reasons for this decline in the ability of the SEM to find a near-optimal value in the presence of interpolation error in the torso input potentials, are not immediately clear. However, it appears that as the residual norm for μ_{min} approaches the value at μ_{max}, the estimate of the appropriate slope is less accurate. The scaling factors which were chosen worked for this particular application, but there is no indication

whether they would be appropriate for any other conditions.

For the potentials measured on the torso surface, the scaled norm SEM selected values in the same range as CRESO, ZC and LC methods. There were no cases when this technique failed to select a regularization parameter. The parameters selected varied with time, decreasing as the magnitude of the input data increased (signal-to-noise ratio increased) and increasing as the magnitude decreased. This relationship intuitively appears appropriate. Therefore, the SEM is an effective technique for determining the regularization parameter, and though it would not always be "the best", it consistently selects an acceptable value.

Chapter 6

Clinical Application: Coronary Angioplasty as a Controlled Model of Ischemia

6.1 Introduction

Percutaneous transluminal coronary angioplasty (PTCA) involves the insertion of a balloon catheter into a patient's coronary artery. The balloon is positioned within an area of major stenosis, and then inflated. With a successful angioplasty treatment, the occlusion is decreased, providing improved blood flow to the portion of the myocardium forming the perfusion bed of the artery. For the period of time during which the balloon is inflated, there is complete disruption of the antegrade flow of blood past the obstruction. This induces a state of acute transient myocardial ischemia, reversible with reperfusion of the occluded artery.

At the cellular level, ischemia is characterized by mechanisms which alter with time. In this study, PTCA induces sudden onset of ischemia for a maximum duration of 3 minutes. During these first few minutes following coronary occlusion, changes follow a very rapid time course [77]. The development of techniques for directly

recording the electrical activity of individual cells [92] facilitated research on myocardial ischemia in animal models—both at the cardiac-tissue [157] and whole-heart [81] levels. This led to extensive investigations of myocardial ischemia [77]. It was found that the resting potential of cells in the ischemic region becomes rapidly less negative as a result of an accumulation of potassium in the extracellular space [65, 66, 77]. Subsequent to this, there are gradual changes in action-potential amplitude and duration [77].

Local depolarization of ischemic cells causes an electrotonic "injury current" to flow between ischemic and healthy tissue. During the diastolic phase, the injury current flows from ischemic to normal cells. DC-coupled amplifiers record this as a negative TQ segment [85], but AC-coupled amplifiers used for clinical ECG recording will set this level as the baseline, deflecting other signals upwards. Once the cells neighbouring the ischemic region have been depolarized, the injury current changes direction and flows towards the ischemic zone. On the ECG, this is observed as local shifts in the ST segment and T wave [82]. This electrocardiographic indicator of ischemia has been well documented in many studies (e.g., [40, 49, 69, 107, 133, 152]). Holland and Brooks have suggested that the magnitude, polarity, and distribution of potentials resulting from this injury current is dependent upon the time elapsed since the onset of the ischemia, as well as its location, spatial extent and severity [69].

ECG signals, ranging from a few leads to many leads used in body-surface potential mapping, have been examined in patients with varying degrees of ischemia [23, 54, 112, 153]. Abnormal ST segments, T waves, and QRS complexes have been identified. In these studies, it was not possible to control factors such as the degree and duration of the myocardial ischemia. PTCA provides an excellent model for examining reproducible, acute ischemia, since it controls the location and duration of artery occlusion, and the patient's condition prior to the ischemic incident may be documented for comparison with that during and following the procedure. Much interest has been shown in this model. Conventional 12-lead ECGs [2, 15, 42, 56, 60, 87, 88, 90, 109, 121, 138, 154, 159, 160, 161] and body-surface

potential mapping data [86, 97, 98, 122, 123, 127, 141, 147] have been recorded before, during, and following PTCA. These studies have examined alterations in ST segment, T wave, and QRS complex. To increase the efficacy of body-surface potential mapping in extracting information about ischemic changes, some investigators [97, 98, 123] have computed inverse-recovered epicardial potential images.

Torso-surface potential maps of the QRS complex and ST segment, with features characteristic of the occluded artery, have been computed from torso-surface potentials collected during PTCA for the three major coronary arteries (i.e., left anterior descending artery, LAD); left circumflex artery, LCx; and right coronary artery, RCA) [47, 127, 141, 147]. The diversions from normal torso-surface potential distributions reflect changes in the epicardial distributions. These patterns, in turn, are due to the presence of ischemia induced by the cessation of blood flow after artery occlusion by balloon inflation.

It is useful to briefly review what the perfusion beds of these arteries are. The left anterior descending branch of the left coronary artery travels down the anterior interventricular groove and often extends past the apex and onto the posterior groove. Diagonal branches perfuse the anterior wall of the left ventricle. The anterior two-thirds of the septum is perfused by septal perforating branches, which also arise from the LAD. Other small branches supply blood to the anterior right ventricle. The left circumflex branch of the left coronary artery travels along the atrioventricular groove with the obtuse-marginal branch carrying blood to the lateral left ventricle, whereas other branches extend to the posterior of the heart. Acute-marginal branches of the right coronary artery perfuse the free wall of the right ventricle. The posterior descending branch courses down the posterior interventricular groove with offshoot septal perforating branches which perfuse the posterior third of the septum [82]. Although this pattern predominates, examinations of human hearts have shown many variations [102]. Important differences can be found on the posterior ventricular wall, where the posterior descending artery may arise from the left-circumflex artery. As well, the circumflex and right coronary arteries may perfuse variable territories of the

posterior left ventricle. The presence of a collateral circulation, where an area of the heart is fed by branches from two different sources, will also affect interpretation of the ischemia produced by PTCA. Collaterals may link distinct arteries or different branches of the same artery [26]. Collaterals appear to develop to a functional extent only in the presence of severe coronary artery disease [26, 133].

Documenting areas where blood flow has decreased will help to identify the ischemic region. ^{99m}Tc sestamibi is a perfusion agent that is taken up by myocardial cells in proportion to the rate of blood flow through the myocardium. It has a slow washout, and demonstrates minimal redistribution [51]. This allows imaging, while still documenting the state of myocardial perfusion at the time the agent was injected, to be performed with a delay of up to six hours. As a result, ^{99m}Tc sestamibi is ideally suited to localizing and assessing the extent and severity of myocardial ischemia during PTCA [14, 16, 17, 46, 51, 52, 64, 124, 148].

The ultimate end-point for noninvasive imaging of epicardial potentials via the inverse problem of electrocardiography is clinical application. Achieving this goal requires assessment of the accuracy of the method in humans. To this end, applications have steered towards pathologies where other evidence provides information on expected results. These include ventricular pre-excitation, myocardial infarction, and the ischemia induced by PTCA.

Shahidi et al. [140] recorded body-surface potentials for a patient with Wolff-Parkinson-White syndrome (WPW) prior to surgery. Epicardial electrograms were recorded in the same patient during surgery, where a left lateral pre-excitation site was identified. A finite element method was used to determine epicardial potentials from the body-surface data. The authors found that the recovered epicardial distribution could determine the left lateral site, but that the distributions measured later in the QRS complex did not compare well with the recorded data. Penney et al. [122] utilized a boundary element method and compared localization of several WPW pre-excitation sites with those documented by catheter ablation, with good results.

Using an inverse procedure based on a resistor network model, Kilpatrick et al. [84]

constructed epicardial ST segment potential distributions for 55 patients with acute myocardial infarction. They predicted which artery contributed to the infarct and compared their results with coronary arteriography analysis. Misclassified patients all had coronary artery disease of the predicted artery, even though it was not involved in the infarction.

MacLeod et al. [98] utilized a boundary-element solution to the inverse problem to interpret body-surface potential maps recorded during PTCA. For seven patients, a comparison was made between the predicted location of ischemia and a qualitative assessment of each patients coronary anatomy, as determined by fluoroscopic examination. There was agreeement in location for all patients. Penney et al. [123] compared localization of PTCA induced ischemia by inverse-recovered epicardial images and radionuclide perfusion images. They found good agreement in localization methods.

The aim of this chapter is to assess the capabilities of the best approaches to the inverse solution—tested in previous chapters—in the investigation of PTCA-induced ischemia. Regional constraints, including spurious-extrema removal, weighted spatial smoothing, and temporal smoothing, will be utilized. The newly introduced Slope Estimation Method will be used to determine the appropriate regularization parameter.

Inverse-recovered epicardial potential images will be examined for expected characteristics of ischemic changes. QRS- and ST-integral difference maps will be assessed for regions of elevation and locations of extrema. Electrograms chosen from the central ischemic zone will be evaluated for changes throughout the depolarization/repolarization cycle. A comparison will be made between ischemic locations identified by noninvasive epicardial potential images and radionuclide myocardial perfusion images. A representative patient will be selected—from the total population of 94 patients—for each artery. Body-surface ECG and epicardial electrograms will be compared throughout the inflation/deflation cycle.

Table 6.1:
Dalhousie University database of body-surface potential mapping data: PTCA Group

	LAD	RCA	LCx
No. of patients	35	36	23
Male/female	21/14	30/6	17/6
Age (yrs)	57 ± 10	56 ± 10	61 ± 10
Heart rate (bpm)	63 ± 11	64 ± 12	58 ± 8
QRS duration (ms)	96 ± 11	96 ± 13	98 ± 11
QTc interval (ms)	436 ± 28	431 ± 22	434 ± 24

LAD, left anterior descending coronary artery; RCA, right coronary artery; LCx, left circumflex coronary artery

6.2 Methods

This study includes a group of 94 patients who underwent 120-lead electrocardiographic body-surface mapping during coronary angioplasty. Electrocardiographic data were collected throughout the inflation/deflation cycle during clinical PTCA procedures. A subgroup of 18 patients completed a radionuclide perfusion imaging section of the study. After balloon-inflation PTCA had successfully dilated the target vessel (a reduction in the stenosis to < 50% of the vessel's diameter), another 60-s inflation was performed. At the start of the inflation, ^{99m}Tc sestamibi was intravenously injected, and 120-lead ECG data were recorded. Single photon emission computed tomography (SPECT) imaging was performed one hour after injection of radionuclide to obtain a scintigraphic "inflation" image; 24 hours later, one hour after a repeat injection of the radionuclide, a scintigraphic "rest" image was acquired. One representative patient for each artery of occlusion will be examined in detail in this study, to detect changes at different times throughout the inflation/deflation cycle.

Patients: Table 6.1 shows the clinical characteristics of the patients who underwent clinically indicated PTCA and were included in this study. Patients had to meet the following criteria: (1) scheduling of PTCA for severe stenosis ($\geq$ 60% diameter

reduction) of the LAD, LCx or RCA arteries, (2) no previous myocardial infarction (MI) or clinical evidence of variant angina, (3) normal global left-ventricular wall motion (ejection fraction $\geq$ 45%), and either normal or only mildly hypokinetic regional wall motion, and (4) normal resting 12-lead ECG. Patients included in the perfusion imaging section of the study were required to have one-vessel disease with diameter of stenosis $\geq$70% by visual examination. Patients originally enrolled in this part of the study would have been excluded if the PTCA procedure was unsuccessful, or any major complication (including acute closure, acute MI, emergency coronary bypass surgery, or repeat PTCA) occurred. The protocol was approved by the institutional review board of the Queen Elizabeth II Health Sciences Centre, and all patients provided written consent prior to participation.

Angioplasty Procedure: Regular PTCA methods were exercised with a No. 8F guide catheter being positioned in the ascending aorta. Following this, an appropriately sized "steerable" balloon dilation catheter (USCI, 2.5 to 3.5 mm diameter, 20–25 mm length) was positioned through the guide catheter across the coronary artery stenosis such that when inflated, the balloon would completely obstruct the coronary artery and eliminate antegrade blood flow. Several recordings of the pressure in the artery under treatment were made before beginning the PTCA procedure, to assess both initial hemodynamics and signal stability. An aspirin dose of 325 mg was administered orally prior to PTCA, and 10,000 U of heparin intra-arterially at the beginning of the procedure. Every reasonable effort was made to restrict administration of intracoronary nitroglycerine until after the research portion of the procedure had been completed. A waiting period of at least 1 minute (as we had previously found that this was the minimal time required for the ECGs to return to a preinjection baseline) after the most recent injection assured that there were no confounding influences from the contrast medium.

The following procedure was followed for participants in the perfusion study. An additional femoral-vein catheter was inserted for radiopharmaceutical administration. Once the operator was satisfied that the target lesion had resolved with one or more

balloon inflations, and that the patient could tolerate a 60-s inflation, an additional 60-s inflation was performed with a standard (non-perfusion-type) angioplasty balloon catheter. At the beginning of this inflation, 20mCi of ^{99m}Tc sestamibi (Cardiolite; DuPont-Pharma, DuPont Pharmaceuticals, North Billerica, MA) was injected into the femoral-vein catheter and quickly flushed with 10 ml of normal saline. After the final coronary angiography was completed, the patient was taken to the nuclear medicine laboratory for SPECT imaging, one hour after injection of radionuclide. Routine post-angioplasty care was given to all patients. A minimum of 24 hours later, the patient had repeat SPECT imaging performed at least one hour after a repeat injection of 20 mCi of ^{99m}Tc sestamibi by intravenous injection.

Electrocardiographic imaging: Prior to initial PTCA studies, some technical changes had to be made to our standard electrocardiographic acquisition system [99]. Data collection during PTCA also required a special set of radiolucent electrodes (In Vivo Metric Systems, Healdsburg, CA). Eighteen flexible strips with 117 electrodes were firmly attached to the patient, using the layout in Fig. 6.1; disposable limb-lead electrodes were attached separately. To enable the patient's arms to move easily during angioplasty, the limb leads were positioned on the torso as suggested by Mason and Likar [101]. (The RA and LA electrodes were mounted slightly higher and more laterally than specified by Mason and Likar, at the acromial end of the clavicle, to make room for the electrodes used in patient monitoring; the LL electrode was affixed along the anterior axillary line on the iliac crest [121].)

Simultaneous 120-lead ECGs were recorded during one or more inflations of the balloon catheter. Inflation time varied from 30 seconds to 3 minutes. Data collection was initiated a minimum of 15 s prior to inflation and continued until at least 15 s after balloon deflation, in order to follow the transition between physiological states throughout a complete inflation/deflation cycle. This study includes data for 202 inflations for 94 patients, including 18 inflations performed for comparison with per-fusion images. The 120-lead ECG data were simultaneously recorded at 500 samples/s with Wilson's central terminal as a reference, using a system based on PDP-11/24
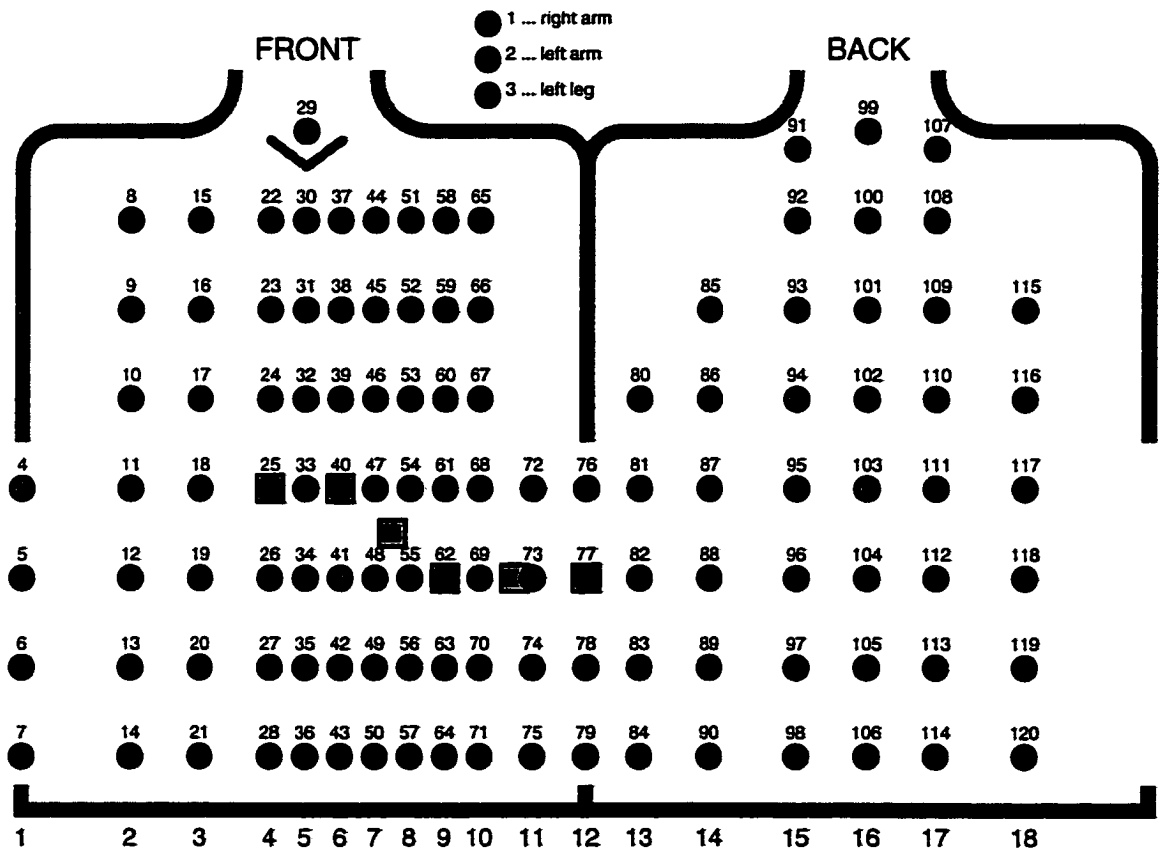
Figure 6.1: Placement of electrodes on the chest for electrocardiographic body-surface potential mapping. Circles mark electrode locations; the row of electrodes 4, ..., 117 was aligned at the level of the fourth intercostal space at the sternum; squares indicate locations of conventional precordial leads V1–V6.

(Digital Equipment Corp., Maynard, MA) computer, with a 12-bit analog-to-digital converter. The data were recorded on magnetic tape and processed off-line on an IBM RS/6000 computer.

The ECG data were signal-averaged in each lead over a multi-second window both pre-inflation (patient at rest) and peak-inflation (immediately prior to balloon deflation). Window lengths varied from 5–25 s and were visually chosen as having a stable QRST complex. All 120 signal-averaged ECG complexes for resting and inflation states were inspected. Poor quality leads were rejected and manual correction of the onsets and offsets of the P wave, the QRS complex, and the T wave was performed. The 117 electrode locations correspond to node locations on the tesselated torso model and are displayed as filled circles in Fig. A.1 of Appendix A. Three-dimensional interpolation was used [116] to generate potentials at the complete set of 352 nodes from the acceptable lead values. Further interpolation was used to calculate mean potential values for the 700 triangles of the torso-heart model's torso surface, as input for the inverse procedure. The same realistic model of the human torso, in which the torso was assumed to be a homogeneous volume conductor, was used for all patients.

An initial estimate of epicardial potential distributions was computed using the triangle-to-triangle torso-heart system and inverse solution with zero-order Tikhonov regularization. The scaled variant of the Slope Estimation Method was used to determine the optimal regularization parameter. Subsequent to this, the composite regional constraint was applied—CRCM (with no temporal component) for processing integral difference maps, and CRC3 (with temporal component to extrema removal section and temporal smoothing)—for time sequences of measured torso-surface potentials.

Inverse-recovered epicardial potential distributions are displayed as isopotential maps on a polar projection of the epicardial surface. Fig. A.2 of Appendix A depicts the 360 triangles which tesselate the ventricular surface; generalized locations of the LAD, RCA and LCx are shown superimposed on the display.

Myocardial perfusion imaging: SPECT imaging was performed using a single-head rotating gamma camera (General Electric 3200 Starcam) with a low-energy, high-resolution collimator. A typical 180° imaging protocol was utilized, acquiring 32 images (64×64 matrix) over a 180° arc extending from 45° right anterior oblique to 45° left posterior oblique with acquisition time of 40 s per projection. Tomographic slices were reconstructed by standard filtered back projection according to the GE CEqual protocol and "raw" volume-weighted polar ("bull's-eye") maps corresponding to rest and inflation were generated. Sestamibi polar difference maps were derived by subtracting the rest map from the inflation map to define the reversible ischemic defect produced by balloon occlusion. Isocontours joining points of the left ventricle with equal difference peak counts were generated. These polar difference maps feature a polar projection of the left ventricle, with the apex at the center, the anterior wall on top, the inferior wall on the bottom, the septum to the left, and the lateral wall to the right.

Angiographic analysis: Angiographic analysis was performed for all study partici-pants. Coronary cineangiograms obtained during the pre-PTCA diagnostic catheter-ization and the PTCA were assessed visually by an experienced interventional cardi-ologist, who was blinded to the results of the electrocardiographic mapping and the sestamibi imaging. Vessel-dilated, pre- and post-PTCA % diameter stenosis, lesion location, and the presence of angiographically visible collaterals were assessed for all patients. The dilated vessel and the lesion location (proximal, mid, or distal) were determined according to the Coronary Artery Surgery Study coronary artery nomen-clature [129]. Angiographically visible collaterals were assessed as being either present or absent from the pre-PTCA diagnostic cineangiogram, and no attempt was made to quantify recruitable collaterals during PTCA. When faint, partial, or complete an-giographic filling of the distal PTCA vessel occurred from ipsilateral or contralateral injection, collaterals were considered to be present; otherwise they were considered absent.

Analysis: The QRS-integral was calculated as a time-integral of instantaneous potential values from the onset to the offset of the QRS complex. The ST-segment integral was similarly calculated over 3/8 of the interval from the J point to the T-wave offset. For each patient, the QRS-integral and ST-integral values for resting maps were subtracted from the corresponding peak-inflation maps. Resulting potentials were in units of microvolt-seconds (μVs). Mean maps were computed for occlusions of each artery. A second set of mean maps was constructed after each individual integral map was normalized. These "normalized" maps allowed all distributions to make an equal contribution to the mean, regardless of the size of the potential changes. Epicardial images were computed for each of these mean difference maps.

Individual ST-integral difference maps for each inflation were converted to epicardial images. Correlation coefficients were calculated for both torso and epicardial distributions to determine the similarity of each map to the mean maps for each of the arteries. Inverse-recovered epicardial potential distributions for each instant in the time sequence from 10 ms before QRS-complex onset to 10 ms after T-wave offset were computed for both resting and peak-inflation data. Electrograms for both resting and peak-inflation maps were displayed for the site which corresponded to the location of the global maximum on the ST-integral difference map.

For the purposes of analysis of radionuclide images, the primary ischemic zone was defined as the region on the perfusion-image map demonstrating a positive change with inflation. For comparison with electrocardiographic images, values corresponding to the locations of the 360 ventricular-surface triangles were extracted. The location of the ischemia was quantified by the center of mass of the positive area of the perfusion difference map. The location of the ischemic zone by epicardial potential imaging was quantified in the same manner, with the center of mass defined as

$$x_c = \frac{\sum_{i=1}^{n} \omega_i x_i}{\sum_{i=1}^{n} \omega_i}; \quad y_c = \frac{\sum_{i=1}^{n} \omega_i y_i}{\sum_{i=1}^{n} \omega_i} \tag{6.1}$$

where $n = 360$, the number of triangles on the ventricular surface, (x_i, y_i) is the location of the triangle centroid on the polar projection of the surface, with $(0,0)$ at the apex, and ω_i are weights defined as the product of the positive value at Δ_i and

the area of Δ_i in the 3D projection.

6.3 Results

PTCA database study: Mean difference maps—depicting difference between body-surface potential distributions at peak inflation and at rest—were calculated for ST and QRS integrals, for 76 inflations in the LAD, 77 inflations in the RCA, and 49 inflations in the LCx. A second set of mean difference maps was calculated from normalized individual difference maps, to allow each distribution the same weight, disregarding the size of changes. The corresponding inverse-recovered epicardial potential images were calculated from each of these mean distributions. All mean difference maps for ST integral are shown in Fig. 6.2.

Characteristics of the mean torso-surface maps for each artery (Fig. 6.2, upper two rows) are similar to those found by others [98, 141]. For LAD occlusion, there is an anterior maximum in the precordial area, with negative values on the posterior torso. For RCA occlusion, the distribution is characterized by an inferior maximum and superior minimum. The maximum is located further to the right in the "normalized" map. For LCx occlusion, there is a large negative region on the anterior torso and positive potentials on the back, with the maximum on the left side. Distributions for the mean difference maps of QRS integral were similar.

The epicardial potential images of the ST-integral mean difference maps (Fig. 6.2, bottom two rows) showed multiple positive extrema for occlusions of each of the arteries. The extrema were located in areas perfused by different branches of the respective arteries. The mean maps for occlusions of the LCx show an area of positive potentials on the left free wall, extending anteriorly from the basal third to the mid third of the wall. At the obtuse margin, and more posterior locations, the positive area extends from base to apex. The maximum is located within the middle third of the obtuse margin. In addition, a local maximum is seen in the middle third of the left posterior surface. This second maximum is not as apparent in the "normalized" map.
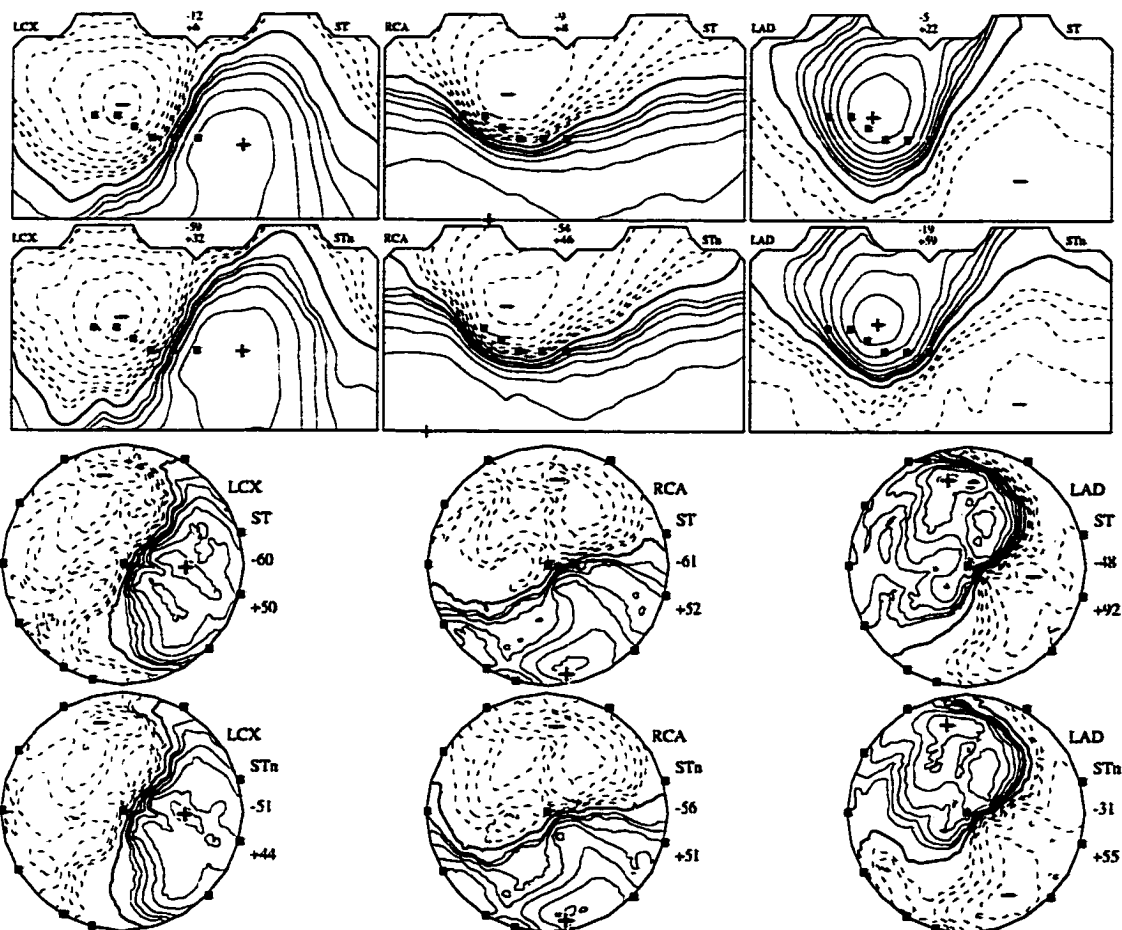
Figure 6.2: Body-surface and epicardial maps of mean differences between ST-integral distributions at "peak-inflation" and "rest" states. The upper two rows show torso-surface distributions of means (top row) and "normalized" means (second row) for three different arteries (LCx, RCA, LAD). The occluded artery is identified in the upper left corner, the maximum and minimum values in the middle, and each map is designated as either ST or STn ("normalized"). The bottom two rows show corresponding inverse-recovered maps on the "bull's-eye" projection of the epicardial surface; all information is printed to the right of each map. All ST-integral values are in units of μVs, and contours are plotted on a logarithmic scale.

These maxima are located in regions perfused by the obtuse marginal and posterior branches of the LCx artery.

Mean epicardial ST-integral images for occlusions of the RCA have a positive region on the posterior surface, extending from base to apex. A maximum is located at the base of the ventricle, near the posterior interventricular groove. A local maximum can be seen on the "normalized" map in the apical third near the groove. There is evidence of other local extrema along the base, between the posterior groove and the acute marginal. These maxima are located in regions perfused by the acute marginal branches and the posterior descending artery. The overlap of positive regions on the posterior epicardial surface within LCx and RCA distributions can be explained by the large diversity in coronary circulation in this region. Ninety percent of the time [82] the posterior descending artery arises from the RCA, but it may extend from the LCx as well. The portion of the left posterior ventricular surface perfused by the RCA can also vary, with the RCA extending as far as the obtuse margin in some cases [102].

Mean ST-integral difference maps on the epicardial surface for occlusions of the LAD have positive potentials extending onto the right and left anterior surfaces. Near the apex, this positive region extends somewhat posteriorly. The maximum is found in the basal third, close to the anterior interventricular groove. A local maximum appears in the middle third of the left anterior ventricular surface. Another local extreme can be seen posterior to the apex, although it is not as apparent on the "normalized" image. These maxima are located in areas perfused, respectively, by the right-ventricular and septal perforating branches of the LAD, the diagonal branches, and the distal branch which typically extends past the apex and into the posterior interventricular groove.

The correlations between each individual inflation's ST- and QRS-integral difference maps and templates consisting of mean difference maps for each groups of patients (LAD, RCA and LCx) were computed for both body-surface and epicardial maps. The number of cases where an integral map for a specific artery most highly

Table 6.2:
Correlation of individual ST-integral and QRS-integral difference maps with mean maps for each diagnostic group (LAD, RCA and LCx ischemia)

Occluded Artery	Correlated Artery	Epicardial Surface				Torso Surface			
		∫ST		∫QRS		∫ST		∫QRS	
		Mean	Norm	Mean	Norm	Mean	Norm	Mean	Norm
LAD	LAD	71	71	60	61	69	71	61	61
	RCA	0	0	10	12	0	0	9	10
	LCx	5	5	6	3	7	5	6	5
RCA	LAD	5	4	19	14	6	5	18	19
	RCA	61	62	45	50	62	63	44	46
	LCx	11	11	13	13	9	9	15	12
LCx	LAD	1	1	6	5	1	1	5	5
	RCA	9	9	10	12	8	9	11	13
	LCx	39	39	33	32	40	39	33	31

∫ST, ST-integral difference maps; ∫QRS, QRS-integral difference maps; Mean, mean integral difference maps; Norm, "normalized" mean integral difference maps; LAD, left anterior descending coronary artery; RCA, right coronary artery; LCx, left circumflex coronary artery

correlated with each of the mean integral difference maps is given, for both torso and epicardial distributions, in Table 6.2.

There were no significant differences in the number of correlations between torso and epicardial surface maps. For the ST integral, the correlation of a map recorded during the individual inflation of an artery with that artery's mean map was the highest in over 93% of cases for LAD, and 80% of cases for both RCA and LCx. Lower values of correlations for the RCA and LCx are a result of variations in coronary circulation, which cause overlapping of perfusion beds of the LCx and RCA. ST-integral matches were higher than those for QRS integral.

Inverse-recovered epicardial potentials for individual ST-integral difference maps were plotted for each inflation studied. (Maps for the 49 LCx inflations are in Fig. 6.3,

for the 77 RCA inflations in Fig. 6.5, and for the 76 LAD inflations in Fig. 6.7.) The site of the maximum positive ST-integral elevation was determined (marked as "+" sign on each epicardial map), and the electrogram for this site was plotted for the "rest" state, the "peak-inflation" state, and the difference between them (for LCx in Fig. 6.4, for RCA in Fig. 6.6, and for LAD in Fig. 6.8). If maps and electrograms in Figs. 6.3–6.8 are read in sequence from top to bottom and left to right, multiple inflations for the same patient come in sequence; the order indicates the sequence in which the inflations were performed. The length of each inflation and the timing between inflations varied.

Epicardial potential images are relatively free of spurious islands of potentials of unexpected sign. Contour lines are quite smooth, even for low integral values. The electrogram traces exhibited little noise, even for segments near the zero-line.

The positive deflection in the ST-integral difference map is related to the area of ischemia. For the LCx occlusions (Fig. 6.3), in general, the positive region is positioned somewhere on the left free wall, as depicted in the mean integral difference map (Fig. 6.2). For several cases, the positive region extended further onto the posterior ventricular surface and the distribution correlated best with the RCA mean map (Fig. 6.2). This occurred for patient 3228 (Fig. 6.3, column 3, rows 2 and 3), where the CC for LCx is smaller than that for RCA. Angiographic analysis determined that the LCx dominated the perfusion of the posterior aspect of ventricles in this case [97].

The maps for RCA occlusions (Fig. 6.5) have a tendency, overall, to exhibit characteristics of the mean map (Fig. 6.2), with positive zones on the inferior ventricular surface. As with LCx occlusions, there is variety in amplitudes and locations of maxima. The major spatial differences are between apical and basal locations, both of which were found in mean maps.

The maps for LAD occlusions (Fig. 6.7) also follow the characteristics of the corresponding mean map (Fig. 6.2), with a positive anterior ventricular region. Sometimes one or other of the specific areas is missing or diminished. For some cases, this may
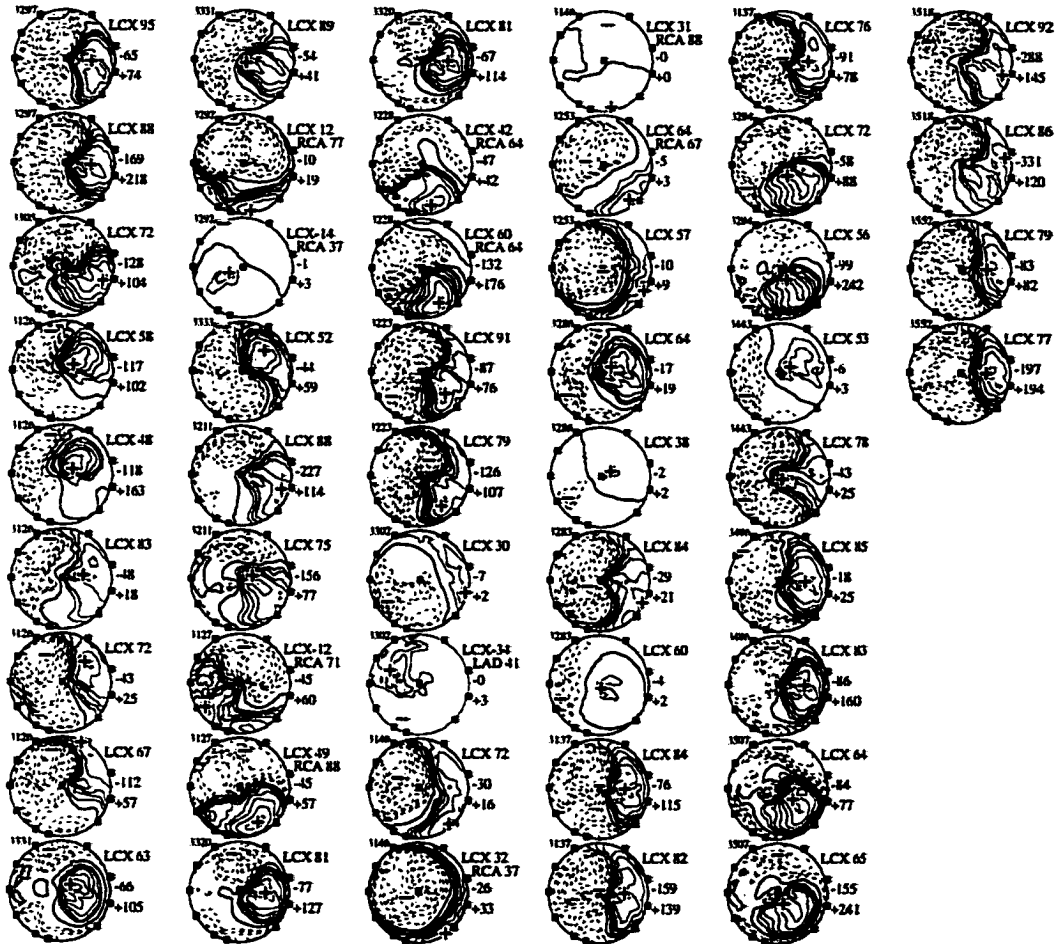
Figure 6.3: Epicardial potential images of ST-integral difference maps ("peak-inflation" minus "rest") for 49 occlusions of the LCx coronary artery. The number at upper left identifies the patient, to the upper right is indicated the occluded artery and % correlation with that artery's normalized mean difference map. If the latter was not the mean map with the largest CC, the artery that correlated best is printed below, along with the % correlation. Minimum and maximum values are in μVs and contours are plotted on a logarithmic scale.
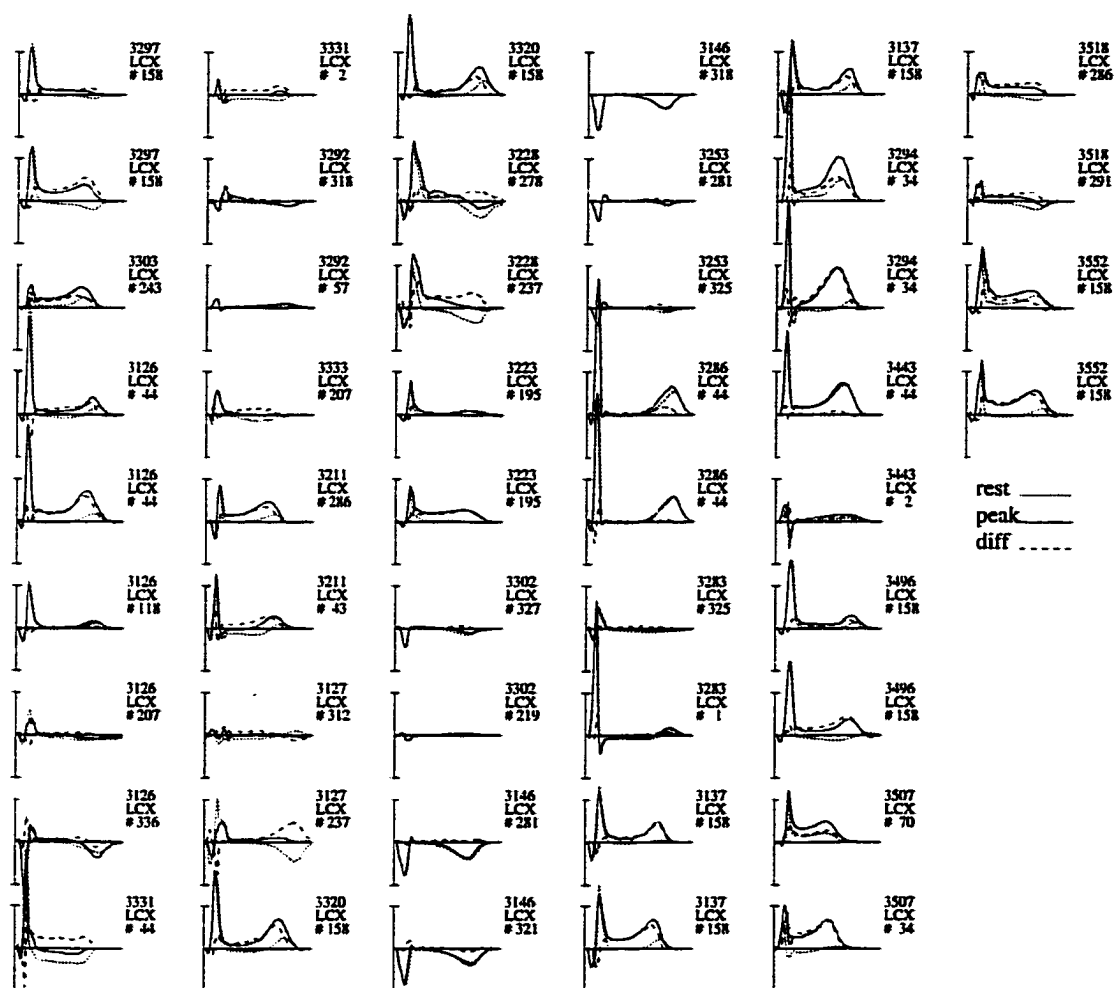
Figure 6.4: Epicardial surface electrograms for "rest" and "peak-inflation" states at the site of maximum ST-integral elevation for 49 LCx occlusions. The scale is 0–500 ms on the abscissa and ±5 mV on the ordinate; rest, inverse-recovered electrogram calculated from preinflation torso-surface recording used for baseline; peak, inverse-recovered electrogram calculated from torso-surface recording at peak inflation (just prior to balloon deflation); diff, difference between "rest" and "peak" electrograms. Next to each frame is the patient identification number, the artery of inflation, and the triangle number giving the spatial localization of the electrogram. For the location of each triangle, see Appendix A, Fig. A.3; it matches the position of the "+" sign on the corresponding epicardial image in Fig. 6.3.
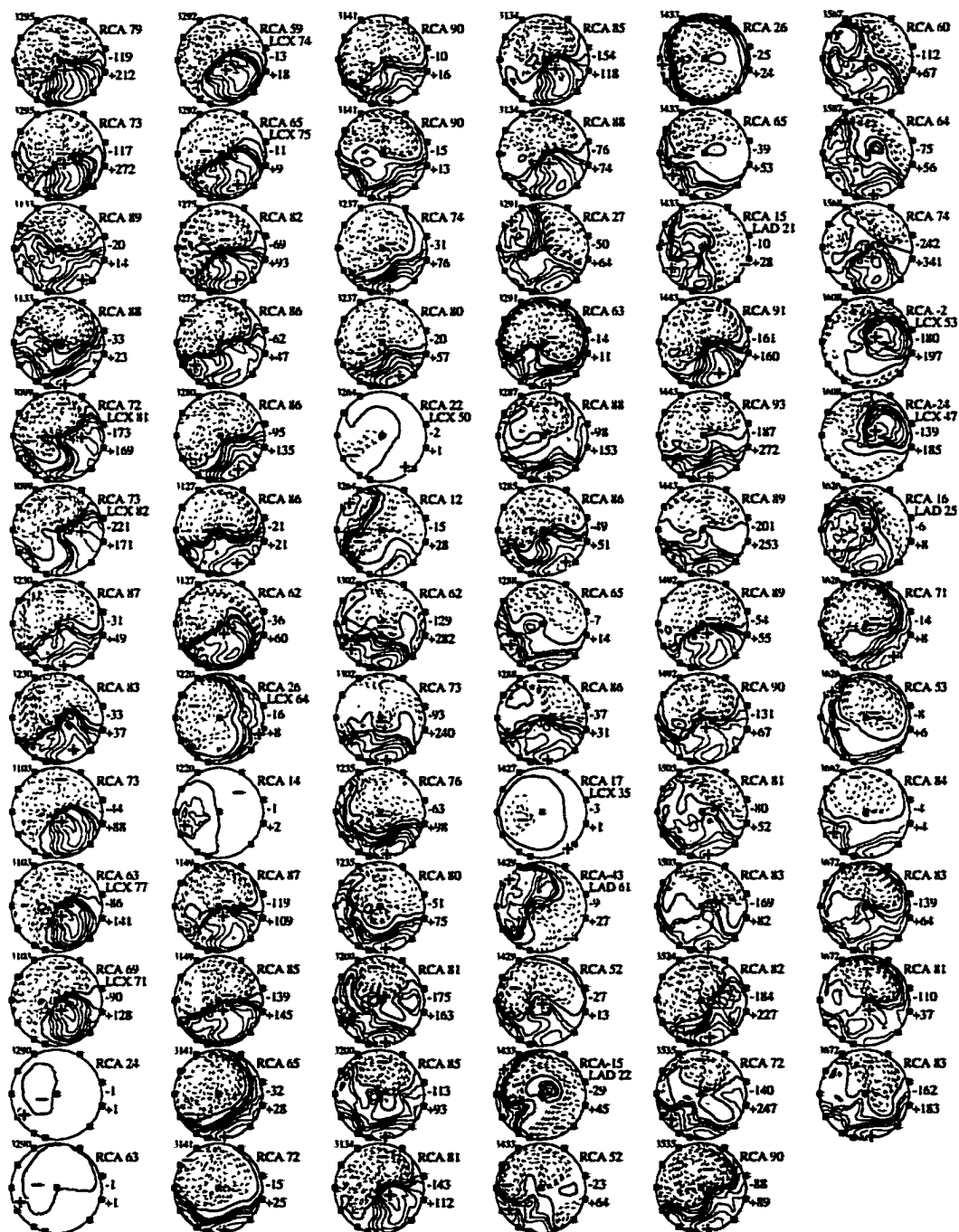
Figure 6.5: Epicardial potential images of ST-integral difference maps ("peak-inflation" minus "rest") for 77 occlusions of the RCA. Format as in Fig. 6.3.
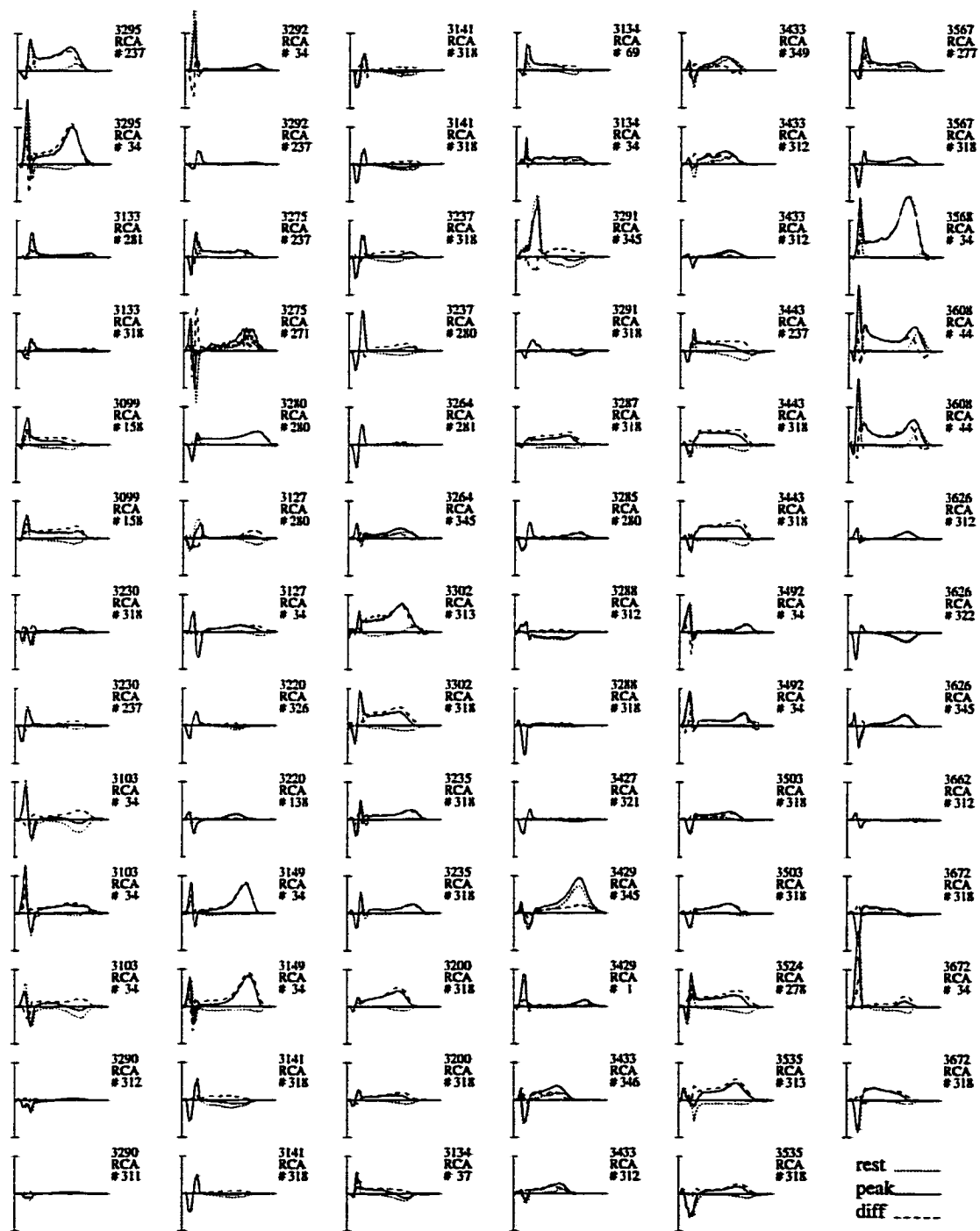
Figure 6.6: Epicardial surface electrograms for "rest" and "peak-inflation" states at site of maximum ST-integral elevation for 77 RCA occlusions. Format as in Fig. 6.4.
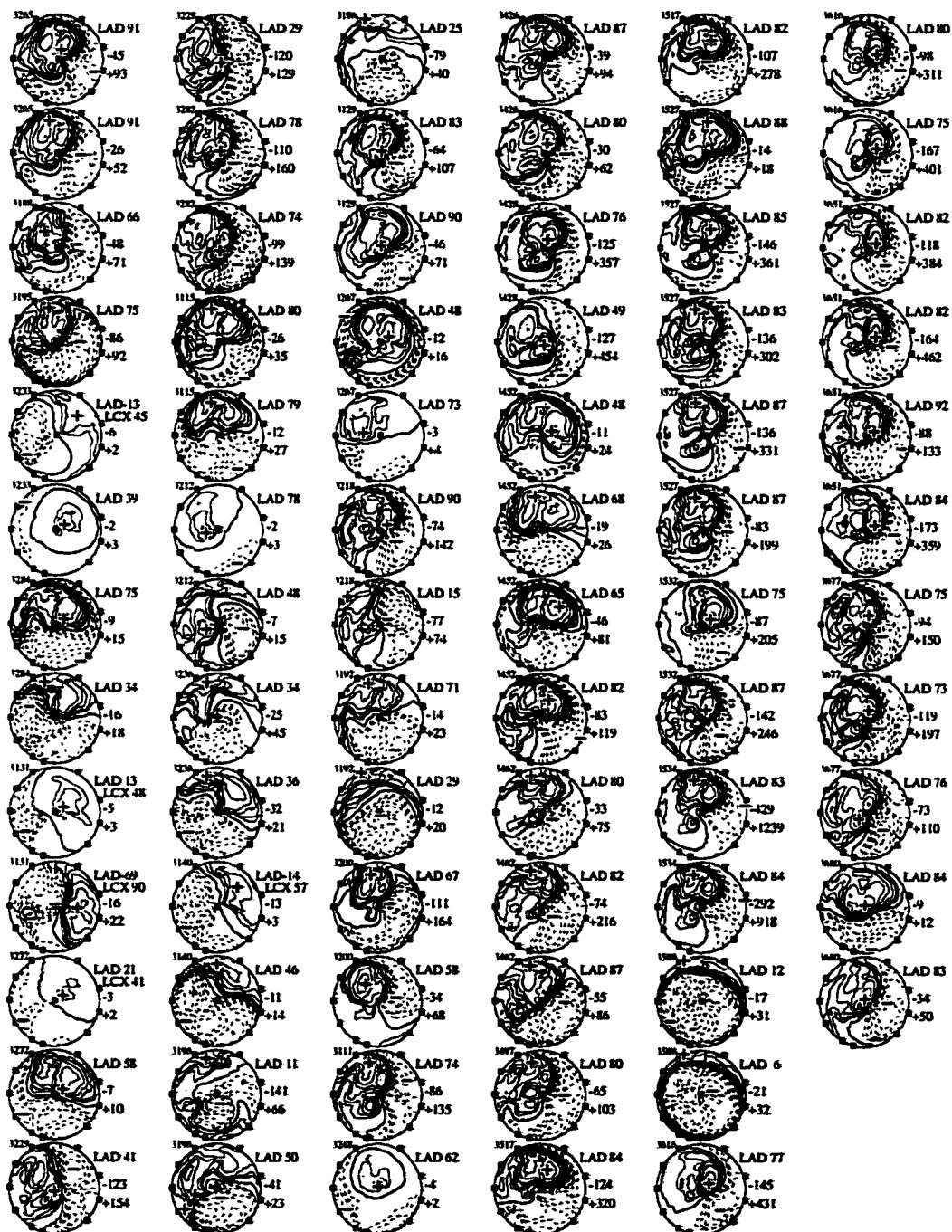
Figure 6.7: Epicardial potential images of ST-integral difference maps ("peak" minus "rest") for 76 occlusions of the LAD. Format as in Fig. 6.3.
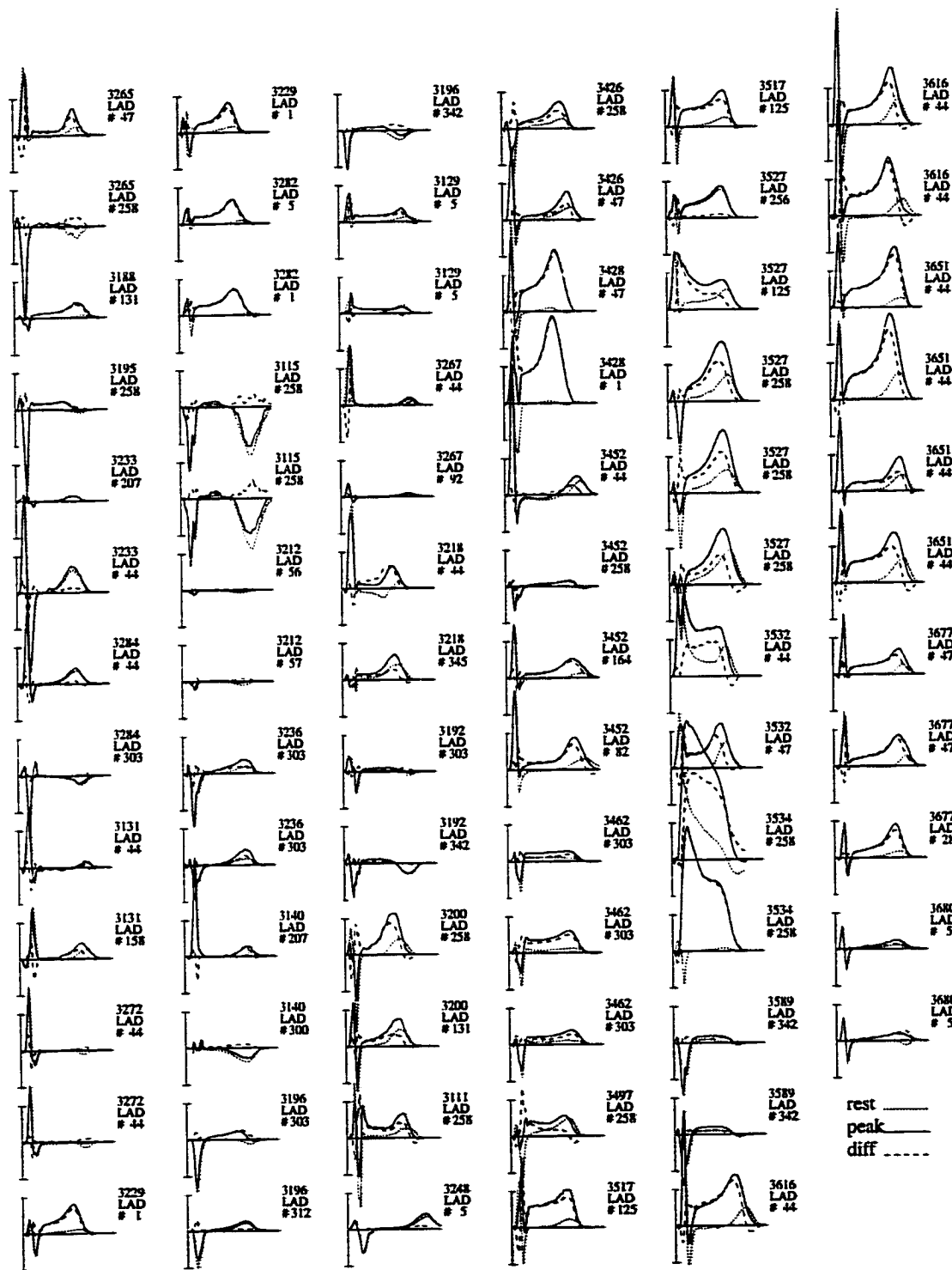
Figure 6.8: Epicardial surface electrograms for "rest" and "peak-inflation" states at site of maximum ST-integral elevation for 76 LAD occlusions. Format as in Fig. 6.4.

be due to the location of the lesion, in others the presence of collateral circulation may be responsible for the results. Epicardial images for patient 3229 (Fig. 6.7, column 1, row 13, and column 2, row 1) are missing the positive region normally seen on the anterior left ventricle with a proximal lesion. Angiographic analysis revealed that the second diagonal branch of the LAD was completely occluded and that this area was now perfused by collaterals of the LCx [97]. An opposite effect was seen for the proximal occlusion of the LAD in patient 3616 (Fig. 6.7, column 6, rows 1 and 2), where the left anterior positive region exists, but those around the anterior interventricular groove and right ventricle are diminished. Collateral circulation was identified in this patient, and it may be responsible for perfusion of this area.

Electrograms recovered at the site of peak ST-integral map differences (Figs. 6.4, 6.6 and 6.8) extract information about changes during the entire QRST complex. Resting and peak-inflation electrograms were aligned by the globally defined (from Frank orthogonal leads) QRS onset. Thus, when interpreting differences, care must be taken that misalignment is not a factor. Despite this caveat, there are several cases where the imaging process has created complexes for "rest" and "peak-inflation" states which are virtually identical. One example is the LCx inflation for patient 3146 (Fig. 6.4, column 4, row 1). The corresponding integral map (Fig. 6.3, column 4, row 1) confirms this lack of change between states. For other inflations, major elevations are visible. Electrograms of the "peak-inflation" state of the RCA occlusion for patient 3568 (Fig. 6.6, column 6, row 3) exhibit an elevated ST segment, and increased R and T waves. There is no change in the initial small Q wave, upstroke of the R wave, or the timing of the J point. However, a shortening of the T-wave offset is visible. These changes are similar to results for epicardial coronary electrograms and ECG measurements, and can be explained by the flow of injury current due to ischemic cells' changes in resting potential and action potential.

Major changes were also seen in electrograms for the two inflations of the LAD for patient 3616 (Fig. 6.8, column 6, rows 1 and 2). The first inflation lasted for 69 s and the second for 108 s. ST-integral map's maximum amplitude rose from 311 μV to

401 μV (Fig. 6.7, column 6, rows 1 and 2). Both peak electrograms have elevated ST segments and T waves, and an elevated (but diminished in relative amplitude) S wave. The downslope of the T wave is shaped differently, with offset earlier than for "rest" state traces. There are no changes to the large R wave. Changes were exacerbated with increased length of recording. Differences during the T-wave interval varied more between inflations due to changes in the shape of the resting T wave. Differences in ST-segment elevation were predominantly near the J point. Differences with duration of inflation were also seen for two inflations of the LCx, lasting one and two minutes, respectively, for patient 3297 (Fig. 6.4, column 1, rows 1 and 2). Two equal-length inflations of the LCx for patient 3320 (Fig. 6.4, column 2, row 9, and column 3, row 1) show consistent "rest" to "peak inflation" changes, with differences over the different inflations.

Variations in coronary circulation, lesion location within the artery, presence of collaterals, duration of inflation, and time since previous inflation may have physiological effects resulting in the differences described here. Noise in body-surface potential data and errors as a result of the inverse procedure may also play a role.

Perfusion-imaging study: Eighteen of the patients in the preceding group were enrolled in the perfusion-imaging study. Angiographic analysis was performed to determine affected artery, location of the lesion within the artery, and the presence of collateral circulation. Results of the angiographic analysis are presented in Table 6.3. There were 5 of the 18 cases where collaterals were identified. No lesions were located distally. Lesion within the RCA were all classified as mid, whereas LCx and LAD lesions were a combination of mid and proximal.

All inflations were for a one-minute duration. Perfusion images of myocardial ischemia during PTCA were obtained using the radiopharmaceutical perfusion agent ^{99m}Tc sestamibi, both near the time of the inflation and 24 hours later. QRS- and ST-integral difference maps ("peak-inflation" minus "rest") for this inflation, as well as maps displaying differences in radionuclide perfusion ("near-peak-inflation" minus "rest") are plotted in Fig. 6.9. Perfusion images are in units of percent count dif-

Table 6.3:

Angiographic characteristics of perfusion-imaging study group

#	Patient ID	PTCA Vessel	Lesion Location	Collaterals
1	3534	LAD	prox	no
2	3428	LAD	mid	no
3	3677	LAD	mid	no
4	3426	LAD	prox	no
5	3497	LAD	prox	no
6	3680	LAD	prox	yes
7	3616	LAD	prox	yes
1	3507	LCx	mid	no
2	3518	LCx	prox	no
1	3568	RCA	mid	no
2	3524	RCA	mid	no
3	3535	RCA	mid	yes
4	3567	RCA	mid	no
5	3503	RCA	mid	no
6	3662	RCA	mid	no
7	3672	RCA	mid	no
8	3626	RCA	mid	yes
9	3429	RCA	mid	yes

LAD, left anterior descending coronary artery; LCx, left circumflex coronary artery; RCA, right coronary artery; prox, proximal lesion.
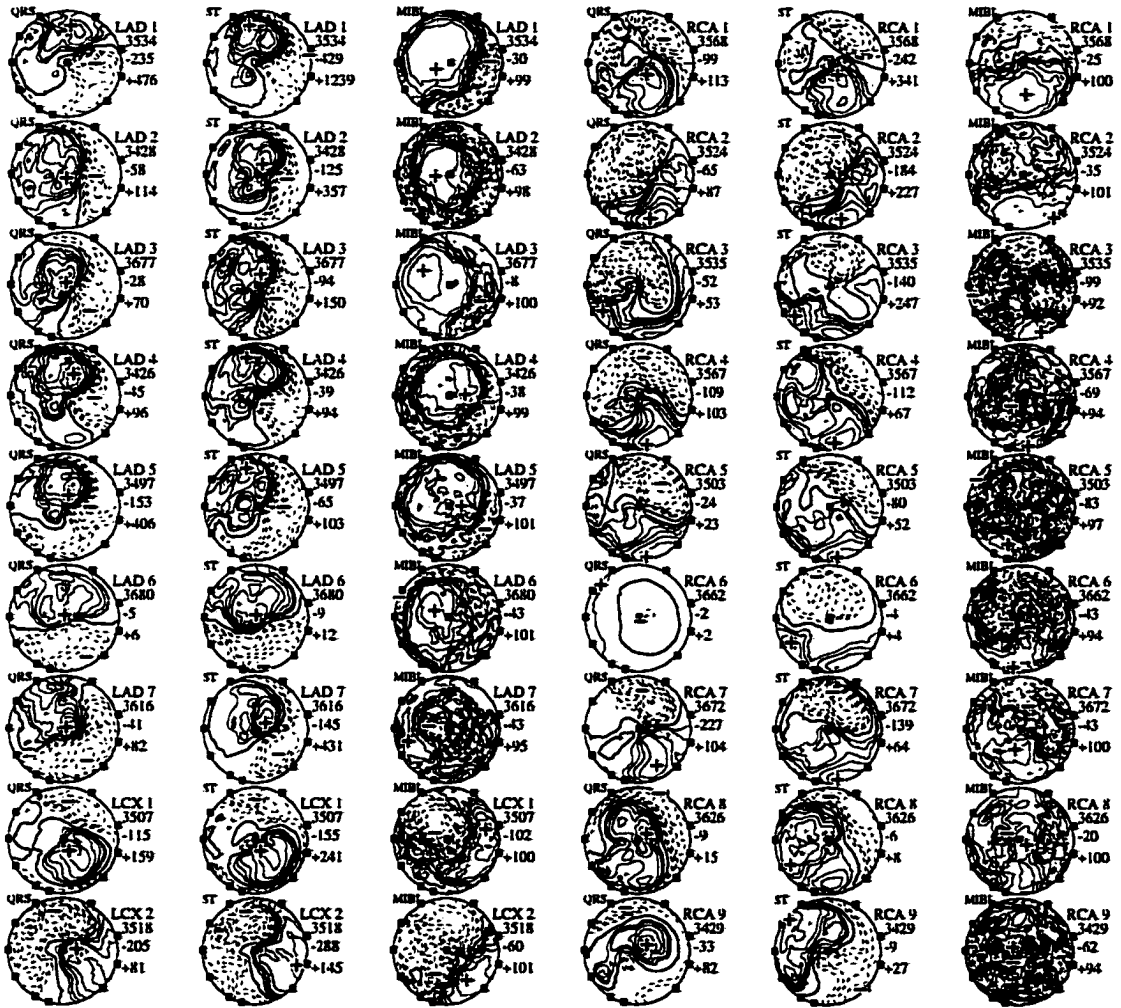
Figure 6.9: Comparison of epicardial "electrophysiological images" and radionuclide perfusion images for patients undergoing PTCA of one of the major coronary arteries. There were 7 cases of LAD occlusion (columns 1-3, rows 1-7), 2 cases of LCx occlusion (columns 1-3, rows 8-9), and 9 cases of RCA occlusion (columns 4-6). Columns, left to right, are inverse-recovered QRS- and ST-integral differences (μVs), and MIBI perfusion images (counts).

ference. Although used here in comparsion with ventricular surface potential maps, the left side of the perfusion maps represents the interventricular septum and not the right ventricle (see Methods). The sestamibi perfusion maps for LAD have large areas of positive values on the anterior left ventricle and the septum. These often extend past the apex. This area corresponds well with that for the electrophysiological images. Inflations of the LCx resulted in images with positive areas on the left free wall and extending onto the left posterior surface, approximating those found for ST-integral differences. RCA maps have positive regions over variable extent of the posterior surface, again resembling results for epicardial electrophysiological images.

The weighted center of mass was calculated for each map to facilitate the comparison of epicardial potential images and sestamibi perfusion images. Comparisons of the location of ischemia identified by QRS- and ST-integral difference images and myocardial perfusion difference images are shown in Fig. 6.10. All patients have good agreement between these diverse location methods. Patients LAD 2 and LAD 3, LCx 1, and RCA 1, all with mid lesions of the vessel, had exceptional similarity of electrophysiological and radionuclide estimates. The QRS-integral estimate for patient RCA 6 was quite removed, but values of differences were very small, and therefore prone to error.

With the exception of patients RCA 8 and RCA 9, where collaterals were present, all positive areas in the ST- and QRS-integral difference maps—indicating the presence of ischemia—were located in regions perfused by the appropriate artery. For LAD inflations, these areas were located on the anterior ventricular surface near the septum, with the location for mid lesions nearer the apex. For both LCx and RCA inflations, positive areas were located on the left free wall, with the mid lesion shifting these areas further towards the apex. Positive areas for inflations of the RCA were generally localized around the posterior interventricular septum; for patient RCA 2, the location of positive area was on the left posterior ventricular surface.

Temporal change study: Three patients were selected for examination of temporal changes during the inflation/deflation cycle – one for each occluded artery. Selection
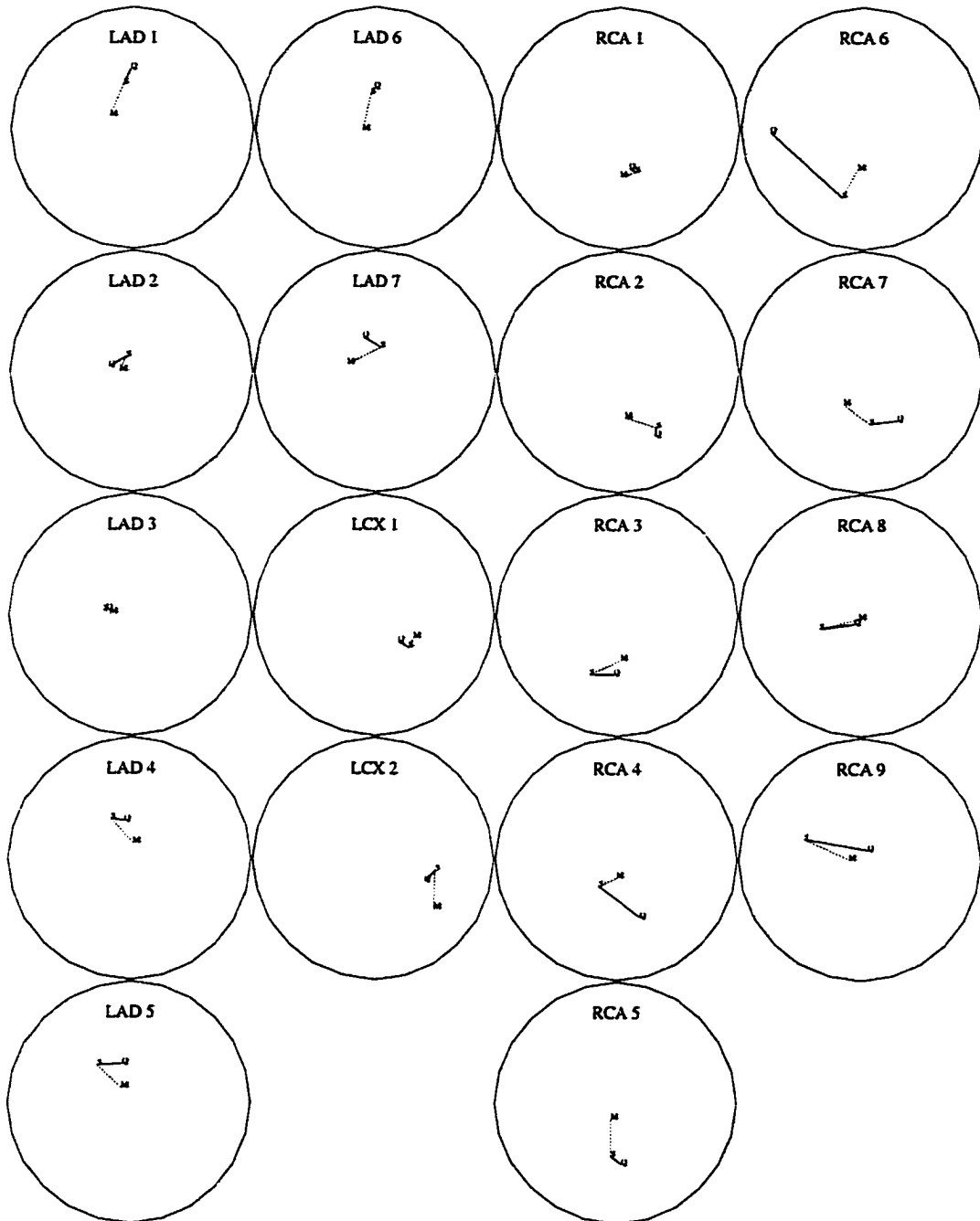
Figure 6.10: Localization of ischemic region by "electrophysiological" imaging and radionuclide perfusion imaging. Locations of ischemic regions identified by inverse-recovered epicardial QRS- and ST-integral difference maps, and those identified by means of ^{99m}Tc sestamibi perfusion imaging are compared for occlusions of the LAD, LCx and RCA coronary arteries. Polar displays are the same as for potential maps, with the apex in the center. M, locus of the center of mass for the area above the threshold count in the perfusion image; S, locus of the center of mass for the positive area in the ST-integral difference map; Q, locus of the center of mass for the positive area in the QRS-integral difference map; loci S and Q are connected by a solid line; loci S and M are connected by a broken line. Identifiers within each display refer to codes from Fig. 6.9.
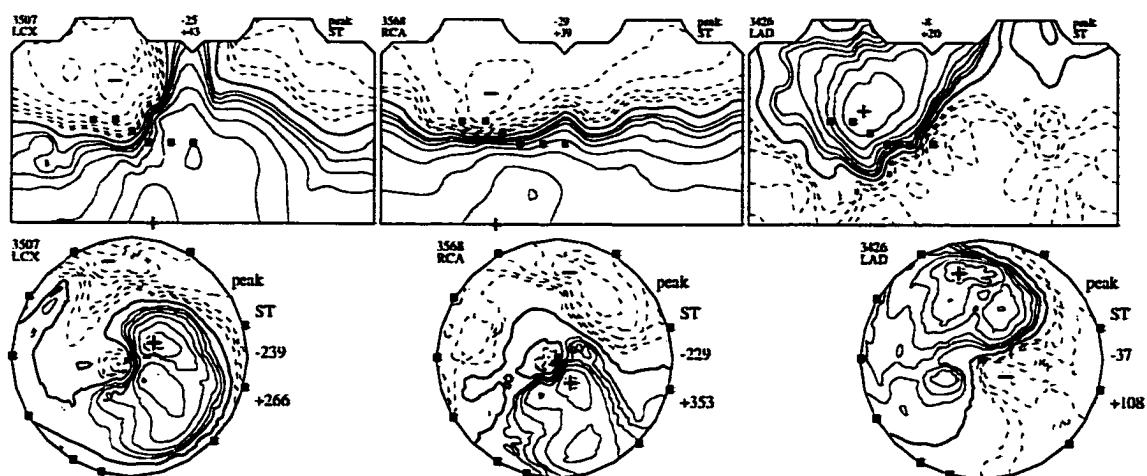
Figure 6.11: Torso-surface and epicardial ST-integral difference maps at peak inflation ("peak-inflation" minus "rest") for patients who underwent balloon inflation of the LCx artery (left column), the RCA (center) and the LAD artery (right). Values are in μVs, contours are plotted on a logarithmic scale.

was based on good quality ECG recordings throughout the cycle and evidence of ischemic changes as seen in ECGs. Signal-averaging windows were set at a 5-s length, starting 15 s before balloon inflation and ending 15 s after inflation terminated. Inflations were 90-s in length for RCA and LCx occlusions, and 120-s length for the LAD occlusion. With this division, there were three resting maps; the first one was chosen as the baseline for comparison of electrograms. Lesions were identified as mid for LCx and RCA, and proximal for LAD. Angiographic analysis for all three patients showed no evidence of collaterals.

Fig. 6.11 shows for each of the three patients ST-integral difference maps ("peak-inflation" minus "rest") on both torso and epicardial surfaces.

A comparison of the torso map in the left column of Fig. 6.11 with the mean ST-integral difference map in the left column of Fig. 6.2 shows that the LCx torso map of patient 3507 has a larger negative area on the superior back. The zero-line passes between precordial leads V3 and V4 instead of between V4 and V5. There is a maximum at the inferior edge, inferior to V4. However, a local maximum is visible near V6 that more closely matches the location of the maximum on the mean map.

The fact that there is a mid lesion in this case may explain discrepancies.

A comparison of RCA torso map of patient 3568 in the middle column of Fig. 6.11 with the mean ST-integral difference map in the left column of Fig. 6.2 shows that locations of maxima match, but there are some changes in the zero line as it passes through the precordial region, between V3 and V4 instead of V5 and V6. The maximum for the LAD map is nearer to V2 then to V3, as in the mean map, and is located more superiorly.

For LCx epicardial map of patient 3507 (Fig. 6.11, left column) the positive region does not extend to the base, in contrast to the mean map in Fig. 6.2. The maximum of the positive region is located on the obtuse margin, but the zone extends more anteriorly. In the RCA map of patient 3568 (Fig. 6.11, middle), the positive region is located on the posterior ventricle with no extension onto the acute margin, as found in the mean map in Fig. 6.2; both maxima are visible, with the near-apical one being the larger. The LAD epicardial map of patient 3426 (Fig. 6.11, right) has the same characteristics as the LAD mean map in Fig. 6.2.

A "bull's-eye" view of electrograms at "rest" and "peak-inflation" states is present for the occlusion of the LCx in Fig. 6.12, for RCA in Fig. 6.13, and for LAD in Fig. 6.14. The asterisk (*) marks the location of the maximum ST-integral difference ("peak-inflation" minus "rest" state). These figures allow one to see comprehensively the changes in electrograms within the ischemic region, as well as changes (or lack of changes) in nearby or distal areas. For all lesions, the amount of elevation in the electrogram increases, moving from the border to more central region of ischemia.

For a more detailed look at changes in cardiac electric signals due to ischemia, the triangle at the site of global maximum of ST-integral changes was selected and both ECGs on the torso surface and epicardial electrograms were plotted, for representative patients of the LCx, RCA, and LAD groups (Figs. 6.15–6.17). Tracings were plotted for a sequence of 5-s windows, starting from the pre-inflation state and continuing throughout inflation and deflation states. To facilitate comparison of evolving signals, a fixed tracing representing the pre-inflation baseline state was copied in every
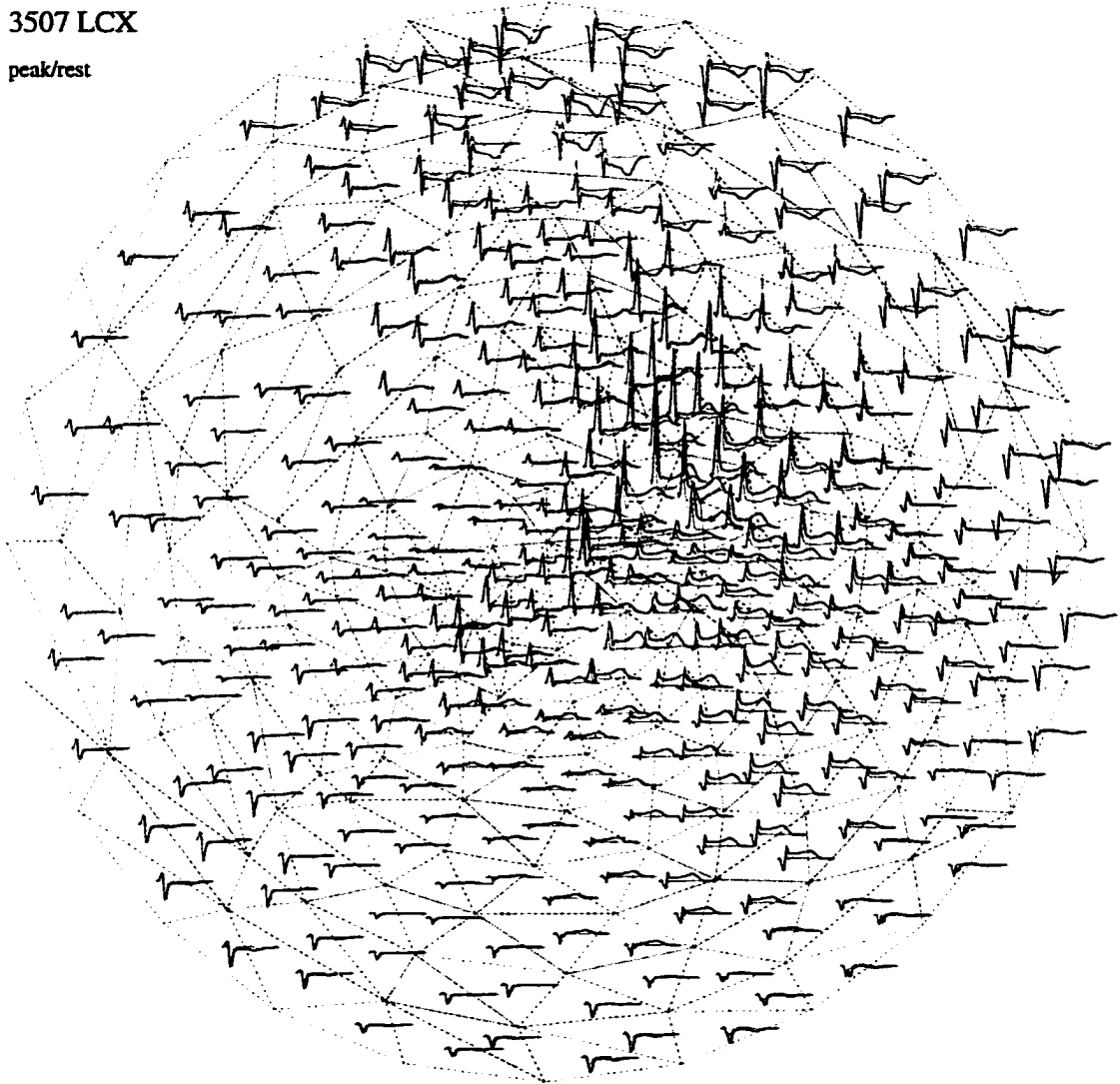
3507 LCX

peak/rest

Figure 6.12: Representative inverse-recovered electrograms on the epicardial surface at "rest" and "peak-inflation" states during a 90-s occlusion of the LCx coronary artery. Each electrogram is associated with one of the 360 triangles of the tesselated epicardial surface; the asterisk (*) marks the location of the maximum difference in the ST integral between "peak-inflation" and "rest" states; electrograms at "peak-inflation" state are drawn as solid lines and those at "rest" are dotted.

3568 RCA

peak/rest

Figure 6.13: Representative inverse-recovered electrograms on the epicardial surface at "rest" and "peak-inflation" states during a 90-s occlusion of the RCA coronary artery. Layout is the same as that in Fig. 6.12.
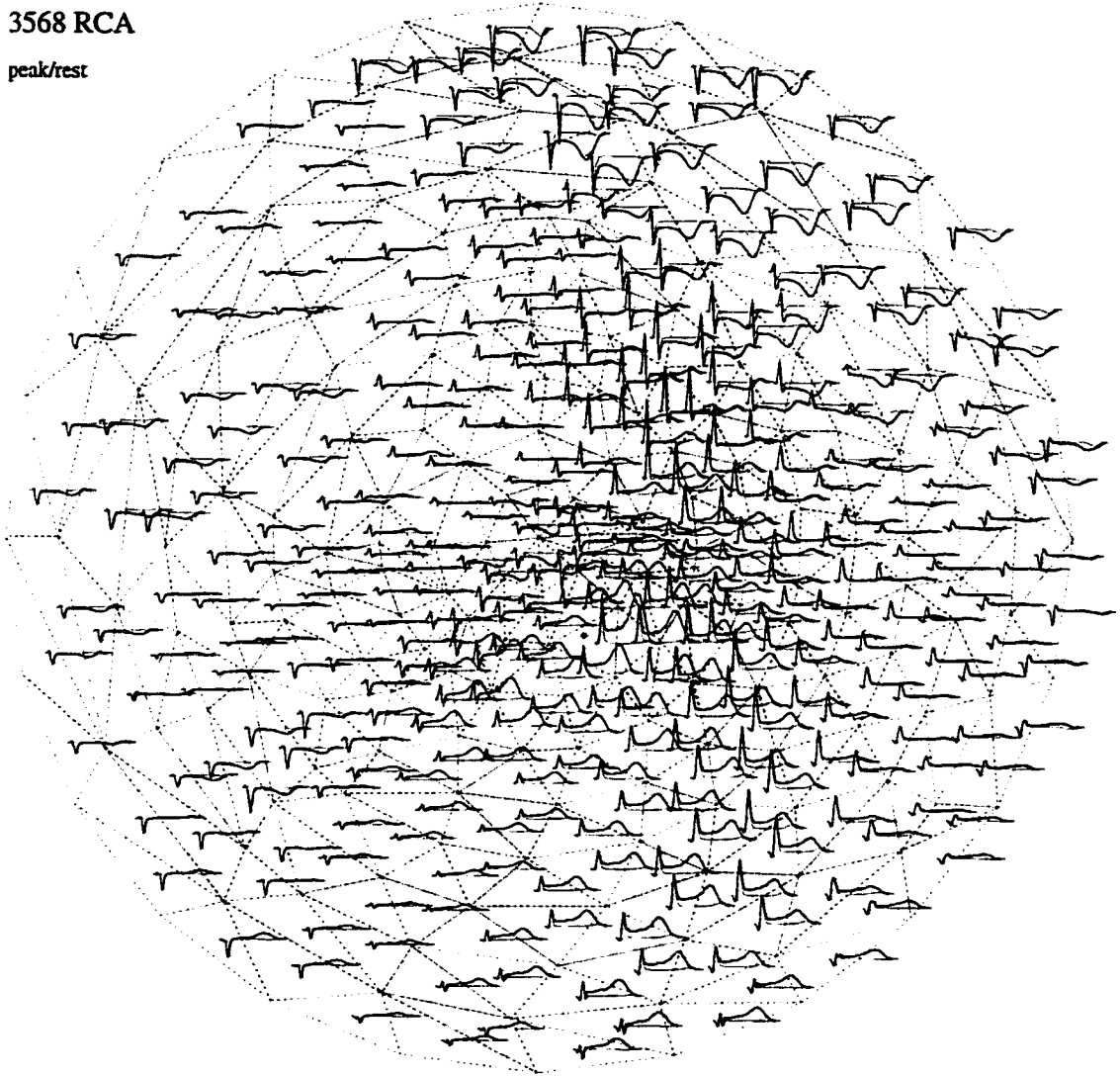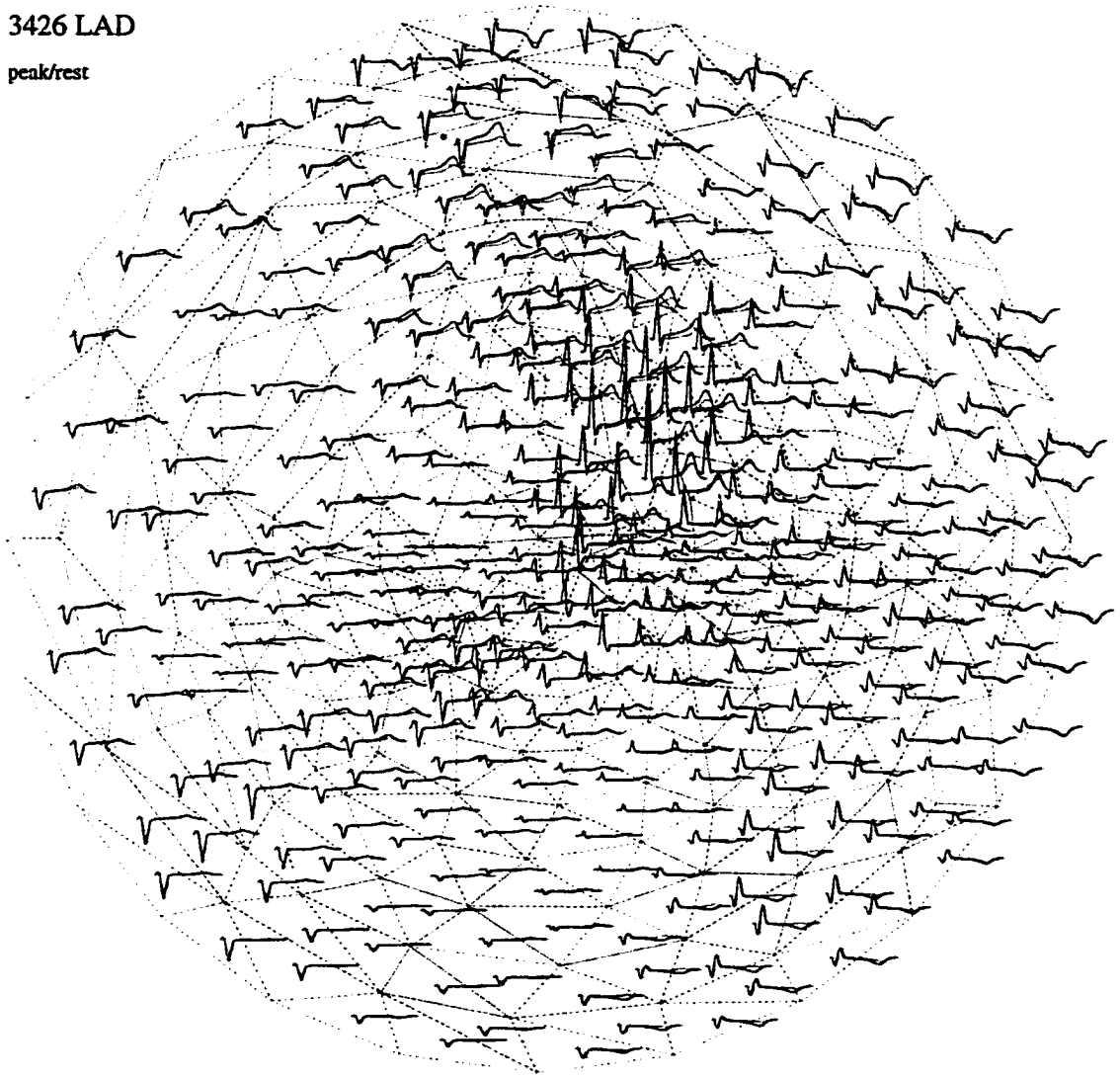
3426 LAD

peak/rest

Figure 6.14: Representative inverse-recovered electrograms on the epicardial surface at "rest" and "peak-inflation" states during a 120-s occlusion of the LAD coronary artery. Layout is the same as that in Fig. 6.12.

window, and a difference between evolving and baseline tracings was plotted as well. The similarity of torso-surface ECGs and epicardial electrograms was noted. Similar changes were evident in both. All changes decreased rapidly with deflation and were near baseline levels by 10–15 s after deflation. An exception was changes noted in the timing of the T-wave offset, which remained fairly constant. It was observed that the peak of the ST-T shifted to the left with duration of inflation, not necessarily accompanied by an increase in height.

Fig. 6.15 shows ECGs and electrograms characteristic of changes due to LCx artery occlusion. (The site of local maximum by precordial lead V6—rather than the actual site of maximum for this patient—was selected for the display, because it was more closely related to the location of the global maximum on the epicardial image.) The baseline trace had a small ST-segment depression. Changes for ECGs and electrograms were similar. After 15–20 s of occlusion, ST-T elevation became evident. The T wave achieved maximal height by 25–30 s, whereas the ST segment, especially near the J point, continued to rise. There was no change in the upstroke of the R wave; however, there were small variations in peak height that appeared to increase after 55–60 s. These changes were easier to see on the electrogram. No change in the offset of the T wave was visible.

Looking at Fig. 6.16, most changes for the RCA occlusion were also visible in both ECG and electrogram traces. Changes in elevation were visible 25–30 s after inflation began. There was a major increase in T-wave height and a sloped change in the ST segment, increasing from J point to T wave. At 30–35 s, the J point was elevated as well. In the ECG, the T wave reached maximum height at 55–60 s. After this time, there were only small changes in T-wave height for the electrogram, with later changes near the J point. There were no changes in R-wave height for the ECG, but on the electrograms they increased from 55–60 s on. Both ECGs and electrograms exhibited a shortened T-wave offset by 30–35 s that increased until 55–60 s.

In Fig. 6.17, ST-T elevation was visible by 25–30 s of inflation in both ECG and electrogram traces for the LAD occlusion. The T wave reached its maximum height
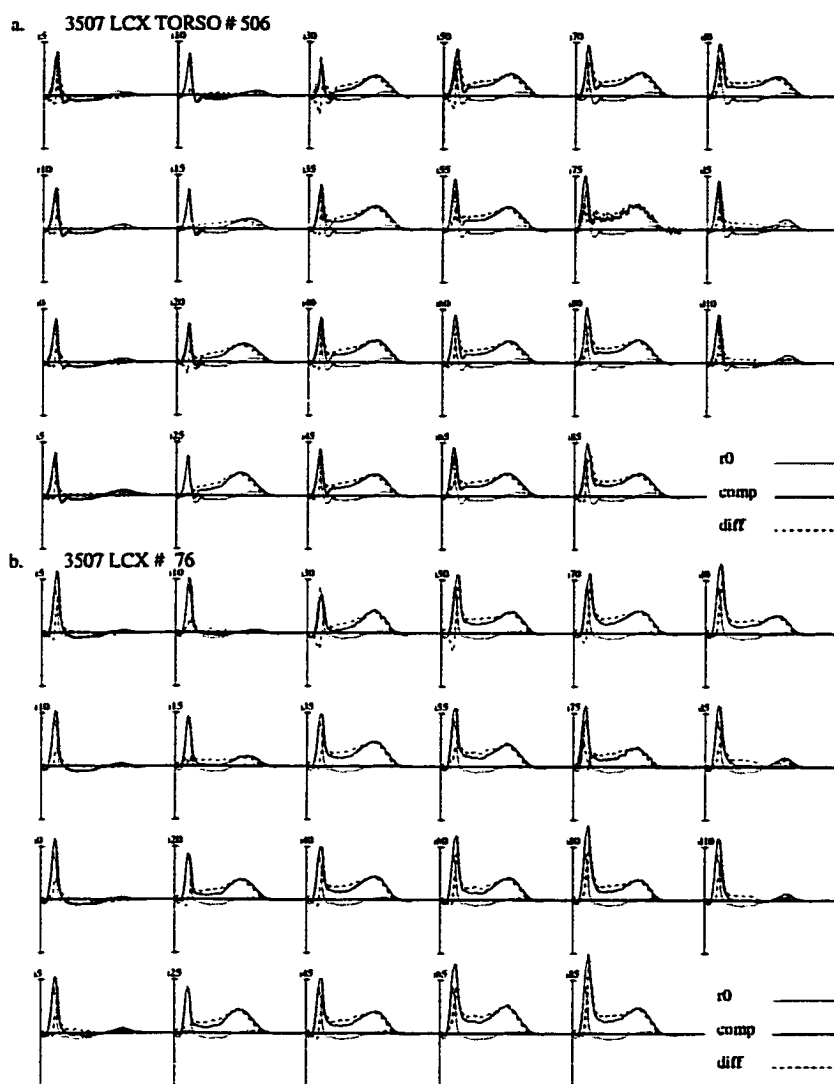
Figure 6.15: Torso-surface electrocardiograms and epicardial electrograms·at sites with the largest ST-integral difference between "peak-inflation" and "rest" states during a 90-s occlusion of LCx coronary artery. Tracings are arranged columnwise for a sequence of 5-s windows (for each of which recordings were signal averaged) with code indicating state (r, rest; i, inflation; d, deflation) and elapsed time in seconds between the commencement of that state and the window's onset; r0, initial tracing at "rest" state; comp, tracing for a given window; diff, difference between "comp" and "r0" tracings; abscissa, time (0–500 ms); ordinate, voltage (±1 mV for ECGs and ±5 mV for electrograms).

Figure 6.16: Torso-surface electrocardiograms and epicardial electrograms at sites with the largest ST-integral difference between "peak-inflation" and "rest" states during a 90-s occlusion of RCA coronary artery. Tracings are arranged columnwise for a sequence of 5-s windows with code indicating state and elapsed time in seconds between the commencement of that state and the window's onset; same layout as in Fig. 6.15.
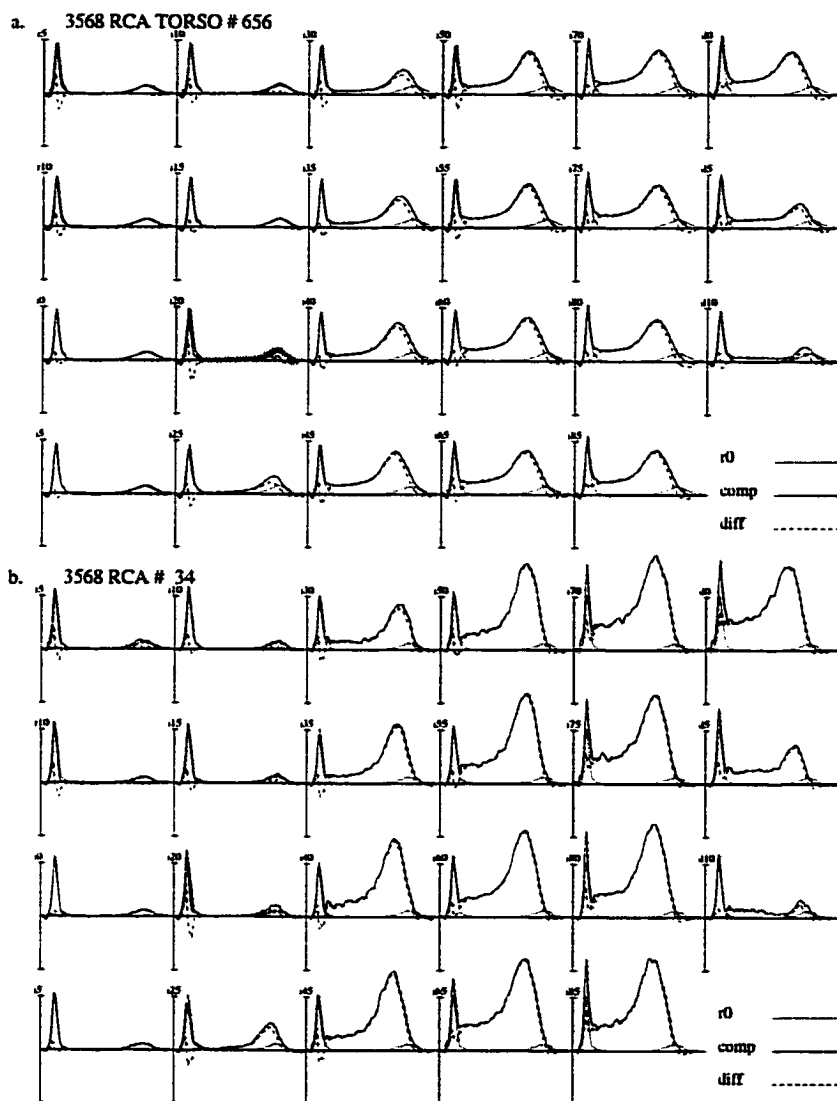
Figure 6.17: Torso-surface electrocardiograms and epicardial electrograms at sites with the largest ST-integral difference between "peak-inflation" and "rest" states during a 120-s occlusion of LAD coronary artery. Tracings are arranged columnwise for a sequence of 5-s windows with code indicating state and elapsed time in seconds between the commencement of that state and the window's onset; same layout as in Fig. 6.15.
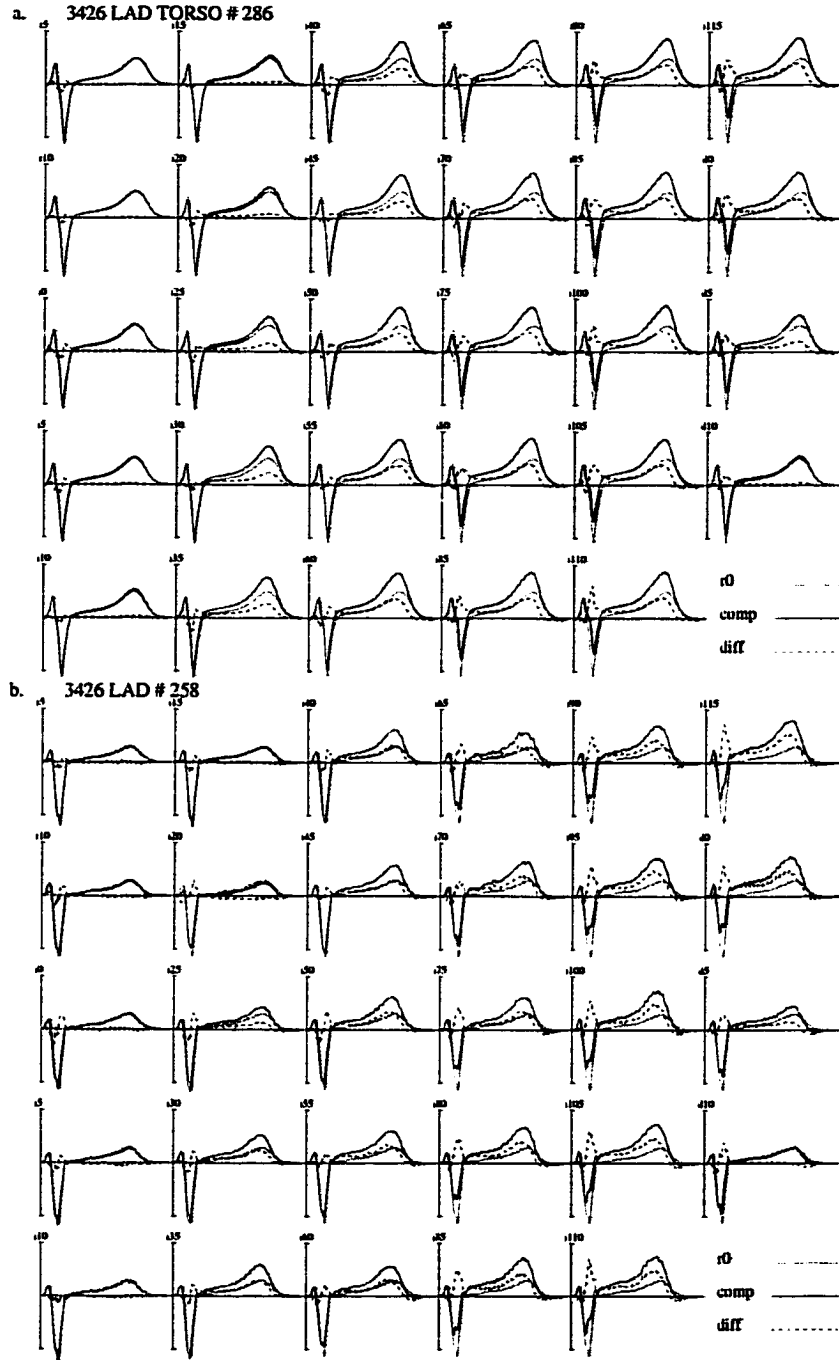
for the ECG by 55–60 s. In the electrogram, it rose continuously until deflation at 120 s. S waves were elevated, but also diminished in relative size at 60–65 s and continued changing until the end of the inflation at 115–120 s. Notching occurred in the electrogram, but not in the ECG signal. The total change in the S wave appeared to match that of the T wave, albeit with different timing. A shortened T-wave offset was apparent in the electrogram by 60–65 s, but not at all in the ECG.

6.4 Discussion

Zero-order Tikhonov regularization was selected for use in clinical application of the noninvasive imaging of epicardial potentials, even though the second-order Tikhonov regularization tended to generate lower relative errors under simulated test conditions. In the presence of interpolation error for 117-lead measured data, the difference in error measures between zero- and second-order regularization was not as significant, since the optimal t-parameters were larger and thus, there was an inherent increase in smoothing. As was shown in Table 5.11, for the test case with measured data, it was not possible to compare t parameters selected by the Slope Estimation Method with those determined by the Combined Residual and Smoothing Operator (CRESO), Zero-Crossing (ZC), and common L-curve methods when using second-order regularization, as these methods failed fairly consistently. On this basis, zero-order Tikhonov regularization was selected for clinical applications. Composite Regional Constraint (CRC) methods were applied to decrease the possibility of there being extraneous areas of incorrect sign in the epicardial image, and to smooth distributions spatially and temporally. The resulting inverse-recovered epicardial potential maps were relatively free of islands of unexpected sign, and along with electrograms, showed sufficient smoothness.

Alterations in ST segments and T waves are the most common and obvious changes in electrocardiographic signals during coronary angioplasty [21, 25, 37, 86, 87, 88, 138,

141, 146, 160]. Therefore, changes in these parameters were evaluated for the inverse-recovered epicardial images.

Epicardial ST-integral difference maps of individual patients matched distributions of corresponding mean maps to a large extent. Correlation results (Table 6.2) indicate that the epicardial images do not add or detract from classification ability, as body-surface maps had the same success rate. When comparing, it must be kept in mind that maps were included in the computation of mean maps solely on the basis of their artery of occlusion (LAD, RCA or LCx), and that differences in lesion location and collateral circulation, which are also determiners of the region of ischemia, were not taken into account.

Several investigators [97, 127, 141, 147] have presented characteristic features of body-surface potential maps during PTCA-induced ischemia. Comparisons facilitate identification of the occluded artery. In this study, characteristic features representative of the artery of occlusion in inverse-recovered epicardial maps established the spatial relationship of ischemic effects more directly. Additionally, epicardial images resolved multiple extrema which appear to coincide with different branches of the main coronary artery. This was most striking for the left anterior descending branch of the left coronary artery. Simulations using a torso tank model [96, 119] demonstrated that multiple extrema on the epicardial surface may be reduced to single extrema on the torso surface. Oster et al. [119] found that they could resolve the multiple sites with noninvasive electrocardiographic imaging. These results support the potential ability of the epicardial images to localize more precisely ischemic zones.

Holland and Brooks [68] examined epicardial electrograms every 10 seconds during coronary occlusion in a pig heart. They found increasing levels of ST-segment shift with increased duration of the occlusion. Initially, changes were rapid, but slowed with time. Dupuoy et al. [37] recorded intracoronary electrograms in patients undergoing PTCA for a proximal LAD stenosis. They found increasing ST-segment elevation from 30–90 s of inflation, with a decreasing rate of change. Results of the present study are indicative of a similar relationship between the degree of ST-segment elevation, as

measured by epicardial ST-integral difference maps and "rest" and "peak-inflation" electrograms, and the duration of artery occlusions.

Epicardial electrograms exhibited elevated ST segments and T-wave increases. Changes generally developed first near the T wave and later near the J point. It was observed that the peak of the altered T wave shifted left with the time of inflation, even if there was no further visible change in peak height. A shortening of the time to T-wave offset for "peak-inflation" versus "rest" state was observed for some cases. This change was most visible at longer occlusion times, and appeared to be related to the shift of the peak. Surawicz et al. [154] examined 12-lead ECGs for 29 patients undergoing PTCA of LAD, RCA and LCx. They found variable changes in corrected QT intervals. Lengthening predominated for LAD and shortening for RCA, but either of these or no change were observed for all occluded arteries. A study during PTCA by Cohen et al. [25] found increased interval length for LAD and no significant change for RCA. The decrease in interval length observed in the present study can be explained by the alterations to the resting potential and the action potential; slowed conduction in the ischemic tissue, delayed depolarization and subsequent repolarization, have been suggested as a possible explanation for the lengthening observed in the other studies [77].

PTCA-induced changes in the QRS complex have been the subject of recent investigation [2, 86, 90, 127, 139, 147, 160, 161], where a major interest has been to differentiate between changes due to primary ischemia, and those where conduction disturbances are implicated. In the present study, the initial deflection of the QRS showed excellent agreement between baseline and inflation electrograms throughout the inflation/deflation cycle. Changes in R- and S-wave amplitude were observed. These were always in the direction of ST-segment change, that is, R waves increased and S waves were diminished. The S-wave changes for the LAD patient (Fig. 6.8) were most striking. Alterations in R-wave height were more variable. If observed at all, changes occurred only in late QRS and with longer occlusions. Surawicz et al. reported similar changes to R waves and S waves [154]. They had recorded only at the

end of a 120 s inflation, so could not corroborate the inflation time results. Fiducial points were not quantified for each electrogram in this study, limiting the interpretation of changes in QRS length. From visual observation, there was no evidence that QRS duration was altered. Both shortened [127] and lengthened QRS [154, 160, 161] have been reported. It has also been suggested that these changes are not a prerequisite to conduction disturbance [2, 139, 147, 160, 161].

Previous studies performed during PTCA have identified that the radiopharmaceutical perfusion agent ^{99m}Tc sestamibi can localize and quantify regions of hypoperfusion produced by balloon occlusions as short as 15 s, without requiring immediate imaging [14, 16, 17, 46, 64, 124, 148]. In this study, the comparison of changes in myocardial perfusion and electrical activity with transient acute ischemia—as documented by radionuclide and epicardial potential imaging during coronary occlusion—reveals that the two methods can localize the ischemia to expected regions. In addition, there was great similarity in the zones identified by each method. The latter method has the advantage of being non-invasive, and posing no risk to the patient, whereas radionuclide imaging is more expensive and involves exposure to radiation. Advances in perfusion imaging, including 3-D visualization [143], will enable comparison of methods for quantifying the extent and severity of ischemia, in addition to the localization presented in this study. Improved methods of recovering epicardial potential images and perfusion information will be invaluable in computer modelling of myocardial ischemia.

The use of a single homogeneous torso model may be a limitation on the accuracy of the inverse-recovered epicardial potentials in individual patients. Theoretical and experimental studies have reported that the most significant effect of not including inhomogeneities is inaccuracy in the amplitude of potentials, and not their distribution [59, 104, 105, 137] or activation pattern [53]. Shahidi et al. [140] found that including inhomogeneities did not improve the results when epicardial potentials recovered from measured BSPM data and potentials recorded via sock-electrodes were compared. In a study with an eccentric spheres model, Messinger-Rapport and Rudy [104] reported

that shifting the heart an amount equivalent to movement during respiration or posture change, resulted in loss of spatial resolution, especially on the posterior region of the epicardium. Arthur et al. [4] have recently suggested a faster and less expensive alternative to magnetic resonance imaging for determining personalized torso and heart geometries.

The electrocardiographic body-surface mapping data reflect ischemic changes in electrical activity within the heart, but the spatial relationships are lost due to eccentricity of cardiac sources and irregular shape of the torso. Noninvasive imaging of epicardial potentials provides an undistorted view of potential distributions and electrograms during the controlled ischemia induced by the balloon-inflation PTCA procedure. There is no evidence that any information visible in BSPM data is lost during this inversion process. What has most obviously been gained is the spatial relationship over the epicardial surface. Imaging captures multiple extrema which conceivably represent central zones of ischemia from different branchings of the occluded arteries. By re-establishing spatial relationships, we increase the potential to more accurately describe the ischemic region. This, in turn, enhances the possibility of identifying the extent and severity of ischemia, to complement localization. Results presented here show promise that this method of noninvasively imaging epicardial potential distributions is sufficiently robust and accurate to warrant use in clinical applications.

Chapter 7

Conclusions

The aims of this study—to refine the solution of the inverse problem for calculating noninvasive epicardial potential images, and to assess the capabilities of this inverse solution with clinical data from patients with acute regional ischemia induced by balloon-inflation angioplasty—have been achieved. The inverse problem of electrocardiography relates body-surface potential distributions with underlying cardiac activity. Three aspects of the inverse solution have been targeted in this study as areas where refinements of epicardial potential images can be obtained: (1) improving the accuracy of the transfer-coefficient matrix relating epicardial and body-surface potentials, (2) imposing regional constraints on the solution, and (3) determining an optimal regularizing parameter.

Specifically,

- For the triangle-to-triangle method of computing the transfer-coefficient matrix, double integrals involving observation and observed triangles, approximated from the centroid of the observation triangle, were replaced by a weighted sum of single integrals evaluated from seven Radon points within the observation triangle. With this refined method, the forward solution achieved remarkable accuracy, improving on the triangle-to-triangle method it replaced, and outperforming the equivalent node-to-node transformation.

196

- Refinements in transfer-matrix coefficient calculations translated into improved solutions to the inverse problem, as measured by relative error. The revised triangle-to-triangle method outperformed the node-to-node method in a large majority of test cases.

- The Slope Estimation Method of determining the optimal *a posteriori* regularizing parameter was robust and consistent in its selection. It never failed to find an acceptable value, and compared very well with the optimal *a priori* parameter over an extensive range of errors.

- The composite regional constraint applied *a posteriori* physiological constraints on the first estimate of the inverse solution. This technique includes three major components, each contributing in differing amounts to the overall quantitative and qualitative improvement in the inverse-recovered epicardial potential images.

  - Spatially smoothing low-level potentials, while retaining high amplitude and large gradient distributions, mitigated the effects of a global regularizing parameter. This component was the major contributor to both quantitative and qualitative improvement. Integral difference maps for epicardial distributions were relatively smooth.

  - Removal of spurious extrema contributed qualitatively to the refinement of the inverse solution. Epicardial-potential images computed from measured data were relatively free of any isolated areas where the sign of the potentials was unexpected.

  - Temporal smoothing has the potential for improving the solution when body-surface data are available for a sequence of time instants. Test ECG recordings were already smooth, especially after previous application of the weighted spatial smoothing constraint, and large differences were not visible. Epicardial electrograms computed from measured data displayed a high degree of smoothness.

Noninvasive imaging of epicardial potentials provides a unique look at integral difference maps and electrograms during the controlled ischemia induced by artery occlusion during balloon-inflation coronary angioplasty. An assessment was made of the capability of the inverse solution, as applied here, to localize the ischemia to a region within the perfusion zone of the artery which was occluded during the angioplasty procedure. Epicardial electrograms were examined for features indicative of underlying ischemia. The following results were noted:

- The inverse solution was capable of localizing the ischemic zone to a region perfused by the occluded artery. There was very good agreement in localization with radionuclide myocardial perfusion images. For this study, angiographic data were not analyzed for the full set of 94 patients included in the PTCA group of the BSPM database. Reconstruction of the coronary circulation from angiographic data will help to identify reasons for deviations from expected patterns.

- There was no evidence that any information visible in body-surface potential maps was lost during the transformation to the epicardial surface. Features of epicardial electrograms in the central ischemic zone compared well with electrocardiograms from regions on the body surface most associated with the occluded artery. The most obvious improvement was the establishment of the spatial relationship over the epicardial surface, allowing a more accurate description of the ischemic region than could be achieved with body-surface data alone.

- Epicardial imaging captured multiple extrema which conceivably represent central zones of ischemia from different branches of the occluded arteries. This enhances the possibility of identifying the extent and severity of ischemia, to complement localization.

Overall, the results presented here hold great promise that the technique of calculating epicardial potentials from multiple electrocardiograms recorded on the body surface will be sufficiently robust and accurate to warrant use in clinical applications.

Appendix A

Tesselated Torso and Epicardial Surfaces

A solution to the forward and inverse problems of electrocardiography, as defined in this study, requires a three-dimensional geometrical description of the realistically shaped torso-heart system. We use a torso (body without extremities and head) as the approximation of body-surface boundary; this truncation is justified in view of the fact that heart-produced potentials diminish rapidly in the extremities.

Our solutions to the forward and inverse problems are based on the boundary element method (BEM), requiring that the surfaces bounding regions of the volume conductor are defined by a set of nodes which are linked to form triangular area elements. If a homogeneous torso model is assumed for the solution in terms of epicardial potentials, only the outer surface of the body, S_B, and the epicardial surface of the heart, S_H, need be defined.

Torso surface

A realistic human torso model was developed in this laboratory from measurements of a single subject. The original version—introduced by Horáček [70] and used since by others [58, 115, 130]—consists of five surfaces: the outer torso surface, two lungs

and two intracavitary blood masses, which are defined by 952 nodes joined to form 1884 triangles. To optimize the forward/inverse solutions, we reduced the number of nodes defining the outer surface. First, each of the 117 electrode locations of the clinical body-surface potential mapping system [110] was matched with a node point, and then additional nodes were placed mid-way between rows of the electrode grid, resulting in a higher spatial density of nodes in the precordial area than on the right anterior chest and back. Node points in the shoulder and neck regions were chosen so as to maintain an adequate and consistent spatial resolution.

The grid size was determined by the 5-cm electrode spacing of the clinical body-surface potential mapping protocol, which uses fixed electrode strips in the vertical direction. The spacing around the circumference of the patient is not fixed, but is still quite regular in that strips are placed to best cover the surface between anatomical landmarks. That is, strips are placed, for example, on the spine, left and right mid-axillary lines, while the area between is covered by regularly spaced strips.

The node points were then joined to form a closed surface of triangular surface elements without overlaps or gaps (tesselation). MacLeod [97] discusses several possible triangularization strategies. We chose to perform a manual triangularization in order to generate triangles of consistent area, but also to maintain reasonably accurate representation of the surface with a minimal number of nodes. The upper and lower ends of the torso at the neck and waist were capped by sets of horizontal triangles. The resulting torso surface used in this study is represented by 352 nodes, which form 700 triangular area elements. An axonometric projection of this torso surface is shown in Fig. A.1

Epicardial Surface

To complete the geometrical information needed for solving the forward/inverse problem as defined in this study, a description of the epicardial surface is also required.
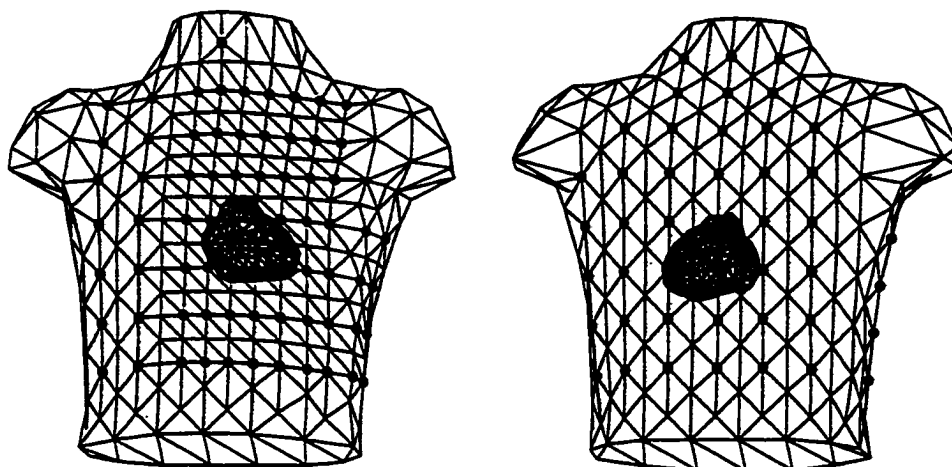
Figure A.1: Anterior and posterior views of the tesselated torso and epicardial surfaces. The torso surface, S_B, consists of 700 triangular area elements with 352 nodes, the epicardial surface, S_H, of 400 triangular area elements and 202 nodes. Filled circles identify the nodes which correspond to the locations of the 117 electrodes used in this laboratory for recording electrocardiographic body-surface potentials.

Sections of a *post mortem* human heart have been previously digitized in this laboratory [95, 134]. The location and orientation of this heart within the torso model was determined from radiographic views of the subject from whom the torso geometry was constructed. The nodes of the epicardial surface were chosen to lie on the outer boundary of 10 slices through the heart, made perpendicular to an axis running from the left-ventricular apex through the root of the aorta; this corresponds to the sections of Durrer et al. [38]. The epicardial surface is represented by 202 nodes which form 400 triangles. Fig. A.1 shows anterior and posterior views of the three-dimensional epicardial surface enclosed by the torso's outer boundary.

Two-dimensional projections

The three-dimensional torso surface and epicardial surface have been projected onto a plane for viewing. Since the three-dimensional form of the torso surface was derived from a two-dimensional grid, there was no need to derive another means of projecting the torso onto a flat surface. The spacing and regular nature of the grid were
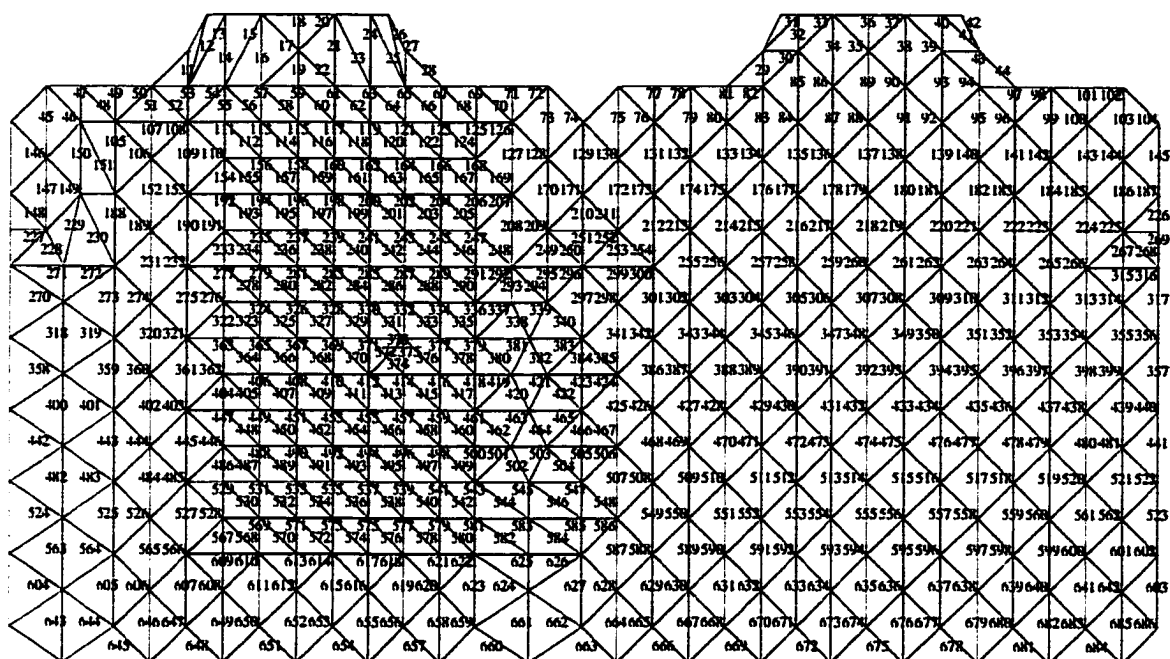
Figure A.2: Two-dimensional representation of the tesselated torso surface. The torso surface consists of 700 triangular area elements with 352 nodes; anterior chest surface is on the left and posterior chest surface on the right; left and right margins correspond to right mid-axillary line; vertical line in the centre corresponds to the left mid-axillary line; top, neck; bottom, waist.

maintained as much as possible. A two-dimensional equivalent of the torso's outer surface, used throughout this dissertation to display body-surface potential maps is in Fig. A.2.

Clinical electrocardiographic recordings yield a maximum of 117 leads (faulty leads reduce this number), from which a complete set of torso potentials at all node points have to be generated. This is both a necessary prerequisite for inverse calculations and a functional requirement for plotting reasonably smooth iso-contour maps. Whereas values at 117 of the 352 node points can be determined directly from the measured data, potentials at the remaining nodes have to be estimated; to perform the latter task, we used a three-dimensional interpolation scheme proposed by Oostendorp et al. [116].

To facilitate display of epicardial potential distributions, it was necessary to develop a suitable projection of the three-dimensional surface of the heart. MacLeod [97] discussed various alternatives for such display. The method we have chosen is a polar projection that has been used by several groups to display isochrone maps in clinical epicardial mapping [13, 35, 34]. The heart is viewed from the apex along the heart axis, with 10 sections—from apex to base—shown in this projection as concentric circles. Figure A.3 shows this two-dimensional *polar* display of the epicardial surface as a tesselation of numbered triangles. At the centre of this polar display lies the apex, surrounded by concentric rings which correspond to the outlines of the slices through the heart—the outermost one corresponding to the atrio-ventricular (A-V) ring. A two-dimensional equivalent of the triangularized epicardial surface, used to display epicardial potential maps is in Fig. A.3.

The main advantage of this form of display is that it contains all of the ventricular surface in a single diagram. The orientation of this display was chosen in such a way that the course of the left anterior descending (LAD) artery would be directed approximately vertically from the top towards the centre; the posterior descending artery runs from the bottom upwards. This perspective allows relatively easy orientation when viewing the epicardial maps. To assist in the interpretation of epicardial maps, Fig. A.4 shows the major coronary arteries projected onto the epicardial polar display. Based on standard views from the textbook of anatomy [102], the coronary anatomy was traced over plots of the three-dimensional triangularized epicardial surface. The triangles in these plots provided a grid with which the location of each of the arteries could then be transposed to a polar plot. The extent and location of the coronary tree was adjusted to resemble that of a normal right-dominant human.
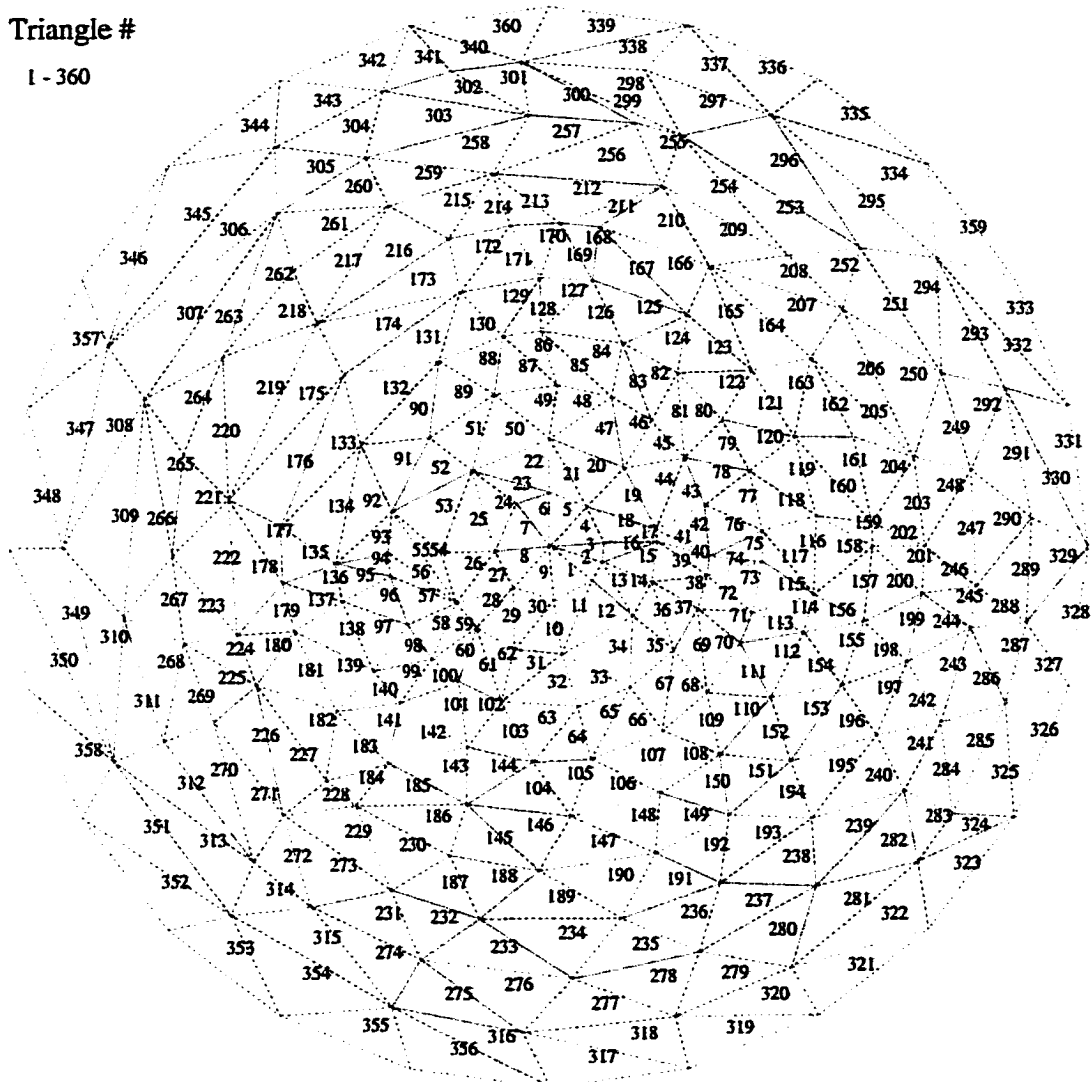
Figure A.3: Polar projection of tesselated epicardial surface. This projection is used to display all epicardial potential distributions and epicardial electrograms in this study. The epicardial surface comprises 360 triangular area elements, projected here so that left-ventricular apex is in the centre, anterior wall on top, posterior wall on the bottom, right-ventricular surface on the left, and left-ventricular surface on the right. Numbers (from 1 to 360) identify individual triangles; the total number of epicardial triangles is 400 (since 40 triangles are needed to close the surface in basal plane).

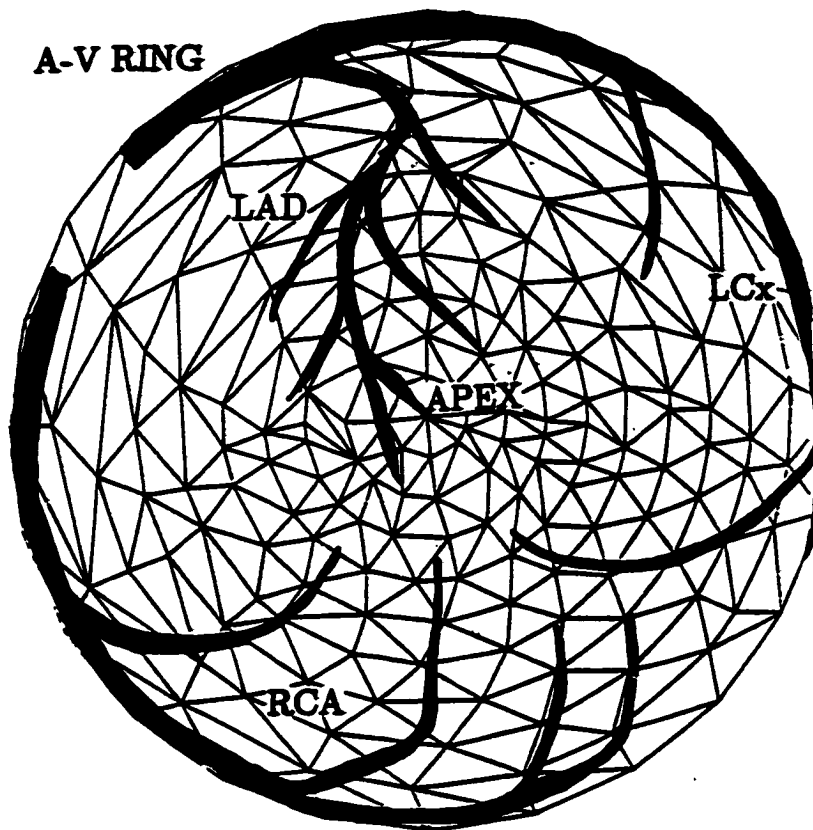Figure A.4: The "bull's-eye" polar projection used for displaying noninvasive epicardial potential images on the ventricular surface. This is an apical projection with the apex in the center and the atrioventricular (AV) groove along the rim. Thick lines define the locations of the left anterior descending (LAD) coronary artery, right coronary artery (RCA) and left circumflex (LCx) coronary artery in this projection.

Appendix B

Propagation Model of Human Ventricular Myocardium

A computer model of propagated excitation in the three-dimensional anisotropic human ventricular myocardium was developed previously in this laboratory [113, 114]. For the purposes of testing the methods of inverse solution presented in this dissertation, we used this heart model to generate oblique double layer sources that represent realistically the actual cardiac bioelectric sources. Two activation sequences were used for testing: one for septal and the other for basal ectopic site of stimulation.

Calculation of extracardiac potentials

First, as in the model of Leon and Horáček[91], the infinite-medium potential ϕ in the extracardiac region was determined from the discretized equation (B.1)

$$\phi = -\frac{\sigma_1}{4\pi\sigma} \int_H \frac{\nabla v \cdot \vec{r}}{r^3} dV - \frac{\sigma_2}{4\pi\sigma} \int_H \frac{\vec{a}_3 \vec{a}_3^T \nabla v \cdot \vec{r}}{r^3} dV \qquad (B.1)$$

where $\vec{a}_3$ is the local direction of the fiber axis, σ is the extracellular conductivity ($\sigma = 2.0$ mS/cm), σ_1 is the transverse conductivity ($\sigma_1 = 0.5$ mS/cm) and σ_2 is the difference between the axial and transverse conductivities of the anisotropic intracellular domain ($\sigma_2 = 1.5$ mS/cm). The potential in (B.1) can be separated into

two parts: the first term represents the contribution of the "isotropic component" predicted by the uniform-double-layer theory; the second term represents the contribution of the "axial component," which accounts for the anisotropic properties of cardiac tissue.

To calculate bounded-medium extracardiac fields, we had to take the volume-conductor effects into account by applying the boundary-element method [70]. The ventricular model was appropriately placed in a torso model; the electric potential was calculated for all node and triangle sites on the epicardial and body surface. The isotropic and axial components of the extracardiac fields were evaluated separately and then combined for the given σ_2/σ_1.

Test distributions

Our computer model of the anisotropic human ventricular myocardium [113] was used to generate two activation sequences: one for left-ventricular septal site of stimulation and the other for basal ectopic site (left postero-paraseptal pre-excitation site in Hren *et al.* [73]). For each activation sequence, body-surface and epicardial potential distributions were calculated at 2-ms intervals for 36 successive instants of time, representing 72 ms of propagated activation. The test data sets of epicardial and torso-surface potential distributions were simulated by the heart model as a sequence of oblique dipole layers as described above. Dipole sources were calculated from the model's output in terms of intracellular potential for every cell of the model. Fig. B.1 shows epicardial potentials for septal activation sequence, and Fig. B.2 shows those for basal activation sequence.

Figure B.1: Epicardial potential maps for septal activation sequence. Columns, from left to right, show 36 consecutive epicardial potential maps generated by the oblique dipole layers representing activation wavefronts, at 2-ms intervals (S-2ms, ...,S-72ms), for the activation sequence initiated at single septal site.
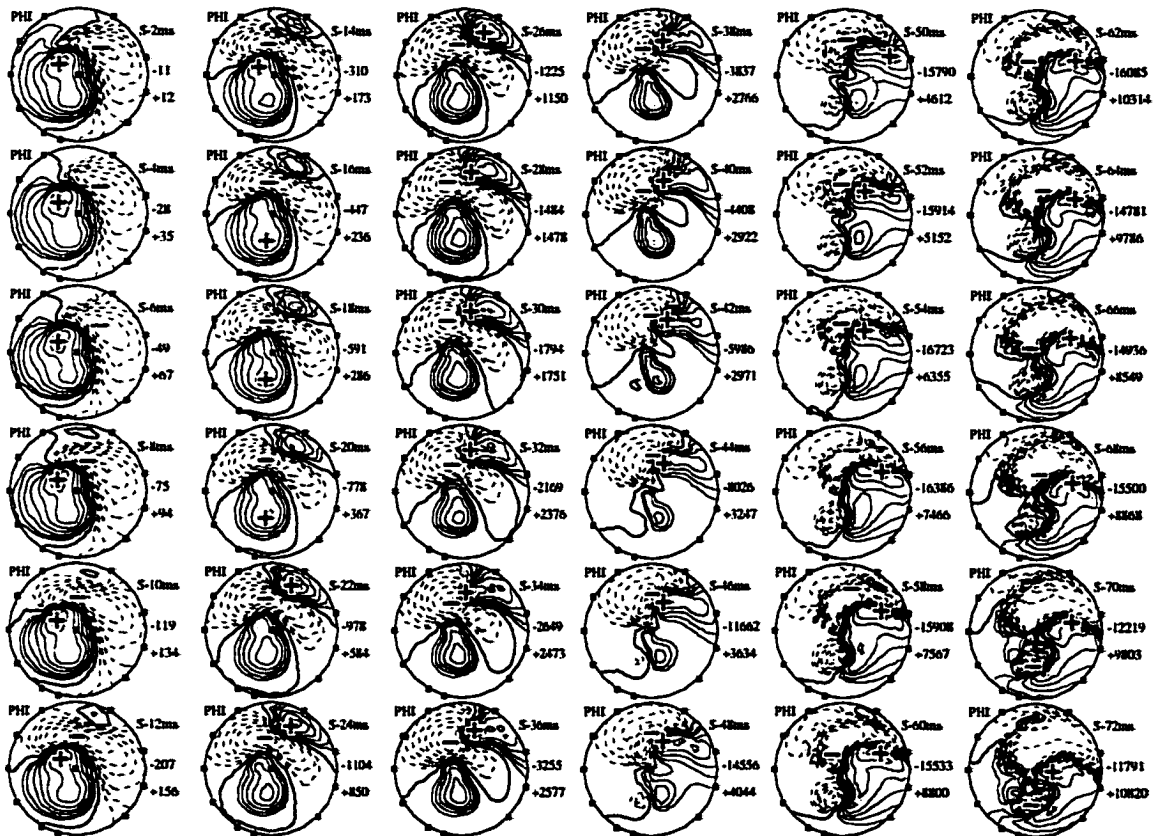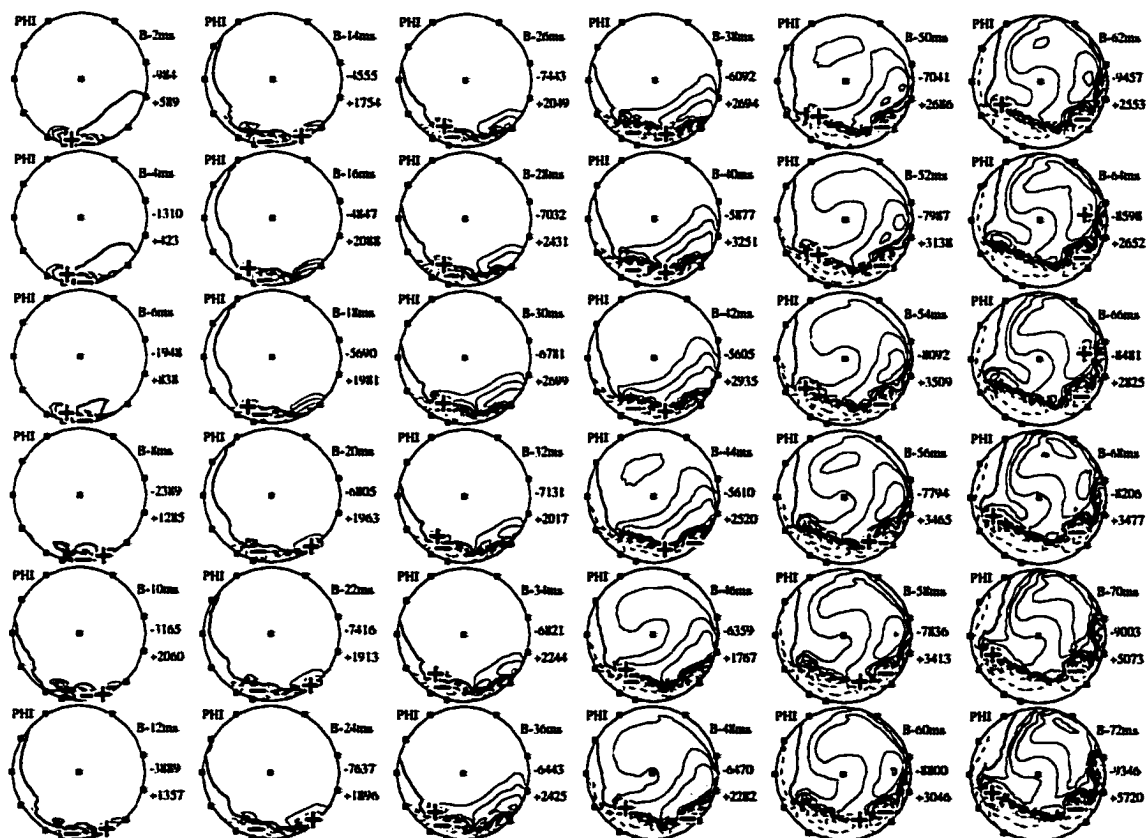
Figure B.2: Epicardial potential maps for basal activation sequence. Columns, from left to right, show 36 consecutive epicardial potential maps generated by the oblique dipole layers representing activation wavefronts, at 2-ms intervals (B-2ms,...,B-72ms), for the activation sequence initiated at single basal site.

Appendix C

Test Distributions

The test data sets of epicardial and torso-surface potential distributions for various single-dipole or multiple-dipole sources were calculated.

The first pair of test distributions (body-surface and epicardial) was generated by a central dipole source.

The second pair of test distribution was produced by three simultaneouly energized eccentric dipole sources with one located in the left-ventricular midlateral wall, one in the right-ventricular midlateral wall, and one near the left-ventricular apex. These three locations were determined by picking a triangle in the appropriate area of the epicardial surface and moving the dipole source inwards 10 mm along the inward-oriented normal to the triangle, and making the dipole direction the same as the outward normal of this triangle.

The third pair of test distributions was calculated for five simultaneously energized eccentric dipole sources; the first three dipoles were the same as in the three-dipole source, and two more dipoles (created in the same manner) were added, one in the mid-anterior wall along the septum, and one in the mid-posterior wall along the septum.

Three more pairs of test distributions were calculated for three single eccentric dipoles at 10-mm depth into ventricular wall. Fig. C.1 shows all six test distributions on epicardial surface.
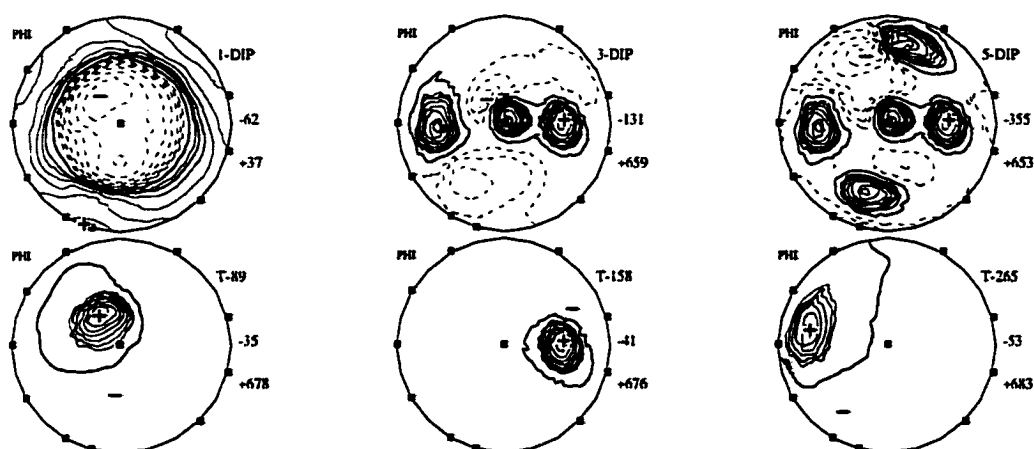
Figure C.1: Epicardial potential maps for single- and multiple-dipole sources. These maps were generated, by solving the forward problem, to serve as diverse test distributions of known potentials. First row shows epicardial potential maps generated by single central dipole (1-DIP), three eccentric dipoles (3-DIP), and five eccentric dipoles (5-DIP); second row shows maps generated by three single eccentric dipoles at 10-mm depth into ventricular wall near $\triangle 89$ (T-89), $\triangle 158$ (T-158), and $\triangle 265$ (T-265).

Bibliography

[1] *The NAG Fortran Library Manual – Mark 15*. The Numerical Algorithms Group Ltd., Oxford, 1988.

[2] S. Abboud, R.J. Cohen, A. Selwyn, P. Ganz, D. Sadeh, and P.L. Friedman. Detection of transient myocardial ischemia by computer analysis of standard and signal-averaged high-frequency electrocardiograms in patients undergoing percutaneous transluminal coronary angioplasty. *Circulation*, 76:585–596, 1987.

[3] E. Anderson, Z. Bai, C. Bischof, J.W. Demmel, J.J. Dongarra, J. Du Croz, A. Greenbaum, S Hammarling, A. McKenney, S. Ostrouchov, and D. Sorensen. *LAPACK User's Guide*. Society for Industrial and Applied Mathematics, Philadelphia, 1992.

[4] R. Arthur, D. Beetner, H. Ambos, and M. Cain. Improved estimation of pericardial potentials from body-surface maps using individualized torso models. *J Electrocardiol*, 31(Suppl):S106–S113, 1998.

[5] A.C.L. Barnard, I.M. Duck, and M.S. Lynn. The application of electromagnetic theory to electrocardiology. I. Derivation of the integral equations. *Biophys J*, 7:443–462, 1967.

[6] A.C.L. Barnard, I.M. Duck, M.S. Lynn, and W.P. Timlake. The application of electromagnetic theory to electrocardiology. II. Numerical solution of the integral equations. *Biophys J*, 7:463–490, 1967.

[7] R.C. Barr, M. Ramsey III, and M.S. Spach. Relating epicardial and body surface potential distributions by means of transfer coefficients based on geometry measurements. *IEEE Trans Biomed Eng*, BME-24:1–11, 1977.

[8] R.C. Barr, T.C. Pilkington, J.P. Boineau, and M.S. Spach. Determining surface potentials from current dipoles, with application to electrocardiography. *IEEE Trans Biomed Eng*, BME-13:88–92, 1966.

[9] R.C. Barr and M.S. Spach. Inverse solutions directly in terms of potentials. In C.V. Nelson and D.B. Geselowitz, editors, *The Theoretical Basis of Electrocardiography*, pages 294–304. Clarendon Press, Oxford, 1976.

[10] R.C. Barr and M.S. Spach. Inverse calculation of QRS-T epicardial potentials from body surface potential distributions for normal and ectopic beats in the intact dog. *Circ Res*, 42:661–675, 1978.

[11] P.H. Bartels, D. Thompson, and J.E. Weber. Construction of the knowledge file for an image understanding system. *Path Res Pract*, 188:396–404, 1992.

[12] Å. Björck. Constrained least squares problems. In P.G. Ciarlet and J.L. Lions, editors, *Handbook of Numerical Analysis, Vol. I: Finite Difference Methods—Solution of Equations in R^n*, pages 589–615. Elsevier, New York, 1990.

[13] G. Bonneau, G. Tremblay, P. Savard, R. Guardo, A.R. Leblanc, R. Cardinal, P. Pagé, and R.A. Nadeau. An integrated system for real-time cardiac activation mapping. *IEEE Trans Biomed Eng*, BME-34:415–423, 1987.

[14] S. Borges-Neto, J. Puma, R.H. Jones, M.H. Sketch Jr., R. Stack, M.W. Hanson, and R.E. Coleman. Myocardial perfusion and ventricular function measurements during total coronary artery occlusion in humans: a comparison with rest and exercise radionuclide studies. *Circulation*, 89:278–284, 1994.

[15] R.K. Bottner, C.J. Moreas, C.R. Green, R.H. Renzi, K.M Kent, and M.W. Krucoff. Quantitation of ischemia during total coronary occlusion with computer-assisted high resolution ST-segment monitoring: effect of collateral flow. *J Electrocardiol*, 19(Suppl):S104–S106, 1987.

[16] S.H. Braat, H. de Swart, J.H. Janssen, P. Brugada, P. Rigo, and H.J.J. Wellens. Use of technetium-99m sestamibi to determine the size of the myocardial area perfused by a coronary artery. *Am J Cardiol*, 66(Suppl E):85E–90E, 1990.

[17] S.H. Braat, H. de Swart, P. Rigo, L. Koppejan, G.A.K. Heidendal, and H.J.J. Wellens. Value of technetium MIBI to detect short lasting episodes of severe myocardial ischaemia and to estimate the area at risk during coronary angioplasty. *Eur Heart J*, 12:30–33, 1991.

[18] D.H. Brooks, G.F. Ahmad, R.S. MacLeod, and G.M. Maratos. Inverse electrocardiography by simultaneous imposition of multiple constraints. *IEEE Trans Biomed Eng*, BME-46:3–18, 1999.

[19] D.H. Brooks, C.L. Nikias, and H.H. Siegel. Comparison and testing of least-squares time domain inverse solutions in electrocardiography. *J Biomed Eng*, 12:503–518, 1990.

[20] D.M. Budgett, D.M. Monro, S.W. Edwards, and R. De L. Stanbridge. Comparison of measured and computed epicardial potentials from a patient-specific inverse model. *J Electrocardiol*, 26(Suppl):S165–S173, 1993.

[21] H. Bush, J. Ferguson, P. Angelini, and J. Willerson. Twelve-lead electrocardiographic evaluation of ischemia during percutaneous transluminal coronary angioplasty and its correlation with acute reocclusion. *Am Heart J*, 121:1581–1589, 1991.

[22] R. Carroll. *Regularization Methods for the Inverse Problem of Electrocardiography*. Master's thesis, Dalhousie University, Halifax, N.S., 1990.

[23] R. Childers. R wave amplitude in ischemia, injury, and infarction. *J Electrocardiol*, 29(Suppl):S171–S178, 1996.

[24] J.C. Clements, R. Carroll, and B.M. Horáček. On regularization parameters for inverse problems in electrocardiography. In D.N. Ghista, editor, *Biomedical and Life Physics*, pages 235–246. Vieweg Verlag, Wiesbaden, 1996.

[25] M. Cohen, S. Scharf, and P. Rentrop. Prospective analysis of electrocardiographic variables as markers for extent and location of acute wall motion abnormalities observed during coronary angioplasty in human subjects. *J Am Coll Cardiol*, 10:17–24, 1987.

[26] R.N. Colley and M.H. Schreiber. *Radiology of the Heart and Great Vessels*. Willams & Wilkins Company, Baltimore, 1978. Third Edition.

[27] P. Colli Franzone, L. Guerri, B. Taccardi, and C. Viganotti. Finite element approximation of regularized solution of the inverse potential problem of electrocardiography and application to experimental data. *Calcolo*, XXII(I):91–186, 1985.

[28] P. Colli Franzone, L. Guerri, S. Tentoni, C. Viganotti, S. Baruffi, S. Spaggiari, and B. Taccardi. A mathematical procedure for solving the inverse potential problem of electrocardiography. *Math Biosci*, 77:353–396, 1985.

[29] R. Courant and D. Hilbert. *Methods of Mathematical Physics, Vol. 1*. Wiley, New York, 1962.

[30] J.J.M. Cuppen. Calculating the isochrones of ventricular depolarization. *SIAM J Sci Stat Comp*, 5:105–120, 1984.

[31] J.J.M. Cuppen and A. van Oosterom. Model studies with the inversely calculated isochrones of ventricular depolarization. *IEEE Trans Biomed Eng*, BME-31:652–659, 1984.

[32] P.J. Davis and I. Polonsky. Numerical interpolation, differentiation, and integration. In M. Abramowitz and I.A. Stegun, editors, *Handbook of Mathematical Functions*, page 893. National Bureau of Standards, Washington, DC, 1972.

[33] J.C. de Munck. A linear discretization of the volume conductor boundary integral equation using analytically integrated elements. *IEEE Trans Biomed Eng*, BME-39:986–990, 1992.

[34] E. Downar, L. Harris, L.L. Mickleborough, N. Shaikh, and I.D. Parson. Endocardial mapping of ventricular tachycardia in the intact human ventricle: evidence of reentrant mechanisms. *J Am Coll Cardiol*, 11:783–791, 1988.

[35] E. Downar, I.D. Parson, L. L. Mickleborough, D.A. Cameron, L.C. Yao, and M.B. Waxman. On-line epicardial mapping of intraoperative ventricular arrhythmias: initial clinical experience. *J Am Coll Cardiol*, 4:703–14, 1984.

[36] S.M. Dunn. An introduction to model-based imaging. *Dentomaxillofac Radiol*, 21:184–189, 1992.

[37] P. Dupuoy, H. Geschwind, G. Pelle, E. Aptecar, L. Hittinger, A. Ghalid, and J. Dubois-Rande. Repeated coronary artery occlusions during routine balloon angioplasty do not induce myocardial preconditioning in humans. *J Am Coll Cardiol*, 27:1374–1380, 1996.

[38] D. Durrer, R.T. van Dam, G.E. Freud, M.J. Janse, F.L. Meijler, and R.C. Arzbaecher. Total excitation of the isolated human heart. *Circulation*, 41:899–912, 1970.

[39] J. El-Jakl, F. Champagnat, and Y. Goussard. Time-space regularization of the inverse problem of electrocardiography. In *Proc IEEE EMBS 17th Ann Int Conf*, 1995. (CD).

[40] V. Elharrar and D.P. Zipes. Cardiac electrophysiologic alterations during myocardial ischemia. *Am J Physiol*, 233(3):H329–H345, 1977.

[41] H.W. Engl and W. Grever. Using the *L*-curve for determining optimal regularization parameters. *Numer Math*, 69:25–31, 1994.

[42] R. L. Feldman, R.G. Macdonald, J.A. Hill, M.C. Limacher, R. Conti, and C.J. Pepine. Effect of propranolol on myocardial ischemia occurring during acute coronary occlusion. *Circulation*, 73:727–733, 1986.

[43] A.S. Ferguson and G. Stroink. Factors affecting the accuracy of the boundary element method in the forward problem—I: Calculating surface potentials. *IEEE Trans Biomed Eng*, BME-44:1139–1155, 1997.

[44] A.S. Ferguson, X. Zhang, and G. Stroink. A complete linear discretization for calculating the magnetic field using the boundary element method. *IEEE Trans Biomed Eng*, BME-41:455–460, 1994.

[45] M. Foster. An application of the Wiener-Kolmogorov smoothing theory to matrix inversion. *J SIAM*, 9:387, 1961.

[46] D.M. Gallik, S.D. Obermueller, U.S. Swarna, G.W. Guidry, J.J. Mahmarian, and M.S. Verani. Simultaneous assessment of myocardial perfusion and left ventricular function during transient coronary occlusion. *J Am Coll Cardiol*, 25:1529–1538, 1995.

[47] M. Gardner, R. MacLeod, R. Macdonald, M. Henderson, G. Adams, T. Montague, and B. Horáček. Detection and localization of myocardial ischemia during coronary artery occlusion in man. *Clin Invest Med*, 13(Suppl C):C64, 1990.

[48] H.L. Gelernter and J.C. Swihart. A mathematical-physical model of the genesis of the electrocardiogram. *Biophys J*, 4:285–301, 1964.

[49] L.S. Gettes. Effects of ischemia on cardiac electrophysiolgy. In H.E. Fozzard *et al.*, editor, *The Heart and Cardiovascular System*, chapter 57, pages 1317–1341. Raven Press, New York, 1986.

[50] H. Gfrerer. An a posteriori parameter choice for ordinary and iterated Tikhonov regularization of ill-posed problems leading to optimal convergence rates. *Math of Comput*, 49:507–522, 1987.

[51] R.J. Gibbons. Perfusion imaging with ^{99m}Tc-sestamibi for the assessment of myocardial area at risk and the efficacy of acute treatment in myocardial infarction. *Circulation*, 84(Suppl I):I-37–I-42, 1991.

[52] R.J. Gibbons, M.S. Verani, T. Behrenbeck, P.A. Pellikka, M.K. O'Connor, J.J. Mahmarian, J.H. Chesebro, and F.J. Wackers. Feasibility of tomographic ^{99m}Tc-hexakis-2-methoxy-2-methylpropyl-isonitrile imaging for the assessment of myocardial area at risk and the effect of treatment in acute myocardial infarction. *Circulation*, 80:1277–1286, 1989.

[53] L. Green, B. Taccardi, P. Ershler, and R. Lux. Epicardial potential mapping: effects of conducting media on isopotential and isochrone distributions. *Circulation*, 84:2513–2521, 1991.

[54] L.S. Green, R.L. Lux, and C.W. Haws. Detection and localization of coronary artery disease with body surface mapping in patients with normal electrocardiograms. *Circulation*, 76:1290–1297, 1987.

[55] F. Greensite, G. Huiskamp, and A. van Oosterom. New quantitative and qualitative approaches to the inverse problem of electrocardiology: their theoretical relationship and experimental accuracy. *Med Phys*, 17:369–379, 1990.

[56] B. Griffin, A.D. Timmis, J.C.P. Crick, and E. Sowton. The evolution of myocardial ischemia during percutaneous transluminal coronary angioplasty. *Eur Heart J*, 8:347–353, 1987.

[57] C.W. Groetsch. *The Theory of Tikhonov Regularization for Fredholm Equations of the First Kind.* Pitman, Boston, MA, 1984.

[58] R. Gulrajani and G.E. Mailloux. A simulation study of the effects of torso inhomogeneities on electrocardiographic potentials, using realistic heart and torso models. *Circ Res*, 52:45–56, 1983.

[59] R.M. Gulrajani, F.A. Roberge, and G.E. Mailloux. The forward problem of electrocardiography. In P.W. Macfarlane and T.D. Veitch Lawrie, editors, *Comprehensive Electrocardiology*, pages 197–236. Pergamon Press, Oxford, 1989. Volume 1.

[60] D. Hamel, P. Savard, D. Derome, L. Legendre, R. Nadeau, M. Debuc, and M. Shenasa. Detection of localized ischemia changes with body surface potential mapping in patients undergoing coronary angioplasty. *Circulation*, 78(Suppl II):II-577, 1988.

[61] P.C. Hansen. Regularization, GSVD and truncated GSVD. *BIT*, 29:491–504, 1989.

[62] P.C. Hansen. Analysis of discrete ill-posed problems by means of the *L*-curve. *SIAM Review*, 34:561–580, 1992.

[63] P.C. Hansen and D.P. O'Leary. The use of the *L*-curve in the regularization of discrete ill-posed problems. *SIAM J Sci Stat Comput*, 14:1487–1503, 1993.

[64] H.L. Haronian, M.S. Remetz, A.J. Sinusas, J.M. Baron, H.I. Miller, M.W. Cleman, B.L. Zaret, and F.J.T. Wackers. Myocardial risk area defined by technetium-99m sestamibi imaging during percutaneous transluminal coronary angioplasty: comparison with coronary angiography. *J Am Coll Cardiol*, 22:1033–1043, 1993.

[65] J.L. Hill and L.S. Gettes. Effect of coronary artery occlusion on local myocardial extracellular K^+ activity in swine. *Circulation*, 61:768–778, 1980.

[66] H.J. Hirche, F.L. Boes, R. Bissig, R. Lang, and M. Schramm. Myocardial extracellular K^+ and H^+ increase and noradrenaline release as possible cause of early arrhythmias following acute coronary artery occlusion in pigs. *J Mol Cell Cardiol*, 12:579–593, 1980.

[67] R. Hoekema. *The Interindividual Variability of the Electrocardiogram*. PhD thesis, University of Nijmegen, Nijmegen, the Netherlands, 1999.

[68] R.P. Holland and H. Brooks. The QRS complex during myocardial ischemia: An experimental analysis in the porcine heart. *J Clin Invest*, 57:541–550, 1976.

[69] R.P. Holland and H. Brooks. TQ-ST segment mapping: critical review and analysis of current concepts. *Am J Cardiol*, 4:110–129, 1977.

[70] B.M. Horáček. Numerical model of an inhomogeneous human torso. *Adv Cardiol*, 10:51–57, 1974.

[71] B.M. Horáček and J.C. Clements. The inverse problem of electrocardiography: a solution in terms of single- and double-layer sources on the epicardial surface. *Math Biosci*, 144:119–154, 1997.

[72] B.M. Horáček, R.G. de Boer, J.L. Leon, and T.J. Montague. Human epicardial potential distributions computed from body-surface-available data. In K. Yamada, K. Harumi, and T. Musha, editors, *Advances in Body Surface Potential Mapping*, pages 47–54. University of Nagoya Press, Nagoya, Japan, 1983.

[73] R. Hren, G. Stroink, and B.M. Horáček. Accuracy of the single dipole inverse solution in localising ventricular preexcitation sites: a simulation study. *Med Biol Eng Comp*, 36:323–329, 1998.

[74] G Huiskamp and A. van Oosterom. The depolarization sequence of the human heart surface computed from measured body surface potentials. *IEEE Trans Biomed Eng*, BME-35:1047–1059, 1989.

[75] G.J. Huiskamp and A. van Oosterom. Tailored versus realistic geometry in the inverse problem of electrocardiography. *IEEE Trans Biomed Eng*, 36:827–835, 1989.

[76] I. Iakovidis and R.M. Gulrajani. Improving Tikhonov regularization with linearly constrained optimization: application to the inverse epicardial potential solution. *Math Biosci*, 112:53–78, 1992.

[77] M. Janse and A. Kléber. Electrophysiological changes and ventricular arrythmias in the early phase of regional myocardial ischemia. *Circ Res*, 49:1069–1081, 1981.

[78] C.R. Johnson and R.S. MacLeod. Local regularization and adaptive methods for the inverse Laplace problems. In D.N. Ghista, editor, *Biomedical and Life Physics*, pages 223–234. Vieweg Verlag, Wiesbaden, 1996.

[79] P.R. Johnston and R. M. Gulrajani. A new method for regularization parameter determination in the inverse problem of electrocardiography. *IEEE Trans Biomed Eng*, BME-44:19–39, 1997.

[80] D. Joly, Y. Goussard, and P. Savard. Time-recursive solution to the inverse problem of electrocardiography: a model-based approach. In *Proc IEEE EMBS 15th Ann Int Conf*, pages 767–768, 1993.

[81] M. Kardesch, C.E. Hogancamp, and R.J. Bing. The effect of complete ischemia on the intracellular electrical activity of the whole mammalian heart. *Circ Res*, 6:715–720, 1958.

[82] A. Katz. *Physiology of the Heart*. Raven Press, New York, NY, 1992. (Second edition).

[83] D.S. Khoury and Y. Rudy. A model study of volume conductor effects on endocardial and intracavitary potentials. *Circ Res*, 71:511–525, 1992.

[84] D. Kilpatrick and S. Walker. A validation of derived epicardial potential distributions by prediction of the coronary artery involved in acute myocardial infarction in humans. *Circulation*, 76:1282–1289, 1987.

[85] A.G. Kléber, M.J. Janse, F.J.L. van Capelle, and D. Durrer. Mechanism and time course of ST- and TQ-segment changes during acute regional myocardial ischemia in the pig heart determined by extracellular and intracellular recordings. *Circ Res*, 42:603–613, 1978.

[86] F. Kornreich, R. MacLeod, V. Dzavik, R. Selvester, A. Kornreich, E. Stoupel, J. deAlmeida, D. Walker, and T. Montague. QRST changes during and after percutaneous transluminal coronary angioplasty. *J Electrocardiol*, 27(Suppl):S113–S117, 1994.

[87] M. Krucoff, Y. Jackson, M. Kehoe, and K. Kent. Quantitative and qualitative ST segment monitoring during and after percutaneous transluminal coronary angioplasty. *Circulation*, 81(Suppl IV):IV-20–IV-26, 1990.

[88] M. Krucoff, A. Parente, R. Bottner, R. Renzi, K. Stark, R. Shugoll, S. Ahmed, J. DeMichele, S. Stroming, C. Green, C. Rackley, and K. Kent. Stability of multilead ST-segment 'fingerprints' over time after percutaneous transluminal coronary angioplasty and its usefulness in detecting reocclusion. *Am J Cardiol*, 61:1232–1237, 1988.

[89] T. Kuwahara and T. Takeda. A formula of boundary integral for potential problem and its consideration. In M. Tanaka and Q.H. Du, editors, *Proc. First Japan-China Symposium on Boundary Element Methods Theory and Applications*, pages 47–56. Pergamon, New York, NY, 1987.

[90] P. Lander, P. Gomis, G. Hartman, K. Gates, J. Petterson, and G. Wagner. Analysis of high-resolution ECG changes during percutaneous transluminal coronary angioplasty. *J Electrocardiol*, 28(Suppl):S39–S40, 1995.

[91] L.J. Leon and B.M. Horáček. Computer model of excitation and recovery in the anisotropic myocardium. I. Rectangular and cubic arrays of excitable elements. *J Electrocardiol*, 24:1–15, 1991.

[92] G. Ling and R.W. Gerard. The normal membrane potential of frog sartorius fibers. *J Cell Physiol*, 34:383–396, 1949.

[93] R.L. Lux. Electrocardiographic mapping: noninvasive electrophysiological cardiac imaging. *Circulation*, 87:1040–1042, 1993.

[94] M.S. Lynn and W.P. Timlake. The numerical solution of singular integral equations of potential theory. *Numer Math*, 11:77–98, 1968.

[95] E. Macchi. *Digital Computer Simulation of the Atrial Electrical Excitation Cycle in Man.* PhD thesis, Dalhousie University, Halifax, N.S., 1973.

[96] R. MacLeod, R. Lux, M. Fuller, and B. Taccardi. Evaluation of novel measurement methods for detecting heterogeneous repolarization. *J Electrocardiol*, 29(Suppl):S145–S153, 1996.

[97] R.S. MacLeod. *Percutaneous Transluminal Coronary Angioplasty as a Model of Cardiac Ischemia: Clinical and Modelling Studies.* PhD thesis, Dalhousie University, Halifax, N.S., 1990.

[98] R.S. MacLeod, M.J. Gardner, R.M. Miller, and B.M. Horáček. Application of an electrocardiographic inverse solution to localize ischemia during coronary angioplasty. *J Cardiovasc Electrophysiol,* 6:2–18, 1995.

[99] R.S. MacLeod, B.K. Hoyt, P.J. MacInnis, R.V. Potter, and B.M. Horáček. A body surface potential mapping unit for recording during coronary angioplasty. In *IEEE Engineering in Medicine and Biology Society 10th Annual International Conference,* pages 97–98. IEEE Press, 1988.

[100] G.M. Maratos. *Time and Frequency Domain Regularization of Solutions to the Inverse Problem in Electrocardiography.* Master's thesis, Northeastern University, Boston, MA, 1992.

[101] R.E. Mason and I. Likar. A new system of multiple-lead exercise electrocardiography. *Am Heart J,* 71:196–205, 1966.

[102] W. McAlpine. *Heart and Coronary Arteries.* Springer-Verlag, New York, 1975.

[103] J.W.H. Meijs, O.W. Weier, M.J. Peters, and A. van Oosterom. On the numerical accuracy of the boundary element method. *IEEE Trans Biomed Eng,* BME-36:1038–1049, 1989.

[104] B.J. Messinger-Rapport and Y. Rudy. The inverse problem in electrocardiography: A model study of the effects of geometry and conductivity parameters on the reconstruction of epicardial potentials. *IEEE Trans Biomed Eng,* BME-33:667–676, 1986.

[105] B.J. Messinger-Rapport and Y. Rudy. Regularization of the inverse problem in electrocardiography: a model study. *Math Biosci,* 89:79–118, 1988.

[106] B.J. Messinger-Rapport and Y. Rudy. Computational issues of importance to the inverse recovery of epicardial potentials in a realistic heart-torso geometry. *Math Biosci,* 97:85–120, 1989.

[107] D.M Mirvis. Physiologic bases for anterior ST-segment depression in patients with acute inferior wall myocardial infarction. *Curr in Cardiol,* 116:1308–1322, 1988.

[108] D.M. Monro, P.J. Bones, R. de Stanbridge, and R.W. Jones. Comparison of epicardial and body surface ECG potentials in man. *Cardiovasc Res,* 20:201–207, 1986.

[109] T.J. Montague, R.M. Miller, M.A. Henderson, R.G. Macdonald, R.S. MacLeod, F.X. Witkowski, and B.M. Horáček. Persistent changes in the body surface electrocardiogram following successful coronary angioplasty. *J Electrocardiol*, 21(Suppl):S91–S98, 1989.

[110] T.J. Montague, E.R. Smith, D.A. Cameron, P.M. Rautaharju, G.A. Klassen, C.S. Flemington, and B.M. Horáček. Isointegral analysis of body surface maps: surface distribution and temporal variability in normal subjects. *Circulation*, 63:1167–1172, 1981.

[111] V.A. Morozov. *Regularization Methods for Ill-Posed Problems*. CRC Press, Boca Raton, 1993.

[112] E. Musso, D. Stilli, E. Macchi, B. Aimi, P. Francescon, L. Cas, C. Manca, M. Kavadias, and F. Kornreich. Diagnostic features of body surface potential maps in patients with myocardial ischemia and normal resting 12-lead electrocardiograms. *Am J Cardiol*, 65:973–979, 1990.

[113] J. Nenonen, J.A. Edens, L.J. Leon, and B.M. Horáček. Computer model of propagated excitation in the anisotropic human heart: I. Implementation and algorithms. In *Computers in Cardiology*, pages 545–548, IEEE Computer Society Press, Los Alamitos, CA, 1991.

[114] J. Nenonen, J.A. Edens, L.J. Leon, and B.M. Horáček. Computer model of propagated excitation in the anisotropic human heart: II. Simulation of extracardiac fields. In *Computers in Cardiology*, pages 217–220, IEEE Computer Society Press, Los Alamitos, CA, 1991.

[115] J. Nenonen, C.J. Purcell, B.M. Horáček, G. Stroink, and T. Katila. Magnetocardiographic functional localization using a current dipole in a realistic torso. *IEEE Trans Biomed Eng*, BME-38:658–664, 1991.

[116] T.F. Oostendorp, A. van Oosterom, and G. Huiskamp. Interpolation on a triangulated 3D surface. *J Comp Physics*, 80:331–343, 1989.

[117] H.S. Oster and Y. Rudy. The use of temporal information in the regularization of the inverse problem in electrocardiography. *IEEE Trans Biomed Eng*, BME-39:65–75, 1992.

[118] H.S. Oster and Y. Rudy. Regional regularization of the electrocardiographic inverse problem: a model study using spherical geometry. *IEEE Trans Biomed Eng*, BME-44:188–199, 1997.

[119] H.S. Oster, B. Taccardi, R.L. Lux, P.R. Ershler, and Y. Rudy. Noninvasive electrocardiographic imaging: reconstruction of epicardial potentials, electrocardiograms, and isochrones and localization of single and multiple electrocardiac events. *Circulation*, 96:1012–1024, 1997.

[120] H.S. Oster, B. Taccardi, R.L. Lux, P.R. Ershler, and Y. Rudy. Electrocardiographic imaging: noninvasive characterization intramural myocardial activation from inverse-reconstructed epicardial potentials and electrograms. *Circulation*, 97:1496–1507, 1998.

[121] M. Papouchado, P.R. Walker, M.A. James, and L.M. Clarke. Fundamental differences between the standard 12-lead electrocardiograph and the modified (Mason–Likar) exercise lead system. *Eur Heart J*, 8:725–733, 1987.

[122] C.J. Penney, J.C. Clements, M.J. Gardner, L.D. Sterns, and B.M. Horáček. The inverse problem of electrocardiography: application to localization of Wolff-Parkinson-White pre-excitation sites. In *IEEE Engineering in Medicine and Biology Society 17th Annual International Conference*. IEEE Press, 1995.

[123] C.J. Penney, L.M. Title, S.E. Iles, J.C. Clements, M.J. Gardner, and B.M. Horáček. Comparison of 'electrophysiologic imaging' and radionuclide imaging in quantification of controlled cardiac ischemia. In A. Murray and R. Arzbaecher, editors, *Computers in Cardiology*, pages 79–82, IEEE Computer Society Press, Los Alamitos, CA, 1995.

[124] M. Pfisterer, J. Muller-Brand, P. Spring, V. Bassignana, and W. Kiowski. Assessment of the extent of jeopardized myocardium during acute coronary artery occlusion followed by reperfusion in man using technetium-99m isonitrile imaging. *Am Heart J*, 122:7–12, 1991.

[125] T.C. Pilkington, M.N. Morrow, and P.C. Stanley. A comparison of finite element and integral equation formulations for the calculation of electrocardiographic potentials - II. *IEEE Trans Biomed Eng*, BME-34:258–260, 1987.

[126] R. Plonsey. *Bioelectric Phenomena*. McGraw-Hill, New York, 1969.

[127] I. Preda, R. Nadeau, P. Savard, D. Hamel, D. Palisaitis, M. Shenasa, and J. Nasmith. QRS alterations in body surface potential distributions during percutaneous transluminal coronary angioplasty in single-vessel disease. *J Electrocardiol*, 27:311–322, 1994.

[128] W.H. Press, B.P. Flannery, S.A. Teukolsky, and W.T. Vetterling. *Numerical Recipes: The Art of Scientific Computing*. Cambridge University Press, Cambridge, 1986. p. 495.

[129] The principal investigators of CASS and their associates. The National Heart, Lung, and Blood Institute Coronary Artery Surgery Study (CASS). *Circulation*, 63(Suppl I):I-1-I-81, 1981.

[130] C.J. Purcell. *A Comparison of Electric and Magnetic Body Surface Mapping Using Single Moving Dipole Inverse Solutions*. PhD thesis, Dalhousie University, Halifax, N.S., 1988.

[131] J. Radon. Zur mechanischen Kubatur. *Monatsh Mathematik*, 52:286–300, 1948.

[132] M. Ramsey III. *Comparison of Epicardial Potentials with Measured and Simulated Torso Potentials for Ventricular Depolarization and Repolarization in the Dog*. PhD thesis, Duke University, Durham, NC, 1974.

[133] K.A. Reimer and R.B. Jennings. Myocardial ischemia, hypoxia and infarction. In H.E. Fozzard *et al.*, editor, *The Heart and Cardiovascular System*, chapter 53, pages 1133–1201. Raven Press, New York, 1986.

[134] H.J. Ritsema van Eck. *Digital Computer Simulation of Cardiac Excitation and Repolarization in Man*. PhD thesis, Dalhousie University, Halifax, N.S., 1972.

[135] H. Roozen and A. van Oosterom. Computing the activation sequence at the ventricular heart surface from body potentials. *Med Biol Eng Comput*, 25:250–260, 1987.

[136] Y. Rudy and B.J. Messinger-Rapport. The inverse problem in electrocardiography: solutions in terms of epicardial potentials. *CRC Crit Rev Biomed Eng*, 16:215–268, 1988.

[137] Y. Rudy and R. Plonsey. A comparison of volume conductor and source geometry effects on body surface and epicardial potentials. *Circ Res*, 46:283–291, 1980.

[138] H. Saetre, R. Startt/Selvester, J. Solomon, K. Baron, J. Ahmad, and M. Ellestad. 16-lead ECG changes with coronary angioplasty: location of ST-T changes with balloon occlusion of five arterial perfusion beds. *J Electrocardiol*, 24(Suppl):S153–S162, 1991.

[139] R.H. Selvester, N.B. Wagner, and G.S. Wagner. Ventricular excitation during percutaneous transluminal angioplasty of the left anterior descending coronary artery. *Am J Cardiol*, 62:1116–1121, 1988.

[140] A.V. Shahidi, P. Savard, and R. Nadeau. Forward and inverse problems of electrocardiography: modeling and recovery of epicardial potentials in humans. *IEEE Trans Biomed Eng*, BME-41:249–256, 1994.

[141] M. Shenasa, D. Hamel, J. Nasmith, R. Nadeau, J.-L. Dutoy, D. Derome, and P. Savard. Body surface potential mapping of ST-segment shift in patients undergoing percutaneous transluminal coronary angioplasty: correlations with the electrocardiogram and vectorcardiogram. *J Electrocardiol*, 26:43–51, 1993.

[142] P.P. Silvester and S. Tymchyshyn. Finite-element modeling of the inhomogeneous human thorax. *Adv Cardiol*, 10:46–50, 1974.

[143] P.J. Slomka, G.A. Hurwitz, G. St. Clement, and J. Stephenson. Three-dimensional demarkation of perfusion zones corresponding to specific coronary arteries: application for automated interpretation of myocardial SPECT. *J Nucl Med*, 36:2120–2126, 1995.

[144] M.S. Spach, R.C. Barr, C.F. Lanning, and P.C. Tucek. Origin of body surface QRS and T-wave potentials from epicardial potential distributions in the intact chimpanzee. *Circulation*, 55:268–278, 1977.

[145] M.S. Spach, R.C. Barr, C.F. Lanning, and P.C. Tucek. Experimental basis of QRS and T-wave potentials in the WPW syndrome: the relation of epicardial to body surface potential distributions in the intact chimpanzee. *Circ Res*, 42:103–118, 1978.

[146] H. Spekhorst, A. SippensGroenewegen, G.K. David, and M.J. Janse. Body surface mapping during percutaneous transluminal coronary angioplasty (PTCA): ST-Segment changes during ischemia. *Circulation*, 78(Suppl II):II–577, 1988.

[147] H. Spekhorst, A. SippensGroenewegen, G.K. David, M.J. Janse, and A.J. Dunning. Body surface mapping during percutaneous transluminal coronary angioplasty: QRS-changes indicating regional myocardial conduction delay. *Circulation*, 81:840–849, 1990.

[148] P.G. Steg, M. Faraggi, D. Himbert, J.-M. Juliard, A. Cohen-Solal, R. Lebtahi, R. Gourgon, and D.L. Guludec. Comparison using dynamic vectorcardiography and MIBI SPECT of ST-segment changes and myocardial MIBI uptake during percutaneous transluminal coronary angioplasty of the left anterior descending coronary artery. *Am J Cardiol*, 75:998–1002, 1995.

[149] W.J. Sternberg and T.L. Smith. *The Theory of Potential and Spherical Harmonics*. University of Toronto Press, Toronto, 1946.

[150] O.N. Strand and E.R. Westwater. Minimum-rms estimation of the numerical solution of a Fredholm integral equation of the first kind. *SIAM J Numer Anal*, 5:287–295, 1968.

[151] A.H. Stroud. *Approximate Calculation of Multiple Integrals.* Prentice-Hall, Englewood Cliffs, NJ, 1971.

[152] B. Surawicz. ST-Segment, T-wave, and U-wave changes during myocardial ischemia and after myocardial infarction. *Can J Cardiol,* 2(Suppl A):71A–84A, 1986.

[153] B. Surawicz. Reversible QRS changes during acute myocardial ischemia. *J Electrocardiol,* 31:209–220, 1998.

[154] B. Surawicz, C. Orr, J. Hermiller, K. Bell, and R. Pinto. QRS changes during percutaneous coronary angioplasty and their possible mechanisms. *J Am Coll Cardiol,* 30:452–458, 1997.

[155] A.N. Tikhonov. On the solution of incorrectly posed problems and the method of regularization. *Sov Math Dokl,* 4:1035–1038, 1963.

[156] A.N. Tikhonov and V.Y. Arsenin. *Solutions of Ill-Posed Problems.* Wiley, New York, 1977.

[157] W. Trautwein and J. Dudel. Aktionspotential und Kontraktion des Herzmuskels im Sauerstoffmangel. *Pflugers Arch,* 263:23–32, 1956.

[158] S. Twomey. On the numerical solution of Fredholm integral equations of the first kind by the inversion of the linear system produced by quadrature. *J Assoc Comp Mach,* 10:97, 1963.

[159] G.S. Wagner, R.H. Selvester, N.B. Wagner, and M.W. Krucoff. QRS changes during acute ischemia induced by balloon occlusion of the LAD artery. *J Electrocardiol,* 20(Suppl):S18–S19, 1988.

[160] N. Wagner, D. Sevilla, M. Krucoff, K. Pieper, K. Lee, R. White, K. Kent, R. Renzi, R. Selvester, and G. Wagner. Transient alterations of the QRS complex and and ST segment during percutaneous tranluminal coronary angioplasty of the right and left circumflex coronary arteries. *Am J Cardiol,* 63:1208–1213, 1989.

[161] N.B. Wagner, C.D. Sevilla, M.W. Krucoff, K.L. Lee, K.S. Pieper, K.K. Kent, R.K. Bottner, R.H. Selvester, and G.S. Wagner. Transient alterations of the QRS complex and ST-segment during percutaneous transluminal balloon angioplasty of the left anterior descending coronary artery. *Am J Cardiol,* 62:1038–1042, 1988.

[162] Y. Yamashita and T. Takahashi. Use of the finite element method to determine epicardial from body surface potentials under a realistic torso model. *IEEE Trans Biomed Eng*, BME-31:611–621, 1984.